# Improving Anionic redox modeling by accounting for collective effects

Jean Vergnet

# Sorbonne Université

ED 397 – Physique et Chimie des Matériaux

*Laboratoire de chimie du solide et énergie – Collège de France*


# Improving anionic redox modeling by accounting for collective effects


By Jean Vergnet


PhD thesis in Chemistry

Directed by Jean-Marie Tarascon

Presented and defended in public on September 9th, 2020

In front of a jury composed of :

| | | |
|---|---|---|
| Dr. Stéphane Jobic | Research Director, IMN, Nantes | Referee |
| Prof. Silke Biermann | Professor, CPHT, Palaiseau | Referee |
| Dr. Laurence Croguennec | Research Director, ICMCB, Bordeaux | Examiner |
| Dr. Benjamin Rotenberg | Research Director, PHENIX, Paris | Examiner |
| Dr. Marie-Liesse Doublet | Research Director, ICGM, Montpellier | Invited |
| Prof. Jean-Marie Tarascon | Professor, Collège de France, Paris | Director |
| Dr. Matthieu Saubanère | Research Fellow, ICGM, Montpellier | Supervisor |

# Acknowledgments

I would like to thank Jean-Marie Tarascon for the opportunity to do research at the College de France, as a master student then as a PhD. Despite his encyclopedic knowledge, he knows how to make things simple and clear and it has been a continuous challenge to do the same.

My grateful thanks also go to Marie-Liesse Doublet, who welcomed me at the ICGM and provided training, discussion, challenge and, last but not least, computational facilities. I have come to learn and respect her unwavering ethics, both in human relations and in scientific reasoning.

Thanks to Matthieu Saubanère, who joyfully transmitted his powerful intuition and enthusiasm for physics, especially in unexpected situations, and there has been many. His crude sarcasms & the poor quality of his jokes fail to hide the kindness and subtlety buried deep within.

Thanks to Gaurav for intense discussion on life and science, to Qing for her strong yet discreet support, for Laurie, Thomas D., Thomas M. and all the other members of the CSE lab. Thanks to Arthur and to the rest of the CTMM for the welcoming atmosphere.

Thanks to Claire Lajoie-Mazenc for providing a refreshing change of perspective, which has proved valuable beyond expectations, and to all the board of the CT-SMP who made it possible.

Thanks to Silke Biermann, who was there at the beginning of this adventure when she introduced me to the field of batteries along with Thierry Gacoin, and is also present at the other end. Thanks to all the jury members for their time reading the manuscript.

Thanks to Flavio and Dylan, for their help in the final steps of writing.

To the Old School Community.

To my friends, old and new.

To my family, and to Estelle, who helped me grow from the challenges I faced.

The Universe in not only queerer than we imagine,
it is queerer than we can imagine.

---

John B. S. Haldane, Possible Worlds

# Batteries and the energy transition

## The challenges of energy transition

Energy demand will grow relentlessly by more than 1% per year, leading to an increase of 35% in 2040[1]. The energy production is responsible for two-thirds of the $CO_2$ emissions because of the use of fossil fuels (coal, oil, and gas). In order to mitigate the associated greenhouse effect, many countries have taken commitment to reduce their emissions thus increasing the part of renewable sources in their energy consumption, either in the transport sector (20% of $CO_2$ emission) or the electricity production (50% of $CO_2$ emissions), as illustrated in fig. 1. Unfortunately, while fossil fuels can be easily stored to adapt the production to the demand, renewable energies are intermittent and they are converted into electricity which cannot be stored. There are thus many systemic challenges to address before turning to an all renewable society. Fortunately, batteries as a means of electrical energy storage, can help bridge these gaps, either for the mobility, the electricity generation, or the grid operation.

## Enabling electric vehicles

Industrial and individual mobility is mainly powered by fossil fuel (<1% electrical cars) because this is the field where replacing fossil fuel proves the most difficult. Indeed, transportation applications require to have a quickly rechargeable and very dense energy source and while this is natural for fossil fuel (diesel 10 kWh/L), it is hard to achieve with electrical energy. However, despite their comparatively lower energy density (Li-Ion: 500 Wh/L), batteries have proven to be a viable solution for short-range application as they could be easily integrated into existing car or bus designs with excellent energy yields. This perspective induced huge investment in battery manufacturing plants to increase

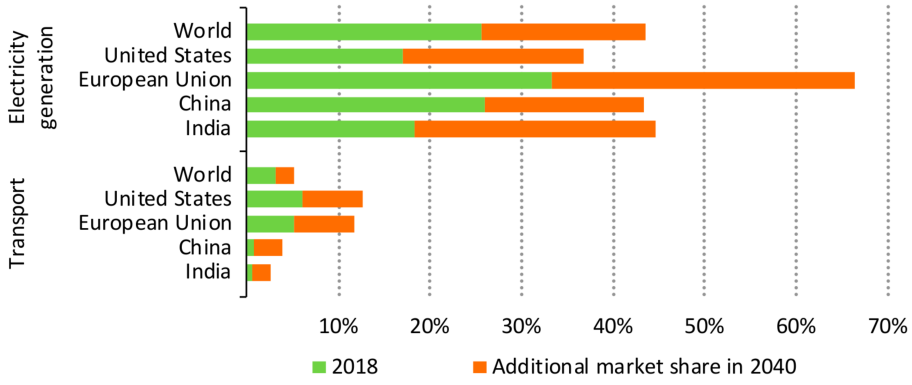


Figure 1: Renewable energy in total primary energy demand by category and region, 2018 and 2040. Adapted from [1].

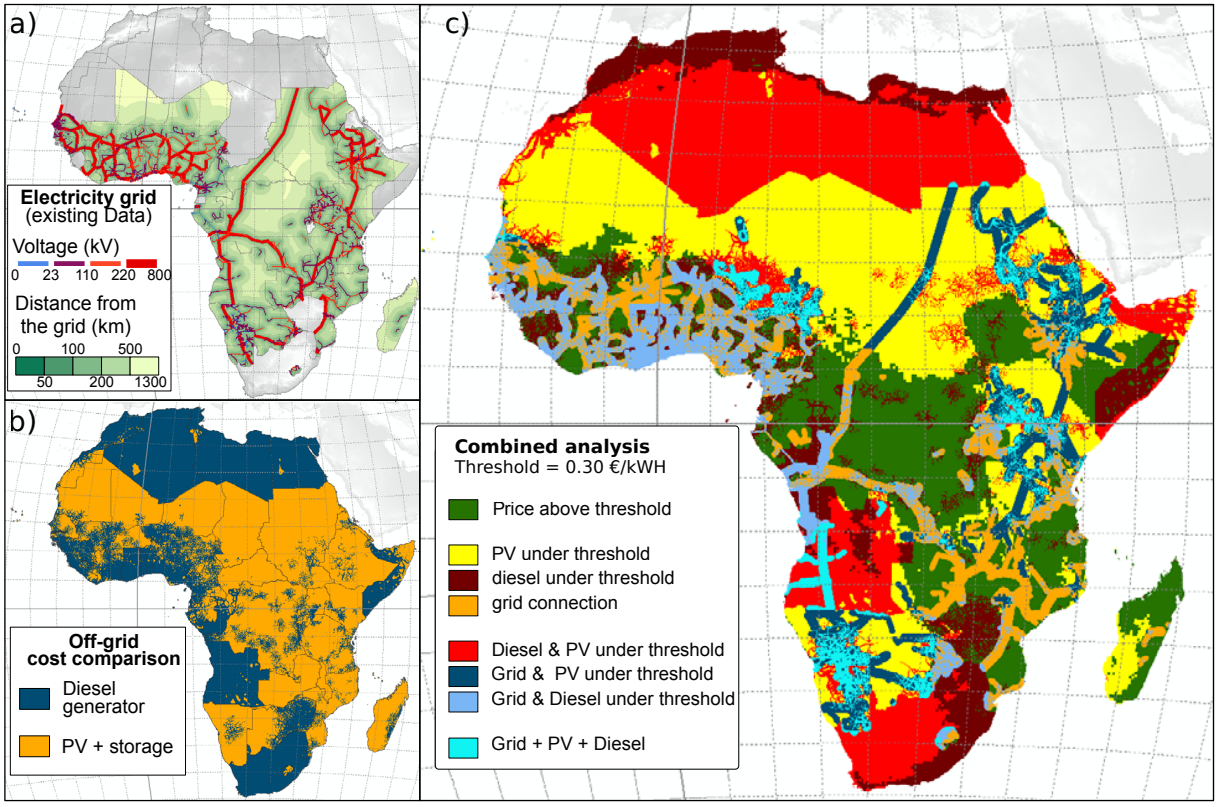


Figure 2: Off-grid options: economic comparison of diesel versus photovoltaic energy (PV) on the African continent. Adapted from [3].

the energy density while decreasing the cost. This price decrease allowed electric vehicle to become competitive with high-end fuel powered cars, thus allowing for the massive electrification of individual electric vehicles.[2] However, this electrification is only useful if the electrical energy consumed by the car comes from decarbonated sources.

## Providing off-grid electricity

Renewable energy sources are, by nature, localized and intermittent. Energy storage, by acting as a buffer between production and consumption, allows to take advantage of this localized production to provide a local yet reliable energy source in remote regions. In non-interconnected zones, such as islands or rural regions (light green zone in fig. 2.a) the development of cheap and powerful batteries (driven by the automotive sector) coupled with the already well developed solar panels technology now provides a cheaper and more reliable access to energy than fuel-based generation (orange zone in fig. 2.b). Therefore, beyond the environmental benefit, batteries provide a social gain by enabling fast and cheap electrification using local micro-grids which may afterwards be connected to the national grids. These regions and their inhabitants represent an important part of the world population, especially in the African continent (yellow zone in fig. 2.c).

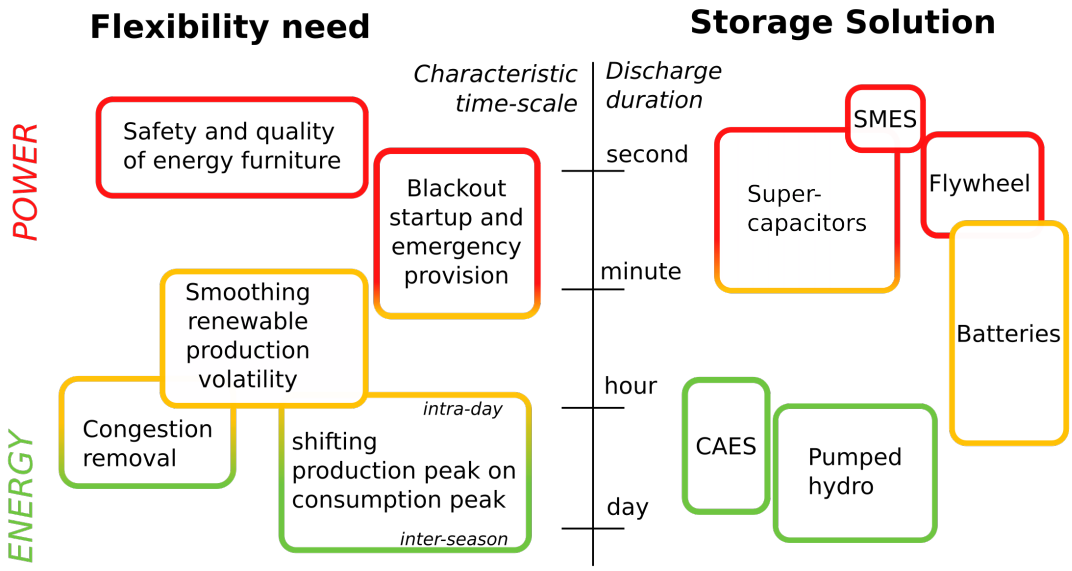


Figure 3: Flexibility needed to mitigate renewable energy penetration and available storage technologies, compared in terms of characteristic use-time. Batteries are the only technology that can smooth the intermittent renewable energy production. From [4].

### Stabilizing the grid to allow renewable penetration

In grid-connected zones, the production of renewable energy also causes stability issues. Here again, energy storage can mitigate instability by buffering the load at the hour time-scale, by displacing the renewable production excess on the consumption peak, or at the minute time-scale, thus reducing the volatility of the production.[5] Furthermore, in these historically centralized grids, the multiplication of energy sources may cause a congestion on the network when favorable weather conditions boost renewable production. In this case, the network insufficient power capacity leads to curtailing the excess of renewable energy production. Storing such over-production allows avoiding the loss of green energy.[6] Finally, increasing renewable energies penetration is also synonym of fewer heat-powered energy production plants relying on mechanical turbines. This decrease has many adverse consequences such as loss of mechanical inertia or difficult grid frequency synchronization (50 Hz), which may also be mitigated by fast-response storage (see pp. 56-95 of ref. [7] for further discussion on a 100% renewable grid).

While many technologies of storage are available, batteries seem to be the most adapted to the problems raised by renewable energy production (see fig. 3).[4], [5] The requirements are numerous and hard to fulfill (e.g. high energy, power, safety, etc). However, recent advances in technology allowed have Li-ion to meet such standards at a commercially sound price. Having understood the crucial role of batteries for the energy transition on a macroscopic level, we will now dive into the material scale, to discuss the state of the art and development prospect of the Li-ion technology.

# List of publications related to this thesis

— in chronological order —


[1] X. Bai, M. Sathiya, B. Mendoza-Sánchez, A. Iadecola, J. Vergnet, R. Dedryvère, M. Saubanère, A. M. Abakumov, P. Rozier, and J.-M. Tarascon, "Anionic Redox Activity in a Newly Zn-Doped Sodium Layered Oxide P2-$Na_{2/3}Mn_{1-y}Zn_yO_2$ ($0 < y < 0.23$)", *Advanced Energy Materials*, vol. 8, no. 32, p. 1 802 379, Nov. 2018.

[2] J. Vergnet, "Stockage électrochimique : revue des technologies émergentes", *REE 2018-5*, vol. 2018, no. 5, pp. 57–70, Dec. 22, 2018.

[3] M. Ben Yahia, J. Vergnet, M. Saubanère, and M.-L. Doublet, "Unified picture of anionic redox in Li/Na-ion batteries", *Nature Materials*, vol. 18, no. 5, pp. 496–502, May 2019.

[4] Q. Wang, S. Mariyappan, J. Vergnet, A. M. Abakumov, G. Rousse, F. Rabuel, M. Chakir, and J.-M. Tarascon, "Reaching the Energy Density Limit of Layered O3-$NaNi_{0.5}Mn_{0.5}O_2$ Electrodes via Dual Cu and Ti Substitution", *Advanced Energy Materials*, p. 1 901 785, Aug. 9, 2019.

[5] S. Saha, G. Assat, M. T. Sougrati, D. Foix, H. Li, J. Vergnet, S. Turi, Y. Ha, W. Yang, J. Cabana, G. Rousse, A. M. Abakumov, and J.-M. Tarascon, "Exploring the bottlenecks of anionic redox in Li-rich layered sulfides", *Nature Energy*, vol. 4, no. 11, pp. 977–987, Nov. 2019.

[6] J. Vergnet, M. Saubanère, M.-L. Doublet, and J.-M. Tarascon, "The Structural Stability of P2-Layered Na-Based Electrodes during Anionic Redox", *Joule*, vol. 4, no. 2, pp. 420–434, Feb. 2020.

[7] J. Vergnet, M. Saubanère, and J.-M. Tarascon, "Estimating anionic redox reversibility using a molecular model", *Manuscript in preparation*, 2020.

# Contents

## Results & Discussion

## Annexes

# List of Abbreviations

COOP Crystal Orbital Overlap Population

HOMO Highest Occupied Molecular Orbital

J-T Jahn-Teller

M.O. Molecular orbital

NMgMO $Na_{2/3}Mg_{1/3}Mn_{2/3}O_2$

NZnMO $Na_{2/3}Zn_{1/3}Mn_{2/3}O_2$

pDOS Projected Density of States

A.R. Anionic Redox

DFT Density Functionnal Theory

DOS Density of States

DRS Disordered Rock-Salt Structure

ELF Electron Localization Function

LMCT Ligand-to-metal charge transfer

RCM Reductive coupling mechanism

TM Transition Metal

XRD X-Ray Diffraction

ZSA Zaanen, Sawatzky and Allen

NCA $LiNi_xCo_yAl_zO_2$

NMC $LiNi_xMn_yCo_zO_2$

SEI Solid Electrolyte Interphase

STEM Scanning Transmission Electron Microscopy

# Nomenclature

| | |
|---|---|
| $\left\langle h^O \right\rangle$ | Number of hole(s) averaged on all oxygens |
| $h^O$ | Number of hole(s) on one oxygen |
| $\chi$ | Electronegativity |
| $\Delta_{CT}$ | Charge-Transfer Energy $\Delta_{CT} = \mu_M - \mu_O$ |
| $\langle n_{MO} \rangle$ | Number of covalent M-O bond averaged over all oxygens |
| $\mu$ | Electro-chemical potential |
| $n_{e^-}$ | Number of electrons in the cell |
| $n_{MO}$ | Number of covalent M-O bond on one oxygen |
| $S$ | Orbital overlap |
| $\vert \mathrm{O}_{2p}$ | Non-bonding oxygen 2p state |
| $\vert \mathrm{O}_{2s}$ | Non-bonding oxygen 2s state |
| $\mathrm{e}^-$ | Electron |
| U | d-band Coulomb Repulsion |

# Introduction

# A Brief history of Li-ion battery through materials

If I have seen further
it is by standing on the shoulders of Giants.

Isaac Newton

The 2019 Nobel Prize in Chemistry was awarded jointly to John B. Goodenough, M. Stanley Whittingham, and Akira Yoshino "for the development of lithium-ion batteries".[8] This is an unmistakable sign of the tremendous role these batteries have played in our modern lives in the past few decades. After shortly describing the main components of a battery, this chapter retraces the emergence and the evolution of the Li-ion battery from the early 1980's to the state-of-the-art commercial batteries and finishes by presenting the main trends in Li-ion research with a special focus on the anionic redox compounds.

## 1 What is a battery ?

### 1.1 Atomic description

A battery is an electrochemical device which converts chemical energy into electrical energy. If this conversion is reversible, i.e. the battery is rechargeable, this device is called a *secondary battery*, or accumulator. This conversion between electrical and chemical energies relies on the exchange of electrons ($e^-$) and positively charged ions between two electrodes, which are thus electrically and ionically conductive. They are most often solids. The ions are transmitted through an electrically insulating media, called the electrolyte, which may be liquid or solid. The transfer of electron occurs through an external electrical circuit which may receive or provide energy to the chemical system.

In order to maintain the charge balance, the movement of both species is closely related (top panel of fig. A.1.a) In discharge, the electrons flow from the negative electrode (anode) to the positive electrode (cathode) and the mobile ions follow this migration to maintain charge balance. In charge, an external voltage is applied to invert the direction of this transfer. This potential difference forces the electrons back into the negative electrode, followed by the positive ions.

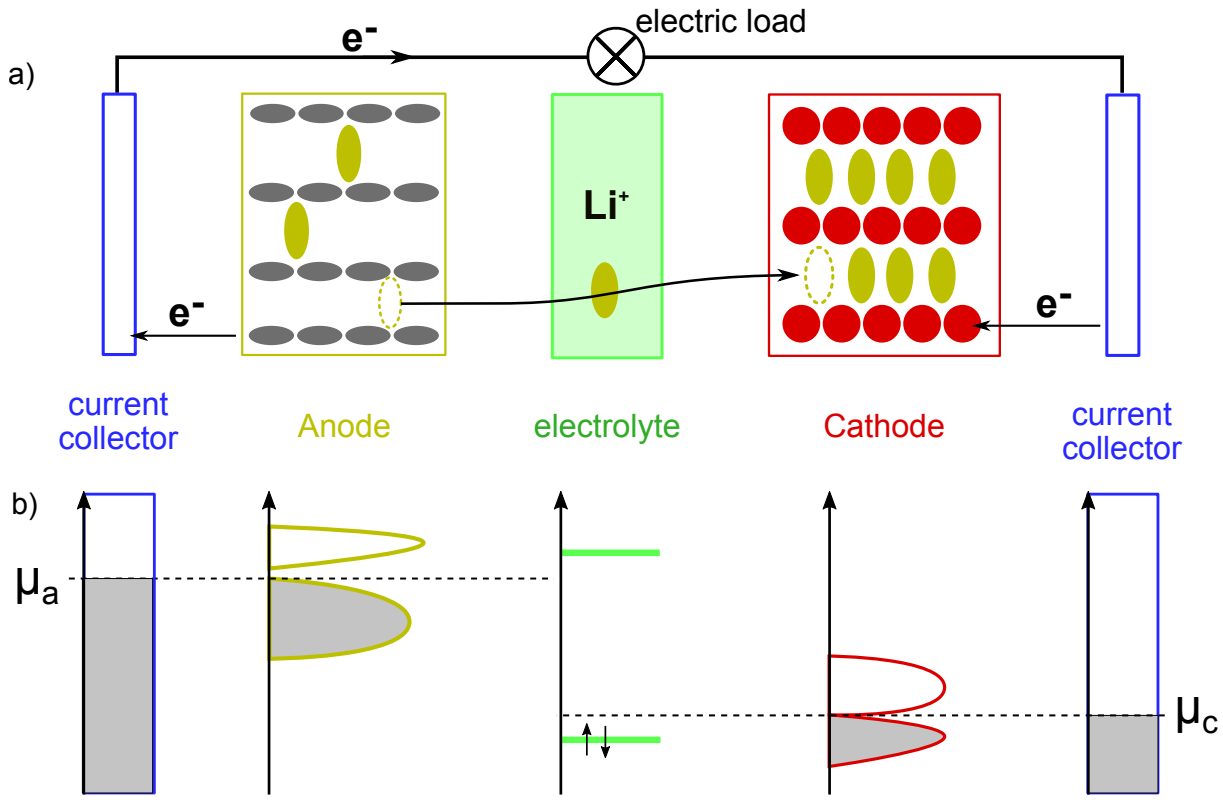


Figure A.1: Schematics of Li-ion battery in discharge. a) Atomic structure: the anode is linked to the cathode via both an ionic conductor media, the electrolyte, or an electronic circuit, composed of two metallic current collectors connected to an external load (⊗). b) Electronic structure: The current collectors are perfect metals, the electrodes are semiconductors (or semi-metal) and, here, the electrolyte is a solution of large bandgap molecules.

There is a wide variety of systems which follow this conceptual description and may thus be called batteries. However the Li-ion technology (and its Na counterpart) are dominating the market thanks to their performances which far exceeds those of other technologies. For the rest of this study, we will therefore focus on alkali-ion technology.

This type of cell is generally composed of a graphite anode, a layered metallic oxide cathode, a liquid electrolyte and two metallic current collectors which may be connected to an external load.

## 1.2 Electronic description

This flow of electrons can be rationalized by considering the electronic structures of each component of the battery (see fig. A.1.b). The current collectors, considered as ideal metals, have a constant density of states (DOS) without gap at the Fermi level. In contrast, the cathode has a gap at the Fermi level since it represents a generic transition-metal (TM) oxide with a partially filled *d*-band. This gap in the *d*-band can be caused either by the crystal field, with a possible Jahn-Teller (J-T) distortion, or by the Coulomb

repulsion between $d$-electrons (Mott-Hubbard gap).[9] The anode may either be a semi-metal (graphite) or a semi-conductor (oxide). The electrolyte is a solution of organic molecules which can either get in contact with the anode or the cathode, and is thus modeled as a single molecule, whose molecular orbital diagram is depicted in green in fig A.1. Based on this electronic picture of the different domain, we can now rationalize the flow of electrons.

To do so, we will rely on the electrochemical potential $\mu$ of each element defined as

$$\mu = \partial E / \partial N$$

where E in the energy of the compound and N the number of its electrons. Thus $\mu$ corresponds to the energy of the Fermi level or equivalently to the energy of the electron of highest energy. Following the conceptual Density Functional Theory (DFT) framework, we can link the electrochemical potential and the electronegativity $\chi$ $\mu = -\chi$.

Following the electronegativity equalization principle, the $\chi$ for the whole compound in its ground state is the average of the $\chi$ of each atom.[10] This principle can then be applied to the battery as a whole. Since the Fermi level of the cathode lies at a lower energy than that of the anode, we have

$$\mu_c < \mu_a$$

where $\mu_c$ and $\mu_a$ are the electrochemical potential of the cathode and anode respectively. If we allow ionic and electrical contact between the two electrodes, the minimization of energy will induce a flow of $e^-$ and $Li^+$ from the cathode to the anode. Thus we retrieve the principle that electrons flow toward the most electronegative compound.

To prevent the self-discharge of the battery (i.e. the flow of electrons in the absence of electrical contact between the current collectors) the electrolyte flooding these electrodes must be electronically insulating. Therefore, its empty levels must not be populated by the anode electrons and its occupied levels must not transfer electrons to the cathode empty levels. This double requirement implies that the bandgap of the electrolyte should be larger than the working voltage of the battery.

The energy of a battery is defined as

$$W = \int V.I.dt = \int V.dC = \langle V \rangle .C$$

, with $V$ the cell voltage (and $\langle V \rangle$ its average), $C$ the capacity, and $I$ the intensity. The energy density (or specific energy) is defined as $W/m$, where m is the mass of active material (i.e. the cathode for our purpose). Similarly, the specific capacity is $C/m$.

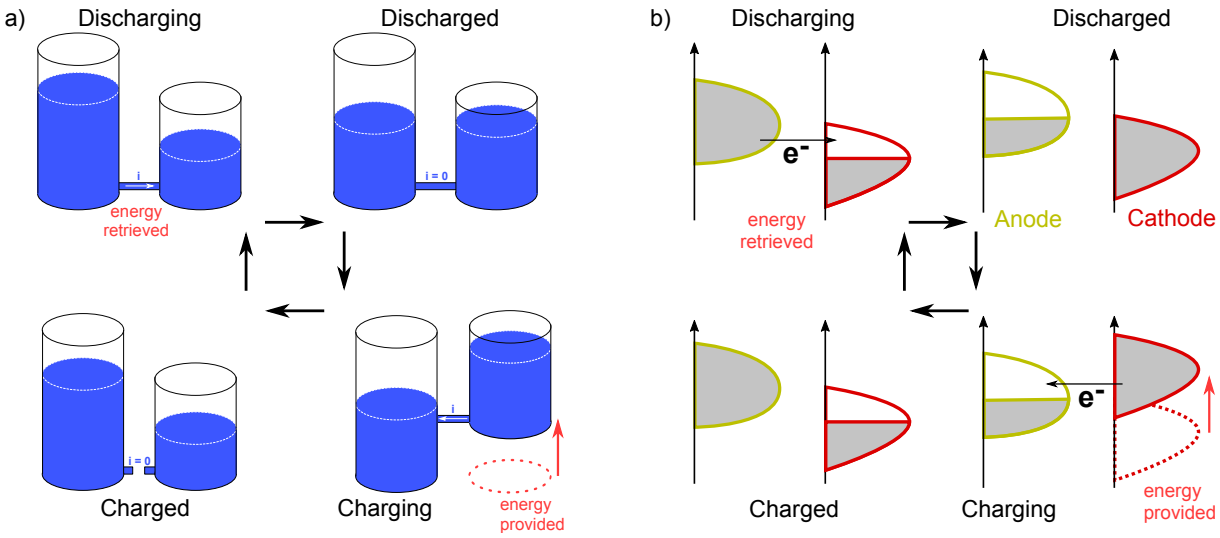


Figure A.2: Water analogy. The water between two tanks (a) follows the same storage cycle as the electrons between the two electrodes of a battery (b).

**Analogy with hydrostatics.** Thanks to similarities in the equations of electrochemical and the gravitational potentials, we can use a powerful analogy between hydrostatics and electrochemistry. The electronegativity equalization principle (which evens out the potential across the system) is analogous to the law of hydrostatics which states that water surface (at atmospheric pressure) should be leveled. Thus the electron flow during charge and discharge to reach this equilibrium is similar to a fluid flowing downward (see fig. A.2). When connecting two water tanks of unequal water height with a pipe, the water will naturally flow downward and energy can be harvested. After some time, the water level in the two tank will be even and no energy can be retrieved: the system is discharged. Now, if we provide some energy to lift one of the tanks, water will flow back. If we disconnect the pipe, we have stored the energy for future use: the system is now charged. As we can deduce, the water tanks represent the electrodes partially filled with electrons. The size of the tank represents the capacity while the water height represents the potential. The pipe represents the external electrical circuit and the lifted tank represents the applied change of potential to one electrode.

# 2 Emergence of the Li-ion battery

## 2.1 Brief history of Li-ion

Modern batteries rely on intercalation compounds composed of a scaffold network – the *host* – which can accommodate ions – the *intercalants* – without major structural changes or volume variation.

The intercalation compounds were already well known at the beginning of the 1970's

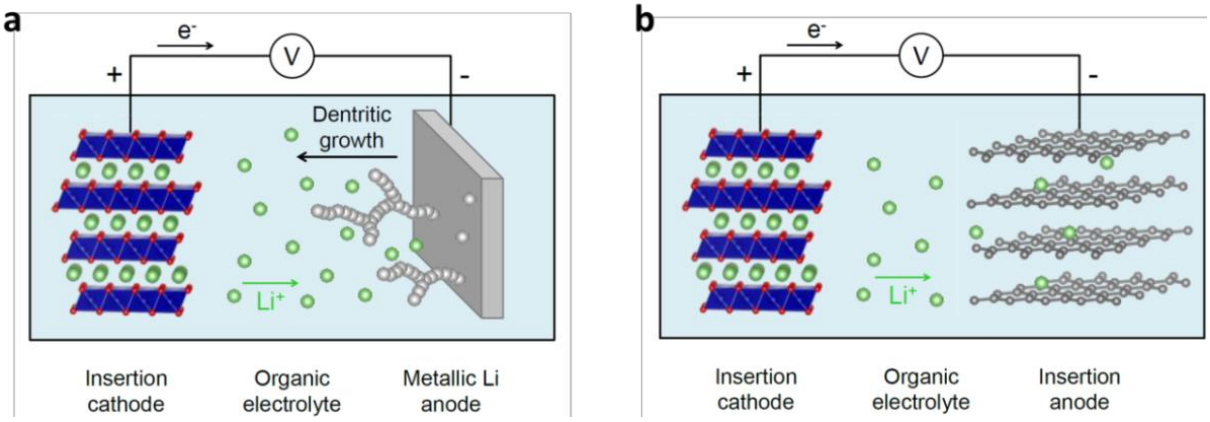


Figure A.3: From Li-Metal to Li-ion. The Li-metal battery (characterized by a Li-metal anode) (a) shows dendritic Li growth which eventually cause short- circuiting thus causing a safety issue. The Li-ion battery (b) having two insertion electrodes is not subject to this risk. The electron/ion flow directions correspond to the charge. From *[14]*.

for their low-dimensional superconductivity.[11] However it was not until 1971 that Rouxel proposed the idea of intercalating lithium for energy storage,[12] which was implemented by Witthigham in 1976 with a $Li_xTiS_2$ cathode and Li-metal anode.[13] Unfortunately, this early battery chemistry could not be commercialized due to dendrite growth which jeopardized its safety. Indeed, when cycling a Li-metal anode, the Li is plated on and stripped off the metal surface. Due to increased electric field on metallic edges, the $Li^+$ cations are preferentially plated on rough surfaces. In turn, this plating increases the surface roughness, eventually leading to dendrite growth towards the other electrode through the separator. The conductive Li dendrite eventually short circuits the two electrodes, thus triggering thermal runaway and sparks, eventually causing fire (see fig. A.3.a).

To address this issue, two directions of research were then envisioned: *i)* the creation of solid electrolyte (or polymer at the time) to control dendrites, leading to lithium metal polymer and *ii)* the use of intercalation compound at both the anode and the cathode (see fig. A.3.b). This intercalation battery which does not rely on plating but on the exchange of a fixed number of Li between two intercalation electrodes, was coined as a "rocking chair battery" by Armand in 1980 [15] and realized by Scrozati in the same year ($LiTiS_2$ / $LiWO_3$).[16] While the concept of modern Li-ion battery was already present at that point, this combination of anode and cathode was not satisfactory application-wise due to poor capacity.

On the cathode side, the use of oxides ($LiCoO_2$) for lithium intercalation was proposed and demonstrated by Goodenough in 1980 to have a much higher voltage than its sulfur counterpart, thus allowing a far larger energy density.[17] Concerning the anode, it was only by 1985 that Yoshino, with his team of Asahi Chemicals, succeeded in using petroleum coke as an anode[18], bringing in the last piece of the puzzle. Subsequent industrial development by Sony thus led to the commercialization of the fist secondary

battery ($LiCoO_2$ / $LiC_6$) in 1991.[19]

The prospect opened by these high-energy batteries sparked a widespread interest and shaped the battery world as we know it today. It is therefore not surprising that the 2019 Nobel Prize was awarded to Wittingham for the invention of the first battery, to Yoshino for the invention of the carbon anode and to Goodenough for the invention of the oxide cathode.[8]

## 2.2 State-of-the-art Li-ion

To achieve ionic intercalation, a cathode compound must have large ionic diffusion pathways, either 1D (channels), 2D (planes) or 3D (network), form ionic bonds with the inserted ion and be able to balance the charge of the ion via the redox of an atom or a group of atoms in the host.

However, there are numerous other requirements for an electrode material beyond the capacity to intercalate lithium.[20] An ideal material should be *electrically conductive* and possess an open-framework structure, for *fast Li diffusion*, with many Li sites available to ensure *a high capacity*. The Li intercalation in these materials should have a negative Gibbs reaction energy (large for the cathode, small for the anode) to ensure *high voltage* and yet, it should not cause (too much) structural change to ensure *reversibility and constant volume*. The delithiated form should have high *thermal and chemical stability*. Finally the electrode should be composed of *inexpensive and sustainable* elements while being *easy to synthesize*. While these requirements are very stringent, the intense research for new materials has lead to the discoveries of several high-performance compounds.

**Anodes.** On the anode side, starting from petroleum coke, the mastering of the solid electrolyte interphase (SEI) has allowed the use of graphite (with capacity of 372 mAh/g). This first step has then led to develop meso-porous carbon (up to 800 mAh/g), with low cost and easy manufacturing, and more recently graphene sheets or nanotubes which reach 1110 mAh/g.[21] Because of their versatility and low cost, carbonaceous compounds are the most widely used anode materials, even though some alternatives exist to target specific application. Among them, lithium titanium oxide offers high power rates and extended lifespan in exchange for a higher cost and lower specific capacity compared to carbon-based anodes.[22] Additionally, Si alloys (on carbon framework) target high capacity applications. Conversion anodes, despite showing attractive capacity, are facing cycling problems which have, so far, prevented their deployment. These results, mainly taken from [21], are summarized in table A.1.

**Cathodes.** On the cathode side, up until the end of the 1990's, there were only three compounds which met the stated requirements – two layered oxides, $LiCoO_2$ and $LiNiO_2$, and the spinel $LiMn_2O_4$.[20] Interestingly, these seminal compounds already contained

| Active anode material | | Capacity (mAh/g) | Advantages | Common issues |
|---|---|---|---|---|
| **Insertion** | Carbonaceous<br>Hard Carbon<br>Nanotubes / graphene | 200 - 1110 | Low potential<br>Low cost<br>Safety | Coulombic efficiency<br>Voltage hysteresis<br>Capacity fading |
| | Titanium oxides<br>$LiTi_4O_5$, $TiO_2$ | 175 – 330 | Extreme safety<br>Cycle life<br>Low cost<br>Power capability | Low capacity<br>High potential |
| **Alloy** | Si, Ge, Sn, Sb<br>SnO, SiO | 600 – 4000 | High capacity<br>Safety | Capacity fading<br>Voltage fading<br>Large volume variation |
| **Conversion** | $MX_y$:<br>M = Fe, Co, Ru, Mn, Ni, Cu<br>X = O, P, S, N | 500 – 1800 | High capacity<br>Low cost<br>Sustainability<br>Low potential (< oxides) | Coulombic efficiency<br>Capacity fading<br>Voltage hysteresis<br>Voltage fading<br>Unstable SEI<br>High cost |

Table A.1: Comparison of Li-ion anode technologies. Adapted from [21].

the essential building blocks used later on. Indeed, the two layered compounds had complementary properties: $LiNiO_2$ showed very good capacity thanks to its two oxidation states ($Ni^{2+}/Ni^{4+}$) but lower stability because of J-T effect in $Ni^{3+}$. Conversely, $LiCoO_2$ showed lower capacity ($Co^{3+}/Co^{4+}$) and better structural stability due to the absence of J-T distortion. This complementarity encouraged for mutual substitution in order to get the better of both.[23] From there, the addition of a third metal added another degree of freedom to optimize the compound. Mn, with moderate capacity and J-T effect, provided an intermediate between Ni and Co, leading to better stability with constant capacity.[24] In contrast, the use of Al, with a fixed oxidation state of +3 and a small radius provided stability and rate capability at the cost of capacity. These substitutions, with varying ratios, have lead to the modern compounds widely used in the industry: $LiNi_xMn_yCo_zO_2$ (NMC) which dominate the market and $LiNi_xCo_yAl_zO_2$ (NCA) for specific power intensive application. Growing ethical and environmental concerns have been a motivation to lower the Co and Ni content, leading to NMC compounds with ever increasing Mn content (NMC 622, NMC 811).[25]

Contrary to layered compounds, the spinel structure could not become commercially viable, despite a vast scientific effort, due to many roadblocks to industrialization. Nevertheless, the research to solve spinel-related issues yielded precious discoveries such as the EC/DMC electrolyte formulation, stable up to 5V, which benefited all Li-ion technolo-

gies.[20] There is now a revival of the research on these materials because they are formed during the cycling of layered compounds and their understanding could help mitigate the voltage fading and the capacity fading, especially in Li-rich layered compounds (see section 3.2).

Later on, the discovery of $LiFePO_4$ by Goodenough's lab in 1997, opened another route of research.[26] The appeal of this compound stems from a higher capacity (with a somewhat lower voltage) than layered oxides, a flat discharge curve and a very good cycling stability. Its very poor electronic conductivity has been overcome by blending nanoparticles of $LiFePO_4$ with carbon, thus shortening the electron pathway within the bad conductor. This achievement opened the way for a vast research on polyanionic compounds (e.g. phosphates, silicates, borates) and their fluorinated derivatives.

All these state-of-the-art cathodes contain transition metal atoms which are both heavier and more expensive than carbon anodes while being less energetically dense. The cathode is thus the bottleneck for both cost and performance improvement in Li-ion batteries.

# 3 Outlook for the future of Li-ion

## 3.1 Research trends for Li-ion

The energy transition calls for batteries which perform better, either in term of cost and lifespan, for the integration of renewable energies, or in terms of density, safety and charging speed for the electrification of transport. To meet these high expectations, several fields of research are intensely investigated.

**Price.** Concerning the price, Na-ion technology seems a cost-effective alternative to Li-ion. Indeed, being very close to Li-ion, Na-Ion can take advantage of the same manufacturing process than Li-ion, thus leveraging the huge industrial investments necessary to build "gigafactories", while allowing to replace expensive materials such as copper current collector by cheap aluminium and Li by Na. Furthermore, when comparing with Li-ion, the slightly lower energy density, due to lower Na insertion voltage, is compensated by a longer lifespan, thus allowing a lower levelized cost of energy.

**Safety.** To improve the lifespan and safety of batteries, the design of room-temperature solid-state electrolyte has been proposed as a solution which avoids flammable electrolyte while preventing dendrite growth and thermal runaway. If using a Li-metal anode and a proper packing layout, this technology may even increase the energy density compared to Li-ion. The main issues are the need for high quality solid-solid interface and the difficulty in finding a solid electrolyte being both stable in a large potential window and ionically conductive.

Concerning the fast charging, efforts have been made to design nano-structured electrodes to enhance the active surface area and thus the rate capability and to work on effective electrode coating to reduce the intercalation kinetic barrier.

**Energy density.** Finally, the increase in energy density of Li-ion can be achieved by increasing either the potential or the capacity of the cathode. In terms of potential, the most advanced cathode materials are already reaching the stability limits of the generic electrolytes. Increasing the cathode voltage therefore implies additional efforts to develop new electrolytes with larger stability windows.[27] Concerning the capacity, if we consider a conventional cationic redox, increasing the capacity requires removing several electrons from the metal which inevitably leads to successive redox couples with distinct insertion potentials.[28] Unfortunately, the second redox potential is generally much lower than the first one so the gain in capacity is mitigated by a decrease of the voltage.[a]

Fortunately, additional capacity can also be achieved by anionic activity. Indeed, since these anions are very electronegative the additional electrons are removed at high potential. Because it allows extra capacity at high voltage, this strategy, coined as the anionic redox (A.R.), has sparked a lot of interest, as illustrated by the numerous compounds that were developed in this framework.

## 3.2 Anionic redox in Li-ion compounds

Early reports of $Li_2MnO_3$ cycling, despite Mn being +IV in the pristine, raised questions about the origin of this unexplained capacity.[29] Since the dichalcogenide layered structure allows various TM substitutions, subsequent reports tried to reproduce and explain this anomalous capacity in partially substituted $Li_2M_xMn_{1-x}O_3$, notably with M=Ni.[30] This study opened the way for various other substitutions [31] eventually leading to the discovery of Li-rich NMC compounds with unprecedented specific energy.[32]

In terms of electrochemical behavior, the Li-rich compounds with $3d$ metal show a specific two-step profile in charge followed by a sloped S-shaped discharge where the cationic activity can never account for the whole capacity. Researchers thus debated over several possibilities starting with the over-oxidation of the TM [29] then with $Li^+/H^+$ cation exchange [33]. Later on, other hypotheses flourished to explain the observed irreversible oxygen loss either by the release of $O_2$ – with decomposition at the interphase [34] – or in the form of $LiO_2$,[33] followed by surface densification.[35] Other reports claimed that after being released, oxygen could be re-accommodated.[36] Finally, after demonstrating that the process also occurred in the bulk, the hypothesis of reversible bulk lattice oxygen activity has been proposed.[32], [37]

[a] Cationic disorder broadens the voltage span of the two processes but does not increase the fundamental capacity.

In order to solve these controversies and propose a satisfactory mechanism, the scientific community looked for simpler anionic redox compounds, with a single metallic center and a more reversible cycling. This was the case of $4d$ lamellar oxide $Li_2RuO_3$. At that time, the mixed anionic and cationic redox were hard to disentangle, leading to the study of the $Li_2Ru_{1-y}Sn_yO_3$ family which only showed anionic redox as tin was electrochemically inactive. The study of this reversible anionic redox compound was the platform for the early description of anionic redox mechanism.[38] Unfortunately, this compound displayed consistent voltage fade. Therefore, in the quest for a completely reversible pure anionic redox compound, Ru was replaced by Ir, thus leading to $Li_2IrO_3$, where the shift from $4d$ to $5d$ metal increased again the TM-O covalency and the cycling reversibility.[14] More recently, $Li_2IrO_3$ was synthesized in a 3D structure which allowed to avoid the degradation associated to TM migration in the Van der Waals gap. The reversibility of this compound was exceptional, leading to the reversible removal of 3 Li / formula with very little voltage fade[39].

This research of simple materials featuring reversible anionic redox, coined as model compounds (or "minimal working example", borrowing a term from computer science) allowed the rationalization of the underlying mechanisms of anionic redox. This has lead to the emergence of the anionic redox model as it was at the beginning of this Ph.D., based on $4d$ and $5d$ mono-metallic layered oxides, which will be presented in the next chapter.

In this chapter, we first introduced the concept of Li-ion battery, from the complementary perspectives of solid-state chemistry and condensed matter physics. We then retraced the emergence of the Li-ion battery, from its first iterations in the early 1980's to the commercially available batteries. Finally we described the main research trends to improve this technology, with a special focus on the experimental quest for higher capacity using anionic redox compounds.

This last topic, here described from an experimental perspective, will be the topic of the second half of this introduction, where we will provide context, explanation and prospects on the theoretical description of this powerful yet often misunderstood phenomenon.

# B Evolution of the anionic redox concept: Influences & state of the art

> The wealth of soft chemistry implied by the occurrence of those holes opens many new and promising prospects. There is a whole chapter on the chemistry of anti-bonds that remains to be written.
>
> Jean Rouxel, 1996 [40]

There are many ways to define anionic redox and both the definition and its understanding have traveled a long journey through chemistry and physics before landing to the concept that is now used in the field of electrochemistry. In this chapter, we will first review the various investigation fields that pre-figured the emergence of anionic redox and helped to define properly. We will then describe the state of the art of the modeling of anionic redox mechanism at the time where this thesis began. Finally, we will list the challenges that this model had to face in the recent years, to keep up with the experimental discoveries.

## 1 Early influences on Anionic Redox concept

The study of electron holes on the anionic network is probably older than the concept of Li-Ion battery itself, as it had already been a very hot topic in the quest for high temperature superconductors. This concept of "oxygen holes" only makes sense in a purely ionic picture of oxides where the electrons are considered to be completely transferred from the metal to the oxygen and any departure from a formal -2 charge on the oxygen is considered an "oxygen hole". Of course, every field of physics and chemistry have acknowledged this departure from the pure ionic picture long ago, leading to different names for this phenomenon: Ligand-to-metal charge transfer in complex chemistry, negative charge transfer in solid state chemistry, electron doped oxides in condensed matter physics,...

In the field of electrochemistry, there has been everlasting debates on the precise definition of anionic redox, but there seems to be a consensus on two minimal requirements. First, the cycling needs to be reversible, so that both oxidation and reduction of the oxygen can be performed without destroying the compound, either in the short or the long term. Second, the compound should display extra-capacity, i.e. exchange more electrons

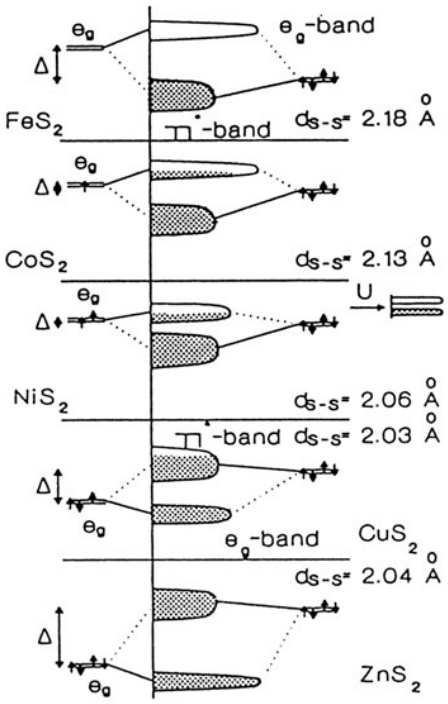


Figure B.1: Nature of the TM-S$^*$ state depending on the relative position of the S-S$^*$ and $M_d$ bands. From [41].

than what could be expected from the sole contribution of the metallic oxidation. Thus we reach the following minimal definition of anionic redox:

> **Anionic redox is a reversible extra-capacity provided by the anionic network.**

In this section, we will first describe how, in the early 1990's, the concept of hole and anti-bond chemistry has been brought to the electrochemistry community in the field of sulfides and selenides. We will then describe how the question was then raised in the oxides in the late 1990's, to explain the anomalous end-of-charge behavior. Finally we will explore the occurrence of anionic redox in non-layered compounds that are the Pnictides in the early 2000's and how they have been key in shaping the modern definition of anionic redox.

## 1.1 Rouxel's anionic polymerization in layered chalcogenides

Jean Rouxel has worked on the transition-metal chalcogenides, of general formula $MX_n$ with X=(S, Se, Te) and M=Fe, Ti. In these compounds, the chalcogenes may form dimers where the antibonding $X_2$ states are partially occupied. If these antibonding states are below the $M_d$ band, the electrons from the metal will reduce the chalcogen and the X-X pairing will not be stable ($FeS_2$ and $CoS_2$ in fig. B.1). However, if the antibonding states

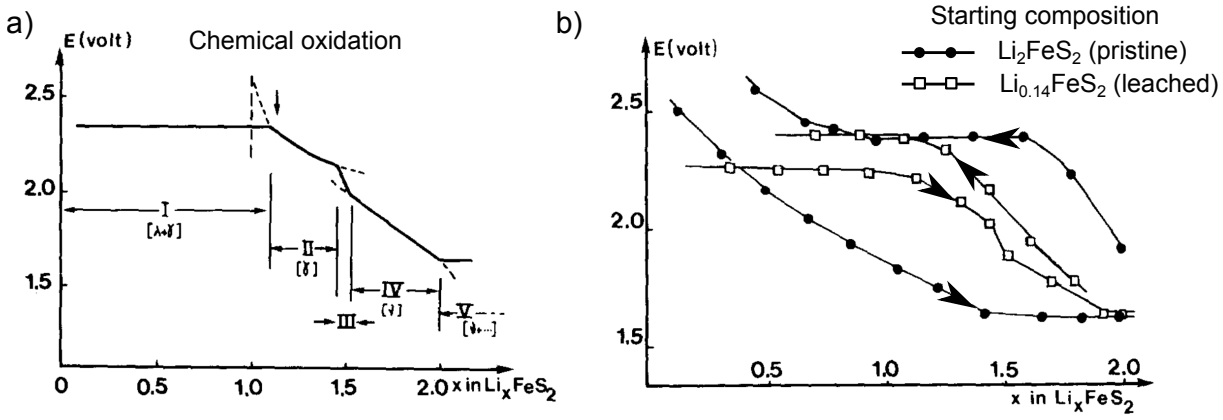


Figure B.2: $Li_2FeS_2$ oxidation. a) Quasi-equilibrium potential obtained from chemically oxidized samples. b) First cycle quasi-equilibrium potentials obtained for $Li_{0.14}FeS_2$ (chemical oxidation) and $Li_2FeS_2$ (pristine). Adapted from [43].

are above the $M_d$ states, the metal will get reduced and holes will appear at the top of the X-X$^*$ band ($CuS_2$ in in fig. B.1). The width of the gap between bonding and antibonding X-X states increases when going from S to Se to Te because the increasing size of the p orbitals allows for a stronger interaction.

This oxidation of the X-X* stabilizes the bonds within the anionic network thus enabling an "anionic polymerization", as coined by Rouxel. This interplay between the electronic and the crystalline structure is the cornerstone of the soft chemistry ("*chimie douce*") approach which allowed to access many new formulations, structures and oxidation states by playing on the relative bands of the elements in the pristine and is still flourishing today.[42]

However, metal substitution is not the only way to modify the number of electrons in a structure. Indeed, in intercalation compounds such as $Li_xMX_2$ , the Li content (and the number of electrons) can be finely tuned either by chemical or electrical deintercalation. This may thus lead to a partial oxidation of the chalcogen network which will then dynamically undergo "anionic polymerization" to lift the resulting degeneracy.

As a proof of concept, Rouxel and coworkers removed up to 2 Li per formula unit (F.U.) from $Li_2FeS_2$ thus leading to $FeS_2$[43]. The voltage curve obtained for the chemically oxidized compounds is shown in fig. B.2.a. From $Li_2FeS_2$ to $LiFeS_2$, the sloped region corresponds to the usual oxidation from $Fe^{+2}$ to $Fe^{+3}$. From $LiFeS_2$ to $FeS_2$, the flat region at high voltage corresponds to the oxidation of the sulfur followed by the reorganization of the network, which can be rewritten as $Fe^{3+}$ ($S^{-}$) ($S^{2-}$). Unfortunately, the neat behavior observed with chemical oxidation cannot be achieved with electrochemical deintercalation. The voltage curve obtained by electrochemical cycling of the pristine (black dots in fig.B.2.b) , features a huge hysteresis. Furthermore the phase suffer from large irreversibility, to the point that the authors could only cycle the chemically deintercalated

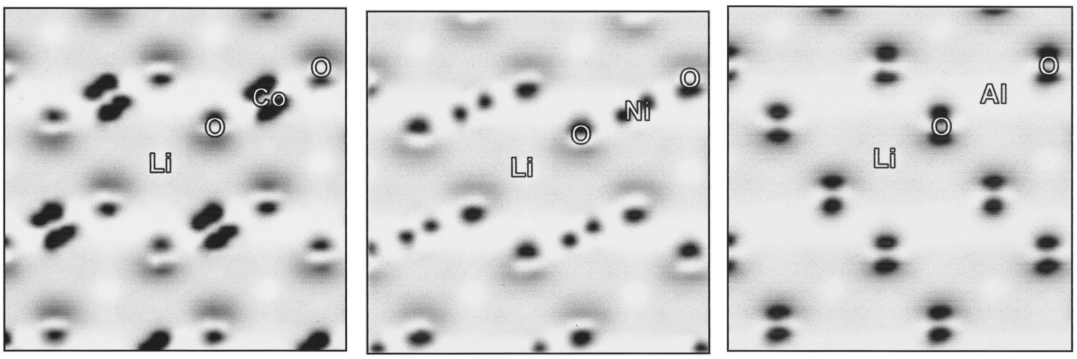


Figure B.3: Density difference upon iso-structural delithiation function of $LiMO_2$ with M=Co, Ni, Al, from left to right, respectively. Adapted from [47].

phase (white squares) against Li-metal.

While this early work is the first example of anionic oxidation in the electrochemical sense, it is clearly not reversible. We see here that reversibility is a key requirement to achieve practical compounds, and explains that it is a criteria to characterize anionic redox.

## 1.2 $LiCoO_2$ end-of-charge: Charge transfer in a layered oxide

At that point, no anionic polymerization had been characterized in the oxides. However, the newly found material, $LiCoO_2$ had already been the subject of much investigation to understand why the cycle life decreased sharply when allowing low Li composition, ($x<0.5$). A huge effort was put to mitigate this issue and understand several unexplained phenomena at the end of charge such as magnetic measurements showing that Co does not reach +IV oxidation state, partial dissolution of Co in the solution[44] and a sharp decrease of the Van der Waals gap.[45] Furthermore, the synchrotron X-Ray Diffraction (XRD) refinements already pointed towards a O-O shortening, reminiscent of the "anionic polymerization". This distortion, absent in $LiNiO_2$, has been proposed as the source of stability of Co compared to Ni layered oxides.[46]

On the theoretical side, Ceder & co-workers addressed this challenging results by studying charge compensation mechanism upon charging. By plotting the difference between the electronic densities of the pristine ($LiMO_2$) and the oxidized compound ($MO_2$) (see fig. B.3), they showed that the created holes are partially localized on the oxygen, indicating negative charge transfer ($e^-$ transferred from O to Co).[48], [49] While this charge transfer increases the oxidation potential in stoichiometric oxides, it does not provide extra capacity compared to pure cationic redox. Therefore, it does not fall within the the electrochemical definition of “anionic redox”, even though all the theoretical components are already present.

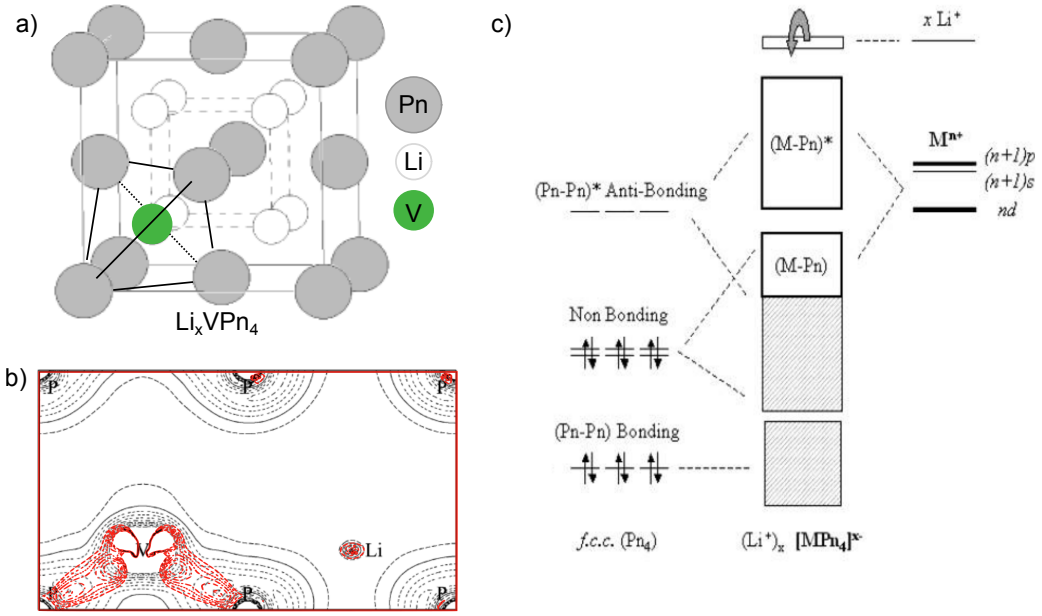


Figure B.4: (a) Structure of $LiVPn_4$ (b) Density of $Li_3VP_4$ (black) and positive density difference (red): $\rho(Li_3VP_4) - \rho(Li_7VP_4)$ (c) Band structure model for the reductive coupling mechanism. Adapted from [50], [51].

It is noteworthy that, in this paper, Ceder *et al.* already refer to $LiAlO_2$, an "hypothetical compound", where the charge compensation for Li removal is bore by oxygen only, thus providing a capacity which cannot come from the metal. It is interesting to see that the extension of this approach leads directly to Li-Air compounds.

## 1.3 Pnictides: Anionic redox in non-layered cathode

At the beginning of the 2000's, Doublet, Monconduit *& al.* discovered a family of compounds, $Li_{11}VPn_4$ with Pn=(P, As), which could reversibly exchange up to 9 Li per metal.[50], [51] The structure (see fig. B.4.a) is composed of $Pn_4$ tetrahedra bearing vanadium in their center. Following a joint experimental and theoretical investigation, 2 intercalation regimes were identified: a cationic regime, at the beginning of charge, from x=11 to x=7, corresponding to the oxidation of vanadium from +2 to +5, followed by a "non-classical regime" from x=7 to x=3 which cannot be described by the sole oxidation of the metal.

In order to study this difference, the author also used a difference of electronic density upon iso-structural delithiation between $Li_3VP_4$ and $Li_7VP_4$ (see fig. B.4.b). Here, the density difference, which globally integrates to -3 electrons, is negative almost everywhere. Interestingly, the author only plot the positive values, which lies exclusively along the Pn-V bond, indicating that, when electrons are removed, the electron density increases in the Pn-V bonds. The authors explain this movement by the «oxidation of the $VPn_4$ group» which occurs in two steps: an oxidation of the pure non-bonding $P_{3p}$ states localized

outside of the tetrahedron, followed by an electron transfer from the pnictogen to the vanadium, thus increasing the electron density on the Pn-V bond.

We note here two important requirements for the anionic redox: First, the need to oxidize *non-bonding states* (as opposed to bonding electrons) to preserve the bonding structure of the compound and prevent material collapse. This in a notable addition to the system studied by Rouxel, which explains the reversibility observed here. The second requirement is to prevent the anionic polymerization by allowing a large distance between the oxidized anions of distinct tetrahedra (even though a thorough delithiation could result in such Pn-Pn bonding). Fortunately, these two criteria (the non-bonding doublets and the large anion distance) are often realized together, due to Coulomb repulsion in the pristine.

This compound, $Li_{11}VPn_4$, is particularly significant as it succeeds in intercalating a large number of Li with a small distortion, thus achieving an extra-capacity due to anionic oxidation while still cycling reversibly. In this sense, even though this term did not exist at the time, this compound has been the first to satisfy the electrochemical definition of anionic redox: a reversible extra-capacity provided by the anionic network. Application wise, however, its voltage was not high enough to reach interesting specific energy, despite its large capacity.

# 2 State of the art of A.R. mechanism in 2017

As we have seen in the previous examples, the theoretical framework associated to anionic redox is a fast moving field which quickly follows the experimental discoveries to provide explanation and, as far as possible, predictions. We will therefore describe the A.R. modeling as it was at the beginning of this Ph.D.

Even though early theoretical works mentioned $O^{2-}/\left(O_2\right)^{2-}$ redox in $Li_2MnO_3$ among other theories as early as 2012,[52] the cycling irreversibility and the mixed anionic / cationic redox prevented the confirmation of this theory. The deciphering of this phenomenon motivated the study of Li-rich layered oxides of $4d$ or $5d$ metals as model compounds, as opposed to the compounds practical of interest, the Li-Rich NMC. Indeed, the $4/5d$-TM oxides show reversible A.R. with a simple stoichiometry, thus allowing easier characterization. Furthermore, from a theoretical standpoint, these model compounds are ordered, which allows easier modeling and simulation. In 2017, the theoretical framework was thus mainly designed to account for these $4/5d$-TM oxides.

To describe the anionic redox models that existed at that point, we will use a mechanistic, as illustrated by the arrows of fig. B.5. We will first study the electronic structure of the pristine, with a focus on the oxygen non-bonding states (a). We will then describe the

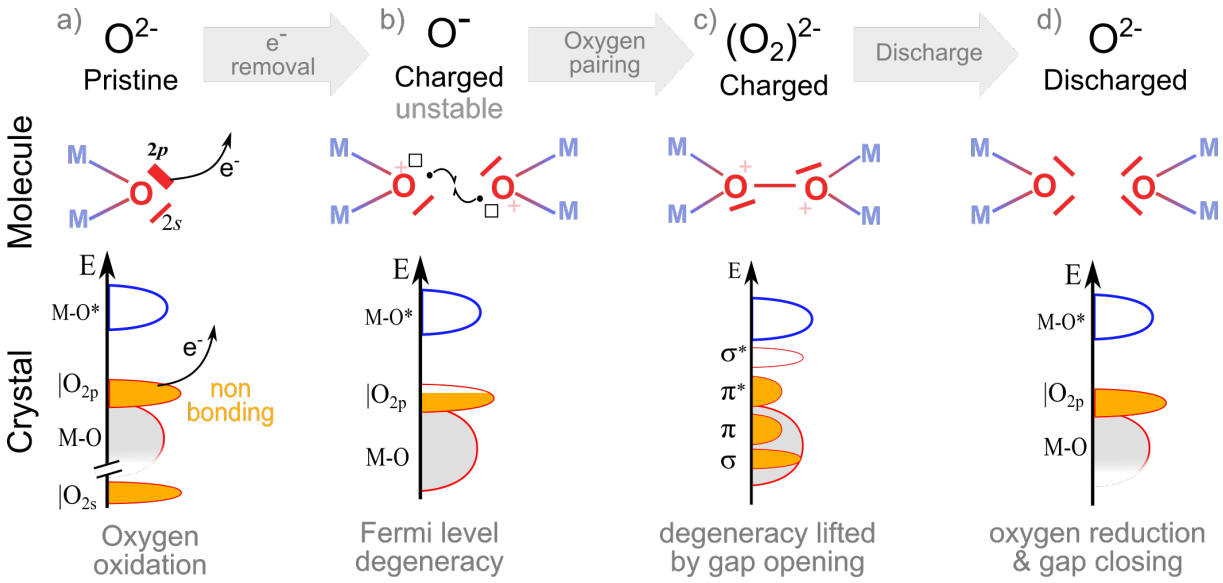


Figure B.5: Electronic structure evolution upon A.R. schematized with a molecular (top) or solid state approach (bottom). The oxidation of the $|O_{2p}$ (a) causes electronic instability (b) lifted by oxygen pairing (c). The discharged structure depends on the reversibility of the distortion (d). The structure corresponds to an ideally reversible $d^0$ metal oxide for simplicity but the mechanism is general.

oxidation of the oxygen and the instability which results in a electronic and structural reorganization (a→b→c). Finally, we will address the question the anionic reduction (c→d) and how to predict its reversibility, depending on the electronic structure of the pristine. For each of these steps, we will expose the widely accepted theory while indicating the debated concepts as well as the shortcomings and blind spots of the various models, in the literature at the time.

## 2.1 Pristine structure of A.R. compounds

### Electronic structure of oxides

In a TM chalcogenide $MX_n$, the overlap between the $M_d$ and the $X_p$ orbitals leads to the formation of bonding $M_d$-$X_p$ and anti-bonding $M_d$-$X_p{}^*$ states. The Charge-Transfer energy $\Delta_{CT}$ is defined as the energy difference between the average electrochemical potentials the metal and oxygen bands. Since, the oxygen is more electronegative than the transition metal (in a chemical sense, without taking $U$ into account, see below), the bonding $M_d$-$O_{2p}$ states have a dominant $O_{2p}$ character, while the antibonding states have a dominant $M_d$ character. Therefore, the charge transfer energy reads :

$$\Delta_{CT} = \mu_{MO*} - \mu_{MO}$$

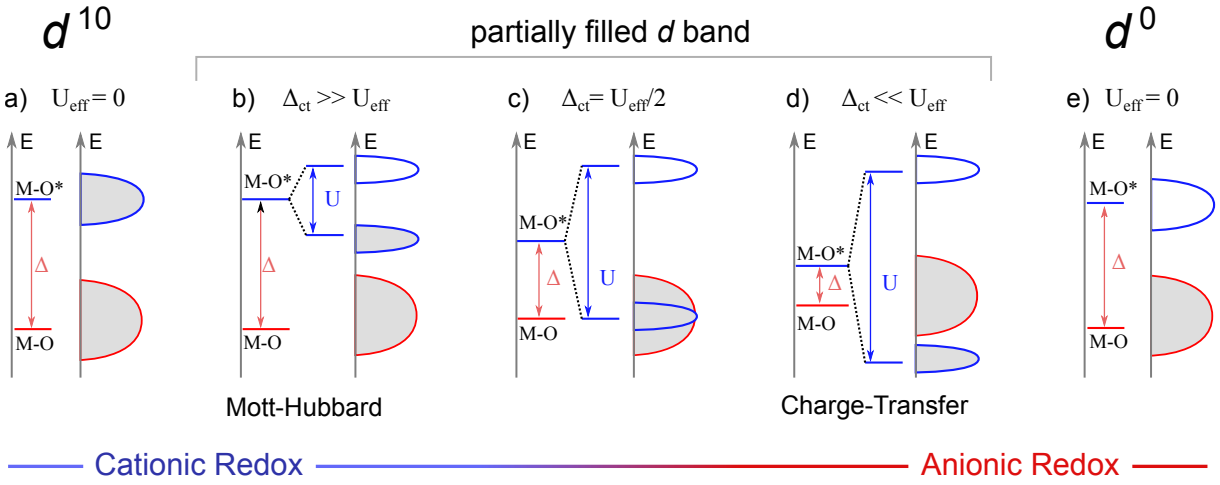


Figure B.6: Electronic structure of oxides in the ZSA model and the corresponding redox mechanism. Metallic states (blue) are split by the spin pairing energy $U$. They are separated from the oxygen states (red) by the charge transfer $\Delta_{CT}$.

In this simple model, if the $d$-band is full ($d^{10}$, fig. B.6.a), the states at the Fermi level will have a dominant M-character, thus the redox can be considered as a classical cationic redox. On the contrary, if the $d$-band is empty ($d^0$, fig. B.6.e), the states at the Fermi level will have oxygen character thus inducing oxygen oxidation upon charge.

For partially filled $d$ band however ($d^1$-$d^9$, fig. B.6.b,c & d), the Coulomb repulsion between $d$ electrons opens a gap in the metal band. The description of the electronic structure thus requires another parameter as proposed by Zaanen, Sawatzky and Allen (ZSA).[53] In their seminal paper, ZSA proposed a simplified description of the oxide electronic structure using two quantities: the charge transfer $\Delta_{CT}$ previously introduced and the Coulomb Integral energy $U$ which represents the energy penalty due to the Coulomb repulsion between to 2 electrons localized on the same orbital of the same metal center.[54] This repulsion opens an energy gap (of energy $U_{\text{eff}}$) between the two spin-orbitals of a singly occupied orbital. Thus this $U$ term leads to a gap opening between the occupied and empty states of the $d$-band only in the case of partially filled $d$-shell.[a]

The value of these gaps determines the relative positions of the occupied M and O bands, thus determining the nature of the oxidized states upon charge. Indeed, if $\Delta_{CT} > U/2$ (fig. B.6.b), the O levels will be lower than the occupied $M_d$ states, thus the bandgap will be equal to $U$ (Mott insulator) and the material will undergo cationic redox. Conversely, if $\Delta_{CT} < U/2$ (fig. B.6.d), the oxygen levels will be above the occupied $M_d$ states and the bandgap will be equal to $\Delta_{CT}$ (Charge-Transfer insulator), thus leading to

[a] In colinear DFT+U, the Hubbard splitting is approximated by a splitting between the up and down spin channels (see Methods).

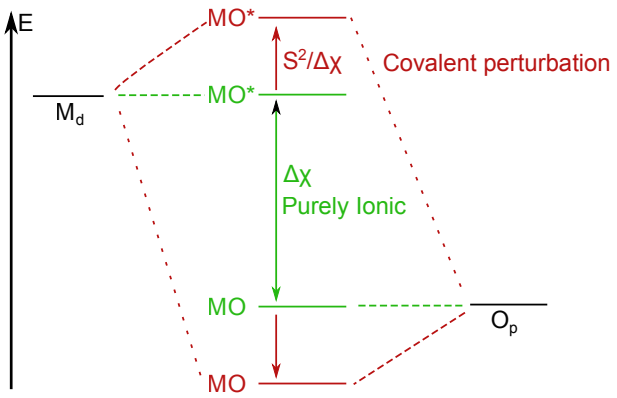


Figure B.7: Purely ionic bond model (green) and covalent perturbation (red).

anionic redox.[b] In the intermediate regime where $\Delta \approx U/2$ (fig. B.6.c), both $M_d$ and O states lie at the Fermi level, thus leading to a mixed cationic and anionic redox.

#### Non-bonding $|O_{2p}$ states

Oxygen redox occurs when the states at the Fermi level have a dominant O character. Unfortunately, in most oxides, these oxygen states are bonding so their oxidation drastically decreases the M-O bond order. This strongly destabilizes the crystal which undergoes irreversible structural degradation causing a decrease of the operating voltage and preventing the re-insertion of alkali, thus also reducing the capacity. In specific conditions however, some of the oxygen states can be non-bonding so their oxidation does not change the M-O bond order. This allows anionic oxidation without destabilizing too much the structure of the compound.

The need for reversibility during anionic redox requires the presence of non-bonding states. This strongly contrasts with the soft chemistry synthesis which precisely relies on anionic oxidation to trigger irreversible transformations and achieve new structures. The occurrence of non-bonding states, which prevents this reactivity, have therefore been overlooked in the context of synthesis (soft chemistry) while they are central for reversibility (anionic redox). Having emphasized the importance of these non-bonding states, we will now details their condition of existence.

In a purely ionic description of the O-M bond, the energy of the atomic level is not modified by the interaction ($\mu_{MO} = \mu_O$ and $\mu_{MO*} = \mu_M$, see energy levels in fig. B.7). In this case $\Delta_{CT} = \Delta\chi$, where $\Delta\chi$ is the difference of atomic electronegativity. When considering a weak covalent interaction as a perturbation from the purely ionic picture in the Rayleigh-Schrödinger perturbation theory[55], the first order correction of the eigenvalue leads to $\mu_{MO} = \mu_O - S^2/\Delta\chi$ and $\mu_{MO*} = \mu_M + S^2/\Delta\chi$ where $S$ is the orbital overlap (in

[b] The tight-binding orbital approach cannot account for localized $d$-electron directly, thus any corrections to the energy of these levels (like adding a U term) prevents the assignation of a bonding character. Therefore stating that "the M-O lies above the M-O$^*$" is meaningless, which solves an apparent incoherence.

red in fig. B.7). Therefore

$$\Delta_{CT} = \Delta\chi + 2\frac{S^2}{\Delta\chi}$$

Thus if $S = 0$ or if $\Delta\chi$ is very large, the covalent perturbation term is zero and the state can be approximated as purely ionic. In such case, the electrons are exclusively localized on the oxygen and they do not form a covalent bond. These states are noted $|O_{2s}$ or $|O_{2p}$ where the vertical bar reminds of the non-bonding doublet in Lewis notation.

In the case of $O_{2s}$, which a very stable, the $\Delta\chi$ with the metal or the Li is always very large. Therefore the $O_{2s}$ levels are always completely ionic and behave like non-bonding states. Unfortunately, precisely because of their stability, these non-bonding $|O_{2s}$ doublet cannot be oxidized. To provide reversible capacity, the oxygen should instead possess non-bonding states lying near the Fermi level which necessarily derive from the $O_{2p}$ orbitals.

For this $O_{2p}$, the criteria to cancel out the covalent perturbation is less straightforward. Indeed, in the case of very electropositive atom such as Li, the $\Delta\chi$ is very large and the doublet behave as non-bonding states. In contrast, the M-O interaction, albeit largely ionic, still induces some $M_d/O_{2p}$ intermixing. Hence the only way to obtain an $O_{2p}$ non-bonding state is to consider a material where one of the $O_{2p}$ has a zero overlap with the metal orbitals.

The existence of $|O_{2p}$ states is therefore determined by the local environment of the oxygen and more precisely, by the layout of its first-neighbor shell. A rule of thumb is that increasing the number of Li around the oxygen decreases the number of $M_d$-orbitals that can interact with the $O_{2p}$ orbitals, thus increasing the number of non-bonding $|O_{2p}$ This rule can however be refined when specifying the symmetry.

Indeed, in the octahedral coordination, the $O_{2p}$ orbitals may form $\sigma$ bonds with the atom they are pointing to and $\pi$ bonds with the other atoms. By neglecting the strength of the $\pi$ bond compared to that of the $\sigma$ bond, Ceder & coworkers proposed that non-bonding orbitals are formed when one of the $O_{2p}$ orbitals points towards two Li atoms, as illustrated in fig. B.8. [56] This translates into a Li-O-Li alignment along the $2p$ axis in the $Li_xM_{6-x}O$ octahedra which is a convenient criterion for the appearance of non-bonding states.

**Wording controversy: "Orphaned states"** To convey the idea that in a Li-O-Li configuration, the $O_{2p}$ cannot form covalent bonds with the metal and can only form pure ionic bonds with the 2 Li, the anthropomorphic metaphor "orphaned state" was proposed. Albeit very striking, this expression is misleading as it does not account for the existence of M-O orbitals with $t_{2g}$ symmetry.

In 2017, the conditions of existence of the $|O_{2p}$ non-bonding states were therefore not completely consensual and some controversies persisted regarding the correct methodology to characterize the non-bonding states.

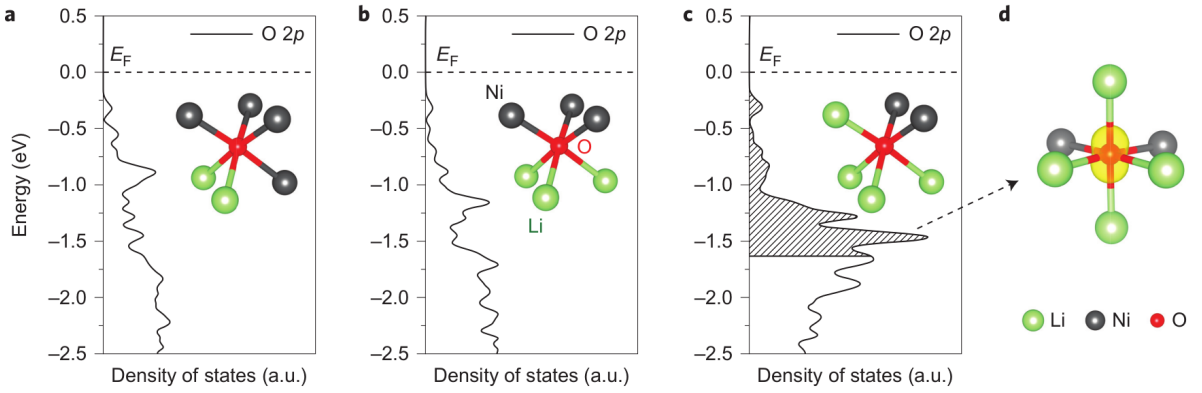


Figure B.8: Impact of decreasing M amount in oxygen's first cationic shell. High metal content of 4 (a) or 3 (b) do not allow for $|O_{2p}$ states. $|O_{2p}$ appear for 2 metal (c) as indicated by a narrow band whose electronic density is plotted using the parcharg method (d). From [56].

However, it was already a sucess because this model allowed to explain why the anionic redox in the Li-rich layered compounds is so reversible compared to other compounds. Indeed, in Li-rich compounds, the amount of available lithium exceeds the number of electron available on the metal, allowing anionic oxidation. However, this condition, which is met in other compounds such as $Li_2FeS_2$, is not sufficient to ensure the reversibility. Indeed, it is the existence of non-bonding states in the local structure of these compounds which prevent the material collapse. The fact that Li-rich oxides satisfy both criteria explains their success in providing reversible extra-capacity. Unfortunately, while the existence of non-bonding doublets allows to prevent the immediate collapse of the structure, it is not sufficient to ensure the long term stability of the battery. Indeed, progressive capacity and voltage fade occur upon extended cycling in most Li-rich oxides and we will now see why.

## 2.2 Oxidation, instability & reorganization

### Origin of the instability

**Electronic instability** To understand the origin of this long term degradation during A.R. process, the first feature to look at is the energy of these $|O_{2p}$ İndeed, to provide stability, these non-bonding states have to act as a "buffer" to prevent the oxidation of bonding states which would jeopardize the compound stability. Fortunately, being non-bonding, these states are neither stabilized nor destabilized by the M-O bonding interaction hence they always lie above the M-O and below the M-O$^*$ so they get oxidized before the M-O.

Indeed, the depletion of non-bonding states causes a degeneracy at the Fermi level. This degeneracy is an unstable situation because any distortion which opens a small gap

at the Fermi level will decrease the energy of the occupied state while increasing the energy of the empty states, thus decreasing the total energy of the compound. This is in line with the 3rd law of the thermodynamics which states that the entropy is nil at zero Kelvin. Indeed, $S = k_b \ln(\Omega) = 0$ implies that there should only be a single electronic state for a given energy thus implying that no degeneracy is thermodynamically stable.

This Jahn-Teller like instability is further amplified by the high chemical hardness of the compound in this narrow non-bonding band. Indeed, recalling that

$$\eta = \frac{\partial^2 E}{\partial N^2} = \frac{\partial \mu}{\partial N}$$

we see that a high hardness corresponds to a large change in electron energy upon oxidation. This means that the energy gap opened by a small distortion on these non-bonding state will be comparatively larger than for bands of lower hardness (e.g. the Jahn-Teller effect for metals). Therefore the energy gain associated to the distortion, which is its driving force, will be all the more higher that the degeneracy occurs in a narrow band.

**Atomic reorganization** As the $|O_{2p}$ gets oxidized, the electronic instability due to the degeneracy of the Fermi level provides a driving force for distortion, i.e. for a reorganization of both the crystalline and the electronic structure to open a gap at the Fermi level. To discuss the nature of these distortions, it might be useful to relate it to the familiar concept of Jahn-Teller (J-T) distortion.

The J-T distortion occurs when the M-O$^*$ band (either $e_g^*$ of $t_{2g}^*$ ) is partially filled, meaning that there is a degeneracy at the Fermi level. This M-O$^*$ degeneracy is lifted by a modulation of the corresponding M-O bond length. By increasing the $M_d$-$O_{2p}$ overlap in some directions while decreasing it in some others, this modulation changes the relative energy of the M-O$^*$ states, which are no longer degenerate. As a consequence, the stabilized level get occupied while the destabilized ones become empty, and the Fermi level lies in between. Since this overlap is stronger for the $\sigma$ bonds of the $e_g$ than for the $\pi$ bonds of the $t_{2g}$, this J-T effect is stronger if the degeneracy lies in the $e_g^*$ (e.g. $Mn^{3+}$) than in the $t_{2g}^*$. Note here that the J-T distortion is a modulation of an existing bond which preserves the symmetry of the structure.

Now coming back to the case of anionic redox, the Fermi level degeneracy occurs in the non-bonding $|O_{2p}$ but the phenomenon is the same: an interaction between the $|O_{2p}$ and another orbital will stabilize some O states while destabilizing others, thus opening a gap in the $|O_{2p}$ band. However contrary tp the J-T case, the initial $|O_{2p}$ is non bonding, therefore the gap opening cannot come from the modulation of an existing interaction. It will instead require the formation of a new bonding interaction which requires a lowering of symmetry.

In 2017, two mechanisms had been proposed to explain the irreversibility of A.R. in

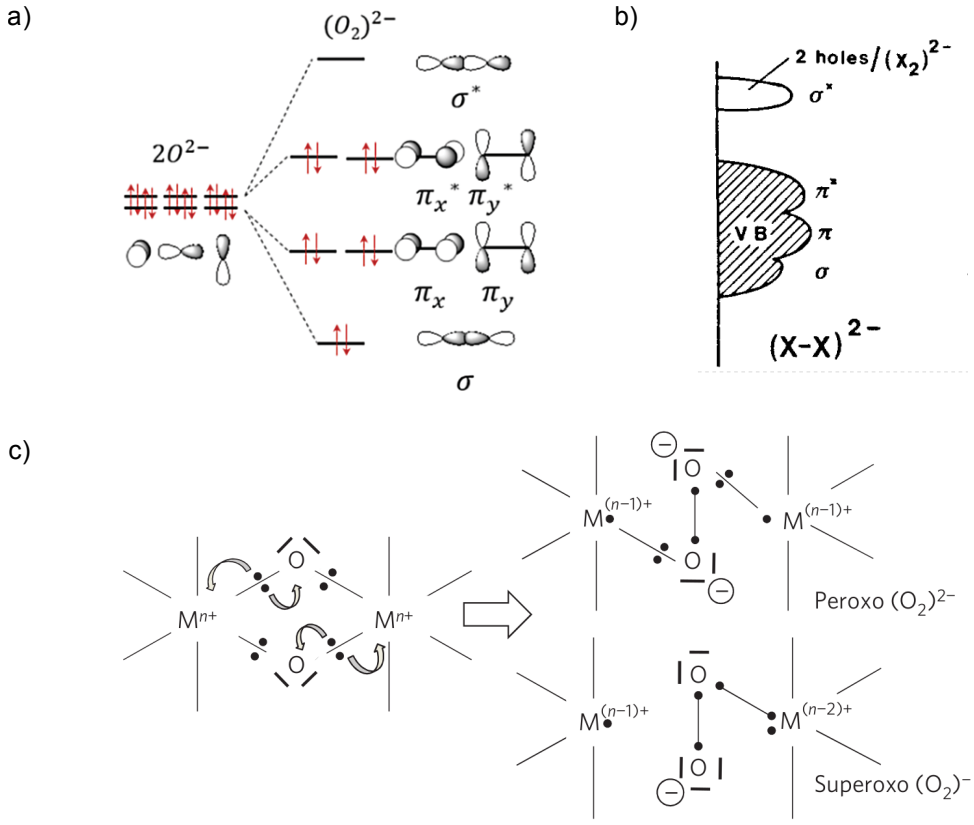


Figure B.9: a): Molecular orbitals of oxygen pair and electron count corresponding to peroxide, adapted form [57]. b) Translation of the molecular vision in terms of bands, adapted from [58]. Unsurprisingly this band diagram, plotted 20 years ago to describe the anionic polymerization of heavier chalcogenides, also stands for oxides. c) Formation mechanism of peroxide and superoxide, from [38] .

$3d$ TM compounds and its reversibility in $4/5d$ TM oxides, the pure oxygen pairing and the reductive coupling with the metal. We will now describe each of them.

#### Pure oxygen distortion: O-O pairing

The direct translation of the "anionic polymerization" concept into oxides has led to the "oxygen pairing" mechanism which is described as the formation of an $|O_{2p} - |O_{2p}$ interaction with bonding and anti-bonding states of $\sigma$ and $\pi$ symmetries (see fig. B.9.a). This pairing allows to locate the holes on the antibonding O-$O_{\sigma^*}$ (see fig. B.9.b), thus opening a gap between this empty band and the occupied O-O states ($\sigma$, $\pi$, $\pi^*$). Given the antibonding nature of the depleted states, this bonding will become stronger with further oxidation.

In order to understand the implication of this distortion for the integrity and stability of the compound, we can, at first, use a Lewis model such as the one sketched in fig. B.9. The accumulation of holes in the $\sigma*$ leads to the formation of peroxides which strongly distort the structure of the material. Furthermore, in this Lewis picture, the formation of an O-O bond entails the cleavage of one of the M-O bonds for each oxygen (see. fig. B.9.c).

This M-O bond cleavage, is a case of *bimetallic reductive elimination* which reduces the two metals to form an O-O bond.

Further oxidation leads to the depletion of the $\pi^*$ levels. The first electron removed causes the cleavage of another M-O bond in one of the two bonded oxygen, leading to a hypothetical super-oxide (see. fig. B.9.c). After removing the second electron from the $\pi^*$, the bond order between the two oxygens is 4, indicative of a double bond, which requires the cleavage of the last M-O bond. The oxygen pair can thus be considered as a molecular di-oxygen "trapped" in the host. This $O_2$ formation can occur as soon as the $\pi^*$ states are higher in energy than the empty M-$O^*$. Indeed, in such case we observe another *bimetallic reductive elimination* which causes further reduction of the metal to form a second O-O bond.

When peroxide or superoxide are formed, the strong distortion of the anionic network together with the weakening of the M-O bond facilitates the migration of the TM in the inter-layer. This explains the bulk disorder occurring in the cationic network upon oxygen oxidation and the huge voltage hysteresis. The formation of molecular $O_2$ is even more detrimental to the material structure. Indeed, since this $O_2$ de-coordinated from the host is notably smaller and less interacting than the $O^{2-}$ ions, it will migrate more easily and eventually leave the material. This migrating $O_2$ is released when it reaches the surface, thus creating vacancies which, after atomic reorganization, lead to a TM-dense phase in the whole bulk (A' phase in [59]).

The instability associated to A.R. leads to the formation of peroxo and $O_2$ gas. Up until 2017, the $O_2$ release was considered the main mode of failure of A.R. compounds. Therefore, a methodology has been proposed to evaluate the stability of a oxidized compound against $O_2$ release. This consists in calculating the $O_2$ release reaction enthalpy $\Delta G_{O_2}$, as the energy difference between the oxidized compound as a reactant and the oxidized compound with oxygen vacancy and molecular $O_2$ as products. The initial methodology used a single oxygen vacancy in a somewhat small supercell without temperature effects (and a empirical correction for molecular $O_2$ energy) to prove that all Li-rich 3d metals oxides were unstable against $O_2$ release after full oxidation ($2e^-$).[57] However, several enhancement have been proposed, such as accounting for the entropy of the gaseous $O_2$ or the proximity oxygen neighbors.[60]

This pure O-O interaction causes the de-coordination of the oxygen from the host, eventually leading to migration, $O_2$ release and phase transition. While this model accounts for the degradation processes observed during A.R. in $3d$-TM oxides, it fails to explain the behavior of heavier TM oxides, which show high cycling stability and low hysteresis. A refinement of the oxygen pairing mechanism has therefore been proposed to explain the role of the metal in enhancing A.R. reversibility in heavy TM-oxides, as we will now see.

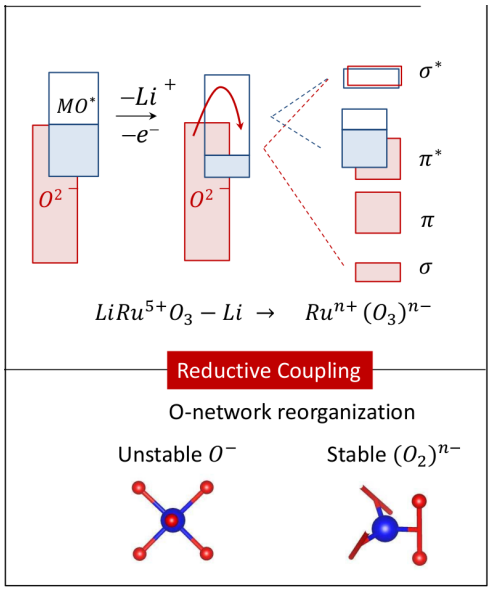


Figure B.10: Reductive coupling mechanism (top) and the associated distortion (bottom). In charge the $MO^*$ get depleted first before getting reduced by a negative charge transfer from the oxygen states, favored by an O-O pairing. From [61].

### Reductive coupling mechanism

The oxygen pairing mechanisms relies on the interaction among $|O_{2p}$ orbitals to open a gap between an empty O-O$\sigma^*$ and an occupied O-O$\pi^*$. Another way to lift the degeneracy consist in coupling $|O_{2p}$ and $M_d$ states to induce a reorganization of the charge which causes the oxidation of the oxygen and the reduction of the metal, as observed in the early work of Doublet *et al.* on $VPn_4$. Since the metal is reduced but the M-X bond is not cleaved, this reorganization was thus coined a *reductive coupling mechanism* (RCM).

From a thermodynamic point of view, the RCM can be described as a cooperative distortion of both the anionic and the cationic network to find a new symmetry which lifts the degeneracy of the $|O_{2p}$ reminding of the J-T mechanisms described above. This new symmetry has been described as a 3 center bond noted M-O-O (see fig. B.10 bottom panel).

However, from a mechanism perspective, this RCM can also be described as a sequence of electron transfers and atomic distortions. In some versions (see fig. B.10 top panel), the oxidation of the metal occurs first, because the $M_d$ orbitals are softer than the oxygen non-bonding pairs. This oxidation is then followed by a slower reorganization of the network which will results in the oxidation of the oxygen and reduction of the metal. However, this mechanism has also been described in the opposite sequence, where the oxygen pair formation occurs first, followed by a covalent interaction between $M_d$ and O-O$\sigma^*$ .[57] The articulation between these distinct sequences was still unclear in 2017. However, we will see, in the next chapters, how some apparent contradictions can be lifted by considering the coexistence of spatially distinct processes in the same compound.

The RCM allows to delocalize the $|O_{2p}$ holes over the M-O-O bond. This new interaction increases the bond strength between the metal and the oxygen pair, thus preventing postponing or preventing the $O_2$ release. This is the first occurrence of a principle that will prove very general: the implication of the metal is beneficial for the reversibility of the anionic oxidation process.

**Wording controversy: The "rotating orbital"** Some authors describe the oxygen pairing as a "rotation" of the $O_{2p}$ orbitals which align to form a $\sigma$ interaction. In this framework, the covalent bond between an oxygen and a transition metal will prevent the "rotation" of non-bonding states, hence preventing the formation of oxygen pairs. In quantum physics, the term "rotation" refers to a change of basis set (unitary matrix transformation). However in the framework developed by Ceder & al., this term describes a change in the probability density of orbitals lying in a given range due to a variation in the $O_{2p}$- $O_{2p}$ or $O_{2p}$-$M_d$ intermixing. Thus even though the wording is different, this study supports the conclusion that metal-oxygen covalency mitigates the degradation associated to anionic redox.

We have thus described the two mechanisms in this state-of-the-art model of 2017. We will now describe how this model can be applied to predict the behavior of each material.

## 2.3 Predicting reversibility

The oxygen pairing mechanism leads first to the migration of the metal and, upon further oxidation, to the irreversible release of $O_2$ gas. However, if the $|O_{2p}$ is able to interact with the metal, through a M-O-O bond, the stability of this interaction will prevent the migration of the metal into the inter-layer and the $O_2$ gas across the network. Thus in this binary model, the A.R. is either totally reversible if the RCM can occur, or totally irreversible if it is not the case. Based on this dichotomy, the reversibility of A.R. depends on the occurrence of the RCM, which is determined by the electronic structure of the pristine.

Indeed, the energy gain due to the RCM is the chemical potential variation of the occupied states due to the $M_d$-$/O_{2p}$ interaction. We have seen in fig. B.7 on page 21 that in the ionic bond model, the energy variation due to covalent perturbation is proportional to $S^2/\Delta\chi$. Using this expression, we can determine a simple criteria for an efficient M-$|O_{2p}$ coupling. Indeed, for the non-distorted symmetry, the $|O_{2p}$ - $M_d$ overlap $S$ is zero. Even in a distorted symmetry, this overlap remains very small because it is a perturbation of the non-bonding symmetry. Therefore, $S^2/\Delta\chi$ can only be non-negligible if $\Delta\chi$ is very small. Consequently, the RCM can only occur if the $M_d$ and $|O_{2p}$ states lie at the same energy.

In order to predict the relative energies of the the $M_d$ and $|O_{2p}$ bands, we come back

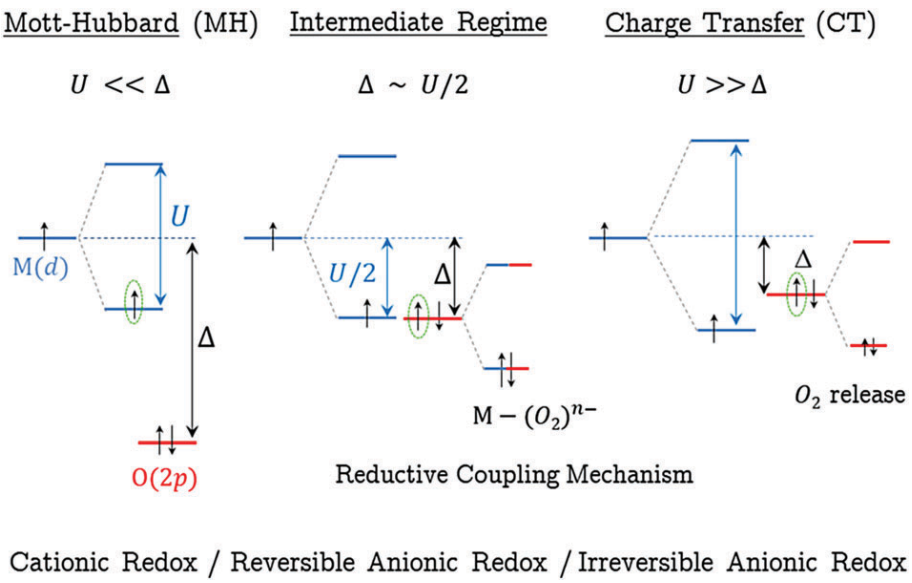


Figure B.11: Linking the ZSA classification (top) with the A.R. mechanism (middle) and the long term reversibility (bottom). The intermediate ZSA regime ($U/2 = \Delta$) allows effficient RCM, thus favoring reversible A.R.[57]

to the ZSA classification of oxide electronic structures. Indeed, Mott-Hubbard insulators ($U/2 < \Delta_{CT}$, see fig. B.11 left) undergo strict cationic redox , until they eventually reach a $d^0$ state in which case they are better described as charge transfer compounds. On the opposite, Charge-Transfer insulator ($U/2 > \Delta_{CT}$, see fig. B.11 right), undergo pure anionic redox. Unfortunately, in this case, there is no accessible M state near the $O_{2p}$ band to perform reductive coupling so the A.R. is irreversible. The sweet spot seems to lie at the crossover between these two regimes, where both $M_d$ and O states lie at the Fermi level. In this case, the small energy difference between $O_{2p}$ and $M_d$ states allows for an efficient RCM leading to a reversible cycling.

Hence up to 2017, the ZSA classification of oxides has been used as the main theoretical tool to predict the reversibility of A.R. in Li-rich oxides, leading to the development of 4 and $5d$ TM oxides which satisfy the requirement for reversible A.R.: $U/2 = \Delta$.

**Controversy: the "Covalency jail"** There was another dissension in the scientific community working on anionic redox theory to determine if M/O covalency was beneficial or detrimental to anionic redox. Indeed, since the work on $LiCoO_2$in the 1990's, it is a well established fact that covalency in itself does not bring extra capacity because the intermixing between $M_d$ and $|O_{2p}$ does not change the number of electrons in the M-$O^*$. Furthermore, larger M-O covalency brings the bonding M-O states lower. Some researchers presented the extra capacity as coming from the M-O states, thus concluding that higher covalency makes anionic redox more difficult, hence leading to yet another anthropomorphic metaphor, the "covalency jail". However, anionic redox is defined by its reversibility which requires to remove electrons from non-bonding states (instead of

bonding ones). While higher covalency indeed stabilizes the bonding states, it does not impact non-bonding ones. On the contrary, a high M-O covalency indicates a small M/O electronegativity difference so that M and O bands will be close to one another. This enhances the efficiency of the RCM, thus mitigating A.R.-induced degradation. We see here that an increased M-O covalency does not provide extra capacity, but enhances the reversibility.

# 3 Outline of the Ph.D.

We described the theoretical background on anionic redox which existed at the beginning of this PhD, from the removal of the electron to the possible structural responses that may follow, depending on electronic structure criteria on the pristine. However, despite its extensiveness, this framework still had some shortcomings or shortcuts. Furthermore, the experimental field of anionic redox has also evolved since then, providing new compounds and behaviors to rationalize. In this section, we will therefore try to summarize the key challenges that will be addressed in the main body of this manuscript in order to provide a united picture of anionic redox, each corresponding to a chapter.

## 3.1 Chapter 1: Refining the model

In the single-site model, we only considered one or two oxygen atoms, eventually adding a metal atom in the case of RCM. While this formalism is perfectly efficient to discuss the orbital reorganization and the iono-covalent interactions, it is more adapted to the description of molecules than solids. The first challenge is therefore to provide a "solid state model" of the A.R. able to account for the occurrence of collective behavior in both the initial electronic state and upon charging.

A recent study showed a drastic difference in the A.R. behavior between two polymorphs of a compound ($Na_2RuO_3$), ordered and disordered.[62] This difference cannot be accounted by the model we just described. Indeed, a solid may have many different environments for the oxygen, either because of non-equivalent crystallographic sites or because of the probabilistic distribution of the cations in the oxygen first cationic shell. A refined A.R. description should therefore integrate the variety of oxygen environments in order to account for *the effect of partial substitution and disorder.*

Another blind spot of the single-site model is that the number of electron exchanged per oxygen is always an integer, disallowing any intermediate states between the $O^{2-}$ (oxo), $O^{-}$ (peroxo) or O (molecular dioxygen). While this remains true in the solid for individual atoms, it is no longer sufficient to describe crystalline sites, because the "amount" of exchanged electron, averaged over an almost infinite number of identical sites, may be any real number. Experimentally speaking, peroxides and oxygen release are often observed

upon anionic oxidation even though the average number of electron removed per oxygen is much lower than one. There is thus a need to *understand the spatial distribution of these holes* which may either condense onto an $O_2$ molecule or stay delocalized over the network. The A.R. modeling can then be refined by integrating the occurrence of non-equivalent oxygen site into the description of the to mechanism (RCM and oxygen pairing).

Furthermore, the occurrence of migration and deformation should also be modeled to explain the degradation upon cycling (voltage & capacity fade,... ) which cannot only stem from oxygen release. A solid state model should therefore account for the *spatial modulation of the mechanisms and for the mechanical stress and strain* associated to oxygen redox.

## 3.2 Chapter 2: Accounting for new compounds

In 2017, the available experimental data was mainly based on Li-rich layered oxides of Ir and Ru, which are late $4d$ and $5d$ transition metals. These late heavy metals form more covalent bonds with the oxygen than the $3d$ metals and have larger orbitals with weaker intra-$d$ band Coulomb repulsion, leading to smaller $U$ term. Therefore most of the heavy TM oxides tend to be Mott insulators $U < \Delta$ or at the crossover where $U/2 \approx \Delta$, contrary to $3d$-TM oxides which tend to be Charge Transfer insulators. This restriction on the available experimental data explains that the framework developed at the time was optimized for (but somewhat limited to) highly covalent oxides. Over the last few years however, the number of compound showing anionic activity has bloomed, with the apparition of many new compositions and structures, displaying unprecedented A.R. behaviors. This new compounds, which cannot be described in the single-state model, should thus serve as benchmark to validate our refined A.R. modeling.

**New cations: Na-Ion and the new "model compounds"** A major feature of the anionic redox was the fact that it could occur in a wide range of compound, whatever the intercalant. As new intercalation chemistry became more mature, the question of how they behaved upon anionic redox naturally reached the scientific community. Since these new intercalants are larger and more polarizable than Li, they allow to stabilize different structures such as alkali deficient layers. However, as for Li, these *s/p* metals are ionically bonded so that they barely impact the electronic structure. The experimental results obtained for A.R. in these novel chemistries allows to question the relation between structure and A.R. reversibility.

Among them, the "Na deficient" layered compounds, of general formula $Na_{2/3}MO_2$ with Na lying in prismatic sites showed hysteresis but no oxygen release. In this family, the compounds $Na_{2/3}M_{1/3}Mn_{2/3}O_2$ with M=Zn or Mg show pure anionic redox, thus playing the role of new "model materials" (as $Li_2Ru(Ir)O_3$ did for the previous model).

**New anions: Coming back to sulfides (& to Rouxel)** While oxygen redox has been framed as a way to reach higher densities, it entails a large instability in the compounds and jeopardizes the stability of the material if pushed too far. Sulfides, being more polarizable, shows a lower electronegativity and a more reversible anionic pairing. Thus the idea to "come back to sulfides" with the theoretical background acquired on oxides to take advantage of the same chemistry with a different objective. This will be the occasion to question the formalism and the proposed mechanism by extending it to a new field, while laying a conceptual and historic bridge between the work of Rouxel and the present model.

## 3.3 Chapter 3: Building new tools

In order to provide quantitative explanation for the behavior of A.R. materials and qualitative guidance for the designs of new compounds, an efficient model should be accompanied by powerful tools. The current model contains two tools: the measure of $O_2$ release enthalpy to determine the stability of an oxidized compound and the $U$ vs $\Delta$ comparison, to determine the type of mechanism occurring in a pristine compound. While these methods are good indicator, they are still fundamentally linked to the framework in which they were developed hence inheriting this binary distinction between totally reversible and completely irreversible A.R. behavior. As the A.R. framework has to evolve to account for more contrasted behavior, so do the tools.

**Estimating oxygen network degradation** The estimation of $O_2$ release enthalpy allows to predict if a compound is stable against $O_2$ release at the end of charge. While $O_2$ release is an important mode of failure, the formation of peroxides is detrimental too and occurs at lower hole concentration. As an example, Na-Deficient layered oxides display hysteresis and voltage fade without oxygen release. The tools needed to study these new compounds should therefore be more sensible to degradation of the material than just $O_2$ release.

**Predicting reversible composition range** The comparison of $U$ vs. $\Delta$ allows to predict the occurrence of the RCM in a compound and thus its reversibility. However this tool, developed in a rigid band structure approach, is based on the electronic structure of the pristine compound. On top of being rather qualitative, it is therefore blind to any electronic reorganization which may provide new coupling upon oxidation. There is thus a need for an enhanced method to follow the mechanism competition during the whole charging process, so as to predict the crossover composition from one mechanism to the other and estimate the corresponding "reversible capacity".

In this chapter, we have shown how the concept of anionic redox has emerged as an electrochemically induced negative-charge transfer. We then described the state-of-the-art A.R. mechanism in 2017: the electronic instability due to oxygen oxidation can be lifted either by an oxygen pairing or a by a reductive M-O coupling. We then demonstrated that this A.R. models had to be adapted to account for newly discovered compounds and to provide new quantitative tools.

This concludes the first part which introduced the A.R. and the challenges it faces. The second part of this manuscript will describe how the work done during this PhD. contributed to address these challenges. We will first describe the refinements to the A.R. model that have become necessary. We will then apply this refined model to two classes of newly characterized compounds. Finally, based on this model, we will expose two newly developed tools which provide quantitative mechanistic analysis and reversibility prediction.

# Results & Discussion

# Refining the A.R. model: accounting for non-equivalent oxygens

> Everything must be made as simple as possible.
> But not simpler.
>
> Albert Einstein

The A.R. mechanisms presented in the previous chapter only describes crystals where all the oxygens react identically (single oxygen site). This model does not account for the presence of non-equivalent sites in solids and it thus fails to describe collective behaviors. In this chapter we will present a refined model which accounts for non-equivalent redox centers.

To do so, we will first introduce some useful quantities to describe *i)* the occurrence of non-bonding pairs and *ii)* the distribution of holes among them upon oxidation. Then, using these descriptors, we will present a refinement of the two A.R. mechanism (RCM and oxygen pairing) which account for the existence of non-equivalent sites within a solid. In the third part, we will summarize these findings to propose a unified picture of anionic redox and briefly compare it to other existing models.

## 1 Local and average descriptors of non-bonding pairs and hole distribution

We have seen in the introduction that the non-bonding $|O_{2p}$ states are paramount to guarantee the reversibility of the A.R. and that their existence depends on the oxygen's local environment. However, in a solid, the number of possible environments for the oxygen atom is very large, even with periodical boundary conditions, since partial substitution lowers the symmetry and requires very large unit cells[a].

In order to adapt the A.R. model to the existence of multiple environments within the same system, we will first derive a correct descriptor for the existence of non-bonding pairs in the solid, based on a statistical approach to the octet rule. After this static description of the pristine electronic structure, we will turn to oxidation to describe the dynamic distribution of electron holes among these non-bonding pairs.

[a] The unit-cell size tends to infinity for perfectly disordered compounds.

## 1.1 Occurrence of lone pairs and the M/O ratio

### Local and average M/O ratio $n_{MO}$

We first consider a generic compound made of oxygen (O), metal (M) and alkali (A). Since the O-A bond is purely ionic, the oxygen state are not modified by the interaction and behave like non-bonding states. In contrast, the M-O bond is considered as purely covalent so that electrons engaged in the O-M bond are shared between M and O. To respect the octet rule, the oxygen should have 4 electron pairs, either bonding or non-bonding. However, due to their low energy, the $O_{2s}$ states will not interact with the metal and also behave as non-bonding $|O_{2s}$ Thus the oxygen can only form up to 3 M-O bonds, noted $n_{MO} \in [0, 3]$ , which corresponds to $4 - n_{MO}$ lone pairs, respectively.

We now consider a generic rock-salt compound $A_{n_A}M_{n_M}O_{n_O}$ which may have several non-equivalent sites for the oxygen. In this compound, each M is surrounded by 6 O, so the total number of MO bonds per formula unit is $6\,n_M$. Hence the average number of MO bonds per oxygen is $\langle n_{MO} \rangle = 6\,n_M/n_O$.

If we now consider a Rock-Salt compound where all the oxygens are equivalent (same crystallographic site). All O have the same number of MO bonds so average $\langle n_{MO} \rangle$ equals the local $n_{MO}$ and the stoichiometry must therefore satisfy:

$$6\,n_M/n_O = \langle n_{MO} \rangle = n_{MO} \in [0, 3]$$

When ensuring the charge balance with A, these ratios corresponds to $AMO_2$, $A_2MO_3$ and $A_5MO_6$ respectively. Some example compounds which satisfy these stoichiometries, $LiCoO_2$, $Li_2RuO_3$ and $Li_5OsO_6$ respectively, are displayed from left to right in fig. I.1. These configurations correspond to 1, 2 or 3 lone pairs, of which one is an $|O_{2s}$ buried deep below the M-O band, and the rest are $|O_{2p}$ pinned on top of this M-O band, as seen in the band structure schemes (see fig. I.1 middle). The lone pair count of this molecular model is further confirmed by the Electron Localization Function (ELF see Methods), shown at the bottom of fig. I.1.

We now come back to Rock-Salt compounds with distinct oxygen crystallographic sites. In this case, the oxygen population can be split into several groups of crystallographically equivalent oxygens. Each of these groups forms an oxygen sub-lattice. In each sub-lattice, the oxygens will have a specific environment leading to a specific number of lone-pair and oxygen activity. These Rock-Salt compounds with non-equivalent oxygen sites can be derived from the 3 "single-site" phases described in the previous paragraph by considering the effect of substitutions.

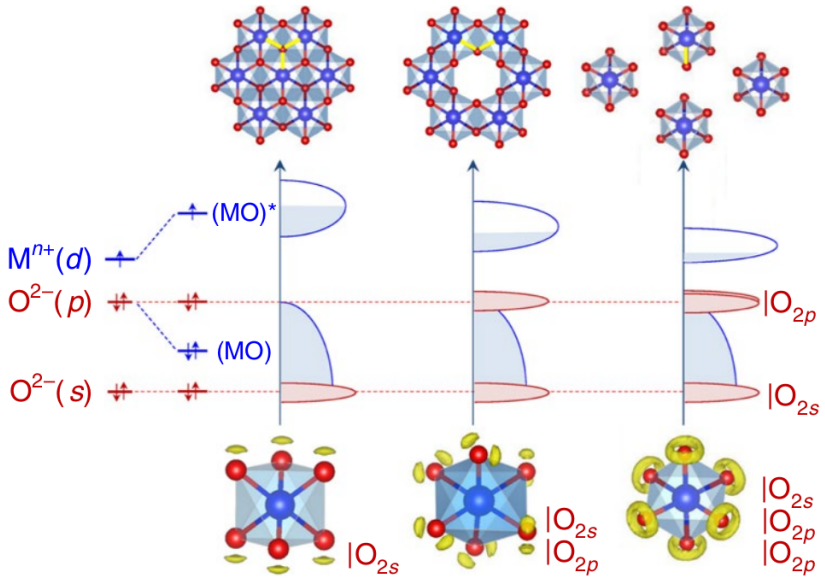


Figure I.1: Schematic crystalline (top) and electronic structures (middle) of $LiMO_2$, $Li_2MO_3$ and $Li_5MO_6$, with ELF of real structures of similar symmetry - $LiCoO_2$, $Li_2RuO_3$ and $Li_5OsO_6$ (bottom). For $Li_5MO_6$, the radial averaging of the 3 lone pairs leads to a ring shaped ELF. From [63].

### Effect of Substitution & doping

The $n_M/n_O$ ratio is a key factor in understanding the bonding configuration of the oxygen. We will therefore begin with the substitutions which leave this ratio unchanged before moving on to those which change the $n_M/n_O$ ratio.

**Constant $n_M/n_O$ ratio** In the single-site model, we classified the cationic species in two categories, A or M, according to the degree of covalency of their bond with oxygen. When replacing an alkali or alkali-earth atom by another very electropositive atom (*s,p* metal), the corresponding bond will remain very ionic (A-O bond). Similarly, when substituting a *d*-metal with another *d*-metal, the M-O covalency, albeit different, still prevents the formation of a lone pair. In both cases, both local $n_{MO}$ and global $\langle n_{MO} \rangle$ will stay constant, and the number of lone pair will remain the same. This is confirmed by the ELF of fig. I.2.a, which keeps the same topology when performing Li/Mg (A/A') or Mn/Ru (M/M') substitutions. Post-metal elements such as Sn may behave like a *sp*-metal as in $LiRu_{2/3}Sn_{1/3}O_2$, or as a *d*-metal if in a high oxidation state, as in $Li_2SnO_3$.

We draw the reader's attention to the fact that the conservation of the $n_M/n_O$ ratio does not imply the conservation of the capacity since both A and M species may be electrochemically inactive and/or activate anionic redox. However, electrochemically inactive species generally possess empty, closed or half-full shells which are isotropic and accommodate distortion more easily, thus increasing the reversibility of A.R. distortion.[64] As such, the effect of each substitution on the overall capacity of a compound is a complex sum of effects, which will be described all along this chapter and summarized in the last

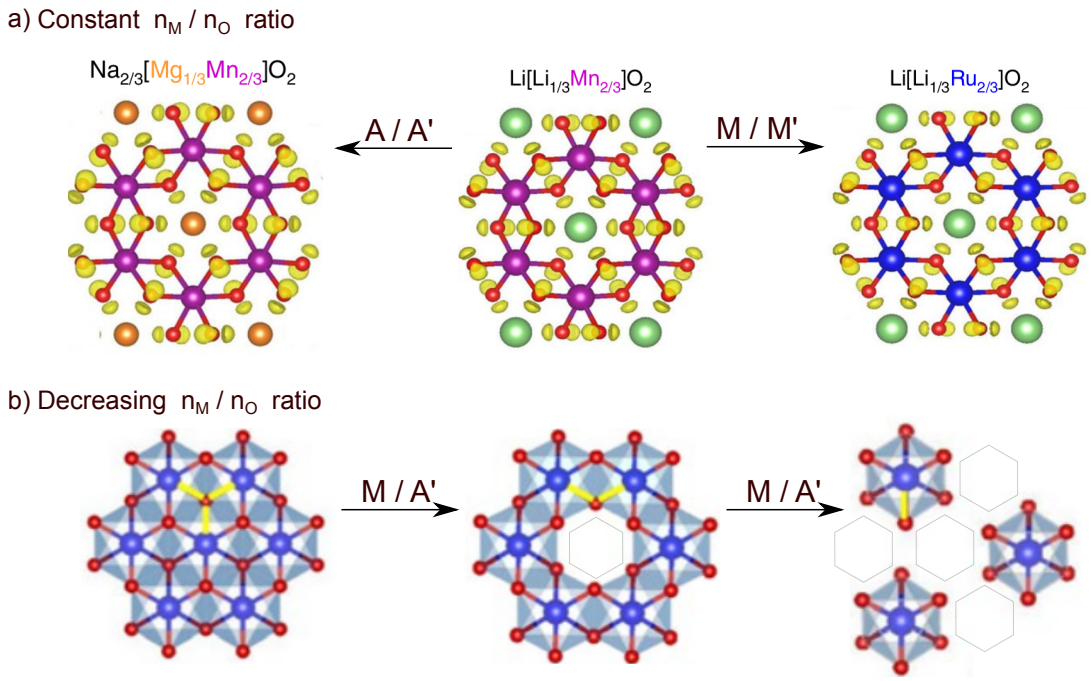


Figure I.2: Effect of substitution on $n_{MO}$ a) Constant $n_{MO}$: A/A' and M/M' substitutions of $Li_2MnO_3$ . b) Decreasing $n_{MO}$: M/A substitution of $AMO_2$ (A treated as vacancies). Adapted from [63].

section.

When starting from one of the 3 "single site" structures identified earlier, a partial A/A' or M/M' substitution (e.g. $A_xM_{y-\delta}M'_\delta O_2$) [b] will lift the equivalence of sites among A and M sub-lattices. As a consequence, even if each oxygen keeps the same $n_{MO}$, the distribution of M/M' and A/A' on each site creates a specific environment for each oxygen. This leads to the differentiation of the oxygen sites into several sub-lattices. The number of non-equivalent sites if finite if the substituted compound is ordered and periodic, or to infinite if the compound is disordered.

It is important to notice that the oxygen populations in distinct sub-lattices differ by both their local order and their long range environment. While the former determines the bonding structure, as we have just seen, the latter also impacts the Madelung energy of the site. Since the energy of non-bonding orbitals is not determined by the local bonding, the electrostatic shift due to the Madelung energy is the main effect on their energy, in the pristine. Therefore, even if 2 oxygen sites have the same $n_{MO}$, they will have distinct long range order and their non-bonding orbitals will not be degenerate, thus having different reactivity upon oxidation.

**Varying $n_M/n_O$ ratio** We now move to describing the substitutions which change the $n_M/n_O$ ratio: In a pristine rock-salt structure, the cation-to-anion ratio $(n_A + n_M/n_O)$ is constrained to 1. As we do not consider O/O' substitution, the only way to change the

[b] or even O/O', when doping with oxygen vacancy, sulfur or selenium

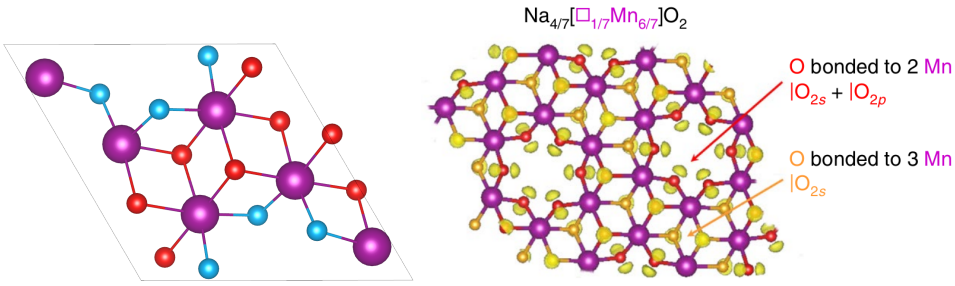


Figure I.3: Distinct oxygen sub-lattices in $Na_{4/7}\left[\square_{1/7}Mn_{6/7}\right]O_2$ (left) and their corresponding non-bonding doublets, visualized by ELF (right)

$n_M/n_O$ ratio is the substitution of a metal by an alkali (M/A), which reduces the $n_M$ and thus the global $\langle n_{MO}\rangle$.

In the case of "single-site" compounds, the $n_{MO}$ is an integer. Starting from $n_{MO} = 3$ (layered $AMO_2$), the successive M/A substitutions lead to the previously identified constrained stoichiometries ($n_{MO} = [2, 1]$, see fig.I.2). Any non-integer $\langle n_{MO}\rangle$ can only be achieved as an average of several local $n_{MO}$ which are always integers.

As previously explained, if the compound is ordered, the number of non-equivalent oxygens will we small and the global $\langle n_{MO}\rangle$ will be a simple fraction of these local environments. This is the case of $Na_2Mn_3O_7$, also written as $Na_{4/7}\left[\square_{1/7}Mn_{6/7}\right]O_2$ where $\square$ is a vacancy in the metal layer. This compound displays 2 distinct oxygen populations (see fig. I.3).[65] Among the 14 oxygens of the unit cell, 8 are surrounded by 3 metals (in red, $n_{MO} = 3$) and 6 are surrounded by 2 metals (in blue, $n_{MO} = 2$). We verify that their weighted average equals to the global $\langle n_{MO}\rangle = 36/14$:

$$\frac{8}{14} * 3 + \frac{6}{14} * 2 = \frac{36}{14} = \langle n_{MO}\rangle$$

The $|O_{2p}$ present in the electronic structure are therefore only localized on the oxygen with $n_{MO}$=2. When oxidizing this compound, the electrons will only be removed from this Li-rich oxygen sub-lattice, while the other one will remain un-oxidized, thus safeguarding the structural integrity and allowing weak hysteresis and good cyclability.

Pursuing further this reasoning, if the global $\langle n_{MO}\rangle$ cannot be obtained as a simple average of 2 local $n_{MO}$, there will be more O sub-lattices and their populations will follow more complex proportionality relations. In some cases, the $n_{MO}$ cannot be written as a sum of fractions (irrational number) so that the number of sub-lattices necessary to achieve this global stoichiometry will be infinite (or equivalently, the site occupancy will be statistical, that is to say, the compound will be disordered).

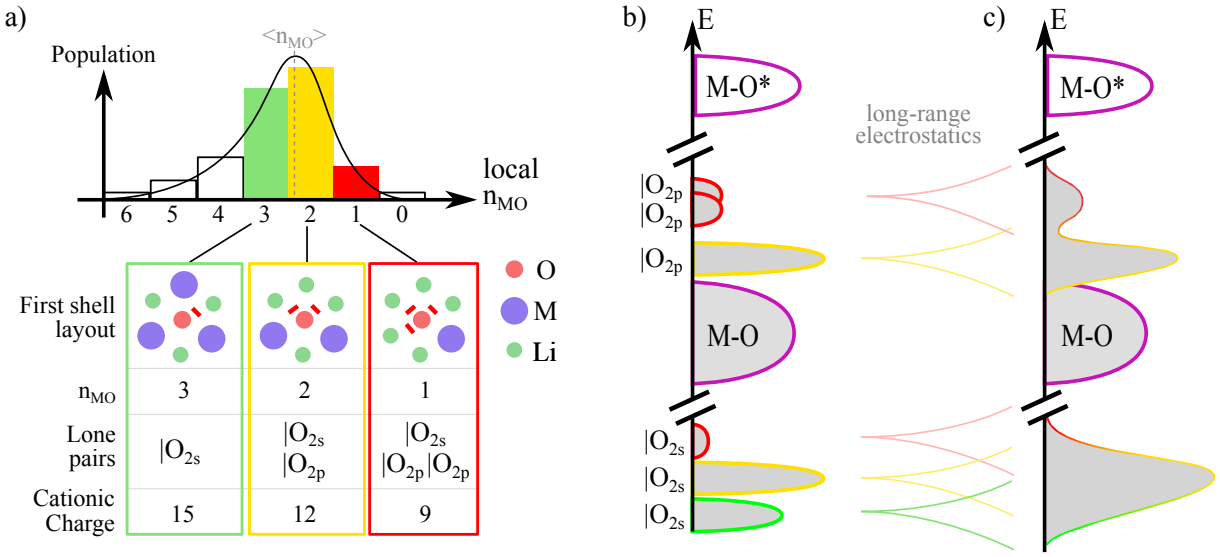


Figure I.4: Statistical distribution of oxygen first shell environment in an Alkali-rich compound ($\langle n_{MO} \rangle < 3$ ) (a) and the corresponding electronic structure in a charge transfer insulator with short-range (b) and long-range (c) electrostatic effects.

### Disorder

The materials with fractional M/M', A/A' or A/M ratios in their stoichiometry can be described as ordered, with several sub-lattices of each type of atom, or as disordered, with a statistical occupancy on each site. The identification of these two definition leads to consider disordered compound as a limit of ordered compound which unit cell is infinite, thus having an infinite number of sub-lattices. Starting from a layered structure, a complete disorder in the cationic networks leads the A and M sites to become equivalent, thus increasing the symmetry of the compound to that of a cation-Disordered Rock-Salt structure (DRS).

In such DRS, the environment on each oxygen site is unique, but there are only 6 different compositions for the first cationic shell which each correspond to an integer value of the local $n_{MO}$ (see fig. I.4.a). Each of these $n_{MO}$ will thus describe the local order of a population of oxygen atoms having the same first shell configuration.[c]

All the oxygens which share the same first cationic shell environment have the same number of lone pairs and a roughly equivalent Madelung energy. Since the energy of non-bonding states is governed by electrostatics, the energy of the $|O_{2p}$ among that oxygen population will be roughly equivalent (see fig. I.4.b). In addition to this short-range ordering, the variations in the long-range order induce slight individual variations of the Madelung energy, thus leading to a broadening of the bands (see fig. I.4.c).

Having described the relative energies of the $|O_{2p}$ for each group, we now describe their relative densities of state. Indeed, the number of oxygens in each of these 6 groups

[c]These oxygens only share an identical first shell composition but they are not cristallographically equivalent, hence they do not form a sub-lattice.

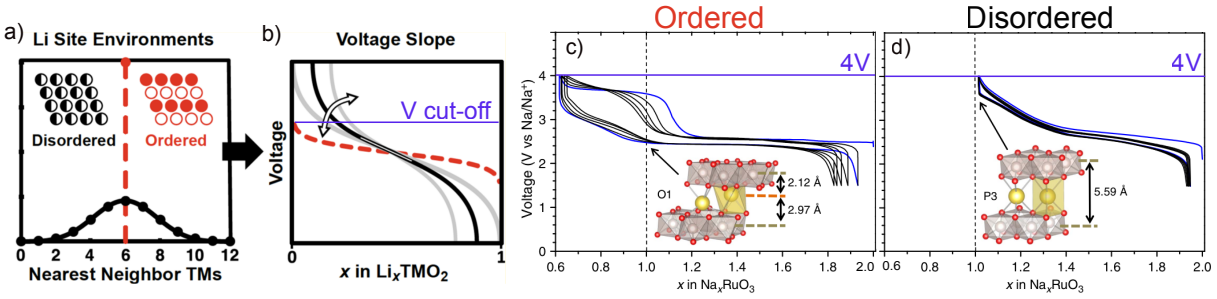


Figure I.5: (a) Statistical distribution of Li first shell environment in ordered (black) and disordered (red) compounds (a) and the corresponding voltage curve (b). Comparison of $Na_2RuO_3$ cycling curve: c) ordered & d) disordered. The slope increase due to disorder induces a higher voltage at the end of charge which is cutoff by the 4V voltage. Adapted from [66] (a, b) and [62] (c, d).

(indexed by their $n_{MO}$) is not equal because these configurations are not equally stable: the environments with a balanced M/O ratio ($n_{MO}$ = 2, 3 or 4) are much more stable than those with unbalanced environment ($n_{MO}$ = 6, 5, 1 or 0). As a consequence, the probability of each local environment follows a statistical distribution which peaks around the global $\langle n_{MO} \rangle$ and flattens quickly at the queue of the distribution, as schematized in the histogram of the fig. I.4.a. Since the number of individual $|O_{2p}$ in each group is proportional to its population size, the $|O_{2p}$ DOS for local orders whose $n_{MO} \approx \langle n_{MO} \rangle$ (green & yellow in fig. I.4b & c) is much higher than for the other ones (red).

We see on this simple scheme that contrary to ordered compounds, where the energy of the lone pair is well defined, the $|O_{2p}$ in a DRS form a continuum because of the variance in Madelung energy. The same reasoning can be applied to cationic levels, as illustrated in fig. I.5.a. This broadening of the electronic levels leads to an increase in the slope of the voltage curves observed for the DRS cathodes during both cationic and anionic redox (fig. I.5.b)[66], [67]. This explains the difference in A.R. behavior observed between ordered and disordered $Na_2RuO_3$ (fig. I.5.c & d respectively).[62] Indeed, due to the increased slope in the voltage curve of the DRS compound, the 4V cutoff voltage limited the oxidation to a small portion of the oxygen population.

We see here that the number of metal atoms in the first cationic shell of the oxygen, either as a local or global quantity is a powerful descriptor to understand the structural and electronic configuration of a pristine compound and the occurrence of anionic oxidation. However, in order to ensure the reversibility of this anionic activity, it is necessary to describe the dynamic response of these lone pairs upon oxidation. This dynamic behavior depends on the distribution of electron holes on the oxygen sites, which also requires an adapted description.

## 1.2 Distribution of oxygen holes

When studying the anionic oxidation, the pertinent descriptor is the number of hole per oxygen, measured either on a specific oxygen – $h^O$ – or as a global average over the compound –$\langle h^O \rangle$. In the single-site model, $h^O = \langle h^O \rangle$ has an integer value: 0 ($O^{2-}$), 1 ($O_2^{2-}$) or 2 ($O_2$ molecular). In a solid, however, $\langle h^O \rangle$ and the individual $h^O$ of each oxygen are not equal. Fortunately, this hole distribution can be rationalized, as we will now see.

### Calculating $\langle h^O \rangle$

To calculate the average number of hole per oxygen $\langle h^O \rangle$, we consider the charge balance during deintercalation:

$$n_A * q_A = n_M * \langle h^M \rangle + n_O * \langle h^O \rangle$$

where $n_M$, $n_O$ and $n_A$ are the number of active metal, oxygen and removed alkali, per formula unit respectively. $q_A$ is the charge of the removed alkali and $\langle h^M \rangle$ is the average holes created on the metal during charge. We will only consider monovalent intercalant such as Li or Na so that $q_A = 1$. Furthermore, we assume that each active metal can stabilize 1 hole so that $\langle h^M \rangle = 1$. Under these assumptions,$\langle h^O \rangle$ is given by:

$$\langle h^O \rangle = \frac{n_A - n_M}{n_O}$$

For the vast majority of compounds, we observe that $\langle h^O \rangle < 1$ even in the case of ideal delithiation ($n_A^{real} = n_A^{ideal}$). In reality, most compounds cannot be completely deintercalated ($n_A^{real} < n_A^{ideal}$), so that $\langle h^O \rangle \ll 1$.

### Effect of substitution

A classic layered oxide ($AMO_2$), such as $LiMnO_2$, is a Mott-Hubbard insulator, which undergoes pure cationic redox (fig. I.6.a). The M/A substitution leads to a Li-rich composition ($A_{1+x}M_{1-x}O_2$) where the x extra-alkali per formula unit (F.U.) in the pristine has to be charge compensated by the oxidation state of the metal. Higher M valence in the pristine means less available M electrons upon charge. Upon oxidation, this discrepancy between an increased amount of Li and a loss of cationic capacity will be compensated by the oxygen activity (fig. I.6.b). In the case of $Li_2MnO_3$, the pristine compound is a Charge Transfer insulator which thus undergoes pure anionic redox.

Starting from this A-rich composition, the partial substitution of the metal by another electrochemically inactive metal (M/M') decreases the contribution of the metallic network to the charge balance ($n_M = 1 + x - \delta$) but not the theoretical capacity, thus

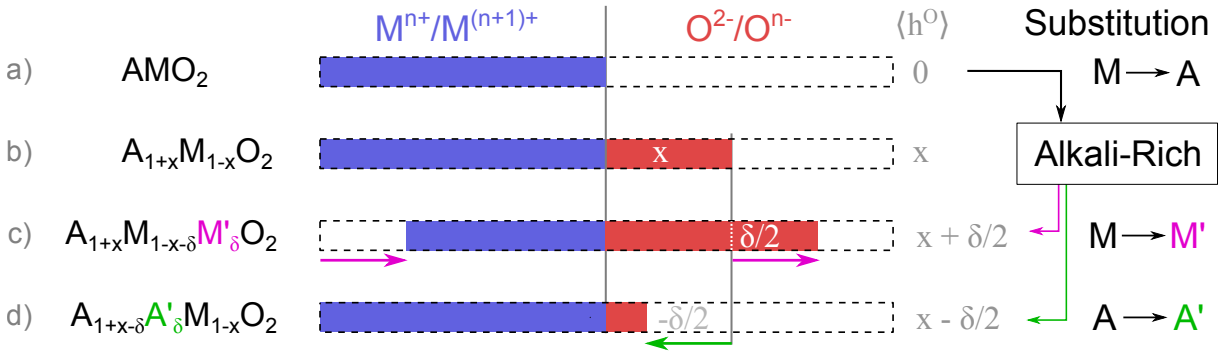


Figure I.6: Effect of substitution on the proportion of cationic (blue) and anionic redox participation (red). In a layered oxide ($AMO_2$) with pure M redox (a), the M/A substitution of x atoms triggers O redox: $h^O = x > 0$ (b). From this A-rich compound, M/M' substitution (inactive metal) of d atoms (c) decreases M contribution at constant capacity thus increasing $h^O$ of $\delta/2$. Alternatively, A/A' substitution (inactive cation) (d) decreases the capacity at constant cationic contribution, thus decreasing $h^O$ of $\delta/2$.

leading to a higher oxidation of the anions (see fig. I.6.c). If this substitution is total ($A_{1+x}M'_{1-x}O_2$), the pristine compound is a Charge Transfer insulator: the metal does not participate to the charge balance at all ($q_M = 0$) so that all the electrons come from anionic oxidation.

Conversely, the substitution of the alkali by an electrochemically inactive species (A/A') will decrease the theoretical capacity ($n_A = 1 + x - \delta$) but not the metallic contribution, hence the $\langle h^O \rangle$ decrease is only bore by oxygen (see fig. I.6, green box). For $\delta \geq 2x$, there is no oxygen redox anymore. The complete A/A' substitution leads to no capacity, so this case is not considered.

We have thus explained the impact of substitution on the average hole population $\langle h^O \rangle$. However, these substitution also determine the distribution of these holes among the oxygens, described by the local $h^O$.

#### From $\langle h^O \rangle$ to $h^O$

The substitution may lead to an ordered compound with a single oxygen site. In this case all the oxygen states are equivalent and the the holes get homogeneously distributed among them, leading to a uniform hole concentration: $h^O = \langle h^O \rangle$.

However, most of the partial substitutions create non-equivalent oxygen sites. Indeed, the substituted compound can be ordered, with few oxygen sub-lattices or disordered, with an infinity of non-equivalent sites. To study these sites, we will only consider their first shell (as done in page ) Furthermore, among these local environments, we will group together those where the oxygen has no $|O_{2p}$ because they will not participate to the anionic redox ($n_{MO} \geq 3$). Therefore, even in disordered compounds, we will only consider 4 types of oxygens, with either 0, 1, 2 or 3 $|O_{2p}$ lone pairs.[d]

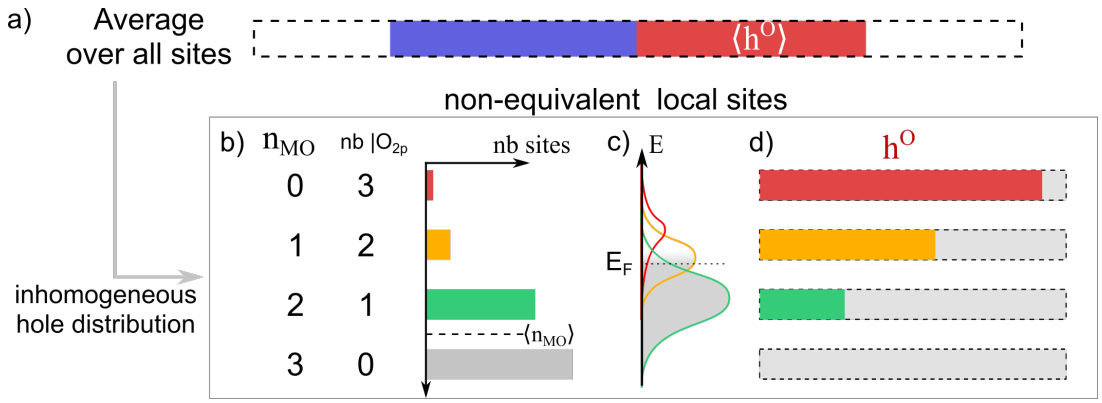


Figure I.7: Distribution of $h^O$ in disordered compound. (a) Average oxygen hole population in a compound. (b) Number of metal in their first shell $n_{MO}$ and number of $|O_{2p}$ (c) Schematic DOS of the corresponding $|O_{2p}$ (d) Distribution of $h^O$ for a given $\langle h^O \rangle$.

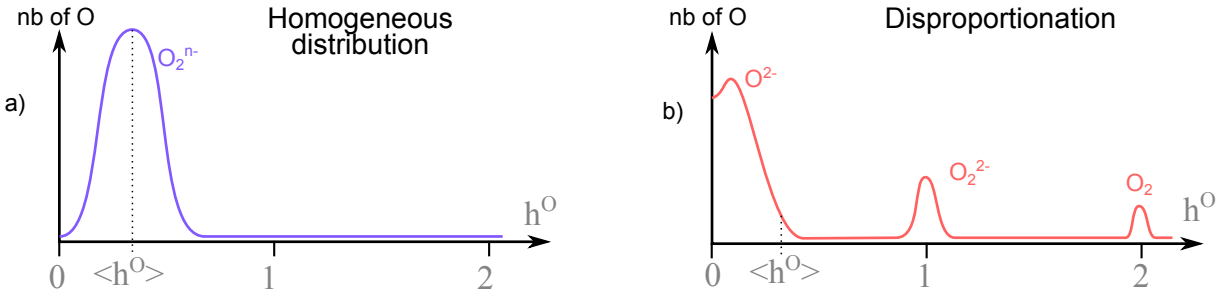


Figure I.8: Schematic histogram of the number of oxygen sites at each oxidation state. a) Homogeneous hole distribution, $h^O \approx \langle h^O \rangle$ for all the oxygens. b) Charge disproportionation, $h^O = 0, 1$ or 2, which correspond to molecular oxidation states of the oxygen.

As previously explained, the lone pairs belonging to oxygen in different environment do not have the same energy: the least stable $|O_{2p}$ belong to oxygens with the lowest $n_{MO}$ and the highest number of $|O_{2p}$ (see fig. I.7.b). These $|O_{2p}$ are therefore higher in energy than the others (fig. I.7.c). Thus upon oxidation, the most unstable oxygens – with the most $|O_{2p}$ – are the most oxidized – highest $h^O$– (fig. I.7.d).

As a consequence, $h^O$ can remain uniform if the oxygens are equivalent or concentrate within a specific oxygen population if the material features very distinct oxygens environments. These two types of hole distributions, schematized in fig. I.8 correspond to the two A.R. mechanisms of the single-site model: the RCM and the pure oxygen pairing, respectively. We will now describe how these mechanisms can be refined by incorporating the two descriptors $n_{MO}$ and $h^O$.

[d]The oxygen with 3 $|O_{2p}$ is surrounded by 6 alkali and not bonding with any metal atom.

# 2 A.R. mechanisms

In real compounds, the oxygen population cannot be reduced to a single type of oxygen. Therefore, the average environment and the hole concentration of individual oxygens differ from the material average. We will now use this distinction to refine both the oxygen pairing and the reductive coupling mechanisms.

## 2.1 The oxygen-pair disproportionation

Starting from a state where the oxygens are homogeneously oxidized, this mechanism causes the holes to localize on some specific oxygens which forms short pairs, while the rest of the oxygen sites get reduced to their pristine state, thus the name of *oxygen-pair disproportionation.*

### Charge disproportionation

In the single-site model of the oxygen pairing mechanism, in the absence of $|O_{2p}$ – $M_d$ interaction, the degeneracy of the partially occupied $|O_{2p}$ is lifted by a O-O interaction which opens a gap between the O-O$\sigma^*$ and the O-O$\pi^*$. Since the O-O$\sigma*$ contains up to 2 electrons per Oxygen pair, the degeneracy can only be lifted if there is exactly 1 electron removed per oxygen, i.e. $h^O = 1$. Correspondingly, we need $h^O = 2$ to reach the electronic configuration of molecular di-oxygen. Unfortunately, in the solid $\left\langle h^O \right\rangle \ll 1$, which means that the number of hole per oxygen cannot be uniformly equal to 1 (let alone equal to 2!) so that the molecular mechanism of oxygen pairing cannot occur uniformly across all the oxygen sites.

In order to achieve a fractional $\left\langle h^O \right\rangle$ while still maintaining a molecular oxygen pairing model for individual atoms, the charge has to disproportionate among oxygen atoms (see fig. I.9.a). In this scenario, the electron holes are localized on a minority of oxygens (red), which reach $h^O = 1$, while leaving the majority (almost) un-oxidized ($h^O \approx 0$) (orange). This allows to open a $\sigma^*/\pi^*$ gap within the oxidized sub-lattice while the $|O_{2p}$ of the non-oxidized sub-lattice stays full, thus lifting the Fermi level degeneracy.

Interestingly, $O^{2-}$ and $O_2{}^{2-}$ molecules have either a full or empty $\sigma^*$, without unpaired electrons. Hence for this disproportionation mechanism, oxygens behave like diamagnetic centers. This contrasts with the RCM (see next section) and this difference will be the foundation of the tool presented in chapter III.

### Structural degradation

The structural reorganization of the oxidized oxygens can be described by the molecular model of the oxygen pairing, with the same consequence on the lattice degradation: The oxidized oxygens will form very short O-O bonds while the rest of the lattice will remain

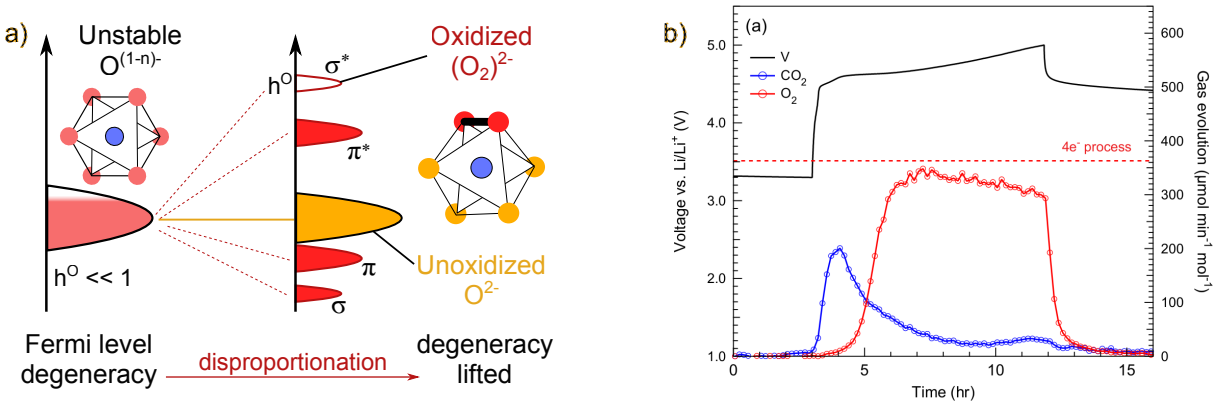


Figure I.9: Oxygen-pair disproportionation mechanism. a) Schematic electronic and structural mechanism. The Newman projection represent an $MO_6$ octahedra getting distorted. b) Oxygen evolution in $Li_2MnO_3$ measured by DEMS: The $O_2$ release occurs right from the very beginning of charge (from [68]).

undisturbed (see Newman projection in fig. I.9.a). These peroxides puts strain on the lattice and the eventual de-coordination of molecular oxygen leaves a vacancy prone to collapse into a denser phase. As the number of oxidized oxygens may be very small, their local hole concentration can reach critical level even if the average $\langle h^O \rangle$ is small. This concentrated distribution explains that in some compounds such as $Li_2MO_3$, the structural degradation occurs at the beginning of charge (see fig. I.9.b).[68]

The existence of non-equivalent oxygen atoms is a prerequisite to the localization of holes. If the oxygen population is already divided in the pristine, the holes will concentrate on the least stable oxygens (with the lowest positive charge in their first shell). This is the case of $Na_{4/7}\left[\square_{1/7}Mn_{6/7}\right]O_2$, which has 2 sub-lattices, and of all the disordered compounds which have an infinite number of non-equivalent sites. However, if all the oxygens have the same local environment, this disproportionation mechanism will need an initial disruption of the symmetry to create distinct first cationic shell compositions.

The migration of a metal (of higher valence than Li) in the Van der Waals gap, is an example of such symmetry break. Indeed, it modifies the first shell of the oxygen atoms forming the initial and final sites in opposite ways, as discussed in the next chapter on Na-deficient compounds (see section on page 75).

It should be noted however that any other type of local distortion such (e.g. creation of a very short peroxo bond or migration of an oxygen, leaving a vacancy) will create distinct oxygen environments in the same way. *The need to create distinct populations of oxygen is the driving force for the structural evolution during the disproportionation mechanism.*

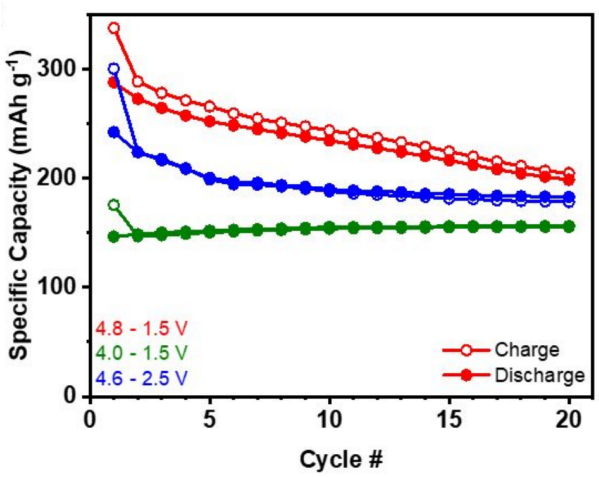


Figure I.10: Loss of capacity upon first cycles in disordered $Li_{1.2}Mn_{0.625}Nb_{0.175}O_{1.95}F_{0.05}$. Green (2.5-4V): No A.R. and no capacity loss. Blue (2.5-4.6V): The peroxides formed in charge are not reduced in discharge hence the capacity decreases in the first 5 cycles then stabilizes. Red (1.5/4.8V): The peroxides formed in charge are forcefully reduced, the structural degradation occurs at every cycle. From [69].

### Disordered Rock-Salt

Interestingly, in cation disordered rock-salt (DRS), all the oxygens are non-equivalent. Some of these oxygens have 2 or 3 $|O_{2p}$ (i.e. with $n_{MO} = 1$ or 0, respectively). As previously explained, these metal-deficient local environment are very unstable so they get oxidized preferentially. Due to that unstable environments, the additional destabilization caused by the oxidation is very likely to trigger a structural reorganization, such as a TM migration and/or the formation of peroxide or $O_2$. This distortion strongly stabilizes the oxidized form of the oxygen, but is very destabilizing for the reduced form. As an example, the shortening of the O-O distance strongly stabilizes oxidized $O^-$, by the formation of an $(O_2)^{2-}$ peroxo bond, but destabilizes the $O^{2-}$, due to electrostatic repulsion. Thus both the oxidation and the reduction will induce structural reorganization, associated with high overpotantial, sluggish kinetics and structural dedragation.

This structural reorganization of the least stable oxygens ($n_{MO} = 1$ or 0) explains that in DRS compounds, the first cycle capacity drop is much larger for A.R. cycling (red and blue curves in fig. I.10) compared to pure cationic cycling (green curve). Furthermore, this model also explains the different regimes of capacity fading observed upon A.R. in DRS. Indeed, if the discharge voltage is not low enough (e.g. 2.5V, see blue curve in fig. I.10), the least stable oxygens oxygen will remain oxidized upon further cycling. Their reorganization will only occur once, hence the resulting loss of capacity will be limited and stabilize after the first few cycles. On the contrary, if the discharge voltage is low enough (e.g. 1.5V, see red curve in fig. I.10), these oxygens are forcefully reduced. This allows to enhance the capacity but it requires a change in geometry at every cycle.

This continuous stress induces a constant degradation of the compound and the capacity keeps decreasing upon extended cycling. This kind of reorganization due to low voltage discharge has recently been characterized in the bulk of Li-rich NMC, which show cationic disorder in the metal layer.[59]

The oxygen pair disproportionation thus allows to fully oxidize the oxygen and obtain very high anionic redox capacity. Yet, this high oxidation induces a structural collapse of the compound. This degradation is reversible on the short term, at the price of high overpotential, but entails an inevitable capacity fade upon long term cycling. This contrasts with the reductive coupling mechanism, which allows for a long term cycling without voltage fade, albeit on a narrower capacity range, as we will now see.

## 2.2 Reductive coupling mechanism and cooperative distortion

In the single-site model of the reductive coupling, the intermixing between 2 $|O_{2p}$ and one $M_d$ bands allows to open a gap in the partially occupied $|O_{2p}$ so as to lift the Fermi level degeneracy. This interaction stabilizes the oxygen charge by a partial delocalization of the electron cloud towards the closest metal. However, the $|O_{2p}$ and the hole it contains are still centered around the oxygen. The number of holes can thus be considered as fractional for each oxygen atom ($h^O < 1$) so that a non-integer average can be achieved while keeping an homogeneous distribution of holes:

$$h^O = \left\langle h^O \right\rangle < 1$$

In order to incorporate non-equivalent sites in the RCM model, we first consider the cooperative distortion since it could not be described in a single site approach. Using the information provided by this structural approach, we then revisit our understanding of the electronic mechanism.

### Structural description of the distortion

From a structural perspective, the RCM is characterized by a cooperative distortion of the whole compound, as characterized experimentally.[70]–[72] In order to rationalize this cooperative behavior, we first consider the distortion of a single $MO_6$ octahedron which consists in the shortening of every other vertical O-O distance of the octahedra (identified by colors in the fig. I.11). This shortening of the O-O bonds can be described as a combination of prismatic and trigonal distortions of the octahedron. The trigonal distortion causes the top (pink) and bottom (yellow) oxygen planes to get closer (grey arrows in fig. I.11.a) while the prismatic distortion entails a rotation of the atoms of the top layer with respect to those of the bottom layer (grey arrows in fig. I.11.b).

We can now use this distortion of the isolated octahedron as the building block to un-

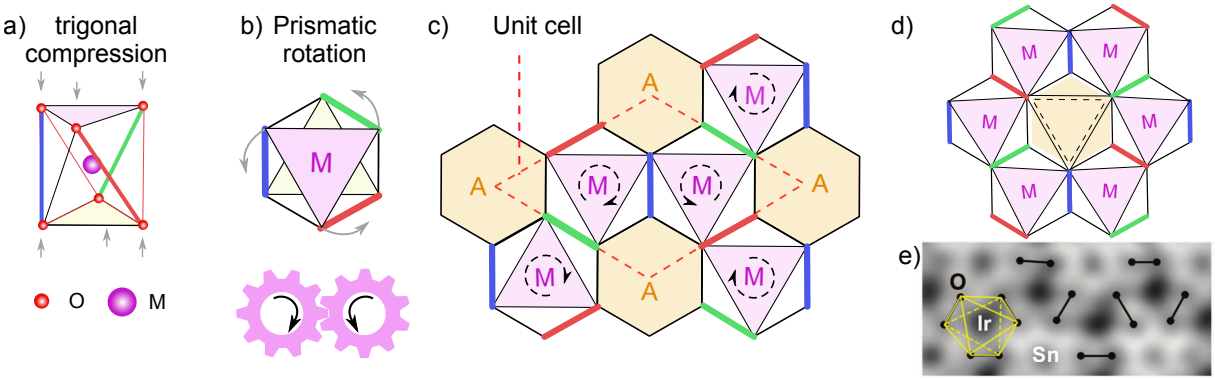


Figure I.11: Structural evolution during cooperative distortion. In the $MO_6$ octahedron, the O-O distance shortening (colored bonds) leads to trigonal compression (a) and prismatic rotation (b). The distortion of individual octahedron are arranged in a cooperative displacement, depicted on the pristine structure (c) which leads to a distorted structure (d). (e) Experimental characterization in $Li_xIrSnO_3$ (from [70]).

derstand the symmetry of collective distortion. Indeed, as for mechanical gears contacting each other, edge sharing octahedra rotate in opposite direction (dashed circular arrows in fig. I.11.b), which leads to a collective distortion where the unit cell is defined by 2 $MO_6$ octahedra (dashed red line in fig. I.11.c). This cooperative movement of all the octahedra of a layer leads to a distorted structure where all the highlighted O-O distances have been shortened (fig. I.11.d), in line with experimental characterization (fig. I.11.e).[70] In this distorted structure, the area of the top and bottom faces of the $AO_6$ octahedron are increased (from dashed to solid triangle in fig. I.11.d), thus decreasing the energy barrier for the out-of-plane migration of the A atom.

From a symmetry perspective, we used the Isodisplace software suite [73] to prove that the space group of the pristine $Na_{2/3}Mg_{1/3}Mn_{2/3}O_2$ ($P6_3/mcm$), obtained by experimental XRD refinement (data in annex, on page 142) does not change when applying pure prismatic and trigonal distortion[e]. Hence the cooperative distortion of individual oxygen-pairs preserves the spacegroup of the pristine[f].

From this conservation of the symmetry, we can draw 2 conclusions: First, the $MO_6$ octahedra in the pristine are already distorted. This distortion may have many explanations, but the pre-existence of an $|O_{2p}$ $M_d$ interaction is plausible and requires further inquiry. Second, the RCM increases this pre-existing distortion, by modulating the interatomic distances, but the symmetry is preserved. In this sense, the RCM is very close to a Jahn-Teller effect seen from a solid state perspective, contrary to what was understood in the single-site model.

In addition to this local distortion of the octahedra, experimental studies indicate

[e] See Methods for the algorithm to reproduce the collective trigonal-prismatic distortion on an arbitrary layered structure.

[f] Without considering Na atoms

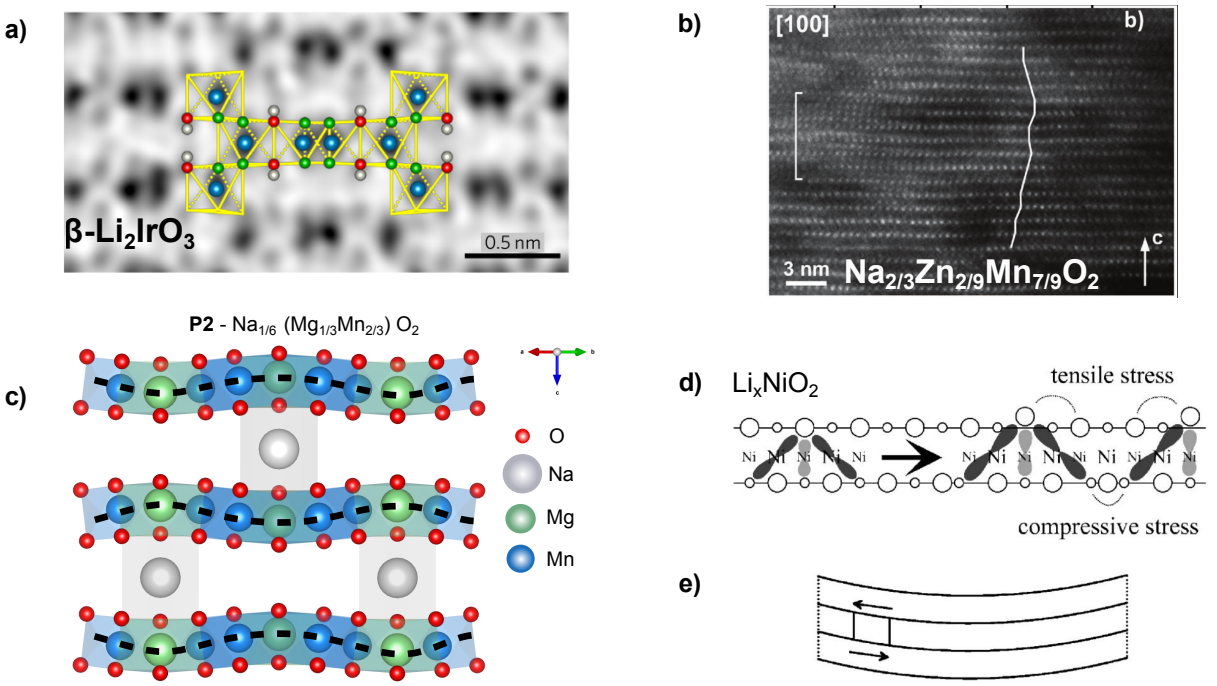


Figure I.12: Corrugation of the layer upon anionic redox. (a) & (b) Experimental evidence via TEM in $\beta$-$Li_2IrO_3$ [39] and $Na_{2/3}Zn_{2/9}Mn_{7/9}O_2$ [74] (c) Relaxed Structure of $Na_{1/6}Mg_{1/3}Mn_{2/3}O_2$ [75] (d & e) Stress due to Jahn-Teller distortion in $LiNiO_2$ layer and the resulting bending of the $NiO_2$ layer [76].

a corrugation of the layers (fig. I.12.a & b).[39], [74] This distortion is confirmed by our computational results (fig. I.12.c) which allowed us to further investigate this phenomenon. Indeed, upon relaxation, the corrugation of the layers of $Na_{1/6}Mg_{1/3}Mn_{2/3}O_2$ lowers the symmetry of the structure from the $P6_3/mcm$ to the $Pnnm$ space group, thus creating non-equivalent crystallographic sites with specific $|O_{2p}$ -$M_d$ interaction strength. However, contrary to the disordered case, these oxygen sites are quite similar because the number metal in their first cationic shell remains identical (e.g. $n_{MO} = 2$ for $Na_xMg_{1/3}Mn_{2/3}O_2$). Hence the dispersion of the $h^O$around $\langle h^O \rangle$ remains small, as confirmed by Bader charge analysis (see Methods).

In order to understand this corrugation phenomenon, we first refer to the corrugation observed in $LiNiO_2$ due to J-T effect.[76] In $LiNiO_2$, the elongated O-Ni-O axes due to the J-T distortion of $Ni^{+3}$ are arranged in trimers. This arrangement causes a monoclinic shear stress (fig. I.12.a) which is accommodated by a bending of the layers (fig. I.12.b). This corrugation has also been studied in $Na_xCoO_2$ in link with Na-ordering.[77]

In the case of A.R., the cooperative distortion pattern follows the honeycomb ordering of the metal (fig. I.11.d). Therefore, the corrugation and the metal ordering have the same periodicity? Consequently, the minima and maxima of the corrugation wave are located onto the alkali octahedra $AO_6$ (green atoms in fig. I.12.c) which are quite flexible since the ionic-bonds are non-directional. In such RCM distorted compound, as for Jahn-Teller

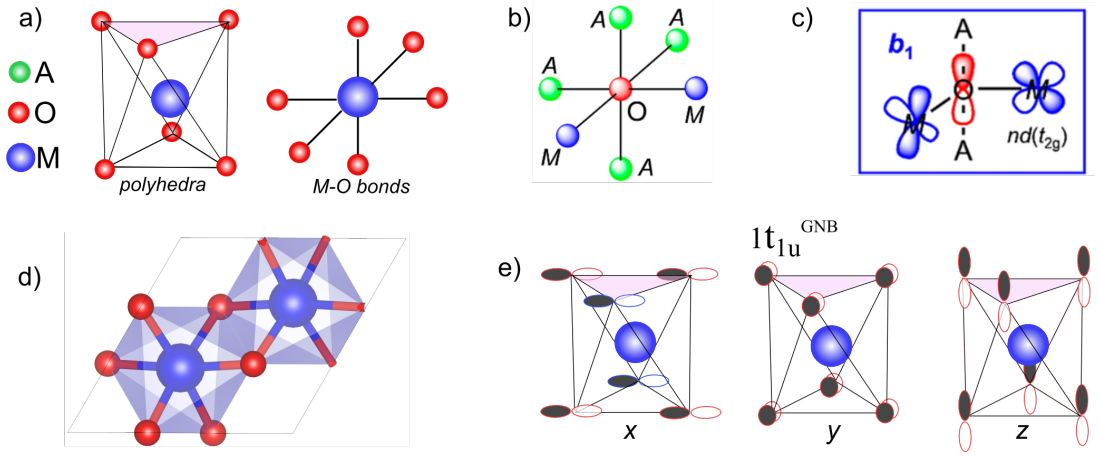


Figure I.13: Point group description of M-O-O bonding. a) $MO_6$ octahedron views. b) $OM_2A_4$ octahedron c) b1 M.O. of $OM_2A_4$. d)$1t_{1u}$ orbital (globally non-bonding) of $MO_6$. e) Unit cell of $V_{1/3}M_{2/3}O_2$ layer. Figures (b) & (c) are adapted from [78].

distorted $LiNiO_2$, the cooperative atomic displacements must correspond to a pattern of the orbital orientation. To identify this orbital arrangement, we thus embark on a molecular orbital investigation of the RCM.

### Molecular orbital approach

From an orbital perspective, Okubo & Yamada[78] used point group symmetry to compare the molecular orbitals (M.O.) of two octahdra : $MO_6$ in classic layered oxide ($O_h$, Metal centered, fig. I.13.a) and $OM_2A_4$ in Li-rich layered oxide ($C_{2v}$[g], oxygen centered, fig. I.13.b). In the latter case, they found that the Highest Occupied Molecular Orbital (HOMO) has a $b1$ (or $b1^*$) symmetry, which translates into a $\pi$ bond between two $M_d$ and the $2p_z$ of the oxygen (fig. I.13.c).

Unfortunately, point group description does not allow for oxygen pairing and it does not account for the periodicity of the lattice which is critical in the case of RCM. To account for such effects, we can determine the band-structure of the compound at the $\Gamma$ point by building the M.O. diagram of the unit cell before adding periodic phase modulation to obtain the M.O. at the other k-points of the Brillouin zone.

Since the contribution of the alkali to the oxygen orbitals is negligible due to the difference in electronegativity, this study can be restrained to the description of a negatively charged metal deficient layer $V_{1/3}M_{2/3}O_2$ where alkali are replaced by vacancies. The unit cell of this layer, $M_2O_6$ (fig. I.13.d) can be described as an $MO_6$ octahedron in contact with another M. The M.O. diagram of $MO_6$, computed in the master's thesis of A. Hagopian (ICGM-CTMM)[79], allows to identify the $1t_{1u}$ orbital as the fragment's HOMO (fig. I.13.e). In this $MO_6$ orbital, some oxygens can form a bonding $\pi$ overlap with the metal (e.g. blue contour orbitals in the $1t_{1u} - x$, left of fig. I.13.e), similar to

[g] $C_{2v}$ is the point group of the $H_2O$ molecule.

that of the $b1$ orbital described by Okubo & Yamada. However, the values of all the M-O overlaps cancel out, whatever the $M_d$ orbital considered. Consequently, this $MO_6$ HOMO orbital is globally non-bonding, in line with results obtained from DFT. By identifying the orbital on the highest non-bonding orbitals, we will understand how their overlap is modified by the cooperative distortion. As of today, the quantitative computation of the $M_2O_6$ M.O. diagram is still an ongoing work.

The elucidation of such M.O. diagram will allow to determine the period of the modulation which favors the identified distortion and thus the point of the Brillouin zone where the gap is opened. From there, it may be possible to describe the distortion of the oxygen network as a Peierls distortion of oxygen chains. If it is the case, this approach may then be extended in 2D by adapting the Fermi surface nesting formalism (described by Canadell & al. for metals [80], [81]) to these oxygen chains.

As this cooperative distortion allows to relieve the stress caused by the M-O-O pairing, it decreases the energy barrier of the RCM in both charge and discharge, which are thus very reversible. This strongly contrasts with the charge disproportionation mechanism, associated to a loss of capacity and voltage decay. This dichotomy clearly identifies the disproportionation as the source of irreversibility upon anionic oxidation. However, these two regimes are always in competition. To predict the reversibility of A.R. in a compound, it is therefore crucial to understand the parameter which determine the outcome of this competition.

## 2.3 RCM vs. disproportionation competition

The competition between the RCM and disproportionation mechanism is determined by the relative stabilization they provide. To determine this stabilization, we use the expression of the energy level variation upon covalent perturbation previously introduced $\Delta\mu \approx S^2/\Delta\chi$. Even in a distorted symmetry, the $|O_{2p}$ - $M_d$ overlap ($S$) is very small, hence the potential difference ($\Delta\chi$) should itself be small so that the stabilization $\Delta\mu$ is non-negligible. In a rigid band model, this mechanisms can only occur in compounds where some states of the $M_d$ band have de same energy as the $|O_{2p}$ in the pristine. In the ZSA terminology, this requires that $U/2 \approx \Delta_{CT}$. As they are quite restrictive, these conditions have only been met in oxides of 4d and 5d metals such as Ir and Ru. However, even though they provide good model compounds, these toxic and expensive metals are not practicals. Thus the community has searched and found alternatives compounds which show some A.R. reversibility even though they do not fulfill the $U/2 \approx \Delta_{CT}$ requirement.

#### Mott-Hubbard insulators

Some of these compounds achieve extra-capacity through A.R. despite being Mott-Hubbard insulators in their pristine state, i.e. $U/2 < \Delta_{CT}$. To explain this behavior,

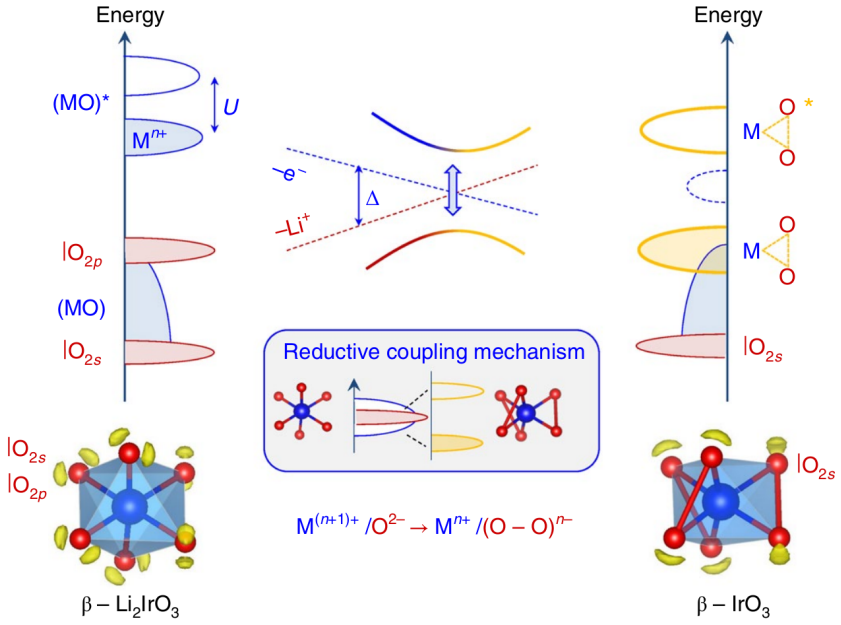


Figure I.14: Occurrence of the RCM upon charging in Mott-Hubbard insulators explained as an *avoided crossing* where the $|O_{2p}$ and the $M_d$ states are remixed. [63]

the theoretical framework should refine the rigid band approximation and consider the electrostatic shifts of Metal and Oxygen bands upon oxidation. Indeed, using a purely ionic image of the solid, it seems logical that the oxidation of the metal will increase its attraction with neighbor anions. Likewise, the removal of Li will decrease the screening between facing oxygens. In terms of electronic structure, this electrostatic effect will entail a stabilization of the metallic states and a destabilization of the anionic states upon cationic redox, thus reducing the $\Delta_{CT}$ as illustrated in fig. I.14. At some point, $\Delta_{CT}$ will verify the condition of $U/2 \approx \Delta_{CT}$ so that the metal and oxygen band will have the same energy, thus allowing an efficient recombination and the creation of M-O-O states via the reductive coupling mechanism[h].

### Charge-Transfer insulators

Looking at the other side of this crossover regime, we also have charge transfer insulators which undergo reversible anionic redox at the beginning of their oxidation before a steep increase in their hysteresis beyond a critical state of charge. This indicates a change in mechanism from RCM to oxygen pairing, explained again by the changes in the relative position of metal and oxygen bands upon redox, as illustrated in fig. I.15. Indeed, at the beginning of the charge (before ①), the $\sigma^*$ states due to oxygen pairing come close to the empty $M_d$ band, thus allowing an efficient recombination.

[h]This mechanisms can also be thought of as an avoided crossing of the $|O_{2p}$ and the $M_d$ states, which requires that these states have a non-zero overlap so that off-diagonal terms in the 2x2 perturbation matrix can effectively change the energies of the perturbed states.

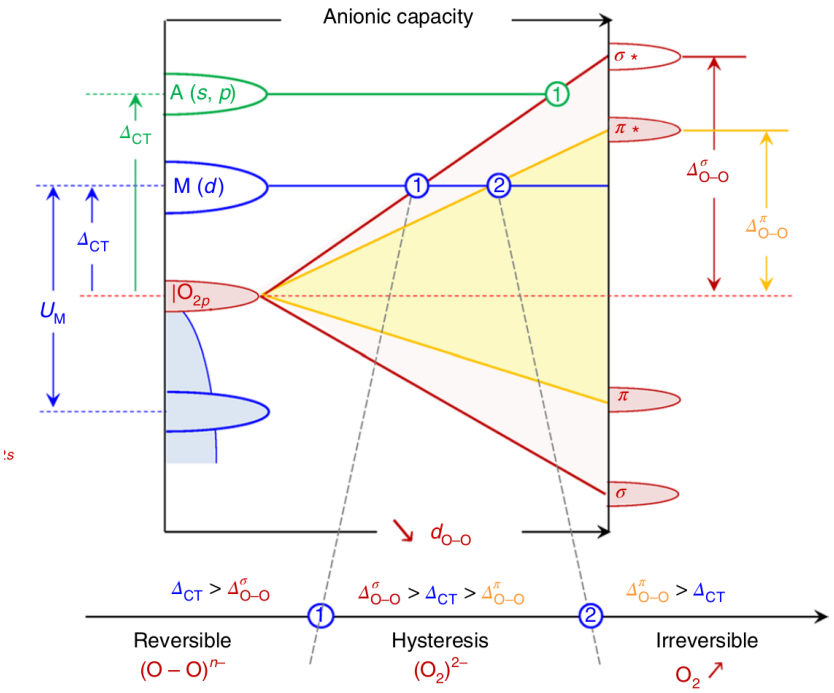


Figure I.15: Reversibility of A.R. in a Charge-Transfer insulator explained by the relative positions of bands upon charging. [63]

Upon further oxidation (between ① and ②), the $\sigma^*$ states get higher in energy than the $M_d$ band, so that the electron within the $\sigma^*$ can transfer to the metal (first *reductive elimination*). This provides a driving force for the disproportionation, thus causing migration and the formation of true peroxo within the layer. Furthermore, due to this band inversion, $M_d$ states are now the lowest empty states so that in discharge, they will get reduced before or along the oxygen. As the reaction path in charge (O oxidation) differs from the one in discharge (M reduction), this band inversion induces a voltage hysteresis, as experimentally demonstrated by Gent & al.[82].

If the oxidation continues (after ② ), the $\pi^*$ states will get higher than the $M_d$ states, thus favoring a $\pi^* \rightarrow M_d$ electron transfer (second *reductive elimination*). This transfer enlists the de-coordination of the oxygen as an $O_2$ molecule. This irreversible elimination leads to capacity loss and the subsequent collapse of the lattice lead to voltage fade.

This account of dynamic band stabilization allows to refine the coarse dichotomy of the single-site model which only differentiates Mott-Hubbard insulators, with pure cationic redox, from Charge-Transfer insulators , which immediately collapse upon A.R. Instead, there is, at any state of charge and in any compound, a competition between (at least) two mechanisms to stabilize the A.R. One is reversible, the other is not. Based on this theoretical framework, we now propose a simple yet powerful model which encompasses the various A.R. behaviors that have been recently reported.

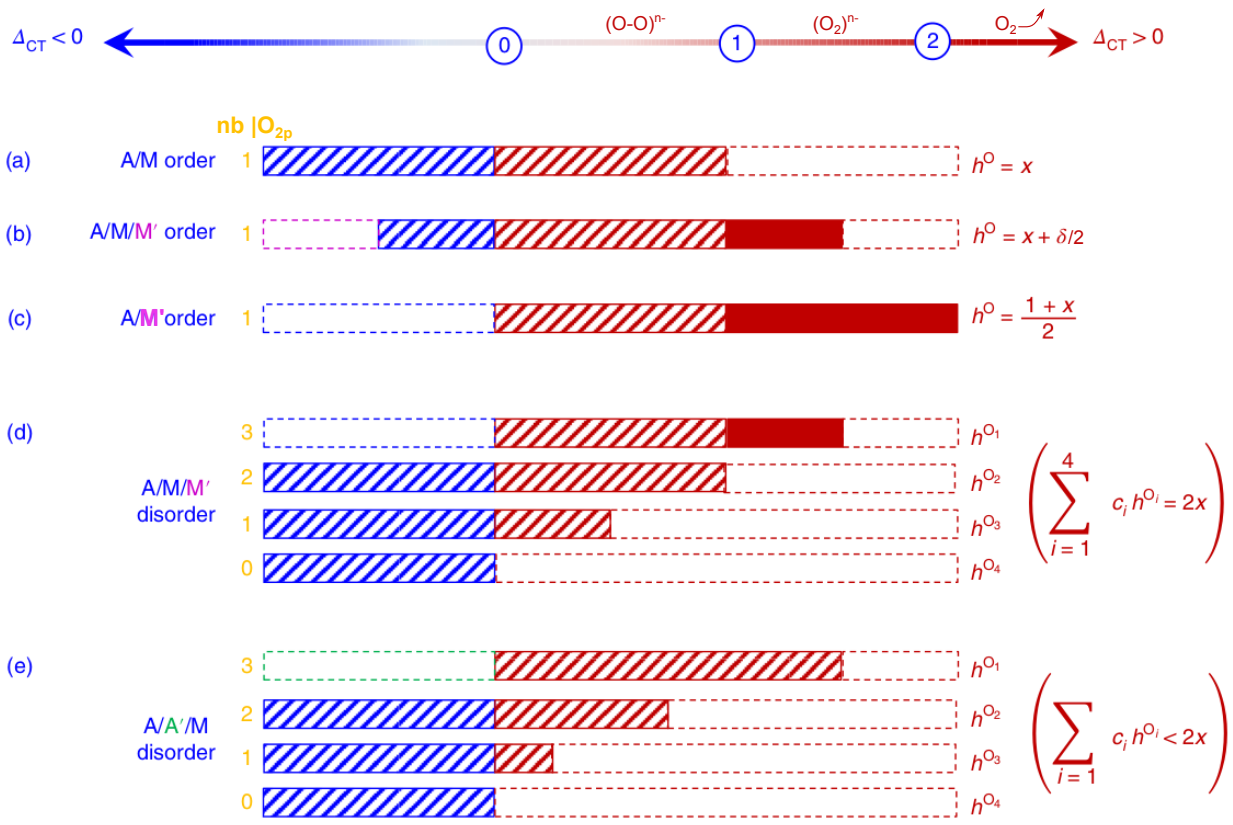


Figure I.16: Summary of the influence of substitution and ordering on the hole distribution among oxygen sites and corresponding A.R. mechanism. M' (pink) and A' (green) are inactive elements forming covalent and ionic bonds with oxygen, respectively. From [63]

# 3 Unified picture of anionic redox

We now describe a method to determine the reversibility of A.R. in a compound from its structure and stoichiometry. We will then conclude this chapter by comparing this model with other mechanisms that have been proposed in the literature.

## 3.1 Predicting the distortion regime and electrochemical curve

Using some approximations on the model, we can predict the reversibility of A.R. in a compound by simply considering its structure and stoichiometry. The first step is to evaluate the average number of hole per oxygen $\langle h^O \rangle$ for the material, which has been done in the previous section. For the ease of reading, the holes distribution on the oxygen populations has been summarized in fig. I.16 for each of the substitution cases considered (A/A' & M/M' with order or disorder).

Thanks to the mechanistic study we know that the oxidation of the oxygen is reversible (RCM) up to a certain threshold (noted $x$) upon which oxidation becomes irreversible (oxygen pairing). Therefore, the second step is to determine the oxidation of the various

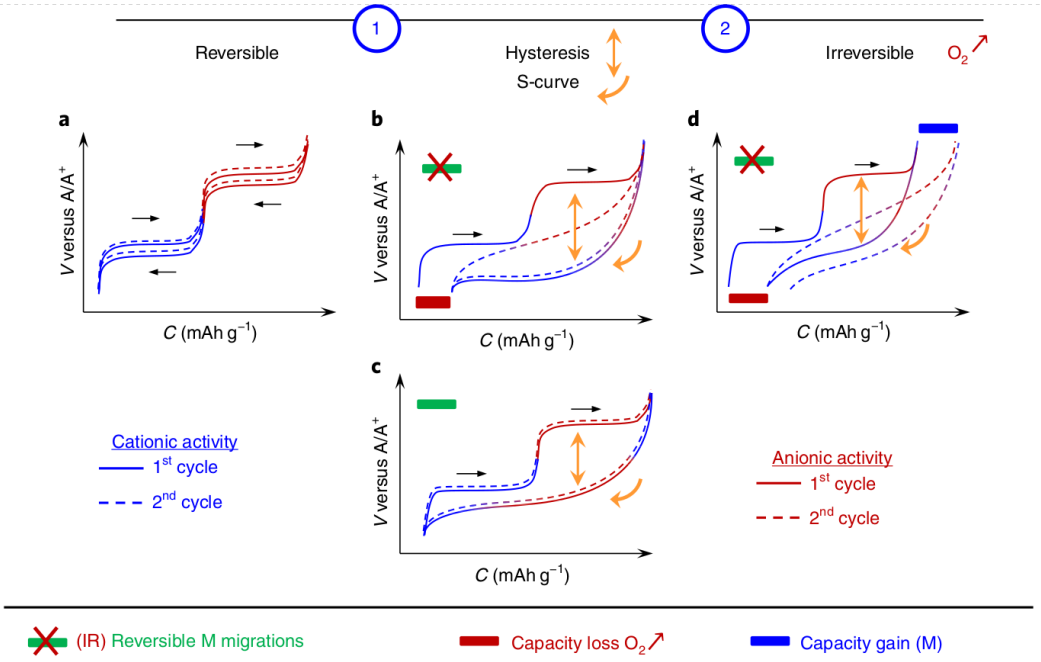


Figure I.17: Electrochemical curves corresponding to each of the A.R. domain defined by $h^O$. (a) Before (1), A.R., proceeding through RCM, is reversible. Between (1) and (2), disproportionation occurs, incurring cation migration. The subsequent disorder causes a slopped voltage curve. (b) If the migrations are irreversible, the capacity fades. (c) If they are reversible, the capacity may be recovered. (d) Beyond (2), the reductive eleimination leads to $O_2$ release in addition to migration, to create disorder and capacity loss. This also causes a reduction of the metal which incurs a transfer from anionic to cationic charge compensation, leading to voltage fade and capacity drift. [63]

oxygen populations in the compound. If $h^O < x$ (red hatching), the oxygen are able to couple with the metal, thus allowing reversible oxidation. In contrast, if $h^O > x$ (solid red) this oxygen population will undergo pure oxygen pairing, leading to local structural degradation. Based on this indicator we can describe the corresponding sequence of electrochemical processes occurring in each type of compound and, from there, the shape of the electrochemical curve, as shown in fig. I.17.

For ordered A/M compounds (fig. I.16.a), the cationic redox consumes $1-x$ electrons, so that $h^O \leq x$. This low $h^O$ implies that the RCM is the dominating mechanism during the whole A.R. The voltage profile of these materials should therefore display two distinct and nicely reversible electrochemical processes – $M^{n+}/M^{(n+1)+}$ and $O^{2-}/O_2^{(2-x)-}$ – and a potential jump between the cationic and anionic reactions (see fig. I.17a). The anionic process should cause a limited polarization since the relative individual displacements are small during cooperative distortion.

The substitution of an active metal by an inactive one (M/M') decreases the cationic capacity while preserving the total capacity, thus causing an increase in $\langle h^O \rangle$ (see fig. I.16.b). After reaching the critical state of charge ($h^O = x$), the RCM cannot stabilize the

holes anymore which will thus disproportionate among the distinct oxygen populations (fig. I.16d). If the oxygen sites are equivalent (ordered compound), cationic migrations will take place to assist this disproportionation by creating disorder. The least stable oxygens will be primarily oxidized, and prone to $O_2$ gas release through partial reduction of the surrounding transition metal. Voltage hysteresis are expected, due to O/M band inversion and structural degradation, which may also cause capacity loss (see fig. I.17.b). If the structural degradation is reversible (e.g. reversible migration), the capacity might be fully reversible (fig. I.17c). However, this requires very low reduction voltages and causes a continuous structural degradation on the long run.

The complete M/M' substitution leads to a pure charge transfer compound, such as $Li_2MnO_3$ where the whole capacity relies on anionic redox (see fig. I.16.c). In this case, the same voltage hysteresis and irreversible degradation are expected. However, in this case, the activation of a metallic redox couple in discharge may partially compensate the capacity loss in the oxygen network, thus leading to a "capacity drift" in the voltage profile (fig. I.17.d). This is the case of $Li_2TiO_3$ or $Li_2MnO_3$, where the couple +3/+4 of Mn and Ti get activated after the first discharge, thanks to the reductive elimination.

Finally, the substitutions of the intercalant by a highly reducing metal (A/A' substitution, see fig. I.16.d) seems to be the only way to achieve a reversible anionic capacity with $h^O > x$ due to the possible stabilization of peroxides ($h^O = 1$) in $M_d$-free/A'-rich environments. However, the statistical weight of the oxygen population with such environment must be significant to benefit the anionic capacity, which implies large A/A' substitution ratio, which decreases the capacity and the electronic conductivity.

## 3.2 Comparison to other models

This model has been designed to account for as many experimental features as possible, such as the disordering or the capacity loss upon anionic redox, as demonstrated in the next chapter. However, other models have also been proposed to account for those facts in a different way. We will shortly review these models and see how they can be reconciled with the framework we just presented.

### High oxidation theory

When the oxidation of oxygen had not been proposed, the oxidation of the metal to high oxidation state was perceived as a the only possible explanation to the extra capacity. This is the case for the early report of $Li_2MO_3$ where the occurrence of Mn(+V) is proposed as the origin of the extra capacity.[29] With the development of advanced A.R. characterization techniques, this theory has however been less invoked as an explanation.

Nevertheless, Van der Ven *& al.* recently proposed a critical reinterpretation of all the existing experimental, arguing that the possibility of metal high oxidation has not

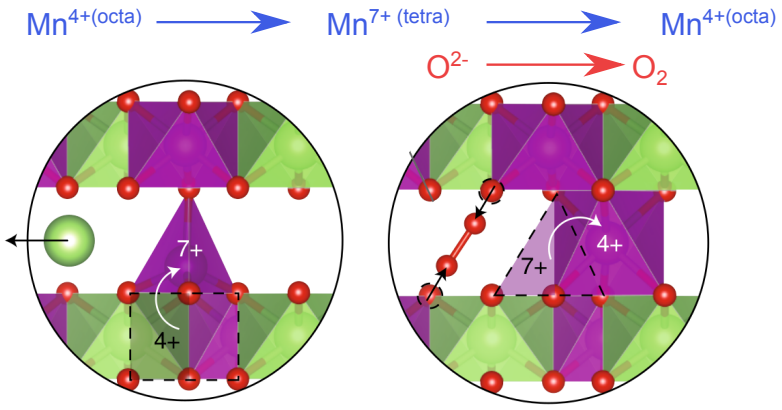


Figure I.18: 2 steps mechanisms with $Mn^{+7}$ as an transition state. Adapted from [83]

been completely ruled out.[83] Indeed, by arguing that charged compounds are easily corrupted by beam damage, they question the results of spectroscopic analyses. Based on this assumption, they propose that in Li-rich Mn-containing cathodes, $Mn^{+7}$ is formed and migrates to tetrahedral sites (fig. I.18 left). The Mn would then react with the oxygen network through a form of localized reductive coupling leading to another migration of the Mn into octahedral site and the formation of oxygen peroxide (fig. I.18 right).

From an experimental point of view, it is clear that $Mn^{+7}$, despite being very unstable, does not dissolve into the electrolyte because it would lead to a purple coloration of the electrolyte which has never been observed. This means that the reductive coupling is faster than the dissolution. In this case, the $Mn^{+7}$ can be considered as a transition state species and the proposed mechanisms can be considered as a kinetically resolved description of the RCM. Thus this model can be inserted within the framework we just proposed, even though its seems hard to back it up with experimental evidence.

### Redefined anionic redox

Another important contribution to defining A.R. framework was brought by Ceder, Chueh and coworkers who re-investigated the $LiRu_xSn_{1-x}O_2$ model compound.[84] In this paper, the authors start by giving an alternative definition of anionic redox:

> "Until now, oxygen redox has been defined as the depopulation of non-bonding (or 'weakly/minimally hybridized') oxygen $2p$ states. However, this definition does not take into account how materials respond to the depopulation of these states, which as we will show later is a crucial component of oxygen redox. So, we provide a more specific definition here: oxygen redox requires the depopulation of non-bonding (or weakly/minimally hybridized) oxygen $2p$ states *wherein the resulting holes reside in predominantly oxygen character orbitals after any structural and electronic reorganization has occurred.*"

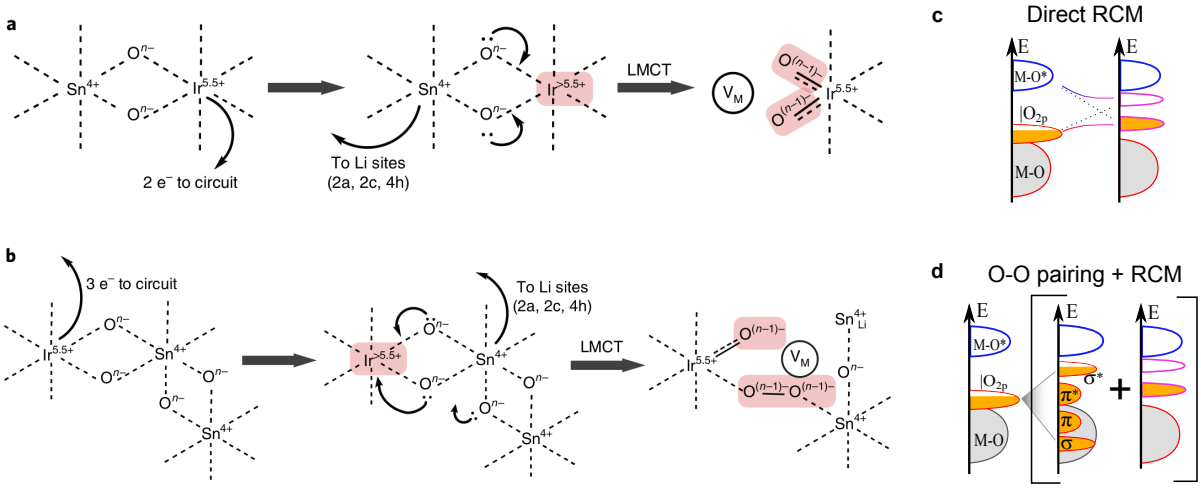


Figure I.19: a) & b) Mechanisms proposed in [84] based on LMCT. c) & d) Corresponding mechanism in our model, based on RCM.

This means that, contrary to our functional definition, based on measurable electrochemical notions (extra-capacity and reversibility), this definition of anionic redox involves the knowledge of the electronic mechanism underlying the distortion. Using the terms introduced earlier in this chapter, we may rephrase it as follow: *"oxygen disproportionation is anionic redox, while RCM is not"*. While this definition is valid and interesting, its efficiency may be questioned. Indeed, it requires to know the distortion mechanisms to decide whether or not a compound undergoes A.R., even though this mechanisms is hard to determine (experimentally or by simulation) and the distinction is not clear since RCM and disproportionation occur sequentially in the same compound.

Apart form this re-definition, this paper also proposes two oxidation mechanisms (see fig. I.19.a & b) based on Ligand-to-metal charge transfer (LMCT in the figure). Since LMCT is here another name for the RCM neither of these two mechanism fall in their definition of A.R., hence the claim that "$LiIr_xSn_{1-x}O_2$ *does not undergo anionic redox*". We see here that it is more a question of definition than a true reinterpretation of the data.

Indeed, the two mechanisms proposed (fig. I.19 a & b), can both be interpreted within the framework described in the previous section: In the first mechanism (fig. I.19.a), the formation of two $Ir_d$–$|O_{2p}$ $\pi$ bonds can be described as a "direct RCM" without any O-O pairing step (fig. I.19.c). The pattern of the two $Ir_d$–$|O_{2p}$ $\pi$-interactions may even be described as a M-O-O bond (even though the symmetry of such bond remains elusive). The second mechanisms (fig. I.19.b) can be described as the simultaneous occurrence of a direct reductive coupling (formation of $Ir_d$–$|O_{2p}$ $\pi$-interactions) and an oxygen pairing,

possibly linked with the migration of the $Sn^{+4}$(fig. I.19.d)[i].

Unfortunately, the experimental data itself and its interpretation are still controversial. Indeed, 2 months after the work from Ceder & al., a paper from Argonne laboratories argued that the holes are indeed localized on the oxygen, because their X-Ray Absorption spectroscopic signature is distinct from that of the Ir holes of the same energy, thus contradicting the hypothesis of "direct RCM".[85]

Interestingly, in the two theories exposed (high Mn oxidation and Ir-mediated A.R.), the oxidation of the metal occurs prior to the RCM. Hence these works provide a kinetic description of the electron transfers while we only described thermodynamic evolution. To reconcile these approaches with our model, we can formulate the hypothesis that the oxidation of oxygen is buffered by the oxidation of the metal to high oxidation state, because of its higher softness compared to oxygen. This charge buffering would then allow for the slow atomic reorganization necessary to stabilize oxygen holes. This metallic charge buffering is however a mere hypothesis and further work is still needed both at the experimental and the theoretical levels to completely understand and describe the RCM charge transfer sequence.

> This concludes the presentation of our state of understanding of the anionic redox, based on a mechanism competition determined by the distribution of holes among the anions. Now that the theoretical foundation is laid, we can re-examine the results of recently reported anionic redox compounds and provide an in-depth interpretation of the mechanisms at play.

[i] Since Ir and Sn at low concentration have the same impact on the XRD Bragg intensity, the authors had to attribute all migrations to Sn (and none to Ir) during the XRD refinement. The nature of the migrated metal thus remains controversial.

# II Describing new compounds: Na-deficient oxides & Li-Rich sulfides

> It doesn't matter how beautiful your theory is,
> if it doesn't agree with experiment, it's wrong.
>
> Richard P. Feynman

In the recent years, two interesting families of A.R. compound have gained increasing attention because they behave very differently from the Li-rich oxides which have been extensively studied already. These two families are obtained by replacing some very ionic elements of the lithium oxides by more polarizable elements, leading to "softer" structures which can accommodate distortion more easily, thus inducing specific A.R. behaviors which differ from Li metal oxides.

We will first study the A.R. behavior of Na-deficient oxides, to compare the effect of Li and Na intercalation. After that, we will investigate the Li-rich sulfides, to understand the origin of the reversible behavior of these compounds. Each of the studies will begin with some key experimental results to characterize the specific A.R. behavior of these compounds before presenting the computational study that was done to model and explain these observations.

## 1 Na-deficient layered oxides

### 1.1 Context: Influence of Na

The occurrence of anionic oxidation is solely determined by the electronic structure of the compound near the Fermi level, which does not depend on the alkali in the limit where it behaves as a "perfect donor". However, the reversibility of this oxidation is determined by the type of A.R. stabilization mechanism, which depends on the crystal structure and its resilience to distortion. This resilience to distortion is linked with the mechanical properties of the compound, which are, in turn, strongly influenced by the nature of the intercalated alkali.

#### Mechanical properties

When comparing the experimental and theoretical elasticity of Na- and Li-based compounds (see table II.1), we find that Na-based compounds display comparatively lower

| Formula | A | DFT | Exp. |
|---|---|---|---|
| A metal* | Li | 13.7 | 13 |
| | Na | 7.8 | 7.5 |
| AF* | Li | 67.3 | 80 |
| | Na | 44.6 | 49.3 |
| ACl* | Li | 31.5 | 35.4 |
| | Na | 23.4 | 26.6 |
| $AMnO_2$† | Li | 118 | |
| | Na | 88 | |
| | K | 63 | |

Table II.1: Evolution of bulk modulus (GPa) with alkali substitution. Refs *: [86] †: [87].

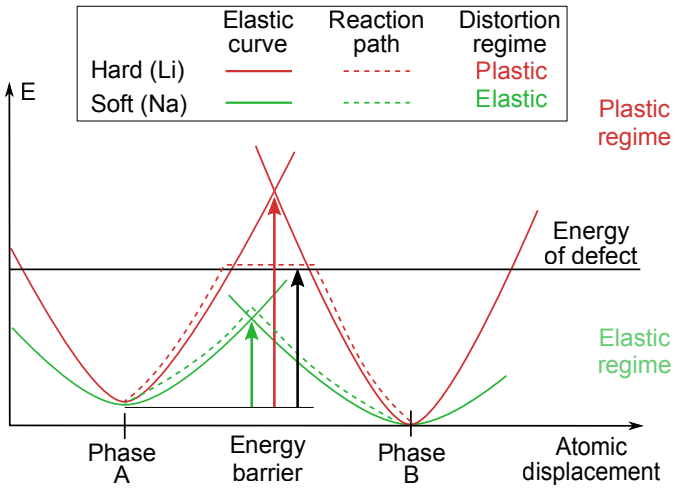


Figure II.1: Comparing phase transition mechanism in soft and hard compounds.

stress/strain ratios. Therefore, if we consider a solid in its ground state atomic configuration, (phase A in fig. II.1), the energy increase (stress) as a function of the strain (atomic displacement from equilibrium) will be lower for Na- than for Li-based compounds.

Upon charge, the ground state configuration changes (phase B), which provides a driving force for an phase transition (A→B). If the phase transition has a weak driving force (e.g. alkali-ordering), the transition will proceed through elastic regime and it will only be observed in coumpounds where the kinetic barrier for elastic deformation is low enough. Hence this phase transition will be more visible for softer compounds (low energy barrier, green arrow in fig. II.1) than for harder ones (high energy barrier, red arrow). This is coherent with the much higher Na diffusion coefficient in $Na_{0.5}CoO_2$ ($D_{Na} \approx 10^{-6}\, cm^2/s$ [88]) than in $Li_{0.5}CoO_2$ ($D_{Na} \approx 10^{-11}\, cm^2/s$ **jangLithiumDiffusionLi2001**), which explains the observation of Na-ordering in charge and discharge which are not detected for Li.

In contrast, the phase transitions can have a driving force which is sufficiently large to overcome high kinetic barriers (e.g. stacking sequence transition). If the energy barrier for elastic deformation is lower than the energy of defect nucleation (black arrow in fig. II.1), the phase transition will proceed through the elastic regime which is reversible (green dashed line). In the opposite case, the transformation will proceed through the plastic regime (dashed red lines). This plastic deformation entails the creation of defects, such as dislocation, migration or cracking that have been extensively characterized theoretically and experimentally in oxide cathodes.[89].

In the previous chapter, we have seen that the cooperative distortion is favored by a lowering of the displacement energy (i.e. elastic regime) while the disproportionation relies on the creation of local defects. Hence the substitution of Li by Na is expected to

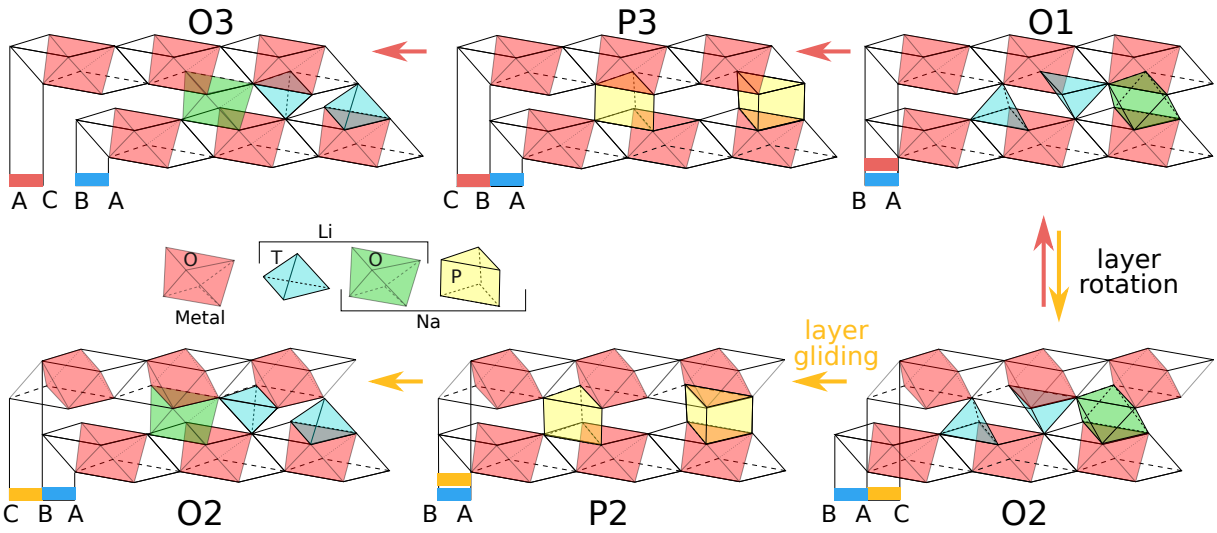


Figure II.2: Nomenclature for stacking types: *P/O/T*: *P*rismatic, *O*ctahedral or Tetrahedral A site. Number: periodicity of the layers. Layer gliding (horizontal) occurs upon cycling while layer rotation (vertical) is impossible. Thus the phase transition only occurs within a stacking family: *[O3/P3/O1]* or *[O2/P2]*.

modify the energy balance between the two A.R. mechanisms. Experiment-wise, we will see that A.R. in Na-ion compounds indeed shows specific features which are not observed in Li-rich compounds. By using our model to explain those features, we will provide valuable insights on the A.R. mechanism in these compounds and validate the correctness of our model.

### Structural description

Beyond the mechanical properties, Na also provides some interesting structural properties since it can form layered phases that are not directly accessible with lithium. Indeed, the available volume in an insertion site increases when going from tetrahedral ($T$) to octahedral ($O$) to prismatic ($P$) coordination. To minimize the strain, the insertion volume should match the volume of the inserted ion.

$Li^+$ ionic radius ($r = 0.9\,\AA$) is much smaller than that of $Na^+$ ($r = 1.16\,\AA$).[90] Consequently, $Li^+$ will lie in smaller insertion sites ($T$ & $O$) leading to *O2* or *O3* structures (see fig. II.2).[91] However, in *O2* stacking, the $O$ sites share one face with a metal octahedron. This is not the case in *O3* stacking which is thus more stable, so that Li-rich compounds are synthesized in *O3*.

Contrary to $Li^+$, $Na^+$ ions will lie in larger sites ($O$ & $P$), thus allowing to stabilize *P2* or *P3* stacking phases. Among these prismatic compounds, the Na-deficient family, *P2*-$Na_xMO_2$, $x < 1$ has proven very interesting for A.R. study.[92]

Indeed, some of these Na-deficient compounds display pure anionic oxidation, without cationic participation – at least in the first charge. These compounds are obtained from *P2*-$Na_{2/3}MnO_2$ by substituting 1/3 of Mn with an electro-positive element (M = Mg,

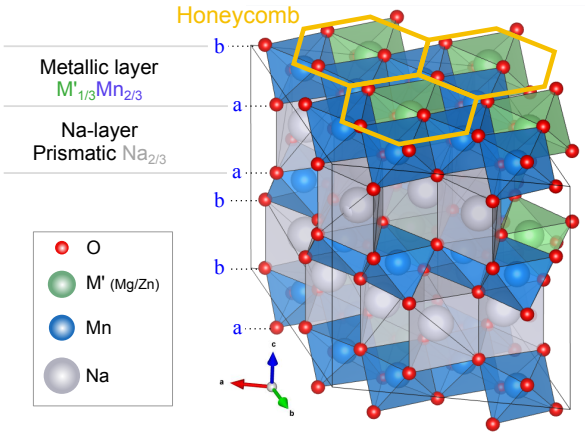


Figure II.3: Structure of $Na_{2/3}M'_{1/3}Mn_{2/3}O_2$.

$Zn^{2+}$). The resulting stoichiometry, $Na^{+}_{2/3}M^{2+}_{1/3}Mn^{4+}_{2/3}O^{2-}_{1/3}$ increases the Mn oxidation state to +IV, which is less active than oxygen $|O_{2p}$ [a] so that the charge balance is only achieved by oxygen oxidation (in the first charge at least). Furthermore, the $(Mn_{2/3}M_{1/3})O_2$ layer has a honeycomb ordering[b] (see fig. II.3) which has been thoroughly studied in Li-rich oxides such as $Li_2MO_3$ to build the single-site A.R. model. Featuring both a "pure anionic oxidation" and a well known structure, these $Na_{2/3}M_{1/3}Mn_{2/3}O_2$ are ideal to test our A.R. model on Na-compounds. As a consequence, they will be the focus of this study.

## 1.2 Experimental questions

When these compounds were synthesized and characterized by our team (thanks to the Ph.D. work of X. Bai [93]), some results clearly differed from those obtained on alkali-rich compounds, thus raising several questions. To contextualize each of these points, we will compare some experimental results across representative Na-deficient compounds, emphasizing the common features and how they question our understanding of A.R.

The first substitution of $Na_{2/3}MnO_2$ by Mg was first realized by Komaba *& al.* in 2014, who reported an "anomalous capacity" in $P2$-$Na_{2/3}Mg_{0.28}Mn_{0.72}O_2$ due to a process at 4.5V (A.R. had not been coined yet).[94] However, it was only in 2018 that Bruce *& al.* rediscovered the anomalous capacity of this compound, finally labeling it as oxygen redox (solid state synthesis, see table II.2).[95] Shortly afterwards, Dai *& al.* synthesized $P2$-$Na_{2/3}Mg_{1/3}Mn_{2/3}O_2$, achieving an exact stoichiometry thanks to an hybrid synthesis method (sol-gel+calcination, see table II.2).[96] Later on, Song & al. synthesized another stacking: $P3$-$Na_{2/3}Mg_{1/3}Mn_{2/3}O_2$.[97].

In the wake of this Mg-substitution trend, $P2$-$Na_{2/3}Zn_{2/9}Mn_{7/9}O_2$ was first synthesized

[a] The electronic configuration of Mn(+IV) *is* $t_{2g}^3e_g^0$ so the oxidation to $Mn^{+5}$ result in an unstable $t_{2g}^2e_g^0$ configuration. Therefore, the $Mn^{+4}/Mn^{+5}$ redox voltage is higher than that of oxygen oxidation.

[b] As explained in the previous chapter, their global M/O ratio of 3/2 translates into an average number of metal per oxygen of $\langle n_{MO} \rangle = 2$, corresponding to honeycomb ordering.

by our team in 2018 (solid state synthesis, see table II.2).[74] More recently, Zheng *& al.* obtained a higher Zn content: *P*2-$Na_{2/3}Zn_{0.28}Mn_{0.72}O_2$ (sol-gel+calcination synthesis, see table II.2) [98] as well as *P*2-$Na_{2/3}Cu_{0.28}Mn_{0.72}O_2$.[99]

Hereinafter, we will be comparing the experimental results of some of the mentioned compounds, $Na_xMn_{1-y}M_yO_2$ with M=Zn, Mg (regrouped in table II.2).

#### Influence of the metal

The voltage curves of the selected compounds (see fig. II.4) all support the existence of two electrochemical processes, separated by an inflection in the curve. The capacity corresponding to the lower voltage process is proportional to the initial amount of $Mn^{+3}$ while the second process occurs at a high voltage (>4V) , suggesting A.R. Indeed, in stoichiometric $Na_{2/3}Mg_{1/3}Mn_{2/3}O_2$ (fig. II.4.d), the absence (or traces) of $Mn^{+3}$ leads to drastically reduced Mn-based capacity ($\approx$ 5mAh/g, ending at C-8) . All of these compounds thus seem to feature A.R.

However, $Na_{2/3}Mg_{0.28}Mn_{0.72}O_2$ & $Na_{2/3}Zn_{0.28}Mn_{0.72}O_2$ display almost identical cycling curves, despite different synthesis and different M'. This seems to indicate that the M' metal only has second order effect compared to stoichiometry in the first few cycles. This raises a first question for our theoretical study: *What is the role of the divalent metal in A.R.* and, more specifically, *what is the difference between Mg and Zn ?*

#### Hysteresis

In discharge, all the compounds feature a sloped curve with minimal capacity loss. Various spectroscopic techniques have been used to further investigate this hysteresis. X-ray Absorption Spectroscopy (XAS) and X-Ray Photo-emission Spectroscopy in $Na_{2/3}Zn_{2/9}Mn_{7/9}O_2$[74], XAS in $Na_{2/3}Mg_{0.28}Mn_{0.72}O_2$ [95] or Resonant Inelastic X-Ray Scattering (RIXS) in $Na_{2/3}Mg_{1/3}Mn_{2/3}O_2$.[96] All of these techniques confirm that in charge the low voltage process is the metallic redox and the high voltage process the oxygen redox. In discharge, they indicate that both anionic and cationic reduction are occurring concomitantly. In the following charge however, the cationic and anionic processes are clearly separated again, even though the loss of oxygen capacity is compensated by Mn redox.[96] In 3*d* Li-rich compounds, the separation of cationic and anionic processes is not as clearly recovered in charge and the capacity fades faster upon cycling. Hence the questions: *Why are the cationic and anionic redox separated in charge and mixed in discharge and why is capacity loss slower ?*

#### Phase transition

This increased reversibility may stem from the specific *P2* stacking of the Na-deficient compounds, as opposed to the *O3* stacking of A-rich compounds. The structural characterization of these *P2* compounds reveals that, upon charging these *P2* phases undergo

| | M' | Precursors* | Synthesis | Stoichiometry | Ref |
|---|---|---|---|---|---|
| Solid-state | Zn | $Na_2CO_3$, $Mn_3O_4$, $Zn[OAc^-]_2$ | Ball-mill, 30 min<br>Annealed: 900°C, 9h, air<br>Re-annealed: 700°C, 12h, air | $Zn_{2/9}Mn_{7/9}$ | [74] |
| | Mg | $Na_2CO_3$, $Mn_2O_3$, MgO | Ball-mill, 2h<br>Annealed: 800°C, 8h, $O_2$<br>Re-annealed: 700°C, Ar | $Mg_{0.28}Mn_{0.72}$ | [95] |
| sol-gel | Zn | $Na[OAc^-]$ $Mg[OAc^-]_2$ $Mn[OAc^-]_4$ | Water + citric acid at 80°C<br>Precalcined: 450 °C<br>Calcined: 670 °C, 10h | $Zn_{0.28}Mn_{0.72}$ | [100] |
| | Mg | $Na[OAc^-]$ $Mg[OAc^-]_2$ $Mn[OAc^-]_4$ | Water + $HNO_3$ at 120°C<br>Precalcined: 450 °C, 2h<br>Calcined: 900 °C, 6h, air | $Mg_{1/3}Mn_{2/3}$ | [96] |

Table II.2: Synthesis of $Na_xMn_{1-y}M_yO_2$ with M=Zn,Mg. The compositions are closer to the ideal one for hybrid sol-gel syntheses than for Solid-state syntheses
*$[OAc^-]$ stands for acetate - $O_2CCH_3$

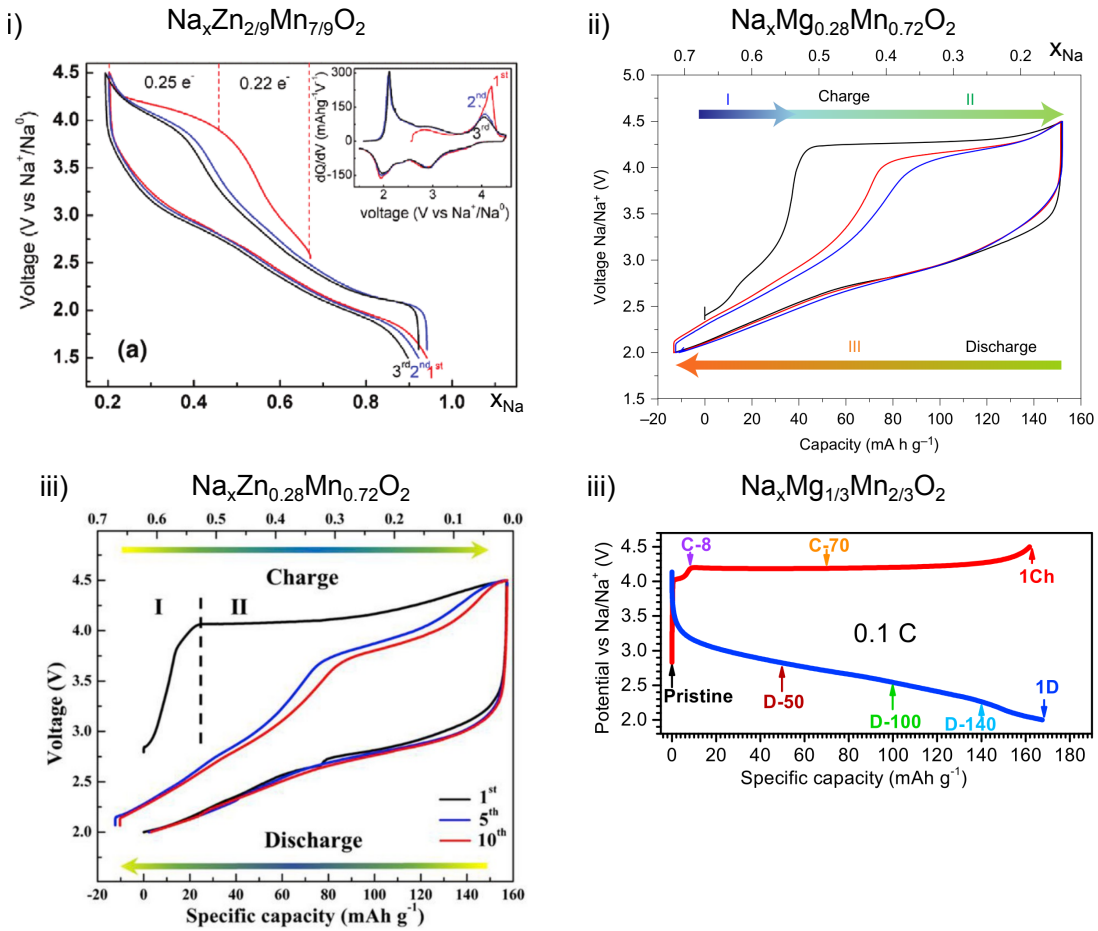


Figure II.4: Cycling of $Na_xMn_{1-y}M_yO_2$ vs. $Na/Na^+$(with M=Zn,Mg ). See table II.2 for references.

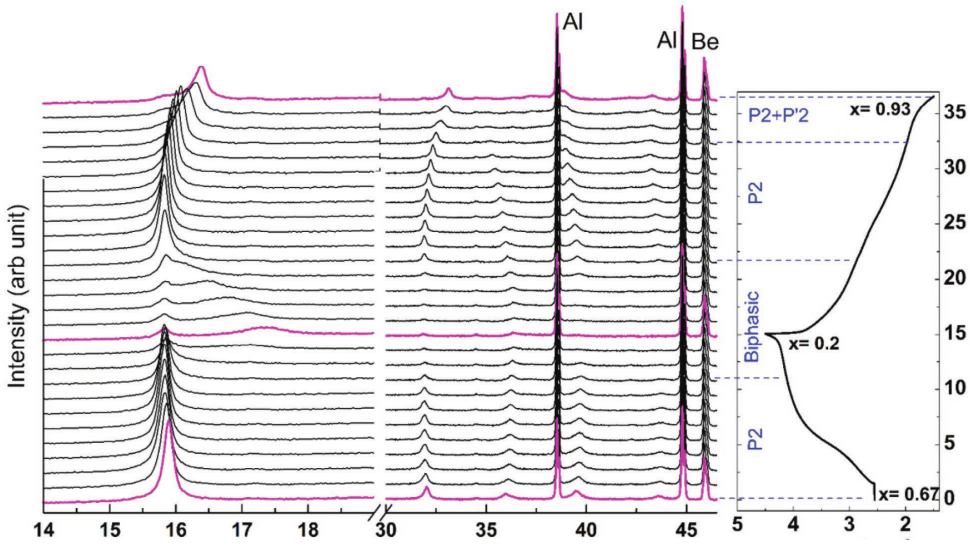


Figure II.5: Stacking phase transitions in $Na_{2/3}Zn_{2/9}Mn_{7/9}O_2$ detected by operando XRD. The anionic redox is associated with biphasic phase transition to *O2* or *OP4*. From [74].

several transitions between *P*- and *O*-stacking phases, as observed experimentally on every Na-deficient compound, using either XRD or TEM (see fig. II.5 for an example in $Na_{2/3}Zn_{2/9}Mn_{7/9}O_2$). [74], [95], [96], [100] Interestingly, for these compounds showing anionic redox, the *P/O* phase transition is postponed to a lower Na content than for compounds showing exclusively cationic redox. Indeed, this P/O transition occurs respectively at $x_{Na} = 0.5$ in $Na_{2/3}MnO_2$ (cationic) [101] and $x_{Na} = 0.3$ in $Na_{2/3}Mg_{0.28}Mn_{0.72}O_2$ (anionic)[95]. Moreover, the fully charged structure of the latter exhibits an unconventional *OP4* structure consisting in an alternating *O-P* stacking sequence[96]. *Why is the $P \rightarrow O$ phase transition postponed in A.R. compounds?*

### Migrations

The occurrence of hysteresis may be caused by cation migrations. However, contrary to the well defined phase transitions, the experimental data concerning the migration in $Na_{2/3}Mg_yMn_{1-y}O_2$ remains controversial. Indeed, on the one hand, Bruce and coworkers asserted that migration did not occur based on electron microscopy (for y=0.28).[95], [102] On the other hand, Dai & al. showed a reversible shift in the spectroscopic signature of the *P2*-$Na_{2/3}Mg_{1/3}Mn_{2/3}O_2$ which they attributed to Mg migration [96] while Song *& al.* showed a migration in *P3*-$Na_{2/3}Mg_{1/3}Mn_{2/3}O_2$.[97] In line with this migration hypothesis, our own data on $Na_{2/3}Mg_{1/3}Mn_{2/3}O_2$, (see fig. II.6) shows an irreversible shift of the Mg signal of Auger electron energy (fig. II.6.a) and X-Ray Photo-emission spectrum (fig. II.6.b & c). These shifts indicate a change of Mg environment, both on the surface and in the bulk, caused by the migration of Mg or of neighboring Mn which seems irreversible, contrary to Dai & al. findings. Finally, in the parent compound $Na_{2/3}Zn_{1/3}Mn_{2/3}O_2$, Zn migration has been unmistakably characterized and it seems to be reversible.[74] Thus

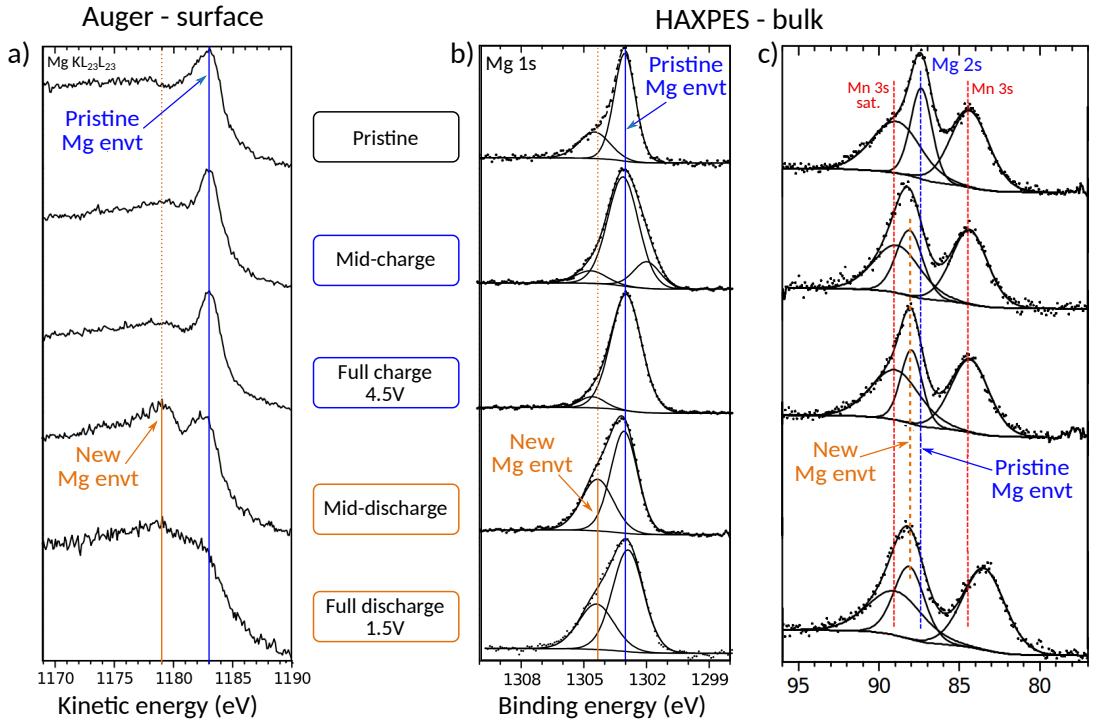


Figure II.6: Spectroscopic signature of Mg migration in Mg in $Na_xMg_{0.28}Mn_{0.78}O_2$ during the first cycle. a) $KL_{23}L_{23}$ edge of Auger spectroscopy, probing the surface of the compound. b) (resp. c) High Angle X-ray Photo-emission Spectroscopy of $Mg_{1s}$ (resp. $Mg_{2s}$), probing the bulk of the compound. Acquired by R. Dedryvère, unpublished

my personal opinion is that migration do occur in $Na_{2/3}Mg_yMn_{1-y}O_2$, even though local electron microscopy imaging may have failed to detect it in [95]. In this case, *why does migration occur at the end of charge ?* Concerning the reversibility of this migration, further characterization is still needed.

This review of experimental data shows that Na-deficient phases display a very specific A.R. behavior which challenges our theoretical framework through several questions:

- What is the role of the divalent metal ? what is the difference between Mg and Zn ?
- What is the origin of the discharge slope and voltage hysteresis ?
- Why is the $P \rightarrow O$ phase transition postponed in A.R. compounds ?
  Is A.R. in *P2* phase more reversible than *O3* phase ?
- Why does migration occurs at the end of charge ?

## 1.3 Theoretical analysis

In order to answer these questions, we have undertaken a thorough simulation and modeling study of these compounds to determine how their behavior could be rationalized within our theoretical framework. For computational purposes, we will use the

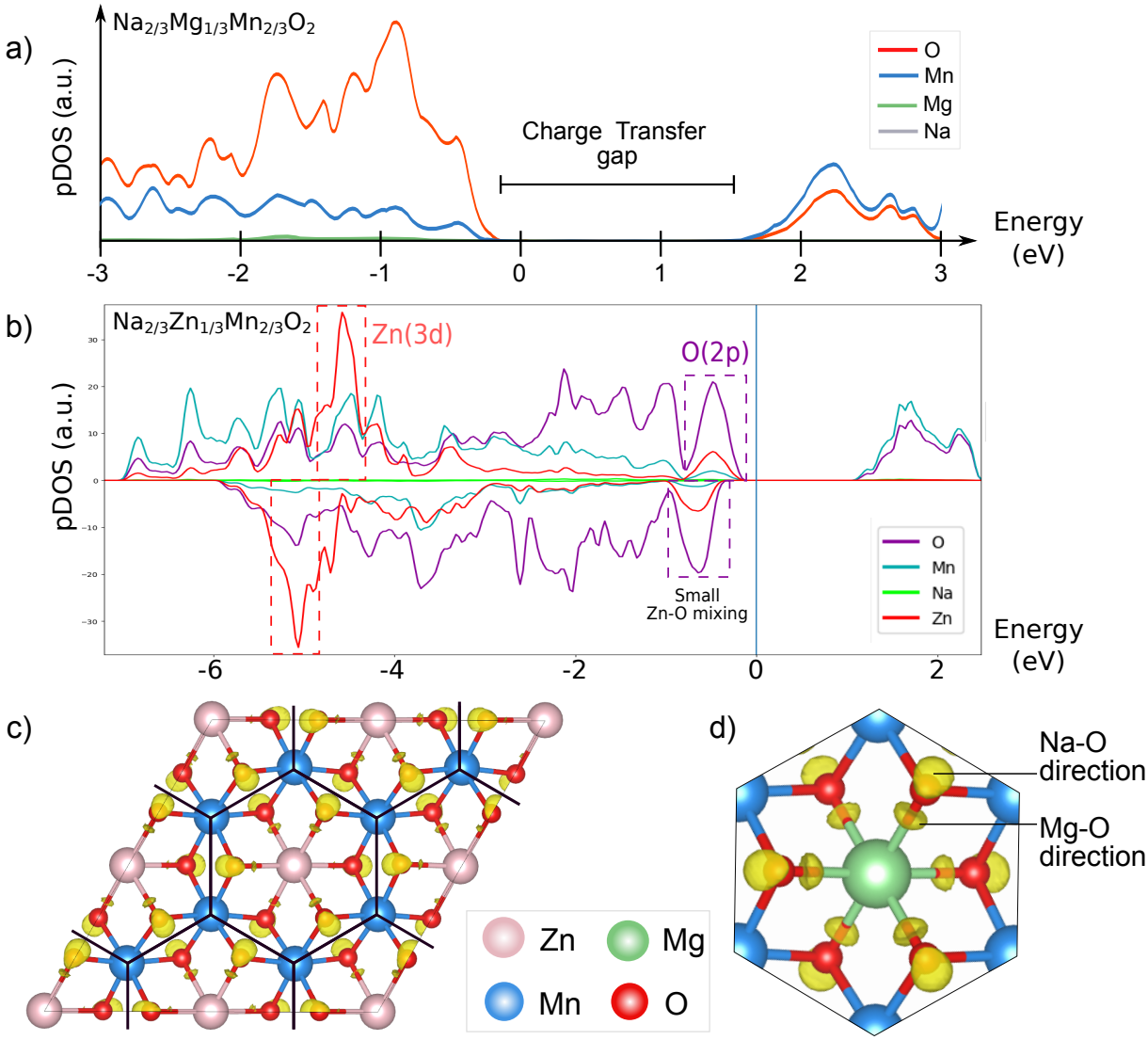


Figure II.7: DOS of $Na_{2/3}M'_{1/3}Mn_{2/3}O_2$ , with M = Zn (a) and Mg (b) and their respective ELF (c & d): (c) TM layer in 221 NZnMO super-cell with honeycomb pattern. (d) Close-up on one honeycomb unit cell for NMgMO.

ideal stoichiometries, *P2*-$Na_{2/3}Mg_{1/3}Mn_{2/3}O_2$ and *P2*-$Na_{2/3}Zn_{1/3}Mn_{2/3}O_2$, which will be referred as NMgMO and NZnMO, respectively.

### Electronic structure evolution

Starting from the ideal *P2* structure with M/M' honeycomb ordering and Na occupying the edges-sharing prismatic sites (see fig. II.3), we first obtained the electronic structure for NMgMO and NZnMO. The element-projected densities of states (pDOS, fig. II.7.a & b) indicate that both compounds are Charge Transfer insulators[c], with a bandgap of ≈1.5 eV. In the case of NMgMO (fig. II.7.a), the absence of Mg contribution in the whole

[c] i.e. where the bandgap separates O and M bands (as opposed to Mott-Hubbard insulator where the bandgap splits the $M_d$ band).

energy range indicates that the $Mg_{2s}$ states are much higher in energy than the $O_{2p}$. As a consequence, the Mg-O bond can be considered as purely ionic, thus leading to a non-bonding $|O_{2p}$ as confirmed by the ELF of NMgMO which display two lobes of identical size around the oxygens (fig. II.7.d).

In the case of NMZnO, the closed-shell $d^{10}$ states are stabilized at 5 eV below the Fermi level (red rectangle in fig. II.7.b). This closed shell configuration and the large potential difference between $Zn_d$ and $O_{2p}$ states strongly impedes their interaction without completely preventing it. Consequently, the Zn-O bond is essentially ionic with a small covalent perturbation, as indicated by the small pDOS of Zn in the energy range of the $|O_{2p}$ (purple rectangle in fig. II.7.b). This small interaction is confirmed by the ELF of NMZnO where the lobe pointing towards the Zn is smaller than the one pointing towards Na. This marginal covalency is however a second order effect since we still see the $|O_{2p}$ lobe in the ELF. Practically speaking, Zn therefore behaves as an (almost) perfect donor, as Mg, so that NMgMO and MZnMO display very similar electrochemical cycling.

Having characterized the pristine states of these compounds, we now turn to their dynamic behavior upon oxidation. Assuming a pure anionic redox in $Na_{2/3}M_{1/3}Mn_{2/3}O_2$ , the average number of holes per oxygen increases from $\left\langle h^O \right\rangle = 0$ to 1/3 when charging from $x = 2/3$ to 0. Using the relative amplitudes of both Mn-O and O-O Crystal Orbital Overlap Population (COOP) along with the pDOS, we can roughly identify the $Mn_d$-$|O_{2p}$ states (yellow in fig. II.8).

As expected, in the pristine, these states lie at the Fermi level and get oxidized upon charge and become unstable. The increasing $M_d$-$|O_{2p}$ interaction, identified at the top of the valence and the bottom of the conduction bands as $x_{Na} = 1/6$ indicates that the main stabilizing mechanism is the RCM. However, the existene of some pure O-O $\sigma^*$ states, at 0.9 eV (red dotted rectangle), indicates a beginning of disproportionation. Thus we see a proof of the coexistence of both RCM and disproportionation.

Upon further charge ($x_{Na} = 0$), the RCM becomes stronger as indicated by the increased energy dispersion of the $M_d$-$|O_{2p}$ states which extend below the Fermi level, thus resulting in a formal reduction of the metal. Concomitantly, the empty O-O $\sigma^*$ states get higher in energy (red dotted rectangle) and clearly separate from the lower $M_d$-$|O_{2p}$ states to reach to bottom of the conduction band. This clearly indicates the occurrence of reductive elimination.

We have thus resolved the sequence of A.R. mechanisms in this compound which undergoes RCM first before a transition towards disproportion at the very end of charge. This heavy reorganization of the electronic configuration must correspond to a strong distortion of the structure which we will now investigate.

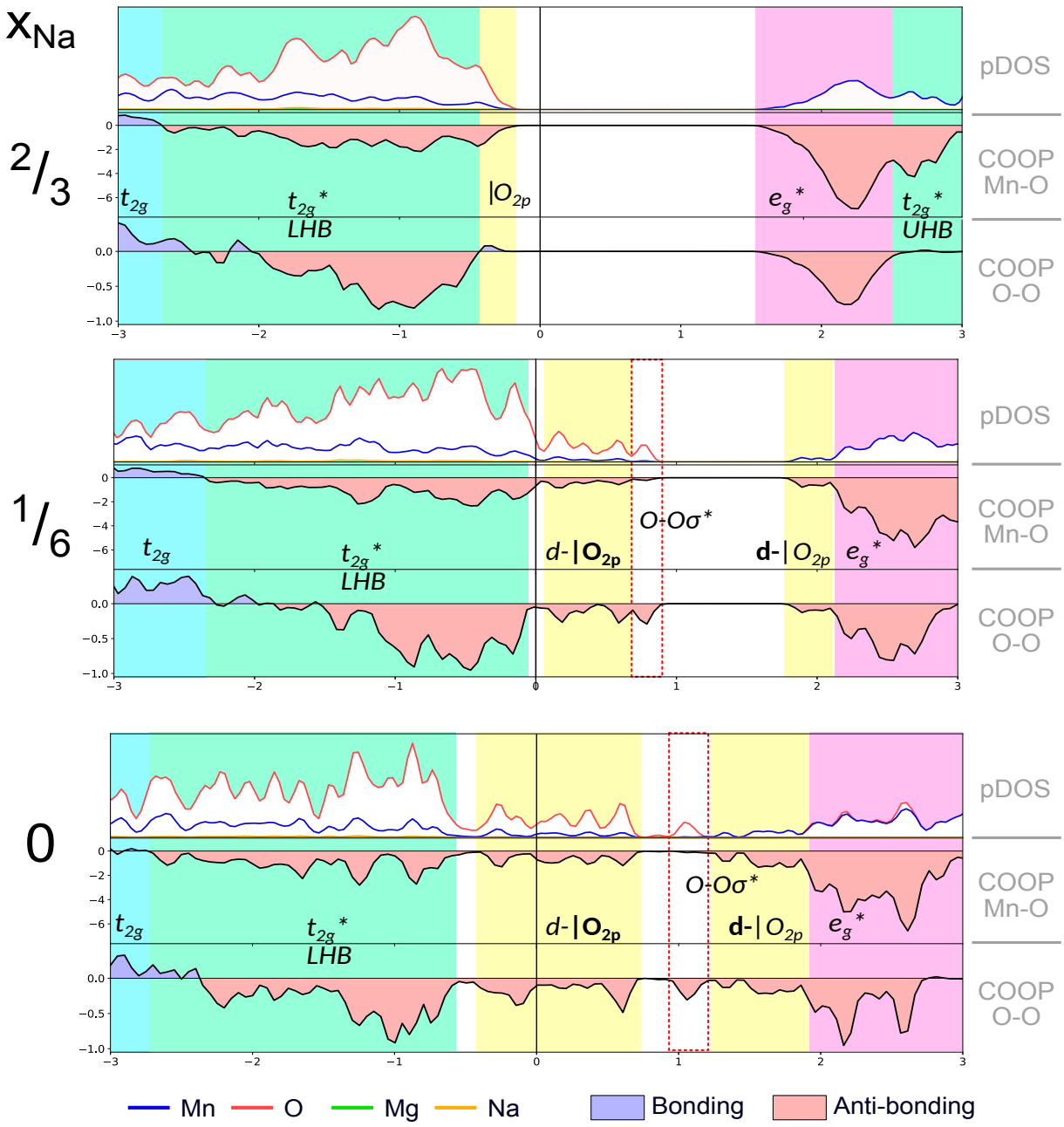


Figure II.8: Evolution of NMgMO electronic structure upon anionic redox (DOS, O-O and Mn-O COOPs). In yellow, the $|O_{2p}$ states at the Fermi level in the pristine ($x_{Na} = 2/3$) get oxidized and hybridized with $M_d$ states upon oxidation ($x_{Na} < 2/3$). In dashed rectangle, some pure O-O$\sigma^*$states. See Methods for orbital identification.

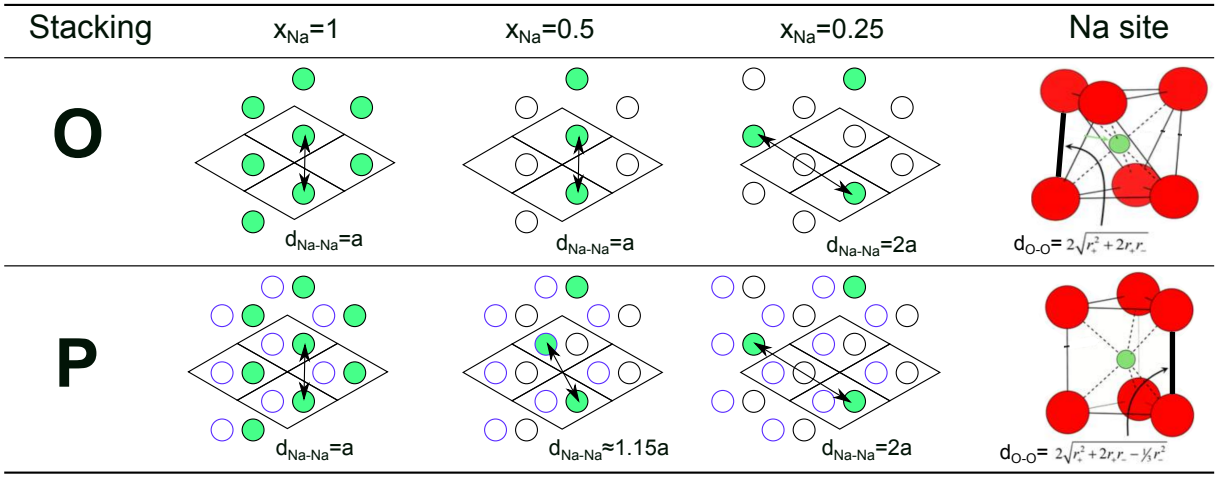


$\mathbf{x_{Na}} = \mathbf{1}$– $d_{Na-Na} = a$ is similar in *P*- and *O*-stacking which have comparable Na-Na repulsion. Besides, the presence of $Mn^{+3}$ causes a J-T distortion of the TM-layer denoted by a ' (prime), e.g. *O2'* or *P2'*.
$\mathbf{x_{Na}} = \mathbf{0.5}$ – In *P*-stacking, the Na get distributed over the two Na sites ($d_{Na-Na} = 2a/\sqrt{3} \approx 1.15a$) so the Na-Na repulsion is lower than for O-stacking. Hence Na-deficient compounds – with a Na ratio close to 0.5 Na/F.U. – are synthesized in *P*-stacking.
$\mathbf{x_{Na}} \leq \mathbf{0.25}$: $d_{Na-Na} = 2a$ is similar in *P*- and *O*-stacking. As Na repulsion and oxygen screening decreases, O-O repulsion becomes prevalent. Inter-layer O-O distance is larger in *O*-stacking which is thus more stable.

Figure II.9: *P/O* phase transitions in classical layered oxide. In *O*-type unit-cell, Na lies in the only octahedral site. In *P*-stacking, the unit-cell has 2 distinct prismatic sites (blue and black circles). Adapted from [90]

### Crystalline structure evolution & distortion

We now investigate the several stacking phase transitions that have been reported via structural characterization. In a classical oxide, these phase transitions are governed by the competition between Na-Na and O-O electrostatic repulsion, as illustrated and explained in fig. II.9. For low Na content, the Na-Na repulsion decreases and the oxygen screening becomes weaker so the electrostatic repulsion between oxygen atoms across the inter-layer becomes increasingly important. For this reason, the prismatic stacking is less stable than the *O*-type stacking because the O-O distance across the layer is much lower (see the $d_{O-O}$ calculation based on ionic radius in fig. II.9). Interestingly, difference in inter-layer O-O distance also modifies the possible oxygen pairing, thus providing a key to understand the differences observed between *O* and *P* compounds upon A.R.

In order to see how the anionic redox impacts this equilibrium, we computed the phase stability diagram of this compound. Since there is no layer rotation upon charge, the P→O phase transition preserves the 2 layer periodicity, hence this phase diagram can be

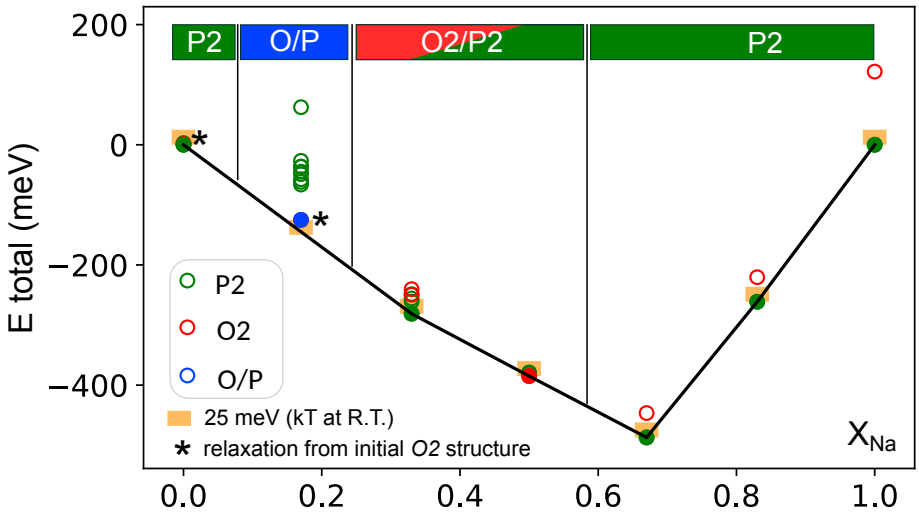


Figure II.10: Formation energy of phases obtained from desodiation of the *P2* and *O2* structures of NMgMO. At a low Na content, the *O2* structures converting to *O-P* hybrid stacking or *P2* are shown in blue. The most stable structure at each composition are highlighted by filled symbols. If the energy above the Hull is higher than thermal agitation energy at room temperature (orange squares) the structure is not stable.[75]

reduced to the comparison of *P2* and *O2* energies. The results, presented in fig. II.10, show that both polymorphs have equivalent stability in the $1/6 < x < 2/3$ composition range. However, the energy of *P2* stacking has been overestimated for $x_{Na} = 0.5$ as Na was constrained to stay on a single lattice[d]. Therefore, the energy crossover should in reality, occur at lower Na content, i.e. around $x_{Na} = 1/6$. At $x = 1/6$, the structure undergoes a partial O/P phase transition, suggesting a *O-P* intergrowth at low Na content. This result is fully consistent with experimental observations of *O-P* hybrid stacking upon deintercalation. This *O-P* coexistence seems to result from a compromise between O-O repulsion, favoring *O* stacking and O-O bonding, which requires *P* stacking. We therefore embark in a thorough comparison of *O* and *P* structures to disentangle these effects.

#### Comparing distortion in *P* & *O* staking

We want to compare *O* and *P* stacking in the whole charge composition range ($0 < x < 2/3$), which corresponds to anionic redox. For $1/6 < x < 2/3$, our results show that both polymorphs conserve their stacking type (*P2* or *O2*) upon relaxation. Thus these stacking types correspond to distinct minima in the potential energy surface of the material, separated by large kinetic barriers which prevents the inter-conversion during the relaxation procedure. This remarkable stability is extremely convenient to investigate the response of each polymorph to desodiation. In this range ($1/6 < x < 2/3$) both structures undergo similar transformation: all oxygens form O-O pairs with one next-

[d]In the discharged structure, Na only lies on one sub-lattice (edge sharing sites). The desodiation algorithm (see Methods section) only removes Na (without moving it), hence the impossibility to populate the other sub-lattice (face sharing sites) for lower Na content.

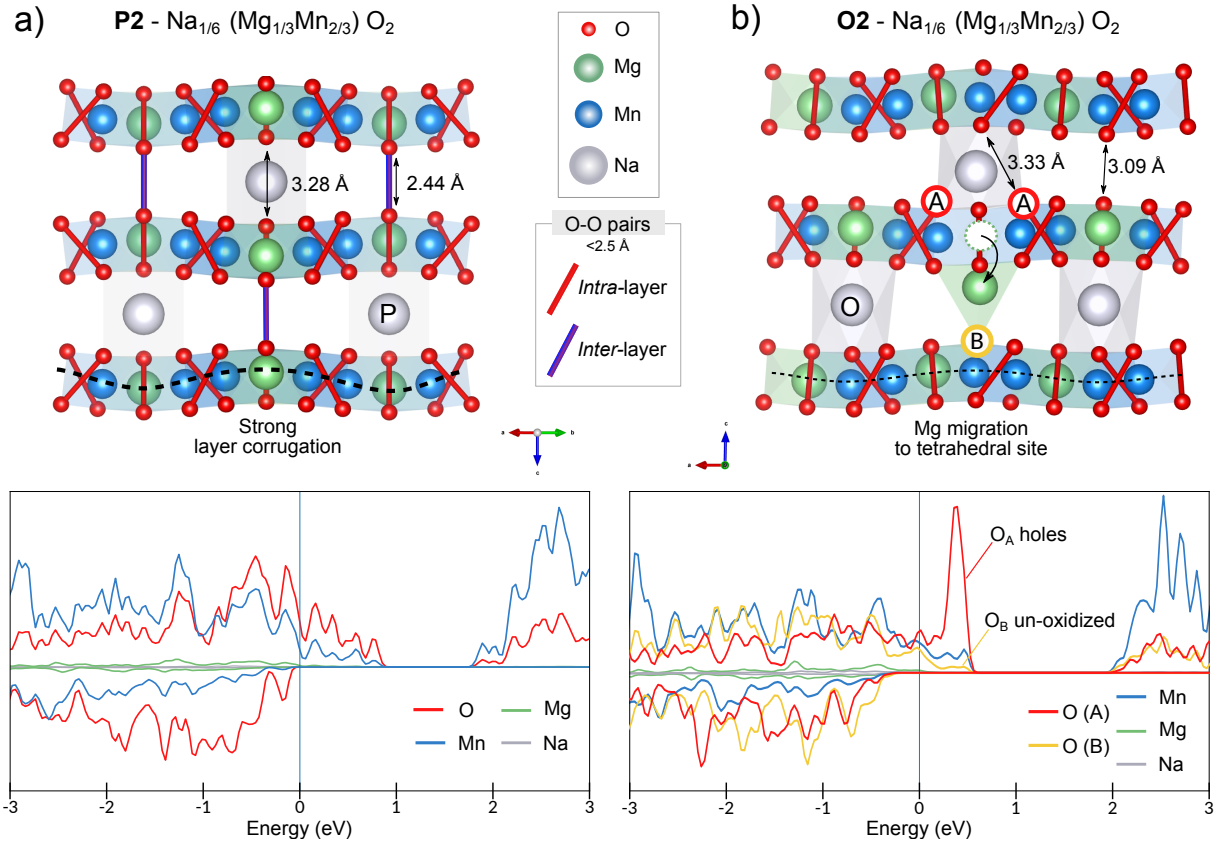


Figure II.11: Comparison of crystalline and electronic structures of NMgMO at x=1/6 in *P2* (a) and *O2* (b) stacking. In *P2* structure, the inter-layer O-O pairing favors cooperative distortion and homogeneous charge distribution. In *O2* structure, without inter-layer pairing, the charge disproportionation is favored by Mg migration.

nearest neighbor while Mn-O bond lengths remain almost constant, thus forming the pattern that we identified as the collective distortion associated to the RCM. *Thus in this composition range, these materials undergo reductive coupling.*

Since the structural effect of oxygen redox increases with $h^O$, we compare the *O* and *P* structures at the lower end of the available composition range, i.e. at x=1/6, both in terms of electronic and crystalline structure (see fig. II.11). The *P2* structure (fig. II.11.a) remains in the *collective distortion regime* which preserves the homogeneity of the oxygen network; i.e., each oxygen pair has an equivalent first shell environment and an equivalent oxidation state $(O\text{-}O)^{n-}$. In addition to the intra-layer O-O pairs, which already existed at higher Na content, this collective distortion now includes short O-O dimers across the Na layer, with an O-O distance lower than 2.5 Å (blue lines in fig. II.11.a). This additional bonding allows to create "O-O chains" along the c-axis where the oxygen holes can be delocalized thus mitigating the destabilization. These weakly bonded chains remind the early stages of "anionic polymerization" developed by Rouxel[e]. Furthermore, these short O-O inter-layer pairs order with Na ions thus inducing a periodic corrugation of the $MO_2$

[e]They also lay the foundation for a description in terms of Peierls distortion

layers, largely discussed in the first chapter.

The occurrence of these inter-layer O-O pairs, only possible in *P*-type stacking, explains that the simulated structures relax to *P2* at x=0 and lead to a collapse of the c parameter, observed experimentally at the end of charge in $LiCoO_2$ among many others.[45] This is the opposite of the behavior expected from a pure electrostatic control which would tend to minimize O-O repulsion by moving to octahedral stacking and enlarging the inter-layer spacing.

Indeed, in the *O2* structure, the oxygens do not face one another across the Na layer so this type of inter-layer O-O pairing coupled to layer corrugation is impossible. Since cooperative distortion is not favored, the disproportionation mechanism becomes more stable thus leading to Mg migration in the Na layer (see in fig. II.11.b). As explained in the previous chapter (see on page 47), this migration modifies the first shell environment of the oxygen forming the initial and final sites of the Mg migration. Indeed, after the migration, the oxygen atoms forming the initial site ($O_A$) are close to a Mg vacancy. They have less cationic charges in their first shell than the rest of the oxygens, so that their Madelung energy is comparatively lower. Therefore, their $|O_{2p}$ states are raised above those of the other oxygens so they will get oxidized first upon charge. On the contrary, oxygens close to a newly migrated Mg ($O_B$) have an excess of cationic charge in their first shell which stabilizes their electronic states, making them less accessible to oxidation. Indeed, we see in the relaxed structure that such un-oxidized oxygens do not form O-O pair. These two effects will entail a higher concentration of holes on $O_A$ and of electrons on $O_B$, compared to the rest of the network, as confirmed by the DOS projected on these specific oxygens.

The presence of strongly oxidized $O_A$ species in the *O2*-type structure obviously questions its stability versus $O_2$ gas release. By comparing the enthalpy of the $O_2$ release reaction, $\Delta H_{O2}$, for both *O2* and *P2*-NMgMO polymorphs (see method and fig. II.12), we confirm that O structures are more prone to oxygen release than P at low Na content, which is again in agreement with the general trends observed experimentally.

This theoretical investigation has thus allowed us to answer the various questions thanks to the refined model of distortion competition proposed in the first chapter. The underlying distortion mechanism explains the difference in stability between alkali-rich compounds in *O*-type stacking and Na-deficient compounds in *P*-type stacking.

This study opens new perspectives because this mechanisms can be applied to the whole family of Na-deficient compounds undergoing pure anionic redox, such as $Na_{2/3}Li_{1/3}Mn_{2/3}O_2$ which have recently been the subject of much attention [102]–[105] and would require further modeling due to the possibility of Na-Li cation exchange. Furthermore, this model could also be used to understand the behavior of compound upon mixed cationic and anionic redox, by modeling the effects of substitution as was done in the first chapter.

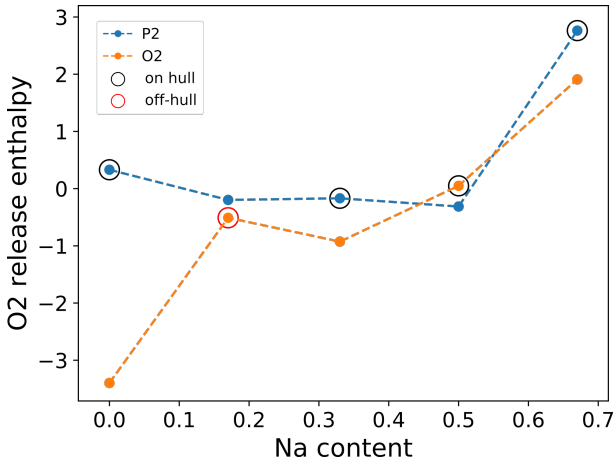


Figure II.12: Comparison of $O_2$ release enthalpy $\Delta H_{O2}$ at 0K for *P2* and *O2* polymorphs of NMgMO. At x=0, both structures relax to *P2* but the structure derived from *O2* has a much smaller inter-layer spacing, which favors oxygen release.

Indeed, several compounds obtained by substitution of Mn by a metal have demonstrated anionic activity. This can occur if the substituting metal has a lower oxidation state, such as Fe, thus forcing Mn to remain in +4 and creating a highly oxidized phase where migrated metal creates non-equivalent oxygens (coined as "Z" phase in [106]). Other compounds, obtained by substituting Mn with another inactive metal such as Ti(+IV), show good cycling stability. In this case, it is the statistical disorder between Mn and Ti which allows to lift the degeneracy between the various oxygen environment – necessary for disproportionation – without further migration [107].

> This study has proven that our A.R. mechanism model can be extended beyond the Li-rich compounds, to cases where the Li intercalant is replaced by Na. We now want to benchmark our model for the substitution of oxygen with sulfur. To this aim, we will now re-investigate compounds which have been thoroughly studied 30 years ago, the lithium sulfide compounds by investigating the effect of overlithiation.

# 2 Li-rich layered Sulfides

While oxygen redox has been framed as a way to reach higher densities, it entails a large instability in the compounds and jeopardizes the stability of the material if pushed too far. Compared to oxygen, Sulfur has a higher polarizability which allows a better stabilization of holes as well as a lower structural stiffness, which decreases the destabilization due to S-S pairing distortion. Both effects thus lead to a more reversible anionic redox than in oxides (for the same oxidation).

This stable ligand–hole chemistry has been thoroughly studied in the 70's, before the bloom of oxide cathodes. However, the exponential growth of computing power has revolutionized the way research is done since then (partly due to battery improvement, by the way). It allowed to develop techniques which require to process a vast amount of data such, such as synchrotron spectroscopy. This family of spectroscopic techniques has proven very efficient for characterizing A.R. processes (see previous section) even though the underlying science still has to be fully understood. Furthermore, this computing power obviously allowed to develop large scale simulations, which, in turn, proved crucial to obtain quantities which could not be measured (e.g. ELF in large super-cells) and develop quantitative models.

Besides, while Li-rich layered compounds are the epitome of A.R. compounds in oxides, the exploration of Li-rich sulfides has not been done yet. This provides a unique opportunity to extend the formalism and mechanisms developed for oxides to this new field. Furthermore, it will also be the occasion to lay a conceptual and historic bridge between the work and wording of Rouxel and the present model that our group has been exploring for several years.

## 2.1 Context

#### From oxides to sulfides

Being larger and more polarizable, the sulfur element is less electronegative than oxygen. It means that S chemical potential $\mu_S$ is higher than that of oxygen $\mu_O$ so that the S band lies at higher energy ($\mu_S - \mu_O \approx 2\,\text{eV}$) as illustrated in fig. II.13 . It means that $\Delta_{CT}^{M-O} > \Delta_{CT}^{M-S}$. This means that M-X bonds will be more covalent in sulfides and prone to ligand-to-metal charge transfer, even in the pristine.

Likewise, the voltage of the cell is proportional to the chemical potential difference between the Fermi level of the anode and that of the cathode, $V = (\mu_A - \mu_C)/\mathcal{F}$. For a given anode (e.g. Lithium metal) the voltage will be smaller for sulfides (see fig. II.16 for an example). However, the better stability of sulfides allows to extend the composition range of reversible cycling, thus allowing for larger capacity. To compete with oxide cathodes in terms of energy density, sulfides thus rely on smaller voltage and larger capacity.

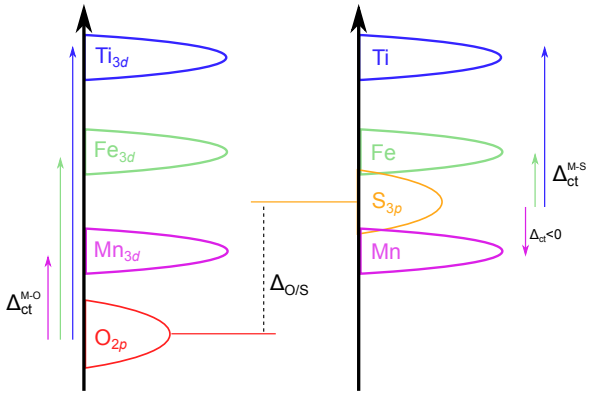


Figure II.13: Electronic and structural evolution from oxide to sulfides. The higher chemical potential of sulfide electrons decreases the values of the charge transfer gaps with various metals, some of them becoming negative (Mn).

Compared to O, the higher polarizability of S means that sulfur is softer, i.e. the chemical potential variation upon electron removal is smaller, as defined in conceptual-DFT. As a consequence, the holes located on sulfur are less destabilizing and the bulk modulus is lower, as in the case of Na/Li substitution.

When considering the competition between RCM and disproportionation, we see that this higher covalency and lower stress/strain ratio tend to favor the cooperative distortion over the pure oxygen pairing, thus foretelling a higher reversibility for A.R. in sulfur than in oxides (for the same oxidation).

### Activation of $Li_2TiS_3$

The existence of $Li_2TiS_3$ indicates that $Ti_d$ band has a higher chemical potential than the $S_{3p}$ band so that the material is a Charge transfer insulator. Therefore, $Li_2TiS_3$ seems a good candidate to study pure anionic redox, due to a clear charge transfer regime and a $d^0$ configuration. Unfortunately, ordered $Li_2TiS_3$ is electrochemically inactive which means that experiment-wise, no lithium can be extracted from the pristine. However, the capacity of the un-substitued compound can also be accessed by heating at 100°C. In addition, the creation of disorder via either partial substitution of metal by Co or Li or via mild ball milling also allows to unlock the A.R. capacity of the compound.

Since the bandgap of such compounds is standard for cathode materials (semi-metal or good semi-conductor) this inactivity is not due to a lack of electronic conductivity. Likewise, ionic conductivity in such layered compound with 2D diffusion does not seem to be an issue either so the activation process of $Li_2TiS_3$ remains a challenge.

In order to study this phenomenon, two strategies have been proposed: the first one, developed by Delmas and coworkers, consists in creating a solid solution between the classical $LiTiS_2$ and $Li_2TiS_3$, to achieve disordered metallic layer and partially reduced titanium [108]. This can also be seen as a partial substitution of Ti by Li.

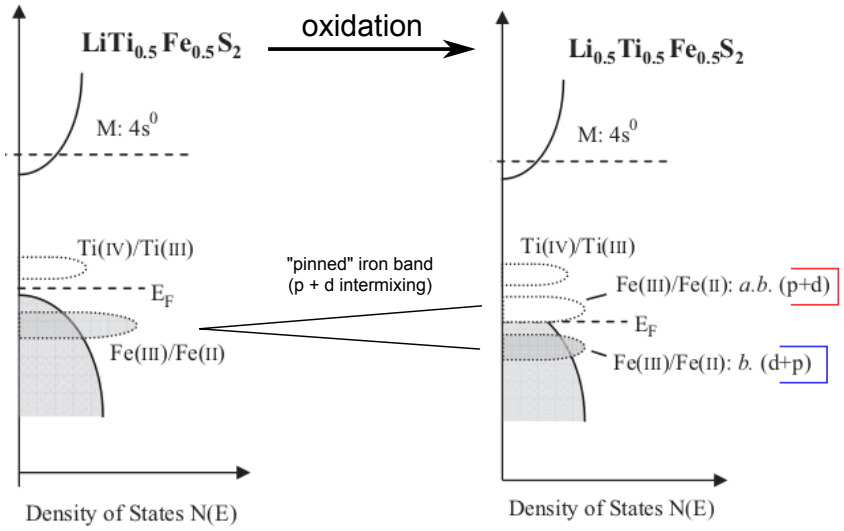


Figure II.14: "Pinning" of $Fe_{3d}$ at the top of the $S_{3p}$. Upon partial depletion, the $Fe^{+2}/Fe^{+3}$ band will hybridize with the sulfide states so that the state at the empty Fe-S states are "pinned" at the Fermi level throughout charge. Adapted from [110].

The other strategy, developed in our group, consists in a partial substitution of Ti by another metal. This second strategy offers the opportunity to use a metal which enhances the reversibility of the anionic redox by favoring the RCM over the disproportionation. To do so, the substituting metal must possess states which overlap the non-bonding orbitals of the sulfur.

Previous studies seem to indicate that the $3d$ states of the iron are "pinned" at the top of the sulfur band[109], [110] (see. fig II.14). This "pinning" is described by Goodenough[110] as $Fe_d$ / $S_p$ interaction which split the Fe band into a empty "p-dominated" band, "pinned" at the top of the bonding M-S states (highlighted in red) and an occupied "d-dominated" band more stable in energy (highlighted in blue). While the wording is different, this seems like another early formulation of the reductive coupling mechanism by which the iron and the sulfur successfully stabilize the holes without destroying the material. The iron is thus a good candidate to favor reversible sulfur redox in titanium sulfide. Our group thus embarked on a study of the $Li_xTi_yFe_zO_2$ system. Here again, the experimental results, gathered in the Ph.D. work of S. Saha[111], raised several questions that have been addressed by a theoretical study.

## 2.2 Experimental results

### Choice of the Fe content

Starting from the structure of $Li_2TiS_3$, the Fe substitutes the cations from the transition metal layer randomly. Assuming a purely ionic compounds with formal oxidation states of Li(+I), Ti(+IV) and Fe(+II), the charge balance imposes to replace 1 Ti and 2 Li

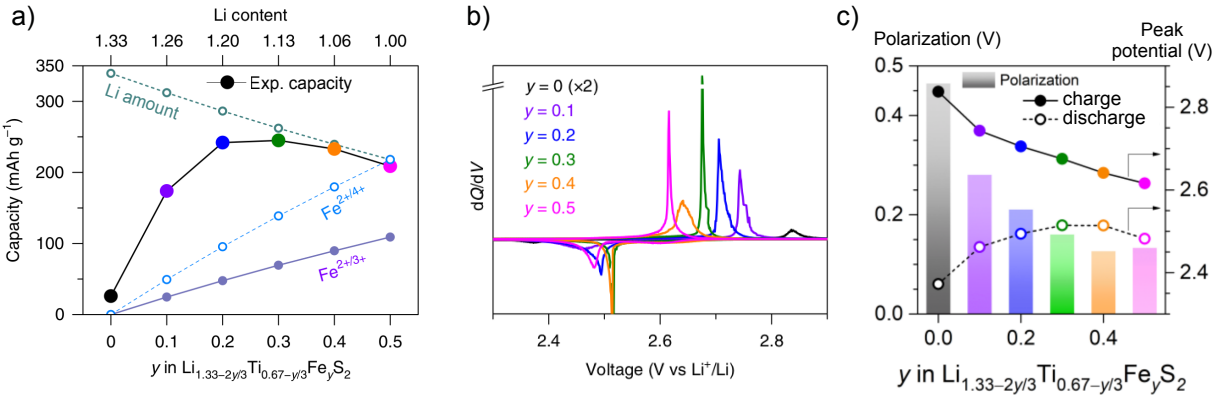


Figure II.15: Electrochemical characterization of $Li_1[Li_{1/3-2y/3}Ti_{2/3-y/3}Fe_y]O_2$ for $y_{Fe} \in [0, 0.5]$. a) Experimental capacity compared to Li-insertion capacity and cationic capacity. b) $\partial Q/\partial V$ plots of the 5 stoichiometries c) Comparison of $\partial Q/\partial V$ peak positions. Adapted from [112].

by 3 Fe, thus leading to the general stoichiometry of $Li_1[Li_{1/3-2y/3}Ti_{2/3-y/3}Fe_y]O_2$, where the layers have been identified. With this stoichiometry, the compound is only Li-rich if $y < 0.5$.

To select the best Fe doping amount, the experimental procedure consisted in sampling the composition range by varying the $y_{Fe}$ parameter from 0 to 1, every 0.1 and comparing the electrochemical performances of the synthesized compounds, displayed in fig. II.15. The electrochemical performances of the 5 $Li_1[Li_{1/3-2y/3}Ti_{2/3-y/3}Fe_y]O_2$ stoichiometries are compared in fig. II.15. In terms of capacity, we see an increase with the Fe content to reach a maximum at $y = 0.3$ (see fig. II.15.a). For that composition, the observed capacity almost equals the theoretical estimate (accounting for both Fe and S redox) while for larger Fe content, both experimental and theoretical capacities slightly decrease. In terms of voltage, we now compare the $\partial Q/\partial V$ plots of the various stoichiometries (see fig. II.15.b) where the peaks indicate the a voltage of the plateau in the classic $Q(V)$ plot. We see that, with increasing Fe content, the voltage of the peak decreases in charge (filled dots in fig. II.15.c) while the voltage of the discharge increases up to $y = 0.3$, before decreasing again (hollow dots in fig. II.15.c). *The origin of this voltage shift is a question which will needs to be addressed in the theoretical study.*

Nevertheless, the compound with $y = 0.3$, $Li_1[Li_{0.4/3}Ti_{1.7/3}Fe_{0.3}]O_2$ , also written as $Li_{1.13}Ti_{0.57}Fe_{0.3}S_2$ and denoted as LTFS hereinafter, provides the best capacity and an acceptably small polarization. It was thus chosen for further experimental characterization.

### Experimental characterization

The electrochemical characterization of LTFS is presented in fig. II.16. The voltage around 2.5V is indeed lower than for oxides. The small polarization observed in galvanostatic measurement (from 0.2 to 0.1V, see in fig. II.16.a) is almost reduced to 0 in GITT

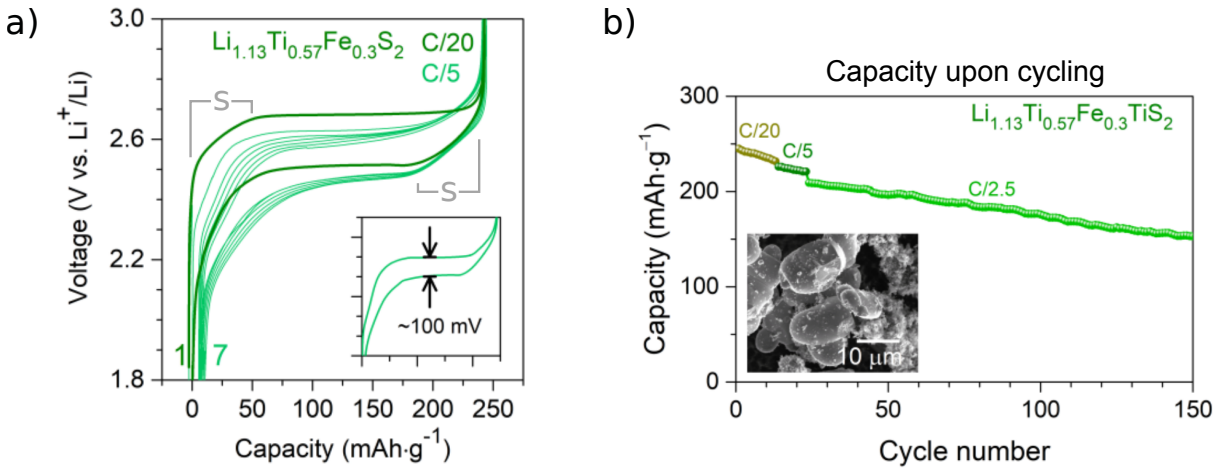


Figure II.16: Electrochemical characterization (voltage, hysteresis & reversibility) of LTFS. Adapted from [112].

conditions. This behavior indicates that the electrochemical transformations are quite reversible with very small kinetic barriers, which decrease even further upon cycling. Such reversible behavior is further confirmed by the relatively good capacity retention, even at "high" rate (2.5C) shown in fig. II.16.b.

Despite the favorable kinetics, the voltage curve upon cycling displays an hysteresis which indicates distinct reaction paths in charge and discharge. Indeed, both charge and discharge begin with a slopped region (grey "S" in fig. II.16.a), which capacity corresponds to the iron oxidation, followed by a flat plateau, attributed to sulfur oxidation. The spectroscopic characterizations of Ti, Fe and S have been acquired ex-situ during the first charge to confirm this mapping. First, in the $L_{2,3}$-edge TEY-XANES[f] spectra of Ti, the constant peak position confirms that the Ti remains in +IV state. The Fe $L_{2,3}$-edge TFY-XANES spectra also confirms that oxidation of iron from +II to +III occurs mainly in the sloped region. Correspondingly, the sulfur L- and K-edge spectroscopy (high-efficiency RIXS mapping) confirms that sulfur is mainly oxidized during the plateau. From a modeling point of view, the favorable kinetics and the hysteresis without capacity loss, both point towards the reductive coupling mechanism.

Having described the electronic evolution, we now turn to structural characterization. LTFS has a layered structure with a 3 layer periodicity and octahedral Li-sites (*O3* stacking), illustrated in fig. II.17.a. The X-ray diffraction refinements indicate that all the sites in the TM-layer are uniformly occupied by a statistical distribution of Ti, Fe and Li. Operando XRD peak positions shows that the *O3* structure is maintained throughout the charge (fig. II.17.b). More specifically, the unit cell parameters undergo a solid-solution evolution during cationic (Fe) redox and a biphasic process during anionic (S) redox.

[f]TEY-XANES: Total Electron Yield mode of X-ray Absorption Near Edge Spectroscopy

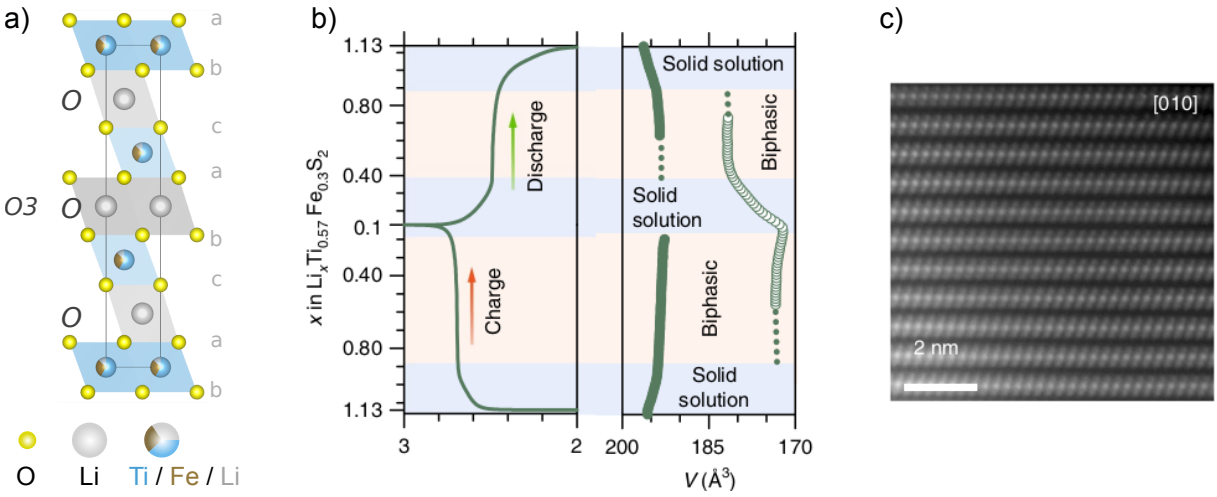


Figure II.17: Structural characterization of LTFS. a) Unit cell showing *O3* stacking and statistical occupancy of metal sites. b) XRD peak positions during operando XRD, showing biphasic processes during A.R. and solid solution during cationic redox. c) STEM imaging of LTFS at the end of charge, showing perfect ordering.

Scanning Transmission Electron Microscopy (STEM) imaging (see fig. II.17.c) and local XRD indicate that there are no TM migrations to the inter-layer at the end of charge. The preservation of the structural integrity upon sulfur oxidation indicates an homogeneous and reversible A.R. mechanisms. This is another hint towards the reductive coupling mechanism. In order to confirm this hypothesis, we now turn to modeling and simulation methods.

## 2.3 Simulation and modeling

### Building the representative unit cell

Before running first principle calculations, we need to obtain a representative unit cell which can be used as an input. To build this unit cell, we simulate the doping of $Li_2TiS_3$ by Fe atoms. We start with the standard $Li_2TiS_3$ unit cell, which is rhomboedral and contains 3 atoms per layer (e.g. 2 Ti and 1 Li in the TM layer). However the physical constraints to simulate Fe doping will force us to take a much larger super-cell for our computational study. Indeed (i), to allow for non-identical ordering in layers, we must take the orthorhombic cell which contains 3 TM layers displayed in fig. II.18.a. . This supercell of dimension 1a*1b*3c is noted "*113*" and contains 36 atoms. Furthermore (ii), when doping with Fe, the charge balance imposes to replace atoms by group of 3: $(1\,Ti + 2\,Li) \rightarrow 3\,Fe$ in each layer, to avoid charged layers. This substitution thus requires an even number of Li atom per layer. Finally, (iii) for the isotropy of the simulation, the super-cell in the layer must be symmetric in a and b. The smallest symmetric unit cell which contains an even number of Li per metal layer is the *223* super-cell, which contains

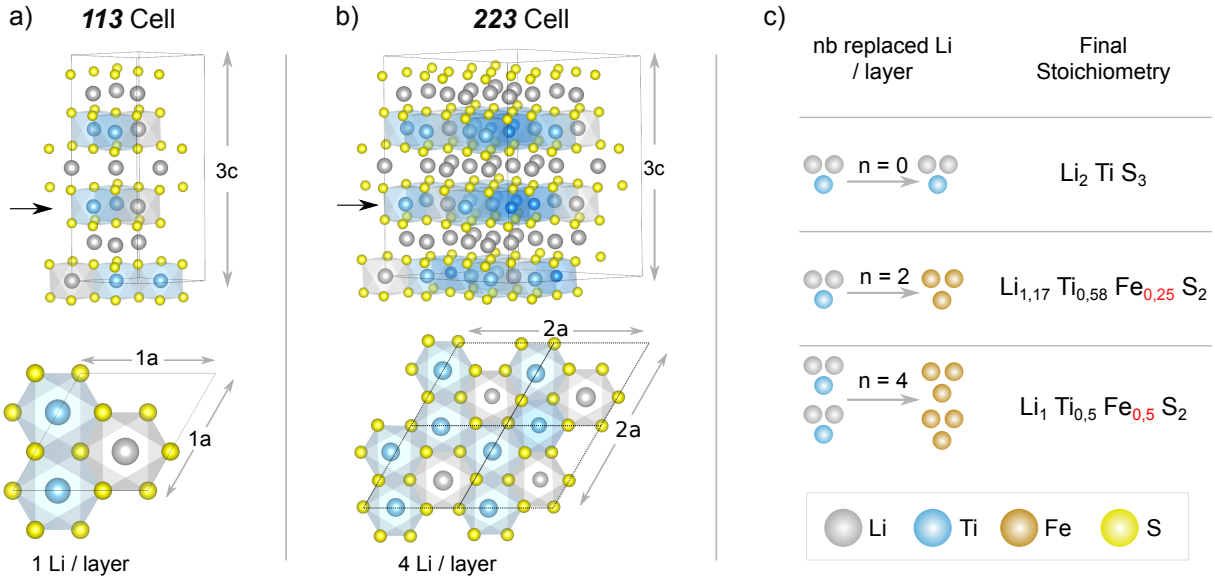


Figure II.18: Building a computational cell for LTFS. 113 (a) and 223 (b) supercells along with one of their layers (indicated by the black arrow) (c) Possible substitutions in a layer of the 223 supercell and corresponding stoichiometries.

144 atoms, as illustrated in fig. II.18.b. The next symmetric supercell with 2n Li/layer is the *443*, with 576 atoms, involves much heavier calculation without providing significant improvement in the description of the disorder[g]. We therefore chose to work with the *223* supercell since it is the smallest cell which allows to respect (i) non-identical ordering of layers, (ii) layer-wise charge balance and (iii) supercell isotropy. In this cell, there are 4 Li per layer which must be replaced following the $(1\,Ti + 2\,Li)/3\,Fe$ ratio, the possible stoichiometries, indicated in fig. II.18.c, are therefore limited to $Li_2TiS_3$ ($y = 0$) which does not contain Fe, $Li_{1.17}Ti_{0.58}Fe_{0.25}S_2$ ($y = 0.25$) and $Li_1Ti_{0.5}Fe_{0.5}S_2$($y = 0.5$), which is not Li-rich. Fortunately, the only "non-trivial" computational stoichiometry achievable ($y = 0.25$) is sufficiently close to the experimental stoichiometry – $Li_{1.13}Ti_{0.57}Fe_{0.3}S_2$($y = 0.3$) – and can thus be used for the theoretical study.

Having determined the stoichiometry of the supercell (composition space), we now seek a relevant ordering to describe the disordered phase (configuration space). The explicit way to account for disorder would be to use the cluster expansion method (see Methods). While this method has been implemented successfully on numerous electrode compounds , it requires a high throughput environment which is not in the scope of our study. We instead used a simpler method to select the representative orderings, which consists in 2 successive substitutions (Ti→Fe) and (Li→Fe). For the (Ti→Fe) substitution, we first generated the 30 Ti/Fe orderings of lowest electrostatic energy, which were then relaxed via DFT to keep only the 5 most stable. For each of these 5 Ti/Fe orderings, we

[g]The short range order will be comparable and the long range order will still be arbitrary, since we do not perform a cluster expansion (see methods).

generated the 3 most stable Li/Ti/Fe ordering of lowest electrostatic energies which were then relaxed via DFT to keep only the most stable Li/Ti/Fe ordering. This structure is assumed to be a good representation of the short range ordering within the disordered LTFS. To obtain delithiated structures, we then used the iterative delithiation described in the Methods section. Having built a valid model for the disordered structure at various Fe and Na contents, we now use first principle calculations to shed light on the experimental results.

#### Explaining voltage shift

We start by addressing the observation of fig. II.15.c that an increase in the Fe content shifts the voltage of the $\partial Q/\partial V$ peak. As we will see in the next paragraph, this peak corresponds to the sulfur redox and a decrease of this S redox potential indicates an increase in the energy of the $|S_{3p}$. However, the energy of the $|S_{3p}$ is only influenced by the electrostatic field in the crystal, measured by the Madelung energy of the sulfur. The increase of the Fe content must therefore cause have an impact on the Madelung energy of the sulfur.

In order to verify this assumption, we performed Bader charge analysis on the atoms and computed the corresponding Madelung energies of the sulfur atoms in the 3 possible stoichiometries, $Li_2TiS_3$ ($y = 0$), $Li_{1.17}Ti_{0.58}Fe_{0.25}S_2$ ($y = 0.25$) and $Li_1Ti_{0.5}Fe_{0.5}S_2$($y = 0.5$). The results, summarized in table II.3, show a 0.27 eV increase of the Madelung energy with increasing Fe content (from -6.2 eV to -5.93 eV) which matches surprisingly well the 0.25 V shift of the $\partial Q/\partial V$ peak voltage (full circles in fig. II.15.c). While the perfect agreement between the experimental and theoretical voltage shifts is most likely fortuitous, the correspondence in the shift trends strongly advocates for the validity of this explanation.

In discharge, the decrease of the charge on the sulfur counterbalances the increase of the electrostatic field, hence a smaller variation range for the Madelung energy, which explains the lower variation of the peak position - 0.15 V (hollow circles in fig. II.15.c). In discharge, for high Fe content (y=0.4, 0.5), the charge variation on the sulfur in smaller hence the mitigation is weaker and we retrieve the trend towards voltage decrease observed in charge.

Having explained this first question, we move towards the characterization of A.R. mechanism in this system, by studying the relation between electronic and crystalline structure evolution upon charging.

#### Electronic structure evolution

The pDOS of LTFS in its pristine state, shown in fig. II.19.a, can be described as the pDOS of $Li_2TiS_3$with the addition of the $Fe_d$ orbitals. $Li_2TiS_3$ is a classical Charge-

**Bader charges** (nb e$^-$)

| $y_{Fe}$ | Fe | | Ti | | S | | Li | |
|---|---|---|---|---|---|---|---|---|
| 0.5 | 1.042 | 0.005 | 1.559 | 0.009 | -1.080 | 0.024 | 0.860 | 0.001 |
| 0.25 | 1.042 | 0.002 | 1.570 | 0.015 | -1.089 | 0.024 | 0.859 | 0.003 |
| 0 | - | | 1.586 | 0.000 | -1.101 | 0.015 | 0.858 | 0.002 |

**Madelung Energy** (eV)

| $y_{Fe}$ | Fe | | Ti | | S | | Li | |
|---|---|---|---|---|---|---|---|---|
| 0.5 | -5.475 | 0.111 | -11.077 | 0.224 | -5.937 | 0.240 | -4.042 | 0.10 |
| 0.25 | -5.520 | 0.060 | -11.323 | 0.316 | -6.055 | 0.264 | -4.023 | 0.115 |
| 0 | - | | -11.643 | 0.008 | -6.204 | 0.145 | -4.020 | 0.108 |

Table II.3: Bader charge analysis and Madelung energy in $Li_1[Li_{1/3-2y/3}Ti_{2/3-y/3}Fe_y]O_2$. Large and small numbers are the average and the standard deviation within the supercell, respectively.

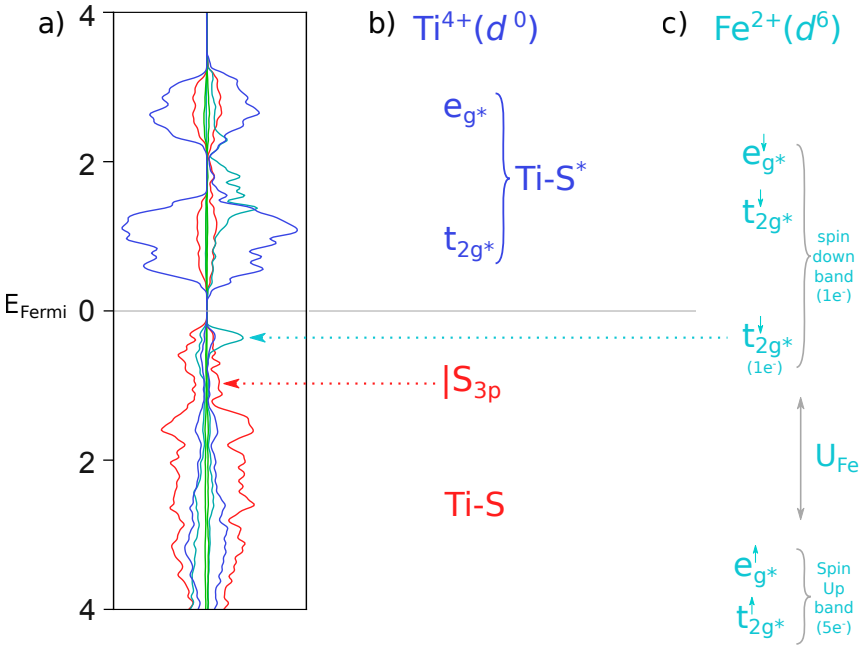


Figure II.19: Simulation and analysis of electronic structure of LTFS. a) Computational pDOS of LTFS. b) M.O. diagram of $Li_2TiS_3$ with empty Ti-S* states (blue) and occupied Ti-S and non-bonding |S3p states (Red). c) M.O. diagram of the Fe-S* states with high-spin $Fe^{+2}$ ($d^6$). The pDOS of LTFS can be described as a that of Fe-doped $Li_2TiS_3$.

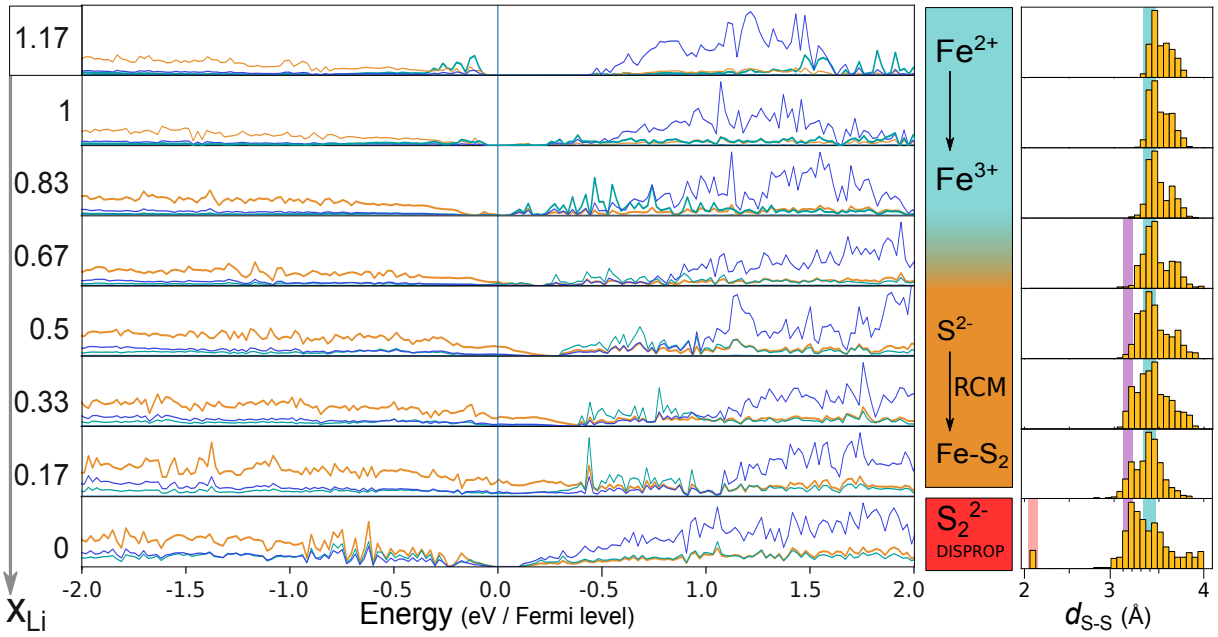


Figure II.20: First principle characterization of A.R. mechanism in LTFS. For each Li content(left), the pDOS (center) and the histogram of S-S distances (right) of the relaxed structure are shown, along with the corresponding mechanism (colored column).

Transfer Insulator with $d^0$ metal (see fig. II.19.b), with empty Ti-S* states (blue) dominated by the metal and occupied Ti-S states (red) dominated by the Sulfur with non bonding $|S_{3p}$ pinned on the top. The $d$-orbitals of Fe (fig. II.19.c) are split by the Hubbard interaction term $U_{\text{eff}}$. As a result the $Fe^{2+}(d^6)$ is in high-spin configuration ($e_g^2$ and $t_{2g}^4$).

Within the DFT+U framework, the lower and upper Hubbard bands are approximated to the spin-up and spin-down bands (see methods) hence, the high-spin configuration of Fe(+II) can be written as $[e_g^{\uparrow}(2),\ t_{2g}^{\uparrow}(3)]$, $[\ t_{2g}^{\downarrow}(1), e_g^{\downarrow}(0)]$, as illustrated in fig. II.19.a[h]. Since the singly occupied $t_{2g}^{\downarrow}$ lies at the Fermi level, it will thus be oxidized before the $|S_{3p}$. This sequential oxidation is confirmed by the series of pDOS in fig. II.20 where 0.25 electrons are removed from Iron ($1e^-$/Fe) from $x_{Li}$=1.17 to $x_{Li}$=0.83 (indicated in cyan), after what sulfur oxidation occurs, indicated in orange. The depletion of $Li^+$ ions stabilizes the cations while destabilizing the anions, thus allowing their respective bands to get closer. However, in addition to the electrostatic shift, we also observe a spreading of the $t_{2g}^{\downarrow}$ and the $|S_{3p}$ states, specially visible at the end of charge (x=0.17), which indicates an $Fe_d$-$S_{3p}$ interaction. This interaction is an electronic indicator of the RCM mechanism.

This mechanism sequence is further confirmed by an evolution of the crystal structure

[h]This identification of spin channels with Hubbard bands leads to incoherence, because the bottom of the "spin-down" band is occupied (which makes sense), even though a "partially occupied upper Hubbard band " does not make sense. Being fully aware of this inaccuracy, we will try to distinguish these two notions, writing about spin channels when analyzing DFT results and about Hubbard bands when discussing theoretical electronic mechanisms.

followed by the histograms of S-S distances, plotted on the right of the fig. II.20 for each composition. Indeed, the S-S distances remain almost constant during iron oxidation (cyan bar at 3.5 Å). Then they show a progressive decrease to 3.2 Å, without getting shorter than 3 Å. This small but visible shortening confirms the occurrence of RCM upon charging.

The case of x=0 differs from the rest of the materials both in terms of electronic and crystal structure. Indeed, the occurrence of a small amount of very short S-S distances (2.1 Å) indicates a disproportionation of the charge leading to the creation of per-sulfures. In this case the total absence of Li ions amplifies the electrostatic shift as well as the global shrinkage of the structure, thus allowing reductive elimination which leads to the complete reduction of iron to Fe(+II) and a partial reduction of Ti to Ti(+III).

This joint experimental & theoretical re-investigation of the Li-Ti-Fe-S system, thus confirms that, upon oxidation, the sulfur is prone to undergo a reversible reductive coupling. This reversibility is further enhanced by the presence of a metallic state available for hybridization at the Fermi level. Such reversible behavior can however only occur over a finite composition range, beyond which the disproportionation takes over, thus inducing reductive elimination and material collapse. This is the same behavior as in oxide except that the amount of hole which can be accommodated by sulfur before triggering irreversible process ($h^{O}_{rev}$) is much larger for the sulfides. Overall, this study confirms that the presented model can also describe sulfur redox after adapting the model parameters.

> We have thus presented two families of compounds to challenge our model of anionic redox, detailing for each of them the experimental details, gathered by our collaborators and the theoretical study that we conducted to account for these results.
>
> In both studies, the computational method to confront the experimental data relies on the same basis: comparing the energy of the two types of mechanisms at each composition. Having devised and verified the robustness of this method on these two cases, we would now like to build tools to enhance the reproducibility and the efficiency of such study. This is the topic of the next chapter.

# III Developing new tools to quantify & predict the reversibility of A.R.

> I suppose it is tempting, if the only tool you have is a hammer, to treat everything as if it were a nail.
>
> Abraham Maslow

The refined A.R. model we have proposed relies on the competition between the RCM, associated to reversible distortions and the disproportionation, which triggers irreversible evolution (cation migration, $O_2$ release). Hence by predicting the relative energies of each mechanism, we can determine the reversibility the A.R. process itself.

This chapter is thus devoted to the elaboration of such energy comparison methods. The first section will describe a generic approach to estimate the energy of the reductive elimination, so as to determine if the material is stable or not at the end of charge. The second section will deal with a more computation intensive method to quantify the relative energies of RCM vs. disproportionation mechanisms for each state of charge in a specific compound.

## 1 Quantifying the energy of reductive elimination

This first method is aimed at predicting if a compound will display hysteresis and capacity fading upon A.R., based on the estimation of the reaction energy of such degradation. Indeed, the irreversible transformations associated to disproportionation derive from the reductive elimination ($e^-$ transfer from O-O$^*$ states to the metal band). By determining the relative positions of the oxygen and the metal bands, we can predict the energy of this electron transfer and, from there, the occurrence of degradation.

### 1.1 Motivation & theoretical context

#### Relative potentials of bands

In the first chapter (see fig. I.15 on page 56, reproduced here in fig. III.1 for convenience) we explained the stability or degradation of a compound upon anionic redox using the relative positions of the $M_d$ band and the antibonding O-O$^*$ orbitals.

The positions of the antibonding O-O orbitals with respect to the initial $|O_{2p}$ level

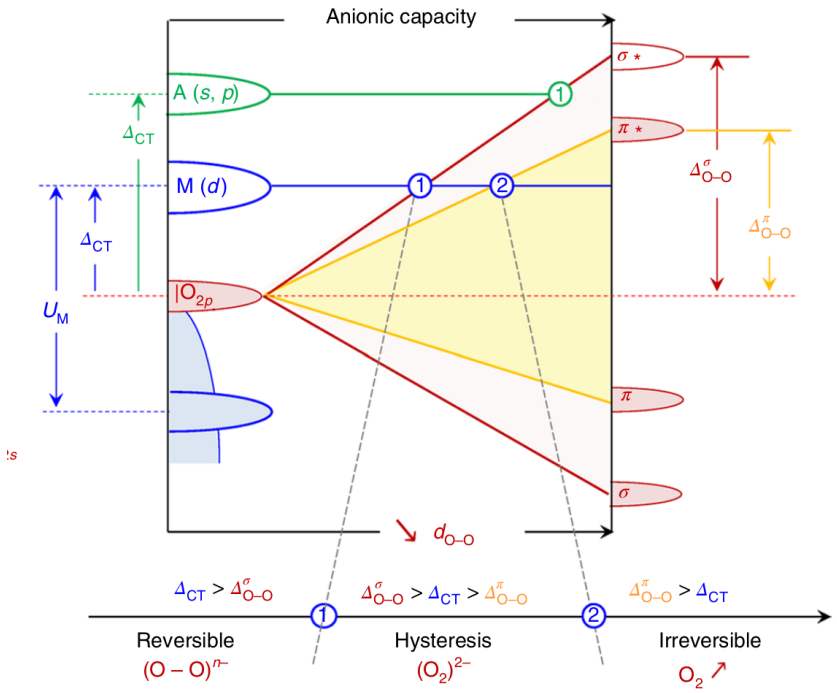


Figure III.1: Explaining A.R. reversibility in Charge-Transfer compounds. All the $\Delta$ are differences of electrochemical potentials $\mu$. (reproduction of fig. I.15 on page 56. From [63].

($\Delta^{\sigma*}_{O-O}$ for the $\sigma^*_{O-O}$ and $\Delta^{\pi*}_{O-O}$ for the $\pi^*_{O-O}$ )[a] are expressed as a function of the $d_{O-O}$distance and not the M-O bond length. Hence this model does not account for the trigonal-prismatic distortion of the $MO_6$ octahedron, necessary to the $|O_{2p}$ -$M_d$ interactions. As a consequence, this model does not describe the stabilization of the A.R. via RCM. Nevertheless, this is a good approximation on some compounds and the quantitative comparison of $\Delta_{CT}$, $\Delta^{\sigma*}_{O-O}$ and $\Delta^{\pi*}_{O-O}$ does provide valuable insight on the reversibility of the oxygen pairing mechanism.

$\Delta^{\sigma*}_{O-O}$ quantifies the gap opening due to oxygen pairing. This gap depends on the O-O bond strength which increases with O-O bond order. This O-O bond order itself depends on the number of oxygen holes $h^O$ in the the $\sigma^*_{O-O}$. In consequence $\Delta^{\sigma*}_{O-O}$ (and $\Delta^{\pi*}_{O-O}$ ) are functions of $h^O$. If we know these 2 functions, we can then predict the reversibility of the A.R. in any compound just by comparing its bandgap to $\Delta^{\sigma*}_{O-O}\left(h^O\right)$. We therefore need to quantify both $\Delta_{CT}$ and the $\Delta_{O-O}$ functions.

As a first approximation, the value of $\Delta_{CT}$ can be assimilated to the bandgap obtained through first principle calculation on the pristine.[b] While this bandgap is slightly inaccurate, this approximation is justified *a posteriori*, because we are interested by the

[a] Since these $\Delta_{O-O}$ are differences of chemical potentials per electron, they have the dimensions of a chemical hardness (for chemists) or a charge susceptibility (for physicists).

[b] This implies to neglect the difference between the fundamental bandgap and the optical bandgap due to the polaron stabilization and to approximate the fundamental bandgap by the Kohn-Sham bandgap.

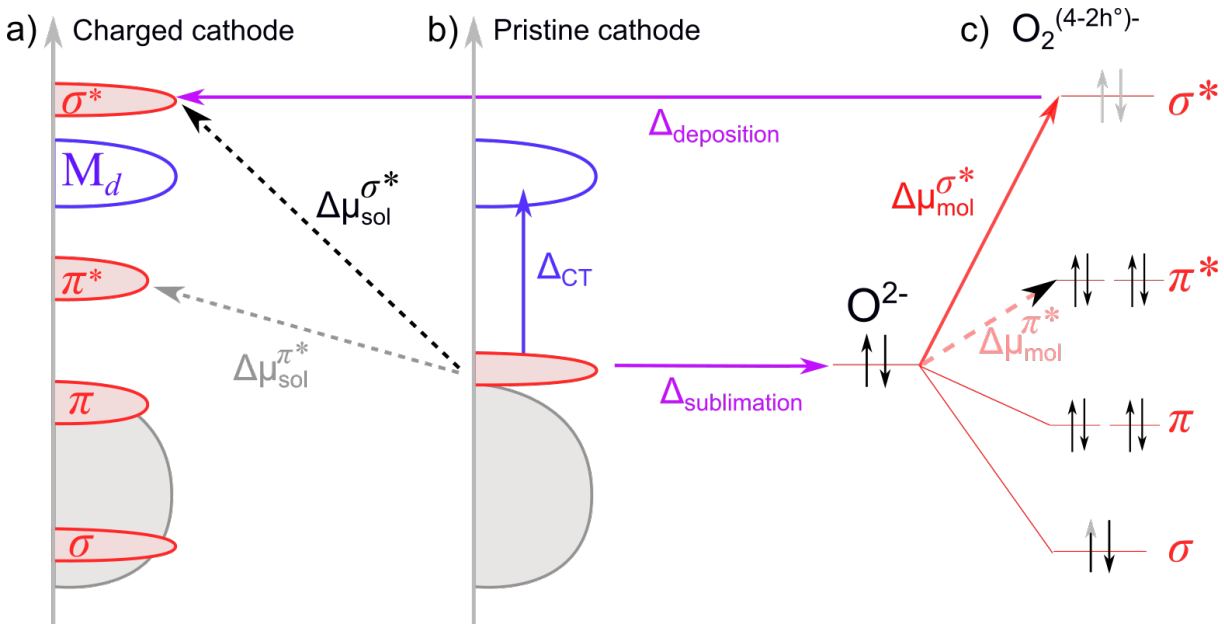


Figure III.2: Gap opening due to oxygen pairing in solid from the pristine cathode (b) to the oxidized compound (a) (direct pathway, $\Delta\mu_{sol}$ ) and in a molecule (c) (indirect pathway, noted $\Delta\mu_{mol}$ red). The difference between these quantities is due to the enthalpy of phase transition between the gas phase and the solid state compound ($\Delta_{sublimation}$ /$\Delta_{deposition}$, in purple).

difference $\Delta_{CT} - \Delta_{O-O}$. Indeed, in addition to being notably larger than the bandgap estimation error ($\Delta^{\sigma*}_{O-O} \approx 10\,eV$, see below), $\Delta_{O-O}$ is also obtained using a first principle scheme, thus mitigating the approximation by some error cancellation.

On the contrary, the determination of $\Delta_{O-O}$ is more problematic since there is no direct way to obtain estimations. The rest of this chapter will therefore be devoted to the description of an indirect method to estimate $\Delta_{O-O}$ .

#### From solid to molecular $\Delta_{O-O}$

To evaluate $\Delta^{\sigma*}_{O-O}\left(h^O\right)$ we can first consider the evolution of the cathode's electronic structure upon oxidation (see fig. III.2 from b to a) . Unfortunately, in such complex compounds, the identification of the O-O$^*$ states is difficult and controversial because they have the same energy as other M-O states and they may also be partially hybridized with M states due to RCM. While the COOP helps to distinguish the different types of O-O and M-O bonds, it is not very accurate and it does not provide the symmetry of the bonds, thus preventing the identification of $\sigma$ and $\pi$ states. We therefore seek a way to disentangle the O-O states from the rest of the electronic structure.

The most obvious way to follow the evolution of the O-O levels upon charging is to study the oxidation of an isolated oxygen pair (see fig. III.2.c). Indeed, since the transfer from the $|O_{2p}$ to the $\sigma^*$ band occurs both in the "direct" and the "decomposed" transformations, we can define a $\Delta_{O-O}$ in both of them. In the solid, this gap

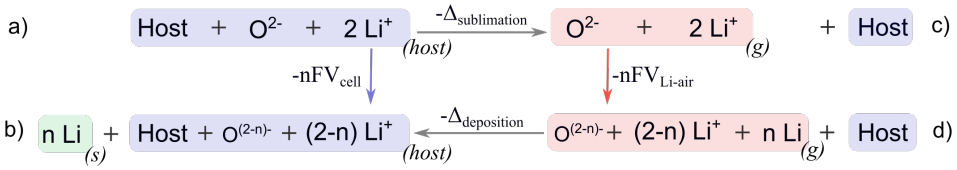


Figure III.3: Anionic redox cycle showing a "direct" reaction ($a \rightarrow b$) or a "decomposed" reaction ($a \rightarrow c \rightarrow d \rightarrow b$). Colors represent phases: blue = solid cathode, green = solid anode and red = gas.

opening $\Delta\mu^{\sigma*}_{sol}$ is hardly measurable, while in the molecule, the gap opening $\Delta\mu^{\sigma*}_{mol}$ is more readily accessible. Unfortunately, these two terms are not equal due to the potential shift when switching between molecule and solid (purple $\Delta$ in fig. III.2): $\Delta\mu^{\sigma*}_{sol} = \Delta_{sublimation} + \Delta\mu^{\sigma*}_{mol} + \Delta_{deposition}$. To replace $\Delta\mu_{sol}$ by $\Delta\mu_{mol}$ in our study, me must assume that $\Delta_{sublimation} + \Delta_{deposition} = 0$. To estimate the validity of this approximation, we need to understand the origin of these shifts.

### Estimating the error

A good way to estimate these terms is to decompose the charging process using a Born-Haber method inspired by ref. [113]. Indeed, by considering two transformation paths from the discharged to the charged states, we can form a thermodynamic cycle (see fig. III.3). The "direct" path (blue arrow) consists in a transfer of Li from the cathode to the metallic Li anode with oxidation of the oxygen and formation of pairs. The "decomposed" path proceeds first through the sublimation of $O^{2-}$ and 2 $Li^{+}$ (grey arrow) from the initial compound (a) into the gas phase (c). The second step is the redox reaction of oxygen and part of the Li in the gas phase (red arrow). The last step is the phase transition from gas to solid (deposition) of the ions into the host and the Li atoms into the metallic cathode (grey arrow).

The energy of the ($a \rightarrow b$) transformation is proportional to the cell voltage. Correspondingly, the ($c \rightarrow d$) transformation can be assimilated to the redox process of an ideal Li-Air battery, hence the notation of its energy as a Li-Air cell voltage. If we push further this comparison, we notice that the host does not play an active role in this cycle, however, it is well known that anionic redox in solid cathode is much more reversible than anionic redox in Li-Air cells. Hence the host could be here considered as a catalyst of the anionic redox, in line with the observation that metal-oxygen interactions enhance the reversibility of the A.R. By considering the reaction of the oxygen in the gas phase, we are completely neglecting the stabilization provided by the metal-oxygen coupling, in line with the initial assumption of this model. As a consequence, the results will overemphasize the irreversibility of the A.R

We now come back to the evaluation of the assumption that $\Delta_{sublimation} + \Delta_{deposition} = 0$. We first notice that during these two transformations, the charge of all the species stays

constant. Therefore, in an ionic picture, both terms will only reflect difference of of Madelung potential in each phases $\Delta_{sublimation} + \Delta_{deposition} \approx E_c - E_a + E_b - E_d$. In the gas phase, the species are very far, thus the Madelung energies of c) and d) will be very similar ($E_c \approx E_d$). In the solid phase, since the host is unchanged, we have $E_b \approx E_a$ and the energy difference only comes from the electron distribution of the inserted Li and O species. Consequently, $\Delta_{sublimation}$and $\Delta_{deposition}$ will mainly cancel out and their sum will translate the change of electrostatic potential due to the reorganization of the M-O bond which is second order compared to the energy of the bond itself. While further studies would be needed to investigate the effect of such second order term, we will neglect it as a first approximation and focus on the determination of $\Delta^{\sigma*}_{O-O}$ and $\Delta^{\pi*}_{O-O}$ in the molecule.

## 1.2 Computational methods and results

### Defining the methodology

In order to determine the opening of the gap upon oxygen pairing, we first study an isolated pair of oxygen atoms, using DFT. In order to minimize the systematic errors, we use the same code as for solids (VASP[114]) which is based on plane wave basis set and thus requires a periodic boundary condition. We therefore placed the two atoms of oxygen at the center of a cubic cell of size a=20 Å to ensure that the interactions between neighbor cells are negligible.

In DFT, the neutral oxygen atom is described by its 6 valence electrons and its pseudo-potential, which accounts for the nucleus positive charge screened by the core $O_{1s}$ electrons. In a cell which contains 2 O, the number of electron is therefore $n_{e^-} = 12$ . Interestingly, $n_{e^-}$ can be modified without changing the number of atoms; In this case, the charge neutrality is preserved using a continuous positive background (following the *Jellium* model). Therefore, by increasing $n_{e^-}$ from 12 to 16 (with 0.5 $e^-$ per step), we simulate the progressive reduction of O, from the $O_2$ molecule to the isolated $O^{2-}$ ions.

As $n_{e^-}$ increases, so does the occupancy of antibonding orbitals. This decrease of the bond order changes the equilibrium geometry, namely an increase the O-O distance, noted $d^{eq}_{O-O}$. This correspondence between $n_{e^-}$ and $d^{eq}_{O-O}$ explains that both variables have been used equivalently to describe the gap opening. This relation is also a good probe to estimate the relevance of our computation, which is critical since the Jellium model may incur some inaccuracies in the charge distribution.

When plotting $d^{eq}_{O-O}$ as a function of $n_{e^-}$ for two oxygen atoms (see fig. III.4.a), we indeed observe a monotonic increase of $d^{eq}_{O-O}$. Unfortunately, even for $n_{e^-} = 16$, the two atoms are still very close ($d^{eq}_{O-O} \approx 1.32$ Å) which is probably due to a charge spill into the cell. Indeed, the Jellium model fails to properly compensate such deviation from the charge neutrality. To mitigate this systematic error while staying in the plane-wave DFT

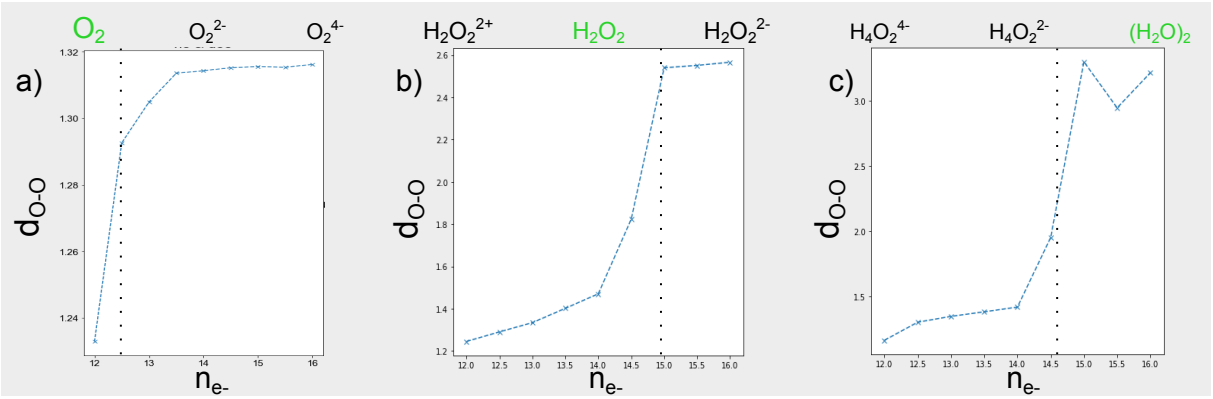


Figure III.4: $d^{eq}_{O-O}$ as a function of $n_{e^-}$ for $O_2$ (a), $H_2O_2$(b) and $2(H_2O)$ (c). Neutral electron counts are highlighted in green.

framework, we need to alleviate this deviation from charge neutrality. We therefore add counter-cations to achieve charge neutrality at other $n_{e^-}$ in the $[12, 16]$ range.

To minimize the steric perturbation, we chose the smallest counter-ions, $H^+$, which were added symmetrically on each oxygen, to give either $H_2O_2$: $n_{e^-} = 14$ or $2.[H_2O]$ : $n_{e^-} = 16$ (see fig. III.4.b & c respectively). In both cases, the variation of $d^{eq}_{O-O}$ as function of $n_{e^-}$ is closer to experimental observations, with a steep increase at $n_{e^-} = 14$ to reach $d^{eq}_{O-O} > 2.5$ Å. While the addition of counter-ions improved the $d^{eq}_{O-O}$ criterion, it also added other degrees of freedom – the positions of the hydrogen nuclei – which also need to be monitored.

In the case of $H_2O_2$, the geometry of the (OH) groups is preserved, with hydrogen staying close to their respective oxygen, thus ensuring the coherence of the results. In the case of $2.(H_2O)$ however, the hydrogen ions get "trapped" between the two oxygens upon relaxation for $n_{e^-} > 14.5$. While this may be interesting for the study of hydrogen bonding, this is a deviation from the "simple counter-ion" behavior which interferes with the quantification of $\Delta^{\sigma*}_{O-O}$. Hence we focus our study on the oxidation and reduction of $H_2O_2$.

### Computational results on $H_2O_2$

Having ensured the coherence of the atomic geometry across the whole $n_{e^-}$ range, we now look at the evolution of the electronic structure in order to determine $\Delta^{\sigma}_{O-O}$. We begin by analyzing the neutral hydrogen peroxide (see fig. III.5). Starting with the total DOS (a), we plotted the ParCharg of each peak (b), to identify the corresponding orbital using a molecular orbital diagram (c). Since we do not have $\mu_{|O_{2p}}$ we cannot measure directly $\Delta^{\sigma*}_{O-O}$ but we can estimate it.

Indeed, we can evaluate the energy difference between the $\sigma$ and the $\sigma^*$, noted $\Delta^{\sigma/\sigma*} = \mu_{\sigma*} - \mu_{\sigma} \approx 14\,eV$. Likewise, we can define $\Delta^{\pi/\pi*} = \mu_{\pi*} - \mu_{\pi}$, where the chemical potential is averaged among the $\pi(y)$ and $\pi(z)$ states, which evaluates here to $\Delta^{\pi/\pi*} \approx 4\,eV$.

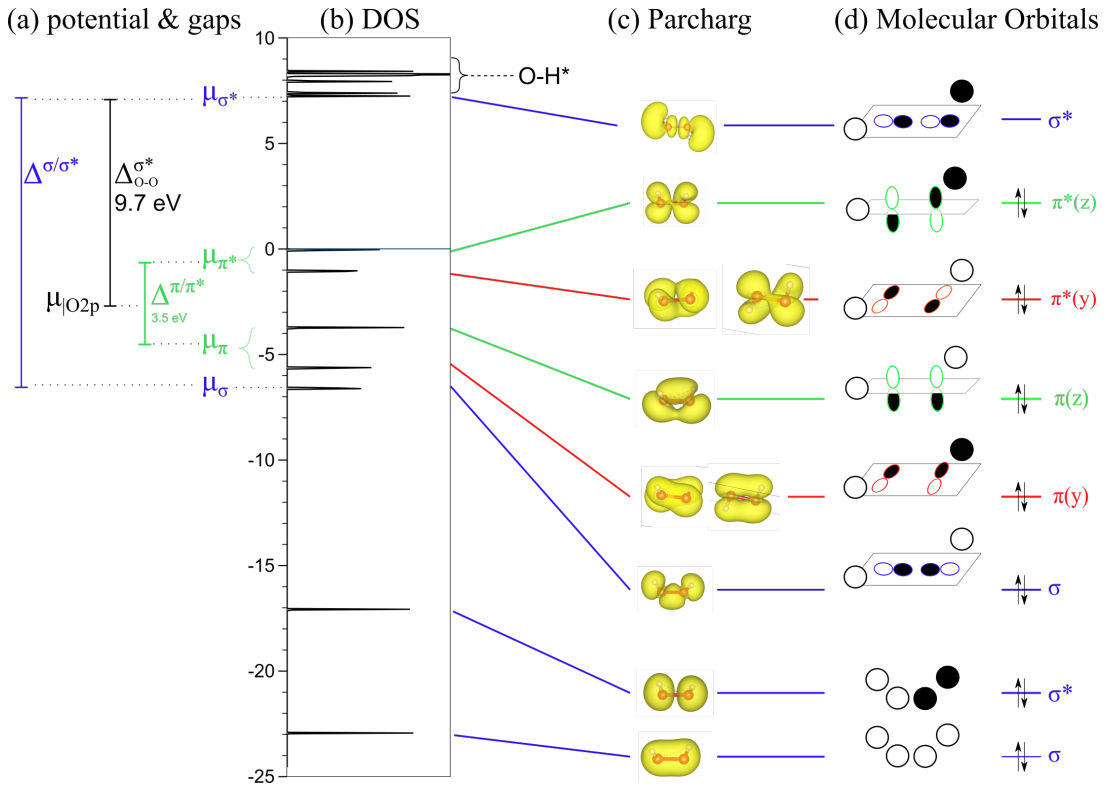


Figure III.5: Analysis of $H_2O_2$ DOS obtained via HSE06 functional. For each peak of the DOS (b), the corresponding Parcharg (c) is attributed to a molecular orbital (d) which allows to estimate the potentials of this orbital (a). In the depicted M.O., O-H overlaps are bonding because O-H* states, with a H-dominant character, are well above the Fermi level.

Furthermore we know that the $\mu_\pi < \mu_{|O_{2p}} < \mu_{\pi*}$. Since $\Delta^{\pi/\pi*} \ll \Delta^{\sigma/\sigma*}$, the error introduced by assimilating the potential $\mu_{|O_{2p}}$ with the barycenter of the $\pi$ and $\pi^*$ bands is small compared to $\Delta^{\sigma/\sigma*}$. Hence using this approximation, we can estimate $\mu_{|O_{2p}}$ and, from there, $\Delta^{\sigma*}_{O-O}$. The error in the position of $\mu_{|O_{2p}}$ is then capped by the gap between the highest $\pi$ and the lowest $\pi^*$. In the HSE06 calculation of fig. III.5, we therefore have $\Delta^{\sigma*}_{O-O} \approx 9.7 \pm 1.7\, eV$

Having studied the neutral $H_2O_2$, we now investigate the impact of charge variation on the electronic structure. For each $n_{e^-} \in [12, 16]$, we plot the atomic geometry and the parcharg of the HOMO (see fig. III.6.a). The most oxidized structure $H_2O_2{}^{2+}$ ($n_{e^-} = 12$) relaxes to a staggered geometry (H-O-O-H dihedral angle of 60° show in the Newman representation of fig. III.6.b). In this configuration, the energy difference between the $\pi(y)$ and the $\pi(z)$ (due to distinct OH overlap) is small, thus allowing a "high spin" configuration $\pi^*(y)^1$,$\pi^*(z)^1$, similar to molecular $O_2$. However, with increasing reduction ($n_{e^-} \in [12.5 - 13.5]$), the structure relaxes to an eclipsed geometry (H-O-O-H dihedral angle of 0°), in which the $\pi(y)/\pi(z)$ gap is larger than in the staggered configuration. Hence the $\pi^*(y)$ becomes filled while the $\pi^*(z)$ is partially empty, leading to a "low spin"

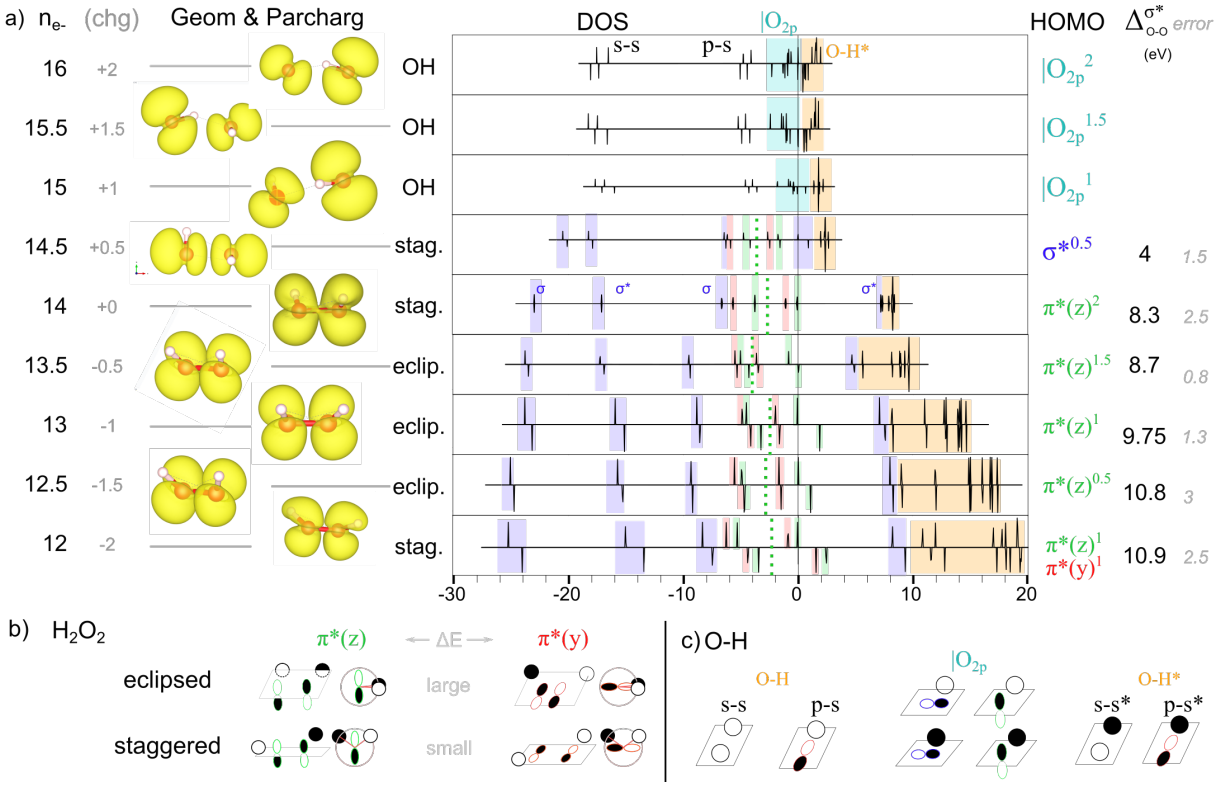


Figure III.6: Analysis of charged $H_2O_2$ for each oxidation state. a) Table showing the geometry of the structure, the nature and the occupancy of the HOMO and the DOS where orbitals have been identified by their color in the molecular orbital diagrams of b) ($H_2O_2$) and c) (HO). The identification of the $\sigma$ and $\sigma*$,in blue, allowed to estimate the $\Delta^{\sigma*}_{OO}$.

configuration. For $n_{e^-} = 14$, the $\pi^*(z)$ is full[c] and the molecule goes back to a staggered geometry, which is more stable due to lower steric destabilization.

For larger electron count, the $\sigma^*$ starts to fill. Therefore, the bonding becomes destabilizing and the structure relaxes to two isolated $OH^{n-}$ ions, linked by a hydrogen bond ($n_{e^-} \in [15-16]$). In this case, each OH fragment has between 7 and 8 electrons, so that the HOMO is an $|O_{2p}$ (see the M.O. diagram of OH in fig. III.6.c). These partially occupied $|O_{2p}$ are highly unstable and they would interact with the metal if it had been included in this modeling (RCM). Their existence here is yet another proof that the metal oxide host is a catalyst of the O-O bond formation.

Having identified the HOMO, we use the same parcharg method to identify the other orbitals of each oxidation state of $H_2O_2$. Each orbital symmetry is indicated by a colored background in the various DOS of fig. III.6.a. (see caption for color mapping). Having assigned an energy to each molecular orbital, we proceed to the quantification of $\Delta^{\sigma*}_{O-O} = \mu_{\sigma*} - \mu_{|O_{2p}}$.

[c] In this calculation, made with PBE, the $\pi^*(z)$ is not full because of a small charge spillage error. This error was absent in the HSE06 calculation shown in fig. III.5. We have kept the PBE result here for the coherence of the bandgap estimation.

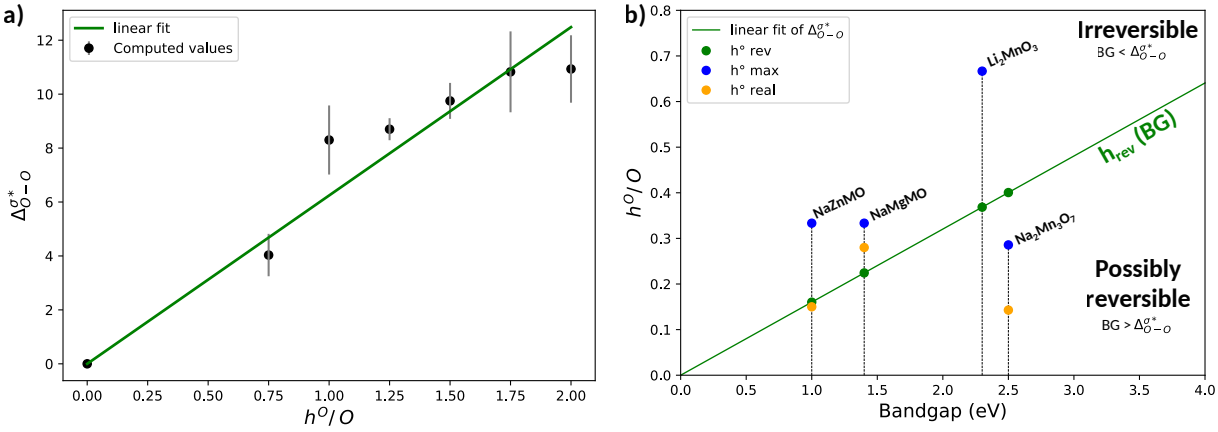


Figure III.7: a) $H_2O_2$ values for $\Delta^{\sigma*}_{O-O}\left(h^O\right)$ and proportional fitting: $\Delta^{\sigma*}_{O-O} = 6.2 * h^O$. b) Determination of $h^O_{rev}\left(\Delta_{BG}\right)$ and comparison with theoretical and experimental $h^O$in selected compounds.

As for the study of neutral $H_2O_2$, $\mu_{|O_{2p}}$ is approximated by the barycenter of the $\pi/\pi*$ bands and the $\mu_{|O_{2p}}$ uncertainty is estimated as half of the gap between the highest $\pi$ and the lowest $\pi^*$. The results allow to give a first approximation of $\Delta^{\sigma*}_{O-O}\left(h^O\right)$ (see fig. III.7.a) which can be roughly fitted by a proportionality relation: $\Delta^{\sigma*}_{O-O} = 6.2\,h^O$. This justifies a posteriori the linear variation of $\Delta^{\sigma*}_{O-O}$ in the first scheme of this chapter (see fig. III.1).

### Discussion

Despite the large uncertainty and a coarse linear fitting, this analytic expression of $\Delta^{\sigma*}_{O-O}\left(h^O\right)$ provides very important information. Indeed, we have demonstrated that reversible A.R. requires that $\Delta_{BG} > \Delta^{\sigma*}_{O-O}\left(h^O\right)$ (where $\Delta_{BG}$ is the pristine bandgap). Hence the maximal value of $h^O$ which satisfies this condition (noted $h^O_{rev}$) is given by $\Delta_{BG} = \Delta^{\sigma*}_{O-O}\left(h^O_{rev}\right)$ is the maximal capacity which allows reversible cycling. By using our analytical fit, we can invert this relation and express the reversible A.R. capacity as a function of the bandgap : $h^O_{rev}\left(\Delta_{BG}\right) = \Delta_{BG}/6.2$ (green line in fig. III.7.b).

The determination of $h^O_{rev}\left(\Delta_{BG}\right)$ allows to draw some general conclusions: Many A.R. compounds are semiconductors with bandgaps $h^O < 1.5\,eV$ for which we predict the onset of irreversibility to occurs for $h^O_{rev} = 0.24$, which is coherent with value of $h^O \approx 0.3$ determined from experimental results.[63] To give an order of magnitude, this capacity amounts to 140 mAh/g in $LiMnO_2$ ($\Delta_{BG} = 1.7\,eV$).

We can then compare $h^O_{rev}$ with the theoretical or experimental values of $h^O$ (blue and orange dots in fig. III.7.b): If $h^O > h^O_{rev}$ (above green line), $\Delta_{BG} < \Delta^{\sigma*}_{O-O}$ so the A.R. will necessarily trigger a reductive elimination, thus creating peroxo-bonds and irreversible migration. If $h^O < h^O_{rev}$ (below green line) $\Delta_{BG} > \Delta^{\sigma*}_{O-O}$ and the compound can undergo RCM until the end of charge. These results explains that the experimental values of $h^O$

(orange dots) tend to be closer to $h^O_{rev}$, since the material cycles very poorly beyond this threshold value.

We must however recall that in this method, we only considered homogeneous hole distribution ($\left\langle h^O \right\rangle = h^O$). In the case of oxygen-pair disproportionation, we can have $\left\langle h^O \right\rangle < h^O_{rev} \ll h^O$, which will lead to local degradation even though the compound lies below the green line. For this reason, $h^O_{rev}$ is only an upper limit for the reversible range of A.R. but $h^O < h^O_{rev}$ does not guarantee reversibility. Despite this caveat, this simple criterion can used for rejecting the bad candidates during high throughput calculations.

## 1.3 Perspectives

While this analysis is powerful, it is still very qualitative. The enhancement of the fit through more accurate calculation and a larger dataset is an ongoing work. However, beyond this incremental enhancement, we can also open some perspective of improvement by refining some core approximations.

### Constrained geometry

An important approximation concerns the treatment of the $\pi$ orbitals. Indeed, the identification of the $\pi$ components is paramount for the estimation of the $\mu_{|O_{2p}}$ which, in turn, impacts the values of $\Delta^{\sigma*}_{O-O}$. Furthermore, this identification of the $\pi$ orbitals is necessary to determine the much smaller $\Delta^{\pi*}_{O-O}$, which would allows for more fine grained determination of $h^O_{rev}$. The problem we faced during the study of this $\pi$ block was the variation of the hydrogen positions at various state of charge, which caused a change in the symmetry of the orbitals, thus preventing an efficient comparison. This caused us to use the average $\pi$ (or $\pi^*$) energy without accounting for the individual orbital types. Another limitation comes from the lack of data points at low $h^O$, which also stems from a change of geometry of the hydrogen (creation of O-H-O configurations). Hence it appears that controlling and mitigating the changes in hydrogen configuration would allows to mitigate these two errors, thus greatly improving our results.

A simple way to prevent this symmetry change consists in constraining the local symmetry of the "OH" fragments. Since the O-H bond length or orientation stays constant, the position of the hydrogen is completely determined by the position of the nearest oxygen. Therefore, the only degree of freedom is the distance between the two 'OH' fragments, parameterized by the O-O distance, noted $d_{O-O}$.

To perform an energy minimization in this setup, we cannot use an ionic relaxation as implemented in VASP (even with constrained axes). However, since the geometry only has a single degree of freedom, we can do this minimization "by hand". Indeed, by plotting $E(d_{O-O})$ we obtain an "energy valley" which minimum indicates the equilibrium geometry under the constraint of "frozen O-H bond".

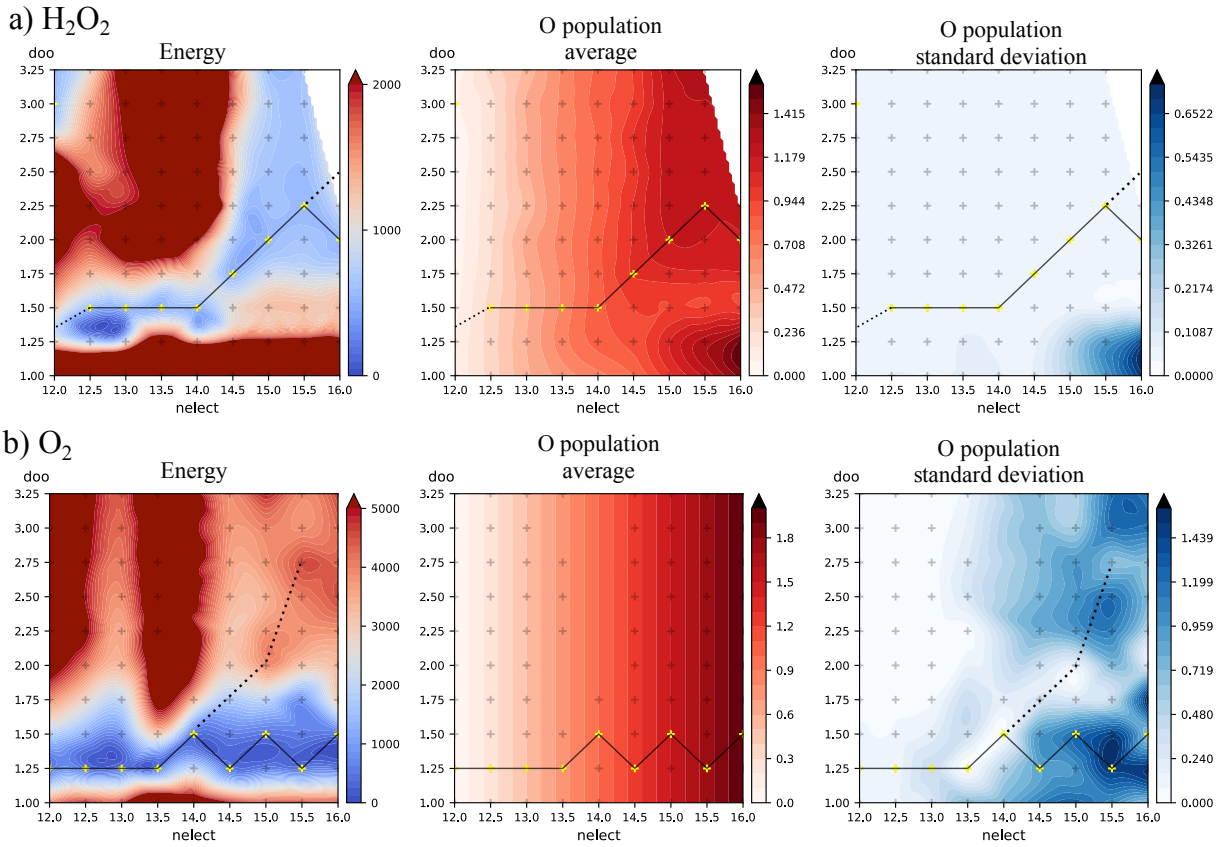


Figure III.8: Landscape sampling of $O_2$ (a) and $H_2O_2$(b) as a function of $n_{e^-}$ and $d_{O-O}$. From left to right, the landscapes represent the energy (low energy in blue, high energy in red) and the average (red) and the standard deviation (blue) of oxygen Bader population.

The fact that our geometry is reduced to a single parameter allows to add the electron count $n_{e^-}$ as a second parameter to go from a 1D-function, a "valley" – $E(d_{O-O})$ – to a 2D-surface, a "landscape" – $E\,(n_{e^-}, d_{O-O})$. Indeed, by assembling the successive $E(d_{O-O})$ (one for each electron count), we obtain a surface where each point correspond to a relaxed structure with specific $(n_{e^-}, d_{O-O})$ values. On each of these structure, we can access various quantities apart from the energy, and we can plot a "landscape" for each of them (see fig. III.8).

We applied this treatment to $H_2O_2$ and to $O_2$ for comparison (see fig. III.8). For $H_2O_2$, the lowest energy path (solid line in the energy landscape) correctly reproduces the progressive dissociation of the two 'OH' fragments when increasing $n_{e^-}$.[d] Furthermore, we see that the average oxygen population along that path follows a progressive increase, which is coherent with the charging of the oxygen. Furthermore, looking at the standard deviation from the oxygen population, we confirm that the charge stays perfectly even between the two oxygen, which is another proof of that the counter-cations provide

[d]The large $d_{O-O}$ for $n_{e^-} = 14$ indicates that isolated $OH^+$ ions are also stable, which is physically meaningful yet out of the scope of this study.

computational stability.

On the contrary, for the $O_2$ molecule, the lowest energy path (solid line in fig. III.8.b) shows that for every electron count, the most stable structure has a $d_{O-O}$ within the 1.25-1.50 range, in line with the results found by relaxing the whole geometry. In order to understand these nonphysical results, we use Bader analysis. The average Bader population of oxygen follows a perfectly regular increase, which was expected since there are no hydrogen to provide alternative Bader basins. However, the standard deviation of the oxygen population indicates a clear disproportionation of the charge for high $n_{e^-}$ at low $d_{O-O}$. This explains why the O-O bond remains short.

Indeed, instead of an identical ionization of the two $O^{n-}$ fragments which separate due to electrostatic repulsion, the disproportionation of the charge leads to an ionic bonding ($O^{(n-\delta)-}$– $O^{(n+\delta)-}$) which stabilizes the geometries with short O-O distances. Interestingly, the homolitic dissociation path does exist, as indicated by a low standard deviation (dotted line). Even though this path is not thermodynamically favored, we can still access to these local minima and conduct our study of the homolitic dissociation. Therefore, this "constrained geometry method" allows escape inherent limitation of DFT with tends to favor oxygen charge disproportionation. It therefore gives access to data points at low $h^O$ without the need for counter cations that re necessary to refine our estimation of $\Delta^{\sigma*}_{O-O}\left(h^O\right)$.

### Extension to sulfides

Since the beginning of this chapter, we have only considered the opening of the gap withing the non-bonding states of the oxygen. However, we have shown that the "anionic polymerization" in sulfides can be described within the same framework, thus allowing us to extend our methodology to this new class of compounds. Since the valence orbitals of the sulfur have a larger principal quantum number, they should be much larger, thus enabling increased overlap, even at larger distance, which should facilitate the electronic convergence and the correct dissociation of the $S_2$ molecule.

For the sake of comparison with the oxygen, we decided to use the same constrained geometry method and build the corresponding landscapes, shown in fig. III.9. For $S_2$, we face the same limitation when simulating the separation of $S^-$ ions, because of disproportionation. As for the oxygen, this problem is mitigated by the addition of hydrogen atoms. We also note that the convergence is easier as the potential wells for each $n_{e^-}$ are deeper, which is coherent with the larger size of the $S_{3p}$ orbitals.

We see that this reduction of the degrees of freedom using a constrained geometry is a powerful and versatile method which allows to isolate the effects of electron count and O-O distance in the quest for the quantification of $\Delta^{\sigma*}_{O-O}$. The study of the orbitals evolution in this constrained geometry is an ongoing work which promises to be exciting.

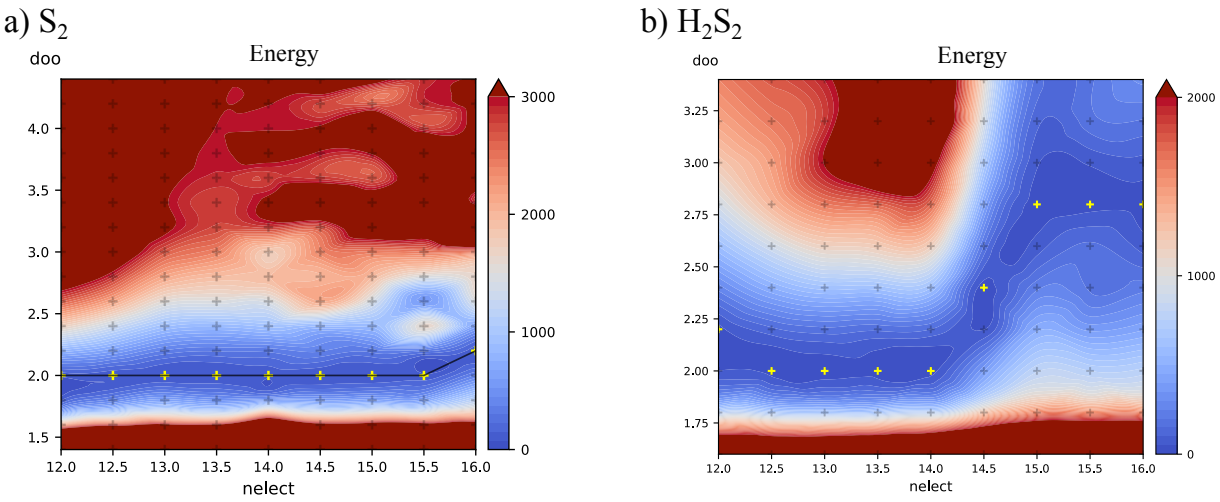


Figure III.9: Energy and charge distribution of $S_2$ and $H_2S_2$, as a function of $n_{e^-}$ and $d_{O-O}$.

We have thus described a method to predict the reversibility of anionic redox based on the comparison of a material bandgap to the gap opening in an oxygen pair. We then obtained a first quantitative approximation using an $H_2O_2$ pair. Finally we opened some perspective by proposing a method based on the sampling of the reaction energy landscape.

We now turn to the second method, equally based on an energy landscape sampling, to predict the reversible cycling range of A.R. in solid state compounds.

# 2 Comparing the RCM and the Disproportionation

The previous method was based on the molecular description of the pairing mechanism, which allowed to build a simple scale to evaluate the reversibility of the A.R. in a compound. Since this scale is based on an abstract O-O pair, it provides results which can be extended to all the oxides with the drawback of being qualitative. However it does not allows to describe collective effects such as collective distortion and charge disproportionation.

This second method is also based on the construction of a potential energy landscape, similar to the previous method with the notable difference that each point represents a complete structure and not an single molecule state such as $H_2O_2$. This allows to account for collective effects such as collective distortion and charge disproportionation which are specific to each material.

## 2.1 Theoretical framework

#### Objective: The ideal energy landscape

In the potential energy landscape approach, we would like to use axes which describe i) the state of charge and ii) the type of mechanism. Interestingly, the two A.R. mechanisms (RCM and the oxygen disproportionation) have distinct effects on structural and electronic reorganization. Likewise, cationic oxidation may also be identified through structural reorganization (e.g. J-T distortion). Consequently, structural and electronic reorganization (i.e. distortion) seems a good metrics to distinguish the types of redox mechanism.

If we can find such variable which takes different values for each type of redox mechanism (cationic, anionic with RCM or anionic with DP), we would obtain a landscape similar to the one sketched in fig. III.10. In this sketch, for a given Li content, the energy surface defines several local minima which represent distinct mechanisms with specific atomic arrangements. The energy barriers between each of these atomic arrangements delineates valleys (indicated by a distinctive color). We see that by identifying the global minimum for each Li-content, we can determine the thermodynamic path (solid line). However, there are also energy barrier associated with delithiation within each of these valleys (light colors). By comparing for each point, the energy cost of delithiation "within the same valley" to the delithiation with a "change of valley", we can also determine the kinetic pathway (grey line). This kinetic path features an hysteresis since the energy barrier are seldom symmetric (indicated by arrows on the grey lines).

The quantitative description of such landscape is the goal of this method. However, in order to simplify the problem, we will only concentrate on the anionic redox, thus ruling

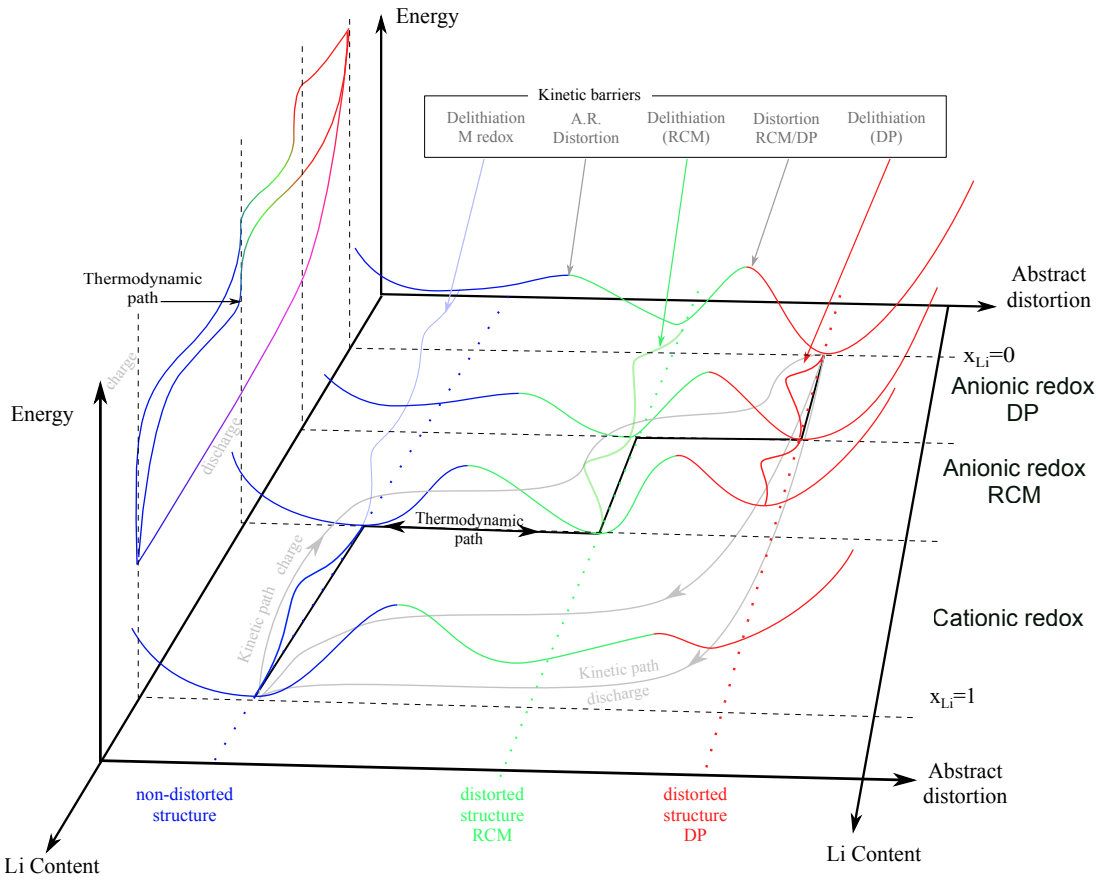


Figure III.10: Ideal energy landscape using the "abstract distortion" as a reaction axis to distinguish the valleys corresponding to cationic (blue) or anionic redox with RCM (green) or DP (red). The thermodynamic path follows the minima of energy at each $x_{Na}$ (solid black line), while the kinetic path follows the lowest energy barrier (grey line) thus displaying hysteresis. Note that there is a statistical distribution of the kinetic trajectories due to the various environments (symbolized by 2 distinct grey lines in discharge).
The voltage curve, on the right, can be understood as a projection of this surface along the "abstract distortion" axis. While the thermodynamic path shows a plateau for each process, the real curve follows the kinetic path, with hysteresis and an S shape in discharge due to a statistical distribution of kinetic trajectories.

out the need to describe cationic redox. For further simplification, we will also neglect the energy barrier associated to delithiation. We will therefore postpone the kinetic study and focus on a thermodynamic picture for the time being. To implement this method, we will focus on *P2*-$Na_xMg_{1/3}Mn_{2/3}O_2$ since we have already a good understanding of its A.R. behavior, while trying to keep the methodology as general as possible. Now that the theoretical framework is laid out and the objective is clear, the main question is *how to find a valid variable to distinguish the different A.R. mechanisms ?*

### Finding a 1D descriptor for the A.R. mechanisms

In order to find such variable, we have tried several strategies. The first one, very close to the method exposed for $H_2O_2$, consisted in mapping the A.R. mechanism to geometric

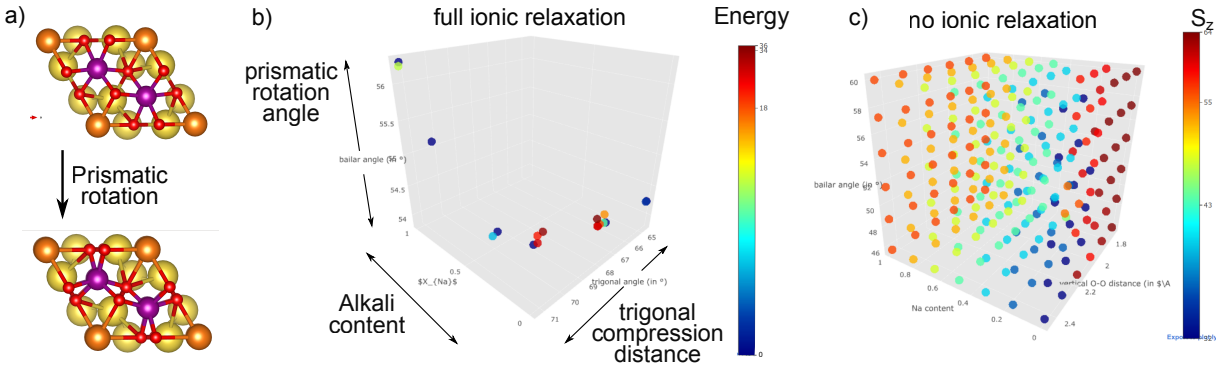


Figure III.11: Geometric descriptor of A.R. mechanism in $Na_xMg_{1/3}Mn_{2/3}O_2$. The axes correspond to the trigonal compression, the prismatic rotation (a) and the alkali content. b) Freely relaxed structure (color = energy above hull). c) Constrained structures spanning the whole configuration space (color = magnetization). Note the progressive decrease of $\langle S_z \rangle$ upon charge, with a anomalously increase of $\langle S_z \rangle$ for very short $d_{O-O}$ (red dots in the far right corner).

descriptors. Indeed, we saw in the chapter 1 that the distortion associated to the RCM is described as a mix of trigonal compression and prismatic rotation (see fig. III.11.a) of every $MO_6$ octahedra leading to the uniform shortening of the O-O bonds. To describe the distortion of the structures, we thus used a 2-dimensional axis (compression + rotation) in addition of the charge axis. In this 3-dimensionnal basis, the freely relaxed structures can be localized (fig. III.11.b). Alternatively we can generate a distorted atomic structure in which every octahedron is distorted using the two parameters described (compression + rotation). By generating structures which span the whole configuration space, we can then obtain a 3D function (fig. III.11.c).

In these graphs, the position identifies the geometry and the state of charge while the color identifies a quantity defined for the whole structure (e.g. energy or total magnetization). The first difficulty with this approach is the reading. Indeed, the need to have a distortion along 2 axis forces to draw in 3d, which is not convenient for printing (even though beautiful interactive 3D plots can be created in HTML via the *Plotly* library[115]). Beyond this practical difficulty, the fundamental roadblock for this approach is that the configuration space sampling via generated structures uses an homogeneous distortion which cannot account for the localized distortion associated to the disproportionation.

Since the geometrical description faces both practical and fundamental drawbacks, we tried to find an electronic descriptor instead. We therefore plotted the total magnetization of the cell ($S_z = n_\uparrow - n_\downarrow$) for the whole configuration range (see fig. III.11.b) and noticed that, for a certain type of distortion (very small $d_{O-O}$), the magnetization had an anomalous behavior. In order to rationalize this behavior, we came back to the electronic mechanisms of A.R This allowed us to understand that indeed, under certain conditions,$\langle S_z \rangle$ can be used as an indicator for the A.R. mechanism. We will now explain

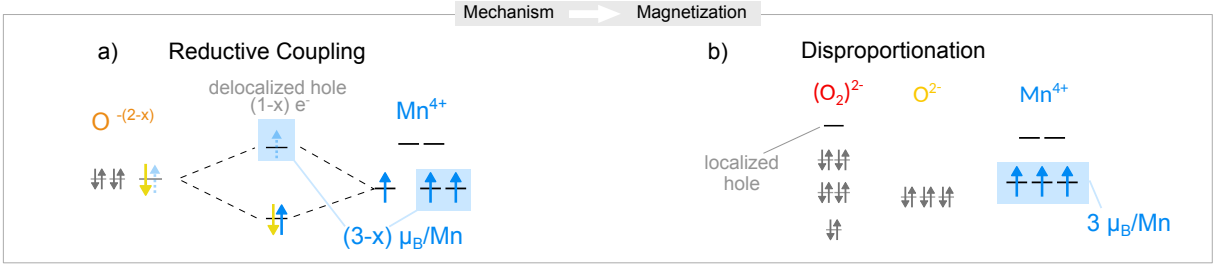


Figure III.12: How the A.R. mechanism determines magnetization. a) The RCM creates partially occupied M-O-O states with anti-ferromagnetic coupling to the rest of the metallic spins. b) The disproportionation of oxygen into paramagnetic species prevents any magnetic ordering between Mn and O.

why.

### From A.R. mechanism to magnetization

In order to use the total magnetization of the cell as a descriptor for the A.R. regime, we must prove that there is a one to one correspondence between them, which requires to prove the two directions of the equivalence. We will start by demonstrating that the A.R. regime determines the value of $\langle S_z \rangle$.

In the case of the RCM, the unpaired electrons of oxidized oxygens get partially paired with unpaired electrons of the Mn magnetic center (high-spin state) through the covalent M-O-O interaction and the creation of d-σ* states (see fig. III.12.a). In that case, oxygens bearing unpaired electrons are magnetic centers, as already evidenced through Electron Paramagnetic Resonance (EPR) measurements in other A.R. cathode materials such as $Li_2Ru_{0.75}Sn_{0.25}O_3$[116]. Compared to the pristine material, the total magnetization of the unit cell $\langle S_z \rangle$ should thus decrease linearly with the concentration of oxygen hole or equivalently with the amount of removed sodium.

In the case of disproportionation (fig. III.12.b), since both oxo- $O^{2-}$ and peroxo- $(O_2)^{2-}$ are closed-shell and non-magnetic species, the total cell magnetization $\langle S_z \rangle$ corresponds to that of the $Mn^{4+}$ magnetic center ($3\mu_B$) and should remain constant during A.R.[e]

### From magnetization to A.R. mechanism

Having demonstrated that the A.R. regime determines the value of $\langle S_z \rangle$, we now want to prove the opposite, namely that the relaxation under a constrained $\langle S_z \rangle$ determines the type of A.R. mechanism. To do so, we first notice that when neglecting the weak spin-orbit interaction, the $\hat{S}_z$ operator commutes with the Hamiltonian ($\langle S_z \rangle$ becomes a good quantum number). This zero commutator implies that the $\hat{S}_z$ eigenspaces are stable during DFT relaxation. Hence, by constraining $\langle S_z \rangle$ during relaxation, we can obtain the

[e]Note that an increase of the total magnetization may occur when the reductive elimination of $O_2{}^{2-}$ and/or $O_2$ enlists a reduction of neighboring $Mn^{4+}$ ($3\mu_B$) to $Mn^{+3}$ ($4\mu_B$).

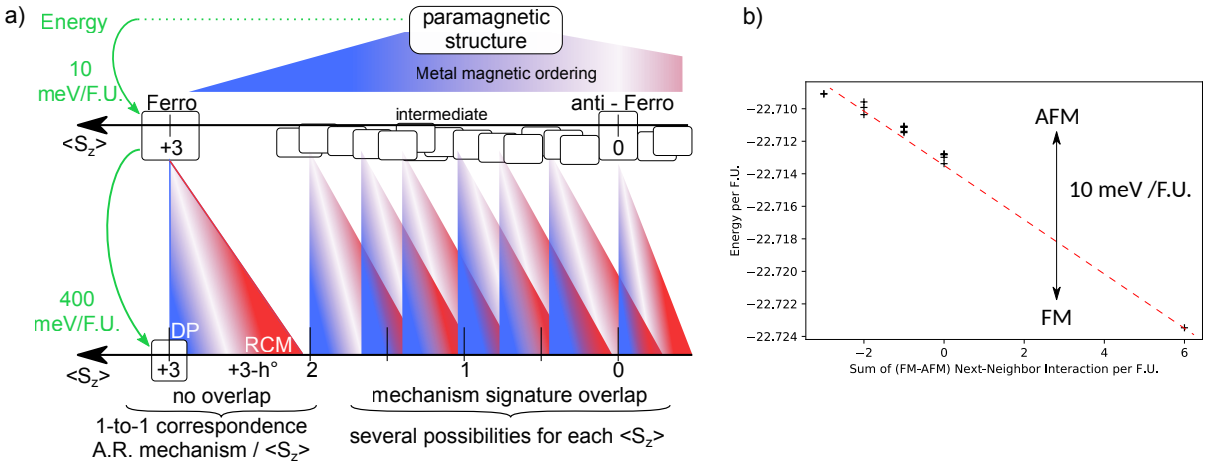


Figure III.13: Comparison of metal magnetic ordering and A.R. magnetic signature in terms of $\langle S_z \rangle$. (a) and energy (b). In terms of $\langle S_z \rangle$, the metal magnetic ordering dominates ($\pm 3 \mu_B/Mn$), and the A.R. signature is second order ($\pm 0.5 \mu_B/Mn$). Each $\langle S_z \rangle$ can be achieved by several magnetic ordering which A.R. magnetic signatures overlap. Around the maximal $\langle S_z \rangle$ (ferromagnetic ordering), there are no overlap, thus allowing a 1-to1 correspondence. In terms of energy, the A.R. mechanism dominates (0.5 eV) and the metal magnetic ordering, estimated in (b) to 10 meV, is second order.

ground state for each $\hat{S}_z$ eigenspace. However, we must be sure that there is a 1-to-1 correspondence between the A.R. mechanism and the $\langle S_z \rangle$ of the cell.

Even though the RCM and the DP mechanisms slightly change the value of $\langle S_z \rangle$, the main contribution to the magnetization is the ordering of high-spin $3d$ metal (see fig. III.13.a). For $\langle S_z \rangle < 3\,\mu_B$/Mn, each $\langle S_z \rangle$ can be achieved by several magnetic ordering. However, $\langle S_z \rangle = 3\,\mu_B$/Mn corresponds to a unique – ferromagnetic – ordering. Therefore, by choosing $\langle S_z \rangle$ close to $3\,\mu_B$/Mn, we impose a ferromagnetic order to the metal. In this case the metal contribution to the magnetization is uniquely determined and constant and the small variations of $\langle S_z \rangle$ are exclusively correlated to the number of unpaired electrons on the oxygen, which determines the A.R. mechanism. This justifies the existence of a 1-to-1 correspondence between the A.R. mechanism and the $\langle S_z \rangle$ of the cell.

The enforcement of such ferromagnetic order is justified because the energy error introduced by assuming a ferromagnetic order is negligible compared to the energy variations caused by the change in A.R. mechanism. Indeed, the magnitude of the magnetic exchange coupling is of the order of magnitude of the energy difference between ferro and anti-ferro magnetic orders. Our results (see fig. III.13.b) show that $E_{ferro}$–$E_{anti-ferro} \approx 10\,meV/F.U.$ This value has to be compared to the depth of the energy valley caused by change of A.R. mechanism around each metallic ordering, which is of the order of several hundreds of meV (see below, fig. III.15). Hence even if the ferromagnetic order is not the most stable, the error introduced does not impact our conclusions. Furthermore, the choice of such ferromagnetic order helps reducing the error due to the single determinant

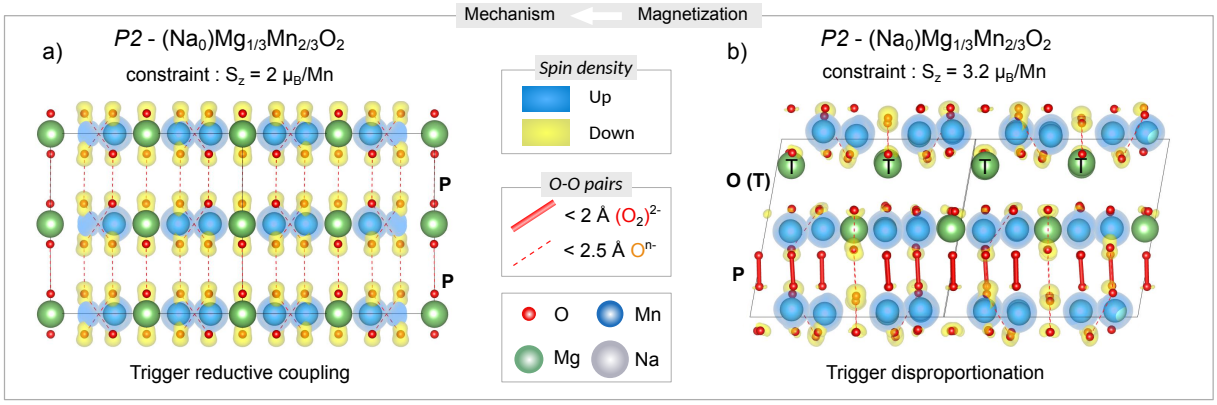


Figure III.14: *P2*-$Na_0Mg_{1/3}Mn_{2/3}O_2$ relaxed under constrained magnetization. (a) $\langle S_z \rangle = 2\,\mu_B$/Mn, leading to the RCM mechanism and (b) $\langle S_z \rangle = 3.2\,\mu_B$/Mn, leading to the DP mechanism. Hence we see that magnetization constraint determines the A.R. mechanism.

approximation of the DFT. Finally, this assumption of a ferromagnetic order is supported by the Goodenough-Kanamori rules which stipulates that, for a 90° M-O-M bond angle, the double-exchange between the two metals should cause a ferromagnetic coupling[f].

As a proof of concept, we relaxed $Na_0Mg_{1/3}Mn_{2/3}O_2$ with a constraint on $\langle S_z \rangle$ (fig. III.14). The structure obtained by imposing $\langle S_z \rangle = 2\,\mu_B$/Mn (fig. III.14.a) features an homogeneous distribution of the minority spin density on the oxygen, along with a very symmetric O-O distortion. Both features indicate a mild and homogeneous oxygen oxidation and pairing, associated to the RCM. In contrast, the relaxation with $\langle S_z \rangle = 3.2\,\mu_B$/Mn (fig. III.14.b) results in a highly distorted structure: the migrations of the Mg in the (upper) inter-layer forced a layer gliding to create O stacking. Concomitantly, the creation of short peroxide bonds across the (lower) inter-layer forced the stacking to remain in P type, thus leading to a highly distorted OP stacking. As expected, the spin density on either the non-oxidized oxygens ($O^{2-}$) or the true peroxide ones ($O_2^{2-}$) is close to zero. This is a clear manifestation of oxygen disproportionation.

Based on these results, we have proven that constraining $\langle S_z \rangle$ around the ferromagnetic ordering ($3\,\mu_B$/Mn) upon charge allows to distinguish between a localized hole pairing on oxygen (formation of peroxo which does not change $S_z$) and a delocalization of unpaired holes over the M-O bonds which decrease the total $\langle S_z \rangle$. We see here that the $\langle S_z \rangle$ is just a convenient "handle" to impose the M-O charge transfer regime, using its magnetic signature. This charge transfer regime determines the energy to a large extent even though the magnetic interactions themselves have very little impact on the energy. Using this "handle" as a descriptor for the A.R. distortion regime and the alkali content as the

[f] While there is no kinetic exchange between the metals, the coulomb-exchange between the orthogonal $O_{2p}(x)$ and $O_{2p}(y)$ favors a triplet for two electrons in different orbitals on the same site (Hund's first rule).

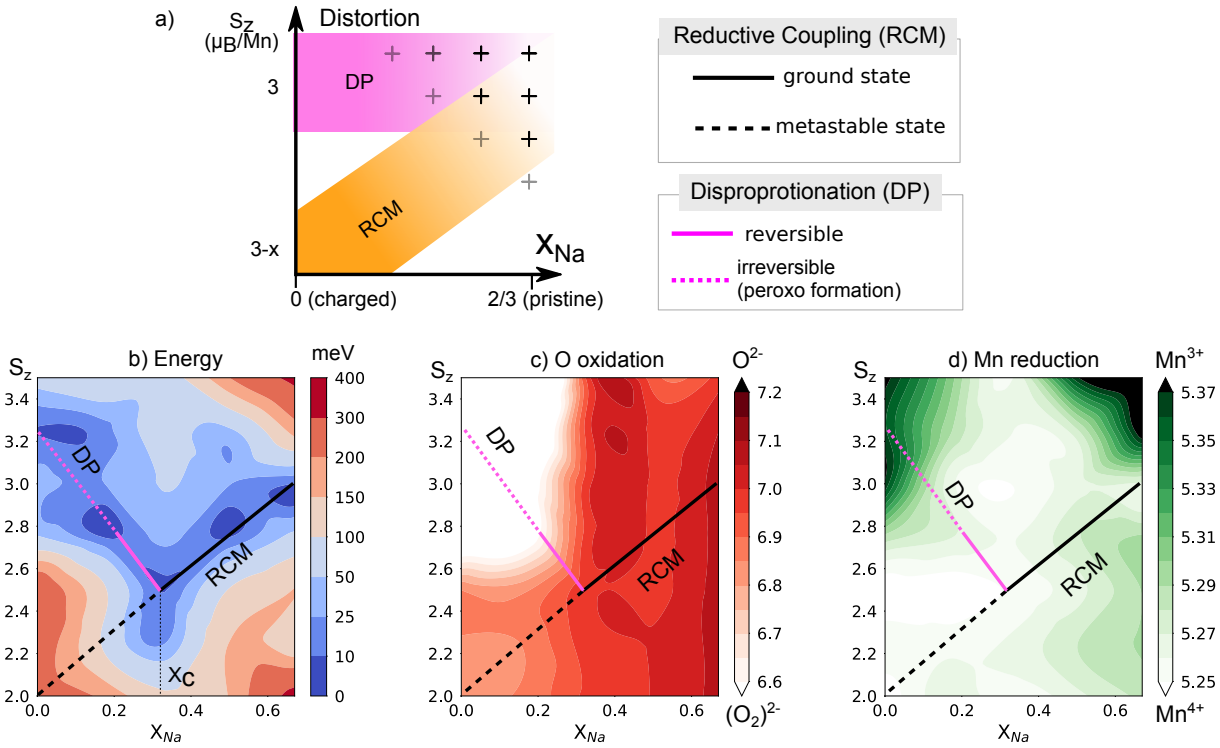


Figure III.15: Magnetic energy landscapes of NaMgMnO. a) Method: Each point of the surface corresponds to a structure relaxed under the constraints determined by its coordinates $(\langle S_z \rangle, x_{Na})$. For each structure, we plotted the energy (b) or the Bader population of the most oxidized oxygen (c) and of the most reduced Mn (e). The value of $\langle S_z \rangle$ indicates the type of mechanism: $3\mu_B/Mn \rightarrow$ DP (pink), $3 - x\,\mu_B/Mn \rightarrow$ RCM (orange). The energy landscape determines the thermodynamic path. The Bader charges determines the reversibility of the mechanism for each structure.

second descriptor, we now have two variables that we can constrain during the structural relaxation. We can therefore proceed to the generation of the energy landscapes.

## 2.2 Results & discussion

Energy and Bader net populations were computed on relaxed 221 super-cells at various Na content under constrained magnetization. Composition ranged from 0 to 2/3 $x_{Na}$ per formula unit, by intervals of 1/6. Magnetization (VASP parameter: *NUPDOWN*) ranged from 2 to 3.75 $\mu_B$/Mn by intervals of 0.25. For each composition, the initial ferromagnetic order on the Mn-sub-lattice was conserved during the relaxation. The surface was then obtained by cubic spline interpolation of these data-points (see fig. III.15.

### Results

The actual results of this method for P2-$Na_xMg_{1/3}Mn_{2/3}O_2$ are shown in fig. III.15. In this figure, we can evaluate which mechanism takes place in a material by following the $\langle S_z \rangle$ variation along the path of lowest energy on the energy surface (fig. III.15.a).

Starting from the pristine ($x = 2/3$) in which the manganese is the only magnetic center (no O oxidation), the minimum of energy corresponds to a magnetization of $\langle S_z \rangle = 3$ (all $Mn^{4+}$ in high spin configuration with ferromagnetic ordering). When removing Na, the linear decrease of $\langle S_z \rangle$ (solid black line) is indicative of the RCM. The decrease in $\langle S_z \rangle$ is pursued down to a value of 2.5, reached for a critical Na composition of $x_{Na} \approx 0.3$. Below this critical $x_{Na}$, the total magnetization along the lowest-energy path starts to increase (solid pink line), indicating the onset of oxygen disproportionation. In this low-$x_{Na}$ region, the RCM (dashed black line) no longer corresponds to the ground state of the material.

To characterize the reversibility of the disproportionation, we monitor the appearance of peroxides and $Mn^{3+}$ via Bader population analysis. For each structure, the charge of the most oxidized oxygen is compared to those of $O^{2-}$ (as in $H_2O$, dark red) and $O_2^{2-}$ (as in $Li_2O_2$, white) in fig. III.15.b. Likewise, the charge of the most reduced Mn is compared to $Mn^{3+}$ (as in $LiMnO_2$, dark green) and $Mn^{4+}$($Li_2MnO_3$, white) in fig. III.15.c. The landscape around the solid and dashed black lines, corresponding to the reductive coupling mechanism (RCM), is characterized by a smooth oxidation of the oxygen and a constant charge on Mn. Conversely, the upper left corner, corresponding to the oxygen disproportionation (DP) highlights a strong oxidation of oxygen, starting at $x_{Na} = 0.3$, while Mn stays (+IV). For lower Na content however, ($x_{Na} = 0.15$), the oxygen charge becomes lower than that of peroxides in $Li_2O_2$ (white zone in fig. III.15.b) and Mn get reduced to $Mn^{3+}$, in line with a $\langle S_z \rangle$ increase beyond the magnetization of the $Mn^{+3}$ ($3\mu_B$). This first region ($0.15 < x < 0.3$, solid pink line) corresponds to the crossover from the RCM to a weak, yet reversible disproportionation, accompanied with migration and $O \rightarrow P$ phase transition. The second region ($x_{Na} < 0.15$, dashed pink line) corresponds to the onset of reductive elimination of the peroxide leading to irreversible $O_2$.

### Discussion

To confirm the occurrence of this crossover regime at $x_{Na} = 1/6$, featuring both the RCM and some disproportionation, and to visualize the shape of the orbitals involved we plotted some parcharg at different energy range for the desodiated phase (see fig. III.16.a). In this figure, we confirm the occurrence of two type of orbitals in the same compound: the M-O-O and M-O-$O^*$ indicative the RCM (fig. III.16.b & c) and some pure O-O, indicative of the onset of the disproportionation (fig. III.16.d). We thereby confirmed that the *P2*-$Na_{1/6}Mg_{1/3}Mn_{2/3}O_2$ displays the electronic signature of both mechanisms, thus validating the occurrence of a crossover region.

This landscape sheds light on experimental data indicating the formation of *O/P*-hybrid stacking phase for $Na_xMg_{1/3}Mn_{2/3}O_2$ at low Na content. Indeed, real compounds tend to display a mixed stacking (*OP4* phase, see fig. III.16.e) over a pure *P2* or *O2*

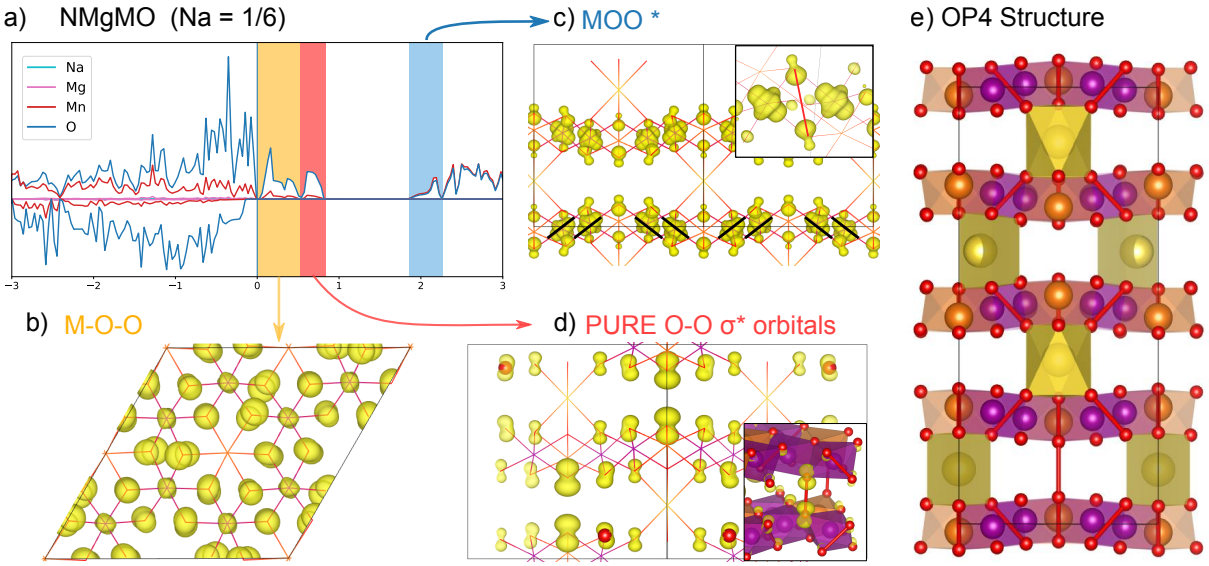


Figure III.16: Analysis of the A.R. regime crossover. The interesting energy ranges identified in the pDOS of $Na_{1/6}Mg_{1/3}Mn_{2/3}O_2$ (a) are used for partial charge projection (b,c and d) to show the coexistence of the two mechanisms. The *OP4* structure (e) represents a structural approach to this crossover.

as a compromise between electrostatic stabilization, which favors *O* stacking, and inter-layer hole delocalization through O-O bonding, which occurs in *P* stacking. Relaxation of an *OP4* cell at $x_{Na} = 1/6$ confirms that the small amount of electrons removed from the oxygen is localized around the prismatic inter-layers O-O pairs and that oxygens in the remaining octahedral stacking are not sufficiently oxidized to trigger Mg migration. The correct description of the coexistence of these two mechanisms is one of the main refinement of the solid state model compared to the single-site one.

## 2.3 Perspective

To assess the robustness of our approach, we extended our protocol to the Mn-based Na-deficient electrodes, $Na_xZn_{1/3}Mn_{2/3}O_2$ and $Na_{4/7}Mn_{6/7}O_2$ and confronted our results to the experimental data.

Our results show that the landscapes of $Na_xZn_{1/3}Mn_{2/3}O_2$ are very similar to those of $Na_xMg_{1/3}Mn_{2/3}O_2$ with disproportionation taking place at low sodium contents. Thus their electrochemical behavior should also be very similar with a large hysteresis and Mg/Zn migration at the end of charge. We note however, that both the RCM/DP crossover (solid black to solid pink) and the reversible/irreversible DP crossover (solid to dashed pink) occur at sightly higher Na content in the Zn compounds than in the Mn compounds. This global similarity and the second-order discrepancy is quite accurately confirmed by all the experimental data available on these compounds, as described in the first half of chapter 2.

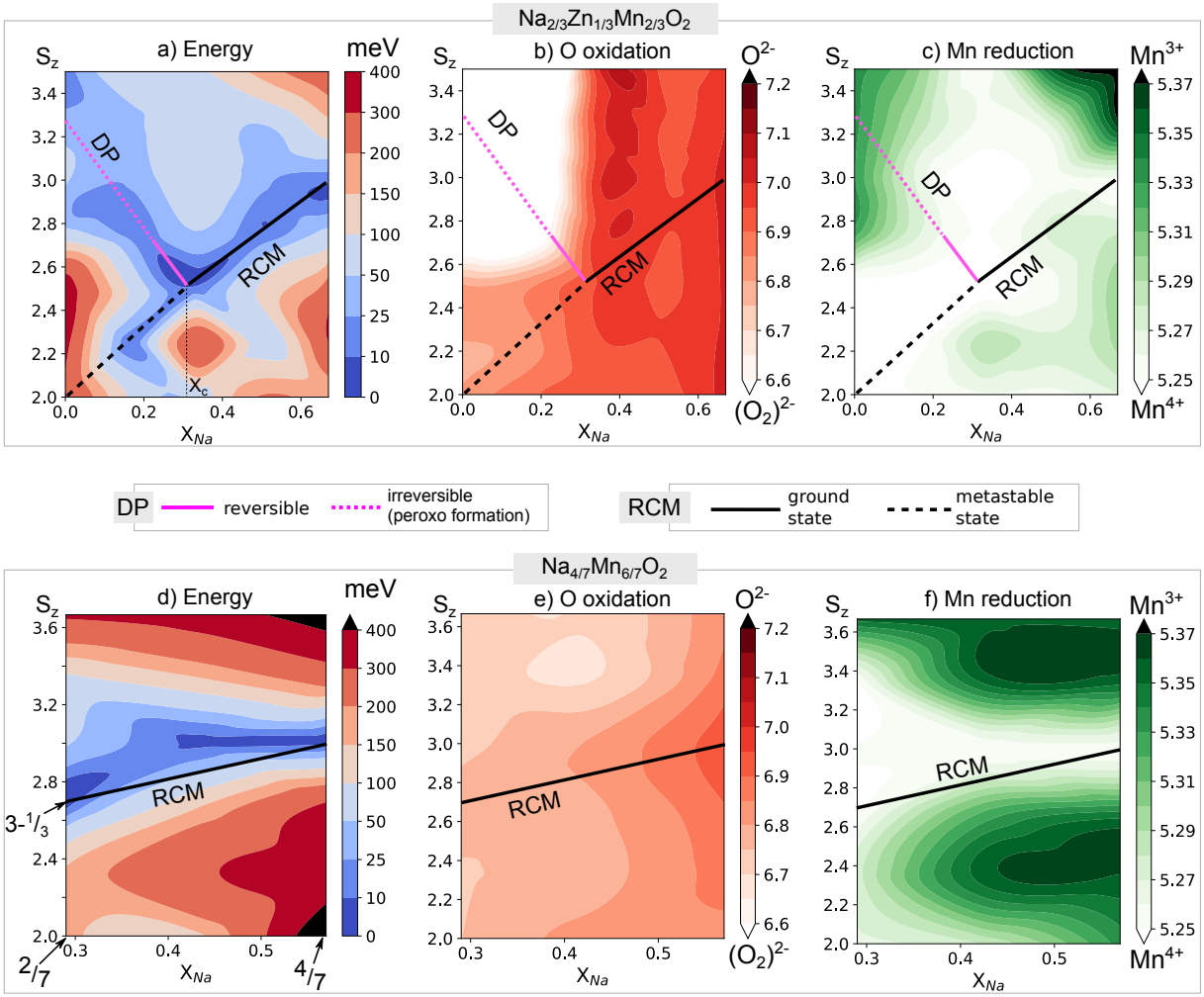


Figure III.17: Energy landscapes, Bader populations of most oxidized oxygen and most reduced Mn of $Na_xZn_{1/3}Mn_{2/3}O_2$ (resp. a, b & c) and $Na_{4/7}Mn_{6/7}O_2$ (resp. d, e & f). $S_z$in $\mu_B$/Mn. (see fig. III.15 for details).

In $Na_{4/7}Mn_{6/7}O_2$, the collective distortion is shown to be favored all along the Na removal so that the charge should be perfectly reversible without voltage hysteresis nor capacity fading. These results are in good agreement with experimental data which show no hysteresis and a small voltage degradation. This was to be expected, given the small amount of electron removed per oxygen for a full oxidation ($\left\langle h^O \right\rangle = 2/7$) which is even lower for the real cycling range of this compound ($\left\langle h^O \right\rangle \approx 1/7$).

We have thus proposed a powerful method to sample the energy landscape based on the magnetic signature of the two oxygen redox mechanisms. The next challenge is now to extend this powerful methodology to other compounds. However, the necessity of the 1-to-1 correspondence of the $\langle S_z \rangle$ with the distortion type is the real challenge because so far, it can only be applied to compounds where the metal has a constant non-zero local magnetic moment (i.e. spectator high spin metals), such as $Mn^{4+}$. A first step would be to apply this methodology to other compounds, which metals show other

magnetic signature such as $d^0$ metals. In this case the 1-to-1 correspondence condition would impose to consider the ordering of oxygen pairs. This would allows to describe metals with lower electronegativity, such as $Ti^{4+}$, which would then open the way for the extension to sulfide, as a second step.

We now have two methods to quantify the A.R. reversibility in a compound. The first method, allows to predict the maximal reversible oxygen capacity $h^O_{rev}$, based on the bandgap of the pristine. The second method uses the magnetic signature of the anionic redox mechanism as a reaction coordinate to quantify the crossover from a reversible RCM to a irreversible disproportionation. While these two tools have already shown their potential, we also proposed several directions of improvement, thus leaving ample room for further research.

# Conclusion

To conclude, we will first recall the reasons that determined the goal and the methodology of the present study. We will then briefly summarize our findings using a slightly different articulation than in the main text, closer to the chronological order of these discoveries. Finally we will propose several perspectives to complement this work.

### Goal & methodology

The harnessing of anionic redox has proved valuable by offering a way to increase the performances of the $3d$ oxide cathodes which already had the highest performances among known compounds. To understand this phenomenon, the anionic redox was first characterized in $4/5d$ metals oxides which offered better reversibility and simpler stoichiometry. Based on this experimental data and on the early theoretical framework of Rouxel's hole chemistry, the contemporary model of anionic redox was proposed. In addition to the anionic polymerization mechanism – also called oxygen pairing – which seemed to be irreversible, another mechanism has been introduced : the reductive coupling mechanism (RCM). Contrary to the oxygen pairing, the RCM provides an enhanced stability to the compound via the formation of an M-O-O bond which enables hole delocalization. Based on this distinction, a Zaanen-Zavatsky-Allen approach (U vs $\Delta$) was used to assign each compound to either one of the two mechanisms. This dichotomy allowed to explain the trend towards stabilization observed when substituting $3d$ metals by a $4/5d$ ones.

While this theory was a clear step forward in the understanding of A.R., it still failed to describe the more subtle behavior variations such as the one observed upon substitution or disorder. Furthermore, this model was based on the approximation that all the oxygen sites are equivalent. This means that the unit cell only contains a few atoms. Hence the description of the interaction within this cell were closer to a molecular description, where the number of holes on the oxygen ($h^O$) is an integer. Unfortunately, for most real compounds, $h^O < 1/3$ even at full charge and there are numerous non-equivalent oxygen sites. Finally, this model was still qualitative and failed to provide quantitative prediction which could serve as a benchmark for the accuracy of the modeling and as a predictive tool for material screening. Hence the goal of this PhD was to refine that model and develop new tools to quantify and predict the type of behavior observed upon anionic redox.

Since the elaboration of this initial model, many other anionic redox compounds have been characterized. Most of them, obtained by metallic substitution of the original lithium oxides, were already well described by the molecular model. However, some compounds,

obtained by substituting either the alkali (Li→Na) or the anion (O→S), showed unexpected behavior. Namely, the Na-Ion anionic redox compounds showed a large hysteresis but a small degradation, while the lithium sulfides showed an even better reversibility with small hysteresis. These type of behavior could not be explained by the molecular model, thus offering the perfect platform to refine the theoretical framework and propose a new model. The method for our study was therefore to gather the main features of these new compounds to adapt the molecular model, without trying to complete an exhaustive (and exhausting!) list of all the A.R. compounds observed since 2017.

## Results

Having described our goal and our method, we therefore began this study with an in-depth investigation of Na-ion oxides, $Na_{2/3}M_{1/3}Mn_{2/3}O_2$ (M = Mg/Zn), which revealed two main findings: 1) The two mechanisms can coexist in the same compound, hence there is a competition which determines the global stability of the compound. 2) The RCM and the oxygen pairing both have very distinct structural signature (cooperative distortion for the RCM and Mg migration for the oxygen pairing). Furthermore, these structural effects are strongly influenced by slight changes in the local atomic arrangement ($P/O$ stacking). The study of the lithium sulfides confirmed these two findings, even though the high polarizability of S ions postponed the onset of irreversibility to a very high state of charge. These two compound-focused studies thus indicated two axes for the reevaluation of the model 1) the description of distortions, which are a link between the electronic and structural responses and 2) the study of the competition between the two mechanisms, which provides a way to quantify the reversibility of A.R..

Following this program, we first re-investigated the links between the electronic instability and the structural response. We discovered that to achieve a fractional $h^O$, the holes could either be localized or delocalized, thus generating two hole distributions which corresponded to the mechanisms previously identified. Indeed, if the holes are localized, they need to follow the molecular picture locally, hence leading to integer occupation number and a necessary disproportionation to achieve a fractional ratio. This charge disproportionation requires to break the crystallographic equivalence between oxygen atoms, either by a preexisting disorder or by a migration upon charging. This disproportionation thus leads to highly oxidized oxygen species, which are hard to reduce, hence explaining the capacity loss, and to cation migrations, which decrease the voltage of the redox couple, thus leading to hysteresis if they are reversible or to voltage decay if they are not. At the other side of the charge distribution spectrum, if the holes are homogeneously shared among the oxygen pairs, they have to be delocalized over the network which necessarily involves the metallic centers. This correlation between the local charges of the oxygen translates into a cooperative distortion of the M-X (X = O, S) bonds. This cooperative

distortion is thus favored by a flawless ordering, to enhance delocalization, and by increased bond elasticity (i.e. bond covalency) to accommodate the local strain without too much stress. This explains the high reversibility of anionic redox in layered sulfide.

This re-evaluation of the model shed light on the correlation between the A.R. mechanisms and the structural stability upon cycling: pure RCM is associated to reversible A.R. while the disproportionation leads to hysteresis and eventually to irreversible performance loss. Thus the study of this mechanism competition and the prediction of its outcome are paramount to identify new A.R. compounds. We therefore sought to develop predictive tools to quantify this competition. The comparison of oxygen environments was the first tool developed because it provided in-depth understanding with back-of-the-envelope reasoning. By considering the capacity associated to each species and the ionicity of the bonds they form, this method allows to estimate the hole distribution in the compound and, from there, the electrochemical behavior. While this method provides powerful chemical insight, it is only qualitative and cannot be used for accurate prediction. We therefore developed a more quantitative method, which consisted in comparing the relative energies of the metal and oxygen bands upon oxidation, in order to predict the occurrence of reductive elimination associated to $O_2$ release. By taking the chemical potential of the oxygen non-bonding states as a reference, the positions of the bands can be identified to the bandgap of the pristine compound and the width of the gap opened upon oxygen pairing. While the bandgap is compound specific, the oxygen pairing gap has to be computed only once, in a molecule. Hence this method provides quantitative result for a variety of compounds at a low computational cost. However, this cost-effectiveness comes at the price of low accuracy. We therefore developed a third method, which is really compound specific. Indeed, by taking advantage of the distinct magnetic signature of each A.R. mechanism, we could use the magnetization of the cell as a descriptor of the type of mechanism. We could thus compare the energies of the two mechanisms at each state of charge and deduce the composition limits of reversible cycling.

### Perspective

While these results provide better answer to previous problems, they also open several new questions and could serve as a platform for many directions of research.

From a formal perspective, the current description of the RCM could greatly benefit from a interdisciplinary reinterpretation. Indeed, in terms of physics, the description of the RCM as an avoided crossing would allow to take advantage of the the theoretical framework and quantitative tools that were developed in this field. Likewise, on the theoretical chemistry side, the study of the oxygen network distortion in terms of hidden nesting of Fermi surfaces, as developed by Canadell[80], [81] would provide valuable insight on the geometry of the structural instabilities observed.

Another direction for research is the kinetic description of the A.R. mechanism. Indeed, several recent theoretical works – seemingly contradictory – could be reconciled by considering that the metal acts as a fast charge-buffer due to its low chemical hardness, to accommodate the holes during the kinetically limiting oxygen pairing, associated to high hardness and high activation barrier for the distortion.

Form an experimental perspective, the next "refinement" of this model will obviously become necessary to account for the results emerging from sulfur redox in all solid state batteries, which allows to investigate the effects of pressure and temperature[117]. On the one hand, higher pressure increases the overlap and hence the energy gap associated to every interaction. On the other hand, higher temperature allows for better lattice kinetics, thus allowing a more reversible migration and pairing. Overall, these two parameters could be used as axes, along with charge and magnetization, to compute exciting yet not printable 4D functions which describe the A.R. reversibility.

Continuing on the improvement of the methods, the most obvious increment would be to achieve a more accurate description of the homolitic cleavage of the O-O bond upon charge, using refined computational methods such as a configuration interaction method to correctly describe the gap opening. This would however require to compute the cathode band structures with the same method and to refine the evaluation of the electrostatic shifts. As for the magnetization method, the next step is to extend these results to other metals, less electronegative, such as Ti, and, from there, to adapt the method to sulfides.

> In this PhD manuscript, we have retraced how the A.R. theory matured by confrontation with experimental results. This deeper understanding will, in turn, help the discovery of new compounds, with improved performances and lower environmental or ecological cost. However, to actually impact the global warming issue, these new compounds will have to reach the industrial stage. This requires not only a in-depth understanding from researchers but also some clever engineering in the later development stages. Hence this study is but a contribution to the collective effort towards a more sustainable future.

# References


[1] D. F. Birol, "World Energy Outlook - 2019", International Energy Agency, 2019, p. 810.

[2] "Global EV Outlook 2017", International Energy Agency, 2017, p. 71.

[3] S. Szabó, K. Bódis, T. Huld, and M. Moner-Girona, "Energy solutions in rural Africa: Mapping electrification costs of distributed solar and diesel generation versus grid extension", *Environmental Research Letters*, vol. 6, no. 3, p. 034 002, Jul. 1, 2011.

[4] J. Vergnet, "Stockage électrochimique : revue des technologies émergentes", *REE 2018-5*, vol. 2018, no. 5, pp. 57–70, Dec. 22, 2018.

[5] OSMOSE, "Comprehensive report on functionalities and services for the power system", European Union's Horizon 2020 research and innovation programme, D 4.1, Jun. 2019.

[6] "Dossier de saisine du projet de démonstrateur RINGO", Comission de régulation de l'Energie, Investissement 2018 de RTE - Annexe F, Nov. 29, 2017.

[7] S. Ruberg, "MIGRATE Deliverable 1.1 : Report on systemic issues", Project MIGRATE (Massive InteGRAtion of power Electronic devices), Dec. 15, 2016.

[8] N. M. A. 2020, "The Nobel Prize in Chemistry 2019", *NobelPrize.org*,

[9] N. W. Ashcroft and N. D. Mermin, *Solid State Physics*. New York: Holt, Rinehart and Winston, 1976, 826 pp.

[10] P. Geerlings, F. De Proft, and W. Langenaeker, "Conceptual Density Functional Theory", *Chemical Reviews*, vol. 103, no. 5, pp. 1793–1874, May 2003.

[11] F. R. Gamble, J. H. Osiecki, M. Cais, R. Pisharody, F. J. DiSalvo, and T. H. Geballe, "Intercalation Complexes of Lewis Bases and Layered Sulfides: A Large Class of New Superconductors", *Science*, vol. 174, no. 4008, pp. 493–497, Oct. 29, 1971.

[12] J. Rouxel, M. Danot, and M. Bichon, "Les composites intercalaires $Na_xTiS_2$. Etude générale des phases $Na_xTiS_2$ et $K_xTiS_2$", *Bull. Soc. Chim*, vol. 11, pp. 3930–3936, 1971.

[13] M. S. Whittingham, "Electrical Energy Storage and Intercalation Chemistry", *Science*, vol. 192, no. 4244, pp. 1126–1127, Jun. 11, 1976.

[14] A. Perez, "Energy storage properties of iridium oxides : Model materials for the study of anionic redox", Ph.D. Dissertation, Université Pierre et Marie Curie - Paris VI, Dec. 19, 2017.

[15] M. B. Armand, "Intercalation Electrodes", in *Materials for Advanced Batteries*, D. W. Murphy, J. Broadhead, and B. C. H. Steele, Eds., Boston, MA: Springer US, 1980, pp. 145–161.

[16] M. Lazzari and B. Scrosati, "A Cyclable Lithium Organic Electrolyte Cell Based on Two Intercalation Electrodes", *Journal of The Electrochemical Society*, vol. 127, no. 3, p. 773, 1980.

[17] K. Mizushima, P. Jones, P. Wiseman, and J. Goodenough, "$Li_xCoO_2$ (0", *Materials Research Bulletin*, vol. 15, no. 6, pp. 783–789, Jun. 1980.

[18] A. Yoshino, K. Sanechika, and T. Nakajima, "Secondary battery", U.S. Patent 4668595A, May 26, 1987.

[19] K. Ozawa, "Lithium-ion rechargeable batteries with $LiCoO_2$ and carbon electrodes: The $LiCoO_2$/C system", *Solid State Ionics*, vol. 69, no. 3-4, pp. 212–221, Aug. 1994.

[20] J. M. Tarascon, "The Li-Ion Battery: 25 Years of Exciting and Enriching Experiences", *Interface magazine*, vol. 25, no. 3, pp. 79–83, Jan. 1, 2016.

[21] S. Goriparti, E. Miele, F. De Angelis, E. Di Fabrizio, R. Proietti Zaccaria, and C. Capiglia, "Review on recent progress of nanostructured anode materials for Li-ion batteries", *Journal of Power Sources*, vol. 257, pp. 421–443, Jul. 2014.

[22] C. P. Sandhya, B. John, and C. Gouri, "Lithium titanate as anode material for lithium-ion cells: A review", *Ionics*, vol. 20, no. 5, pp. 601–620, May 2014.

[23] C. Delmas, I. Saadoune, and P. Dordor, "Effect of Cobalt Substitution on the Jahn-Teller Distortion of the $NaNiO_2$ Layered Oxide", *Molecular Crystals and Liquid Crystals Science and Technology. Section A. Molecular Crystals and Liquid Crystals*, vol. 244, no. 1, pp. 337–342, Apr. 1994.

[24] H.-J. Noh, S. Youn, C. S. Yoon, and Y.-K. Sun, "Comparison of the structural and electrochemical properties of layered $Li[Ni_xCo_yMn_z]O_2$ (x = 1/3, 0.5, 0.6, 0.7, 0.8 and 0.85) cathode material for lithium-ion batteries", *Journal of Power Sources*, vol. 233, pp. 121–130, Jul. 2013.

[25] L. Mucha, T. C. Frankel, and K. Domb Sadof. (Feb. 28, 2018). Perspective | The hidden costs of cobalt mining.

[26] A. K. Padhi, "Phospho-olivines as Positive-Electrode Materials for Rechargeable Lithium Batteries", *Journal of The Electrochemical Society*, vol. 144, no. 4, p. 1188, 1997.

[27] L. Chen, X. Fan, E. Hu, X. Ji, J. Chen, S. Hou, T. Deng, J. Li, D. Su, X. Yang, and C. Wang, "Achieving High Energy Density through Increasing the Output Voltage: A Highly Reversible 5.3 V Battery", *Chem*, vol. 5, no. 4, pp. 896–912, Apr. 2019.

[28] J. Lee, D. A. Kitchaev, D.-H. Kwon, C.-W. Lee, J. K. Papp, Y.-S. Liu, Z. Lun, R. J. Clément, T. Shi, B. D. McCloskey, J. Guo, M. Balasubramanian, and G. Ceder, "Reversible Mn2+/Mn4+ double redox in lithium-excess cathode materials", *Nature*, vol. 556, no. 7700, pp. 185–190, Apr. 2018.

[29] P. Kalyani, S. Chitra, T. Mohan, and S. Gopukumar, "Lithium metal rechargeable cells using $Li_2MnO_3$ as the positive electrode", *Journal of Power Sources*, vol. 80, no. 1-2, pp. 103–106, Jul. 1999.

[30] Z. Lu and J. R. Dahn, "Understanding the Anomalous Capacity of Li / $Li[Ni_xLi_{(1-2x)/3}Mn_{(2-x)/3}$ $O_2$ Cells Using In Situ X-Ray Diffraction and Electrochemical Studies", *Journal of The Electrochemical Society*, vol. 149, no. 7, A815, 2002.

[31] M. M. Thackeray, S.-H. Kang, C. S. Johnson, J. T. Vaughey, R. Benedek, and S. A. Hackney, "$Li_2MnO_3$-stabilized $LiMO_2$ (M = Mn, Ni, Co) electrodes for lithium-ion batteries", *Journal of Materials Chemistry*, vol. 17, no. 30, p. 3112, 2007.

[32] H. Koga, "Study of Li-rich lamellar oxides as positive electrode materials for lithium-ion batteries", Ph.D. Dissertation, Université Sciences et Technologies-Bordeaux I, 2013.

[33] A. D. Robertson and P. G. Bruce, "Mechanism of Electrochemical Activity in $Li_2MnO_3$", *Chemistry of Materials*, vol. 15, no. 10, pp. 1984–1992, May 2003.

[34] N. Yabuuchi, K. Yoshii, S.-T. Myung, I. Nakai, and S. Komaba, "Detailed Studies of a High-Capacity Electrode Material for Rechargeable Batteries, $Li_2MnO_3$ -$LiCo_{1/3}Ni_{1/3}Mn_{1/3}O_2$", *Journal of the American Chemical Society*, vol. 133, no. 12, pp. 4404–4419, Mar. 30, 2011.

[35] A. R. Armstrong, M. Holzapfel, P. Novák, C. S. Johnson, S.-H. Kang, M. M. Thackeray, and P. G. Bruce, "Demonstrating Oxygen Loss and Associated Structural Reorganization in the Lithium Battery Cathode $Li[Ni_{0.2}Li_{0.2}Mn_{0.6}]O_2$", *Journal of the American Chemical Society*, vol. 128, no. 26, pp. 8694–8698, Jul. 1, 2006.

[36] S. Muhammad, H. Kim, Y. Kim, D. Kim, J. H. Song, J. Yoon, J.-H. Park, S.-J. Ahn, S.-H. Kang, M. M. Thackeray, and W.-S. Yoon, "Evidence of reversible oxygen participation in anomalously high capacity Li- and Mn-rich cathodes for Li-ion batteries", *Nano Energy*, vol. 21, pp. 172–184, Mar. 2016.

[37] H. Koga, L. Croguennec, M. Ménétrier, K. Douhil, S. Belin, L. Bourgeois, E. Suard, F. Weill, and C. Delmas, "Reversible Oxygen Participation to the Redox Processes Revealed for $Li_{1.20}Mn_{0.54}Co_{0.13}$ $Ni_{0.13}O_2$", *Journal of The Electrochemical Society*, vol. 160, no. 6, A786–A792, 2013.

[38] M. Sathiya, G. Rousse, K. Ramesha, C. P. Laisa, H. Vezin, M. T. Sougrati, M.-L. Doublet, D. Foix, D. Gonbeau, W. Walker, A. S. Prakash, M. Ben Hassine, L. Dupont, and J.-M. Tarascon, "Reversible anionic redox chemistry in high-capacity layered-oxide electrodes", *Nature Materials*, vol. 12, no. 9, pp. 827–835, Jul. 14, 2013.

[39] P. E. Pearce, A. J. Perez, G. Rousse, M. Saubanère, D. Batuk, D. Foix, E. McCalla, A. M. Abakumov, G. Van Tendeloo, M.-L. Doublet, and J.-M. Tarascon, "Evidence for anionic redox activity in a tridimensional-ordered Li-rich positive electrode $\beta$-Li2IrO3", *Nature Materials*, vol. 16, no. 5, pp. 580–586, Feb. 27, 2017.

[40] J. Rouxel, "Anion - Cation Redox Competition and the Formation of New Compounds in Highly Covalent Systems", *Chemistry - A European Journal*, vol. 2, no. 9, pp. 1053–1059, Sep. 1996.

[41] R. Brec, P. Deniard, and J. Rouxel, "Chalcogenides: Electronic Properties", in *Progress in Intercalation Research*, Springer, 1994, pp. 177–221.

[42] S. Sasaki, D. Driss, E. Grange, J.-Y. Mevellec, M. T. Caldes, C. Guillot-Deudon, S. Cadars, B. Corraze, E. Janod, S. Jobic, and L. Cario, "A Topochemical Approach to Synthesize Layered Materials Based on the Redox Reactivity of Anionic Chalcogen Dimers", *Angewandte Chemie International Edition*, vol. 57, no. 41, pp. 13 618–13 623, Oct. 8, 2018.

[43] A. Dugast, R. Brec, G. Ouvrard, and J. Rouxel, "$Li_2FeS_2$, a cathodic material for lithium secondary battery", *Solid State Ionics*, vol. 5, pp. 375–378, Oct. 1981.

[44] G. Amatucci, "Cobalt dissolution in $LiCoO_2$-based non-aqueous rechargeable batteries", *Solid State Ionics*, vol. 83, no. 1-2, pp. 167–173, Jan. 1996.

[45] G. G. Amatucci, "$CoO_2$, The End Member of the $LiCoO_2$ Solid Solution", *Journal of The Electrochemical Society*, vol. 143, no. 3, p. 1114, 1996.

[46] J. M. Tarascon, G. Vaughan, Y. Chabre, L. Seguin, M. Anne, P. Strobel, and G. Amatucci, "In Situ Structural and Electrochemical Study of $Ni_{1-x}Co_xO_2$ Metastable Oxides Prepared by Soft Chemistry", *Journal of Solid State Chemistry*, vol. 147, no. 1, pp. 410–420, Oct. 1, 1999.

[47] M. K. Aydinol, A. F. Kohan, G. Ceder, K. Cho, and J. Joannopoulos, "Ab initio study of lithium intercalation in metal oxides and metal dichalcogenides", *Physical Review B*, vol. 56, no. 3, p. 1354, 1997.

[48] M. K. Aydinol, A. F. Kohan, and G. Ceder, "Ab initio calculation of the intercalation voltage of lithium-transition-metal oxide electrodes for rechargeable batteries", *Journal of power sources*, vol. 68, no. 2, pp. 664–668, 1997.

[49] G. Ceder, Y.-M. Chiang, D. R. Sadoway, M. K. Aydinol, Y.-I. Jang, and B. Huang, "Identification of cathode materials for lithium batteries guided by first-principles calculations", *Nature*, vol. 392, no. 6677, pp. 694–696, Apr. 1998.

[50] M.-P. Bichat, F. Gillot, L. Monconduit, F. Favier, M. Morcrette, F. Lemoigno, and M.-L. Doublet, "Redox-Induced Structural Change in Anode Materials Based on Tetrahedral $(MPn_4)^{x-}$ Transition Metal Pnictides", *Chemistry of Materials*, vol. 16, no. 6, pp. 1002–1013, Mar. 2004.

[51] M.-L. Doublet, F. Lemoigno, F. Gillot, and L. Monconduit, "The $Li_xVPn_4$ Ternary Phases (Pn = P, As): Rigid Networks for Lithium Intercalation/Deintercalation", *Chemistry of Materials*, vol. 14, no. 10, pp. 4126–4133, Oct. 2002.

[52] R. Xiao, H. Li, and L. Chen, "Density Functional Investigation on $Li_2MnO_3$", *Chemistry of Materials*, vol. 24, no. 21, pp. 4242–4251, Nov. 13, 2012.

[53] J. Zaanen, G. A. Sawatzky, and J. W. Allen, "Band gaps and electronic structure of transition-metal compounds", *Physical Review Letters*, vol. 55, no. 4, p. 418, 1985.

[54] J. Hubbard, "Electron Correlations in Narrow Energy Bands", *Proceedings of the Royal Society A: Mathematical, Physical and Engineering Sciences*, vol. 276, no. 1365, pp. 238–257, Nov. 26, 1963.

[55] J. J. Sakurai and J. Napolitano, "Chapter 5", in *Modern Quantum Mechanics*, 2nd ed, Boston: Addison-Wesley, 2011.

[56] D.-H. Seo, J. Lee, A. Urban, R. Malik, S. Kang, and G. Ceder, "The structural and chemical origin of the oxygen redox activity in layered and cation-disordered Li-excess cathode materials", *Nature chemistry*, vol. 8, no. 7, pp. 692–697, 2016.

[57] Y. Xie, M. Saubanère, and M.-L. Doublet, "Requirements for reversible extra-capacity in Li-rich layered oxides for Li-ion batteries", *Energy & Environmental Science*, vol. 10, no. 1, pp. 266–274, 2017.

[58] J. Rouxel, "Some solid state chemistry with holes: Anion - cation redox competition in solids", *Current Science*, vol. 73, no. 1, pp. 31–39, 1997. JSTOR: 24098143.

[59] W. Yin, A. Grimaud, G. Rousse, A. M. Abakumov, A. Senyshyn, L. Zhang, S. Trabesinger, A. Iadecola, D. Foix, D. Giaume, and J.-M. Tarascon, "Structural evolution at the oxidative and reductive limits in the first electrochemical cycle of $Li_{1.2}Ni_{0.13}Mn_{0.54}Co_{0.13}O_2$", *Nature Communications*, vol. 11, no. 1, p. 1252, Dec. 2020.

[60] A. Tygesen, J. Chang, T. Vegge, and J. M. García Lastra, "Computational Framework for a Systematic Investigation of Anionic Redox Process in Li-Rich Compounds", Nov. 20, 2019.

[61] M. Saubanère, E. McCalla, J.-M. Tarascon, and M.-L. Doublet, "The intriguing question of anionic redox in high-energy density cathodes for Li-ion batteries", *Energy & Environmental Science*, vol. 9, no. 3, pp. 984–991, 2016.

[62] B. M. de Boisse, G. Liu, J. Ma, S.-i. Nishimura, S.-C. Chung, H. Kiuchi, Y. Harada, J. Kikkawa, Y. Kobayashi, M. Okubo, and A. Yamada, "Intermediate honeycomb ordering to trigger oxygen redox chemistry in layered battery electrode", *Nature Communications*, vol. 7, ncomms11397, Apr. 18, 2016.

[63] M. Ben Yahia, J. Vergnet, M. Saubanère, and M.-L. Doublet, "Unified picture of anionic redox in Li/Na-ion batteries", *Nature Materials*, vol. 18, no. 5, pp. 496–502, May 2019.

[64] A. Urban, A. Abdellahi, S. Dacek, N. Artrith, and G. Ceder, "Electronic-Structure Origin of Cation Disorder in Transition-Metal Oxides", *Physical Review Letters*, vol. 119, no. 17, Oct. 25, 2017.

[65] B. Mortemard de Boisse, S.-i. Nishimura, E. Watanabe, L. Lander, A. Tsuchimoto, J. Kikkawa, E. Kobayashi, D. Asakura, M. Okubo, and A. Yamada, "Highly Reversible Oxygen-Redox Chemistry at 4.1 V in $Na_{4/7\text{-}x}[\square_{1/7}Mn_{6/7}\ ]O_2$ ($\square$: Mn Vacancy)", *Advanced Energy Materials*, vol. 8, no. 20, p. 1 800 409, Jul. 2018.

[66] A. Abdellahi, A. Urban, S. Dacek, and G. Ceder, "Understanding the Effect of Cation Disorder on the Voltage Profile of Lithium Transition-Metal Oxides", *Chemistry of Materials*, vol. 28, no. 15, pp. 5373–5383, Aug. 9, 2016.

[67] ——, "The Effect of Cation Disorder on the Average Li Intercalation Voltage of Transition-Metal Oxides", *Chemistry of Materials*, vol. 28, no. 11, pp. 3659–3665, Jun. 14, 2016.

[68] J. Rana, J. K. Papp, Z. Lebens-Higgins, M. Zuba, L. A. Kaufman, A. Goel, R. Schmuch, M. Winter, M. S. Whittingham, W. Yang, B. D. McCloskey, and L. F. J. Piper, "Quantifying the Capacity Contributions during Activation of Li $_2$ MnO $_3$", *ACS Energy Letters*, vol. 5, no. 2, pp. 634–641, Feb. 14, 2020.

[69] Y. Yue, N. Li, L. Li, E. E. Foley, Y. Fu, V. S. Battaglia, R. J. Clément, C. Wang, and W. Tong, "Redox Behaviors in a Li-Excess Cation-Disordered Mn–Nb–O–F Rocksalt Cathode", *Chemistry of Materials*, vol. 32, no. 11, pp. 4490–4498, Jun. 9, 2020.

[70] E. McCalla, A. M. Abakumov, M. Saubanere, D. Foix, E. J. Berg, G. Rousse, M.-L. Doublet, D. Gonbeau, P. Novak, G. Van Tendeloo, R. Dominko, and J.-M. Tarascon, "Visualization of O-O peroxo-like dimers in high-capacity layered oxides for Li-ion batteries", *Science*, vol. 350, no. 6267, pp. 1516–1521, Dec. 18, 2015.

[71] G. Assat and J.-M. Tarascon, "Fundamental understanding and practical challenges of anionic redox activity in Li-ion batteries", *Nature Energy*, vol. 3, no. 5, pp. 373–386, May 2018.

[72] G. Assat, A. Iadecola, C. Delacourt, R. Dedryvère, and J.-M. Tarascon, "Decoupling Cationic–Anionic Redox Processes in a Model Li-Rich Cathode via *Operando* X-ray Absorption Spectroscopy", *Chemistry of Materials*, vol. 29, no. 22, pp. 9714–9724, Nov. 28, 2017.

[73] B. J. Campbell, H. T. Stokes, D. E. Tanner, and D. M. Hatch, "*ISODISPLACE* : A web-based tool for exploring structural distortions", *Journal of Applied Crystallography*, vol. 39, no. 4, pp. 607–614, Aug. 1, 2006.

[74] X. Bai, M. Sathiya, B. Mendoza-Sánchez, A. Iadecola, J. Vergnet, R. Dedryvère, M. Saubanère, A. M. Abakumov, P. Rozier, and J.-M. Tarascon, "Anionic Redox Activity in a Newly Zn-Doped Sodium Layered Oxide P2-$Na_{2/3}Mn_{1-y}Zn_yO_2$ ($0 < y < 0.23$)", *Advanced Energy Materials*, vol. 8, no. 32, p. 1 802 379, Nov. 2018.

[75] J. Vergnet, M. Saubanère, M.-L. Doublet, and J.-M. Tarascon, "The Structural Stability of P2-Layered Na-Based Electrodes during Anionic Redox", *Joule*, vol. 4, no. 2, pp. 420–434, Feb. 2020.

[76] J.-H. Chung, T. Proffen, S. Shamoto, A. M. Ghorayeb, L. Croguennec, W. Tian, B. C. Sales, R. Jin, D. Mandrus, and T. Egami, "Local structure of $LiNiO_2$ studied by neutron diffraction", *Physical Review B*, vol. 71, no. 6, p. 064 410, Feb. 22, 2005.

[77] M. Roger, D. J. P. Morris, D. A. Tennant, M. J. Gutmann, J. P. Goff, J.-U. Hoffmann, R. Feyerherm, E. Dudzik, D. Prabhakaran, A. T. Boothroyd, N. Shannon, B. Lake, and P. P. Deen, "Patterning of sodium ions and the control of electrons in sodium cobaltate", *Nature*, vol. 445, no. 7128, pp. 631–634, Feb. 2007.

[78] M. Okubo and A. Yamada, "Molecular Orbital Principles of Oxygen-Redox Battery Electrodes", *ACS Applied Materials & Interfaces*, vol. 9, no. 42, pp. 36 463–36 472, Oct. 25, 2017.

[79] A. Hagopian and M.-L. Doublet, "Origine orbitalaire de la redox anionique dans les matériaux d'électrode enrichis en lithium", Master's Dissertation, Université de Montpellier, May 7, 2018.

[80] M. H. Whangbo and E. Canadell, "Analogies between the concepts of molecular chemistry and solid-state physics concerning structural instabilities. Electronic origin of the structural modulations in layered transition metal dichalcogenides", *Journal of the American Chemical Society*, vol. 114, no. 24, pp. 9587–9600, Nov. 1992.

[81] E. Canadell and M. H. Whangbo, "Conceptual aspects of structure-property correlations and electronic instabilities, with applications to low-dimensional transition-metal oxides", *Chemical Reviews*, vol. 91, no. 5, pp. 965–1034, Jul. 1991.

[82] W. E. Gent, K. Lim, Y. Liang, Q. Li, T. Barnes, S.-J. Ahn, K. H. Stone, M. McIntire, J. Hong, J. H. Song, Y. Li, A. Mehta, S. Ermon, T. Tyliszczak, D. Kilcoyne, D. Vine, J.-H. Park, S.-K. Doo, M. F. Toney, W. Yang, D. Prendergast, and W. C. Chueh, "Coupling between oxygen redox and cation migration explains unusual electrochemistry in lithium-rich layered oxides", *Nature Communications*, vol. 8, no. 1, p. 2091, Dec. 2017.

[83] M. D. Radin, J. Vinckeviciute, R. Seshadri, and A. Van der Ven, "Manganese oxidation as the origin of the anomalous capacity of Mn-containing Li-excess cathode materials", *Nature Energy*, vol. 4, no. 8, pp. 639–646, Aug. 2019.

[84] J. Hong, W. E. Gent, P. Xiao, K. Lim, D.-H. Seo, J. Wu, P. M. Csernica, C. J. Takacs, D. Nordlund, C.-J. Sun, K. H. Stone, D. Passarello, W. Yang, D. Prendergast, G. Ceder, M. F. Toney, and W. C. Chueh, "Metal–oxygen decoordination stabilizes anion redox in Li-rich oxides", *Nature Materials*, Feb. 4, 2019.

[85] L. Li, F. C. Castro, J. S. Park, H. Li, E. Lee, T. D. Boyko, J. W. Freeland, Z. Yao, T. T. Fister, J. Vinson, E. L. Shirley, C. Wolverton, J. Cabana, V. P. Dravid, M. M. Thackeray, and M. K. Y. Chan, "Probing Electrochemically Induced Structural Evolution and Oxygen Redox Reactions in Layered Lithium Iridate", *Chemistry of Materials*, vol. 31, no. 12, pp. 4341–4352, Jun. 25, 2019.

[86] J. Paier, M. Marsman, K. Hummer, G. Kresse, I. C. Gerber, and J. G. Ángyán, "Screened hybrid density functionals applied to solids", *The Journal of Chemical Physics*, vol. 124, no. 15, p. 154 709, Apr. 21, 2006.

[87] M. de Jong, W. Chen, T. Angsten, A. Jain, R. Notestine, A. Gamst, M. Sluiter, C. Krishna Ande, S. van der Zwaag, J. J. Plata, C. Toher, S. Curtarolo, G. Ceder, K. A. Persson, and M. Asta, "Charting the complete elastic properties of inorganic crystalline compounds", *Scientific Data*, vol. 2, no. 1, p. 150 009, 1 Mar. 17, 2015.

[88] G. J. Shu and F. C. Chou, "Sodium-ion diffusion and ordering in single-crystal P2-$Na_xCoO_2$", *Physical Review B*, vol. 78, no. 5, p. 052 101, Aug. 8, 2008.

[89] A. Mukhopadhyay and B. W. Sheldon, "Deformation and stress in electrode materials for Li-ion batteries", *Progress in Materials Science*, vol. 63, pp. 58–116, Jun. 2014.

[90] M. D. Radin and A. Van der Ven, "Stability of Prismatic and Octahedral Coordination in Layered Oxides and Sulfides Intercalated with Alkali and Alkaline-Earth Metals", *Chemistry of Materials*, vol. 28, no. 21, pp. 7898–7904, Nov. 8, 2016.

[91] C. Delmas, C. Fouassier, and P. Hagenmuller, "Structural classification and properties of the layered oxides", *Physica B+C*, vol. 99, no. 1, pp. 81–85, Jan. 1, 1980.

[92] J.-P. Parant, R. Olazcuaga, M. Devalette, C. Fouassier, and P. Hagenmuller, "Sur quelques nouvelles phases de formule $Na_xMnO_2$ ($x \leqslant 1$)", *Journal of Solid State Chemistry*, vol. 3, no. 1, pp. 1–11, Feb. 1971.

[93] X. Bai, "Chimie du redox anionique dans les oxydes lamellaires pour accumulateurs sodium-ion", Ph.D. Dissertation, Université Toulouse III - Paul Sabatier, Mar. 3, 2020.

[94] N. Yabuuchi, R. Hara, K. Kubota, J. Paulsen, S. Kumakura, and S. Komaba, "A new electrode material for rechargeable sodium batteries: P2-type $Na_{2/3}[Mg_{0.28}Mn_{0.72}]O_2$ with anomalously high reversible capacity", *J. Mater. Chem. A*, vol. 2, no. 40, pp. 16 851–16 855, 2014.

[95] U. Maitra, R. A. House, J. W. Somerville, N. Tapia-Ruiz, J. G. Lozano, N. Guerrini, R. Hao, K. Luo, L. Jin, M. A. Pérez-Osorio, F. Massel, D. M. Pickup, S. Ramos, X. Lu, D. E. McNally, A. V. Chadwick, F. Giustino, T. Schmitt, L. C. Duda, M. R. Roberts, and P. G. Bruce, "Oxygen redox chemistry without excess alkali-metal ions in $Na_{2/3}[Mg_{0.28}Mn_{0.72}]O_2$", *Nature Chemistry*, vol. 10, no. 3, pp. 288–295, Mar. 2018.

[96] K. Dai, J. Wu, Z. Zhuo, Q. Li, S. Sallis, J. Mao, G. Ai, C. Sun, Z. Li, W. E. Gent, W. C. Chueh, Y.-d. Chuang, R. Zeng, Z.-x. Shen, F. Pan, S. Yan, L. F. Piper, Z. Hussain, G. Liu, and W. Yang, "High Reversibility of Lattice Oxygen Redox Quantified by Direct Bulk Probes of Both Anionic and Cationic Redox Reactions", *Joule*, vol. 3, no. 2, pp. 518–541, Feb. 2019.

[97] B. Song, E. Hu, J. Liu, Y. Zhang, X.-Q. Yang, J. Nanda, A. Huq, and K. Page, "A novel P3-type $Na_{2/3}Mg_{1/3}Mn_{2/3}O_2$ as high capacity sodium-ion cathode using reversible oxygen redox", *Journal of Materials Chemistry A*, vol. 7, no. 4, pp. 1491–1498, 2019.

[98] W. Zheng, Q. Liu, Z. Wang, Z. Yi, Y. Li, L. Cao, K. Zhang, and Z. Lu, "Stabilizing the oxygen lattice and reversible oxygen redox in Na-deficient cathode oxides", *Journal of Power Sources*, vol. 439, p. 227 086, Nov. 2019.

[99] W. Zheng, Q. Liu, Z. Wang, Z. Wu, S. Gu, L. Cao, K. Zhang, J. Fransaer, and Z. Lu, "Oxygen redox activity with small voltage hysteresis in $Na_{0.67}Cu_{0.28}Mn_{0.72}O_2$ for sodium-ion batteries", *Energy Storage Materials*, vol. 28, pp. 300–306, Jun. 2020.

[100] E. Zhao, Q. Li, F. Meng, J. Liu, J. Wang, L. He, Z. Jiang, Q. Zhang, X. Yu, L. Gu, W. Yang, H. Li, F. Wang, and X. Huang, "Stabilizing Oxygen Lattice and Reversible Oxygen Redox Chemistry through Structural Dimensionality in Li-rich Cathode Oxides", *Angewandte Chemie International Edition*, Feb. 1, 2019.

[101] R. J. Clément, P. G. Bruce, and C. P. Grey, "Review—Manganese-Based P2-Type Transition Metal Oxides as Sodium-Ion Battery Cathode Materials", *Journal of The Electrochemical Society*, vol. 162, no. 14, A2589–A2604, 2015.

[102] R. A. House, U. Maitra, L. Jin, J. G. Lozano, J. W. Somerville, N. H. Rees, A. J. Naylor, L. C. Duda, F. Massel, A. V. Chadwick, S. Ramos, D. M. Pickup, D. E. McNally, X. Lu, T. Schmitt, M. R. Roberts, and P. G. Bruce, "What Triggers Oxygen Loss in Oxygen Redox Cathode Materials?", *Chemistry of Materials*, vol. 31, no. 9, pp. 3293–3300, May 14, 2019.

[103] K. Du, J. Zhu, G. Hu, H. Gao, Y. Li, and J. B. Goodenough, "Exploring reversible oxidation of oxygen in a manganese oxide", *Energy Environ. Sci.*, vol. 9, no. 8, pp. 2575–2577, 2016.

[104] E. de la Llave, E. Talaie, E. Levi, P. K. Nayak, M. Dixit, P. T. Rao, P. Hartmann, F. Chesneau, D. T. Major, M. Greenstein, D. Aurbach, and L. F. Nazar, "Improving Energy Density and Structural Stability of Manganese Oxide Cathodes for Na-Ion Batteries by Structural Lithium Substitution", *Chemistry of Materials*, vol. 28, no. 24, pp. 9064–9076, Dec. 27, 2016.

[105] X. Rong, E. Hu, Y. Lu, F. Meng, C. Zhao, X. Wang, Q. Zhang, X. Yu, L. Gu, Y.-S. Hu, H. Li, X. Huang, X.-Q. Yang, C. Delmas, and L. Chen, "Anionic Redox Reaction-Induced High-Capacity and Low-Strain Cathode with Suppressed Phase Transition", *Joule*, vol. 3, no. 2, pp. 503–517, Feb. 2019.

[106] E. Talaie, V. Duffort, H. L. Smith, B. Fultz, and L. F. Nazar, "Structure of the high voltage phase of layered P2-$Na_{2/3-z}[Mn_{1/2}Fe_{1/2}]O_2$ and the positive effect of Ni substitution on its stability", *Energy Environ. Sci.*, vol. 8, no. 8, pp. 2512–2523, 2015.

[107] C. Zhao, Z. Yao, J. Wang, Y. Lu, X. Bai, A. Aspuru-Guzik, L. Chen, and Y.-S. Hu, "Ti Substitution Facilitating Oxygen Oxidation in $Na_{2/3}Mg_{1/3}Ti_{1/6}Mn_{1/2}O_2$ Cathode", *Chem*, Aug. 2019.

[108] F. Flamary-Mespoulie, A. Boulineau, H. Martinez, M. R. Suchomel, C. Delmas, B. Pecquenard, and F. Le Cras, "Lithium-rich layered titanium sulfides: Cobalt- and Nickel-free high capacity cathode materials for lithium-ion batteries", *Energy Storage Materials*, vol. 26, pp. 213–222, Apr. 2020.

[109] J. M. Tarascon, F. J. DiSalvo, M. Eibschutz, D. W. Murphy, and J. V. Waszczak, "Preparation and chemical and physical properties of the new layered phases $Li_xTi_{1-y}M_yS_2$ with M = V, Cr, or Fe", *Physical Review B*, vol. 28, no. 11, pp. 6397–6406, Dec. 1, 1983.

[110] J. B. Goodenough and Y. Kim, "Locating redox couples in the layered sulfides with application to $Cu[Cr_2]S_4$", *Journal of Solid State Chemistry*, vol. 182, no. 10, pp. 2904–2911, Oct. 2009.

[111] S. Saha, "Exploration of ionic conductors and Li-rich sulfides for all-solid-state batteries", Ph.D. Dissertation, Université Pierre et Marie Curie - Paris VI.

[112] S. Saha, G. Assat, M. T. Sougrati, D. Foix, H. Li, J. Vergnet, S. Turi, Y. Ha, W. Yang, J. Cabana, G. Rousse, A. M. Abakumov, and J.-M. Tarascon, "Exploring the bottlenecks of anionic redox in Li-rich layered sulfides", *Nature Energy*, vol. 4, no. 11, pp. 977–987, Nov. 2019.

[113] M. Saubanère, M. B. Yahia, S. Lebègue, and M.-L. Doublet, "An intuitive and efficient method for cell voltage prediction of lithium and sodium-ion batteries", *Nature Communications*, vol. 5, ncomms6559, Nov. 24, 2014.

[114] G. Kresse and J. Hafner, *Vienna Ab-Initio Simulation Package*, version 5.4.4, University of Vienna, 2017.

[115] *Plotly API for Python*, version 4.1.0, Ploty, 2019.

[116] M. Sathiya, J.-B. Leriche, E. Salager, D. Gourier, J.-M. Tarascon, and H. Vezin, "Electron paramagnetic resonance imaging for real-time monitoring of Li-ion batteries", *Nature Communications*, vol. 6, no. 1, p. 6276, May 2015.

[117] F. Marchini, S. Saha, D. Alves Dalla Corte, and J. M. Tarascon, "Li-Rich Layered Sulfide as Cathode Active Materials in All-Solid-State Li-Metal Batteries", *ACS Applied Materials & Interfaces*, acsami.9b22937, Mar. 23, 2020.

[118] S. P. Ong, W. D. Richards, A. Jain, G. Hautier, M. Kocher, S. Cholia, D. Gunter, V. L. Chevrier, K. A. Persson, and G. Ceder, "Python Materials Genomics (pymatgen): A robust, open-source python library for materials analysis", *Computational Materials Science*, vol. 68, pp. 314–319, Feb. 2013.

[119] M. Ångqvist, W. A. Muñoz, J. M. Rahm, E. Fransson, C. Durniak, P. Rozyczko, T. H. Rod, and P. Erhart, "ICET - A Python Library for Constructing and Sampling Alloy Cluster Expansions", *Advanced Theory and Simulations*, vol. 2, no. 7, p. 1 900 015, 2019.

[120] I. N. Levine, *Quantum Chemistry*, Seventh edition. Boston: Pearson, 2014, 700 pp.

[121] G. I. Csonka, J. P. Perdew, A. Ruzsinszky, P. H. T. Philipsen, S. Lebègue, J. Paier, O. A. Vydrov, and J. G. Ángyán, "Assessing the performance of recent density functionals for bulk solids", *Physical Review B*, vol. 79, no. 15, p. 155 107, Apr. 10, 2009.

[122] A. V. Krukau, O. A. Vydrov, A. F. Izmaylov, and G. E. Scuseria, "Influence of the exchange screening parameter on the performance of screened hybrid functionals", *The Journal of Chemical Physics*, vol. 125, no. 22, p. 224 106, Dec. 13, 2006.

[123] G. Kresse and J. Furthmüller, "Efficient iterative schemes for *ab initio* total-energy calculations using a plane-wave basis set", *Physical Review B*, vol. 54, no. 16, pp. 11 169–11 186, Oct. 15, 1996.

[124] P. E. Blöchl, "Projector augmented-wave method", *Physical Review B*, vol. 50, no. 24, pp. 17 953–17 979, Dec. 15, 1994.

[125] G. Kresse and D. Joubert, "From ultrasoft pseudopotentials to the projector augmented-wave method", *Physical Review B*, vol. 59, no. 3, pp. 1758–1775, Jan. 15, 1999.

[126] S. Grimme, S. Ehrlich, and L. Goerigk, "Effect of the damping function in dispersion corrected density functional theory", *Journal of Computational Chemistry*, vol. 32, no. 7, pp. 1456–1465, May 2011.

[127] S. Grimme, J. Antony, S. Ehrlich, and H. Krieg, "A consistent and accurate *ab initio* parametrization of density functional dispersion correction (DFT-D) for the 94 elements H-Pu", *The Journal of Chemical Physics*, vol. 132, no. 15, p. 154 104, Apr. 21, 2010.

[128] S. L. Dudarev, G. A. Botton, S. Y. Savrasov, C. J. Humphreys, and A. P. Sutton, "Electron-energy-loss spectra and the structural stability of nickel oxide: An LSDA+U study", *Physical Review B*, vol. 57, no. 3, pp. 1505–1509, Jan. 15, 1998.

[129] G. Henkelman, A. Arnaldsson, and H. Jónsson, "A fast and robust algorithm for Bader decomposition of charge density", *Computational Materials Science*, vol. 36, no. 3, pp. 354–360, Jun. 2006.

[130] A. D. Becke and K. E. Edgecombe, "A simple measure of electron localization in atomic and molecular systems", *The Journal of Chemical Physics*, vol. 92, no. 9, pp. 5397–5403, May 1990.

[131] A. Savin, O. Jepsen, J. Flad, O. K. Andersen, H. Preuss, and H. G. von Schnering, "Electron Localization in Solid-State Structures of the Elements: The Diamond Structure", *Angewandte Chemie International Edition in English*, vol. 31, no. 2, pp. 187–188, Feb. 1992.

[132] S. Maintz, V. L. Deringer, A. L. Tchougréeff, and R. Dronskowski, "LOBSTER: A tool to extract chemical bonding from plane-wave based DFT: Tool to Extract Chemical Bonding", *Journal of Computational Chemistry*, vol. 37, no. 11, pp. 1030–1035, Apr. 30, 2016.

[133] L. Wang, T. Maxisch, and G. Ceder, "Oxidation energies of transition metal oxides within the GGA + U framework", *Physical Review B*, vol. 73, no. 19, p. 195 107, May 4, 2006.

[134] A. Togo and I. Tanaka, "First principles phonon calculations in materials science", *Scripta Materialia*, vol. 108, pp. 1–5, Nov. 2015.

# Annex : Computational methods

Computers are useless, they can only give you answers.

Pablo Picasso

In this annex, we will describe the tools used during this PhD in an order which follows the workflow of a computational chemistry project illustrated in fig. 1. Indeed such study is always structured by an initial input which has to be refined and adapted to be suitable for DFT calculation. The DFT output is then processed to yield results. If these results are not satisfactory, another iteration of formatting and relaxation is required.

This presentations of the methods will therefore begin with the tools used in pre-processing, to design the super-cells given in input to a DFT code, with a special emphasis on disorder. We will then briefly recapitulate the principle of DFT and our choice of parameters. We will then describe the various methods used for the analysis of the DFT results. The last section of this chapter will be devoted to the description of the ReadWrite package, which was used as a growing repository to regroup and articulate all the methods used, so as to ensure efficiency, consistency & continuous improvement.

## Methods

### Pre-processing tools

#### Initial structures

**Stacking structures** Starting from the experimental *P2* structure obtained by XRD refinement, partial occupancies have been rounded up to avoid disorder. From these perfect *P2* structure, *O2* and *OP4* structures were derived by layer gliding using the Python Material Genome library[118]. This requires to glide both the $MO_2$ layer and the Na atoms that are directly above it. Likewise, the *O3* structure have been derived from the *P2* structure by a gliding of the oxygen planes only.

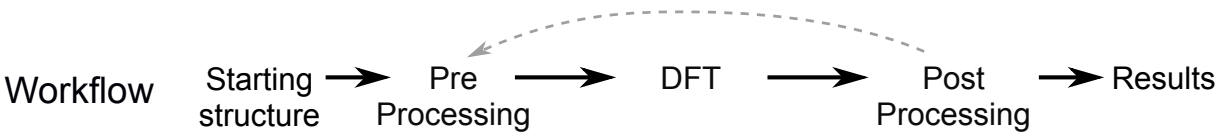


Figure 1: Computational chemistry workflow.

**Disorder** The generation of disordered structures from this perfect structures have been realized by the method described in the chapter II.2. because the cluster expansion method is too long and not in the exact scope of this study (even though they have been tested using the *ICET* library[119]). Indeed, the Cluster expansion method consists in 1) calibrating an effective Hamiltonian (made of atom-pair, triplet and tetrahedron interactions) of several hundreds of DFT converged structures, 2) using this Hamiltonian to estimate the energy of all the structures in the configuration space and 3) find the structure which possesses the same number of pair/triplet/tetrahedra as the whole configuration space (weighted by the energy of each component) and 4) use this structure as a representative of the average disorder. Of course, the larger the structure, the more accurate the estimate. While this technique is very powerful to study fully disordered compounds such as alloys with a small amount of components, its becomes very expensive when considering ionic, anisotropic and partially ordered structures such as electrodes.

### Desodiated structures

To obtain the desodiated structures, we iteratively removed the Na nuclei according to their Madelung energy (assuming integer oxidation state for every ion). This technique is less accurate but much faster than the enumeration of all permutations for each composition. Removing two distinct Na sites at each iteration (either highest or second highest Madelung energy) allowed for the creation of distinct Na-orders for each Na content. From there, we used the structures on (or near) the convex hull to perform further analysis.

## Density Functional Theory

**Self-consistent equation** The first Hohenberg-Kohn theorem states that the ground-state properties of a many-electron system are uniquely determined by its electron density that depends on only three spatial coordinates. The second Hohenberg-Kohn theorem defines an energy functional for the system and proves that the correct ground-state electron density minimizes this energy functional.

The integration from a possible many-body wavefunction $\phi$ to a possible electron density $\rho$ is an injective mapping (several $\phi$ integrate to the same $\rho$ while some $\rho$ cannot be represented by any $\phi$). Unfortunately, the DFT principle only applies if the density can be represented by an existing $\phi$. To ensure this representability, the Kohn-Sham DFT replaces the $\phi$ of interacting electrons by a fictious $\phi$ of non-interacting electrons of the same $\rho$. Since this non-interacting $\phi$ can be represented by a single Slater determinant, it also drastically increases the computational efficiency while preserving the accuracy while preserving the physical meaning of the density. The physical meaning of the wavefunction is however greatly impaired. [120]

The wavefunction $\phi$ depends on the Hamiltonian which depends on $\rho$ which is determined by $\phi$. Thus the Shrodinger equation is self-consistent. This equation is therefore solved iteratively until the variation in either $\phi$, $\rho$ or $E$ is lower that a threshold. *We used an energy threshold of* $10^{-5}\,eV$.

**Functionals** The effective potential includes the external potential and the effects of the Coulomb interactions between the electrons, e.g., the exchange and correlation interactions. The modeling of exchange and correlation interaction is the main difficulty of modern DFT. The simplest approximation is the local-density approximation (LDA), which is based on a uniform electron gas with the same density as the system. The exact exchange energy obtained from the Thomas–Fermi model and the correlation energy is fitted. Hence the LDA only depends on the number of electrons. To refine the estimation of the exchange-correlation, new functionals were proposed by taking higher orders in the spatial Taylor expansion: the generalized Gradient approximation uses $\nabla n$ and meta-GGA also use $\nabla^2 n$.[120] *We generally used the PBE-54 flavor [121] and the hybrid HSE06 [122]when specifically mentioned.*

**Periodic boundaries** If the external potential is periodic, as in the case of crystals, Bloch's theorem states that the wavefunctions are also periodic and can be expressed as Bloch orbitals: a periodic functions $u\,(r)$ modulated by a phase $\exp\,(ik.r)$. Thus for crystals, DFT can be reformulated by expressing the periodic K-S orbitals as a linear combination of planewaves. *This is the core principle of the Vienna Ab-Initio Simulation Package (VASP), which was used for the whole study[123].*

The density near the nuclei oscillates at a very high frequency so it must be described by very short wavelengths. To minimize the computational costs, the potential of the nuclei screened by their core electrons are approximated by pseudopotentials, thus allowing to reduce the number of planewaves required to describe the system to a finite number (and fortunately low enough for application). *We thus used the Projector augmented-wave method which derives from this concept[124], as implemented in VASP [125], and we generally limited the planewave energy to 600 eV.*

**Ionic relaxation** Once the electronic density is known for a set of atomic coordinate, the Hellman-Feynman theorem states that the derivative of the atomic energy with respect to nuclei coordinates (i.e. the electrostatic force exerted on the nuclei) is the Coulomb interaction of point charge nuclei and smeared electrons. Using these forces (and the nuclei repulsion), the nuclei positions can be relaxed in the direction of the forces. Since the position of the atoms depend on the forces which depend on the density which depends on the position of the atoms, this is also a self-consistent equation which is iterated until the variation in the forces is lower than a threshold.[120] *We used a threshold of* $10^{-3}\,eV/\mathring{A}$.

**Corrections** Additional terms can be added to the functionals to account for specific effects. Since we studied layered compounds structured by Van der Waals gaps, we always used a correction to account or long range interactions due to Van Der Waals interactions *(Becke-Jonson damping DFT-D3)*[126], [127].

Another term can be added to account for the Coulomb repulsion within $d$ orbitals. In the simplified (rotationally invariant) approach to the LSDA+U, introduced by Dudarev et al. [128], the Hubbard interaction is implemented as a penalty to the total energy that forces the on-site occupancy matrix towards having either 1 or 0 occupation coefficient on each site[114]. When spin channels are treated independently, this translates into one spin channel of the $d$-block being populated (occupancy =1) and the other being empty (occupancy =0) without considering the possible spin orderings (others than ferromagnetic). Thus the DFT+U opens a gap between the spin channels instead of opening a proper Hubbard gap. This approximation leads to identify the lower and upper Hubbard bands to the spin-up and spin-down bands. *We therefore always included a U correction (rotationally invariant)[128] (*$U_{Mn}$ *= 3.9 eV,* $U_{Fe}$*=2 eV).*

## Post-processing of DFT result

In K-S DFT, $\rho$ is a meaningful quantity (it converges towards the real density) while $\phi$ was just a fictious function of non-interacting electrons (which cannot represent the real wavefunction). Therefore method based on the density are much more reliable than those based on orbitals. That being said orbital based methods are very powerful and useful for qualitative analysis.

### Density based analysis

**Bader integration** Starting from the density, the identification of atoms in molecule proves very helpful to quantify atom-wise properties and their evolution. This identification relies on the definition of the domains in which the charge can be attributed to an atom. Since the nuclei are positively charged, the density of isolated atoms decreases with the radius. If two atoms are nearby, their respective basins are separated by the surfaces where $\nabla\rho = 0$. This analysis allows to define Bader population ($\int \rho$ in the basin) from which the Bader charge can be computed, by subtracting the number of valence electron. Using this Bader charge, one can calculate a Madelung energy which take into account partial the partial charge transfer associated to covalent bonding (contrary to formal charges which assume purely ionic bonds). *We used the code from Henkelman's group[129].*

**Electronic response functions**

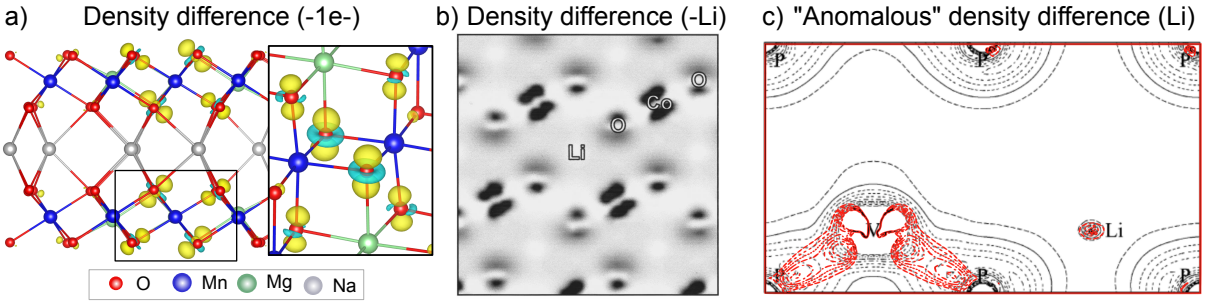


Figure 2: Electronic responses to oxidation, computed by decreasing the number of electron directly (a) or by changing the number of Li (negative (b) and positive charge variations (c)).

**Fukui Function** The Fukui functions represent the density associated to the frontier orbitals, which are basically the HOMO and LUMO in a molecule and represent the reactive orbitals upon reduction or oxidation in a crystal. These orbitals depict the variation of density upon a change in electron count, while the external potential remains constant (i.e. constant number and position of the nuclei). Computationally speaking, they can be computed as the difference between the $\rho$ of a structure and the $\rho$ of the same structure (no ionic relaxation) after a change of the electron number (*NELECT* tag in VASP):

$$f = \rho\left(N_{e-} - 1\right) - \rho\left(N_{e-}\right)$$

This change in the electron count will create a charged structure (fig. 2.a). This calls for the introduction of a charged background (Jellium model).

**Iso-structural delithiation** To avoid this jellium artifact, which is prone to errors in planewave DFT, the removal of an electron can also be matched by the removal of a $Li^+$, while keeping the position of the other atoms constant. This is the approach adopted by Ceder *& al.* in their seminal work on $LiCoO_2$to characterize the occurrence of anionic participation to the redox process (fig. 2.b):

$$f = \rho\left(N_{Li} - 1\right) - \rho\left(N_{Li}\right)$$

However, as it comes from the covalent intermixing of $O_{2p}$ and $M_d$, this participation does not bring extra capacity and is, as such, not considered as anionic redox. Thus this method is not sufficient to characterize anionic redox.

In their work on Pnictides, Doublet *& al.* used a refinement of this approach by considering only the "anomalous" variation of charge upon iso-structural delithiation, i.e. the electron density increase upon Li removal (see fig. 2.c). While this method allowed to evidence the RCM, it was not sufficient to localize non-bonding states, unlike the ELF

as we will now see.

**Electron Localization Function** The Electron Localization Function (ELF) was first proposed by Becke and Edgecombe for molecules [130] and adapted to solid by Savin *& al.* [131]. To describe the physical meaning of the ELF, which values are defined in $[0, 1]$, Savin *& al.* stated that "Values are close to 1 when in the vicinity of one electron, no other with the same spin may be found, for instance as occurs in bonding pairs or lone pairs. Small values are typical for the region between two electron shells (Pauli principle). In a homogeneous electron gas, ELF = 0.5". Interestingly, lone pairs being more localized than bonding pairs, they have a higher ELF value. Using a high value threshold, the ELF can thus discriminate and locate the non-bonding electrons. In conclusion, we can say that the ELF is a reliable and accurate tool for visualization and characterization of oxygen non-bonding pairs.

### Kohn-Sham Orbital based analysis

**Projection in real space: Parcharg** The most direct orbital based method is to plot the PARtial CHARGge density method (coined as Parcharg), which consists in summing the probability density of all the KS orbitals within a specified energy range. Unfortunately, this energy criteria is not sufficient to discriminate the bonding or non-bonding nature of the orbital. While this method has been extensively used to plot the electronic states at the tom of the valence band, this method is far less accurate than the density difference method we introduced earlier, since it relies on fictious KS orbitals.

**Crystal Orbital Overlap Population** The crystal orbital overlap population (COOP) was computed using the LOBSTER program [132]. By comparing a the same time the pDOS, the COOP of the Mn-O bonds and of the intra-layer O-O bonds we can guess an orbital type to every part of the DOS, as in the fig. II.8 on page 73 (reproduced in fig. 3 on the facing page ).

- $e_g^*$ (pink): $S_{\text{M-O}} \ll 0$ and $S_{\text{O-O}} \ll 0$
- $t_{2g}^*$ (green): $S_{\text{M-O}} \ll 0$ and $S_{\text{O-O}} \approx 0$ (if empty)
- $\text{Mn}_d$-$|\text{O}_{2p}$ (yellow): $S_{\text{M-O}} < 0$ and $S_{\text{O-O}} < 0$.
- $t_{2g}$ (blue): $S_{\text{M-O}} \gg 0$ and $S_{\text{O-O}} \approx 0$ (if empty)

This method is however very qualitative since it is based on the comparison of projection of KS orbitals. We can still observe the evolution of the orbitals upon charging.

### Energy based DFT results

**$O_2$ release** $\Delta E_{O2}$was obtained following Xie *& al.* [57]: we first computed the energy of the $O_2$ molecule $E(O_2)$ corrected with the empirical parameter given by Ceder's

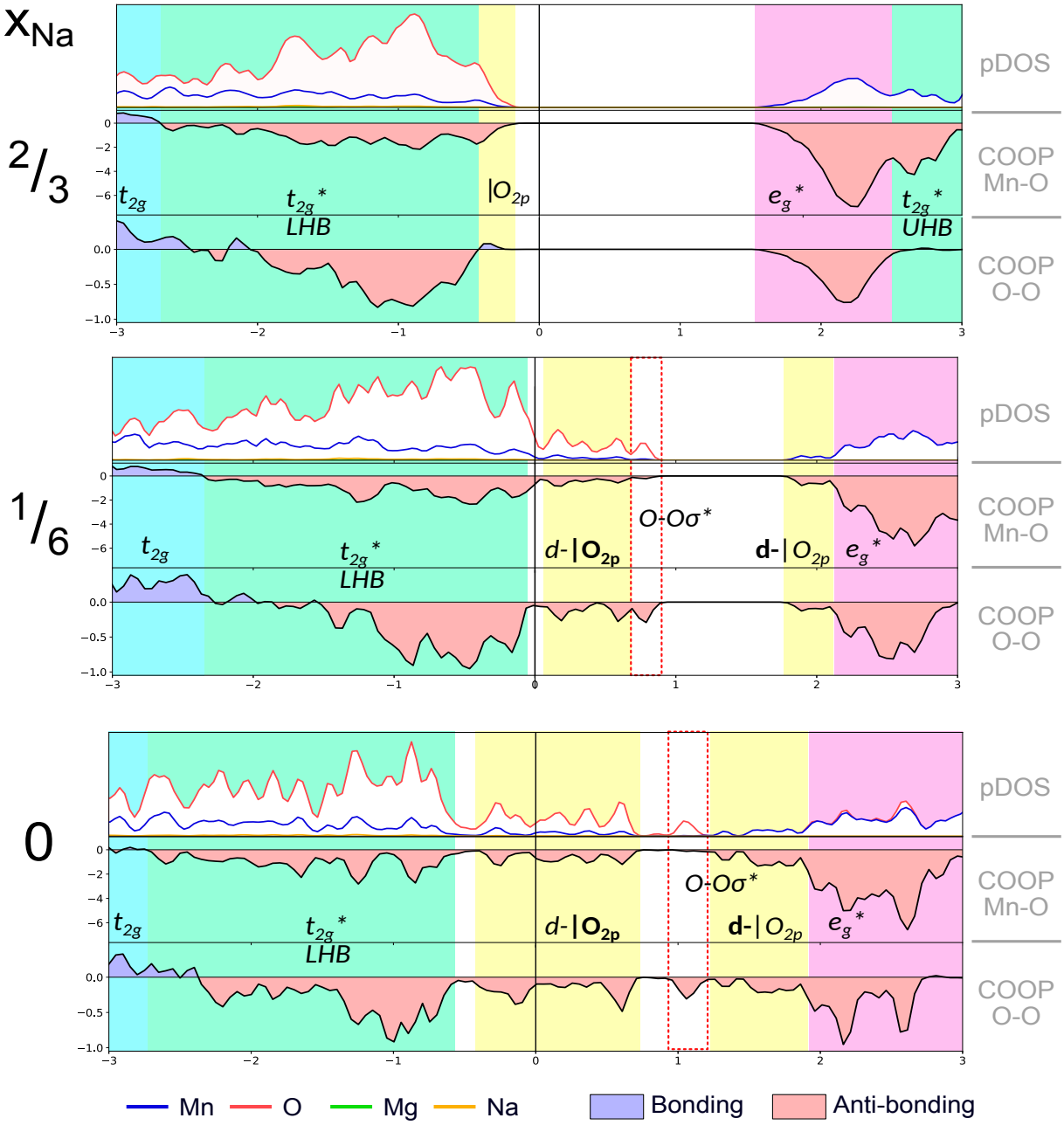


Figure 3: Evolution of NMgMO electronic structure upon charging (DOS, O-O and Mn-O COOPs) where orbital have been identified. The scale for the Mn-O coop is 6x larger than for O-O.

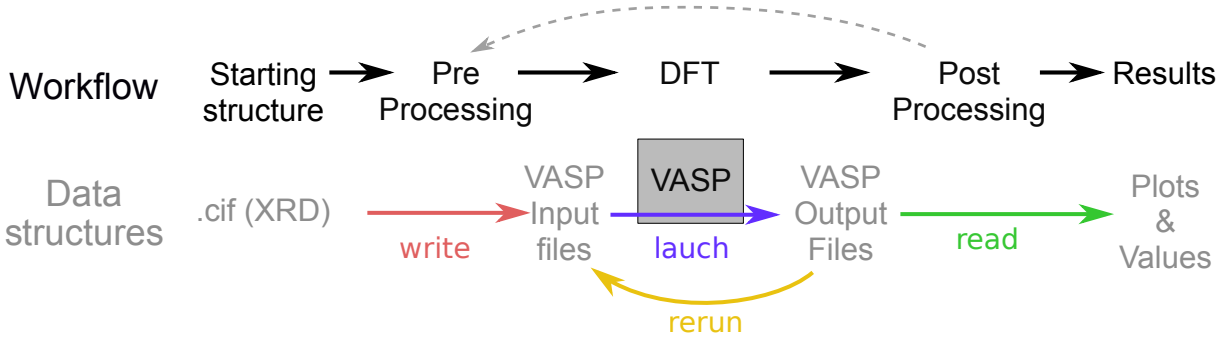


Figure 4: Computational chemistry workflow and scope of the developed *ReadWrite* python package

group[133]. Then, for a given relaxed structure, with $N_O$ oxygen atoms, of energy $E(N_O)$, we removed the most oxidized oxygen (lowest Bader population) and computed the energy of the fully relaxed oxygen-deficient structure $E(N_O - 1)$. When neglecting the influence of entropy, the $O_2$ release enthalpy is then given by:

$$\Delta E_{O2} = [E(N_O - 1) + \frac{1}{2}E(O_2)] - E(N_O)$$

**Phonon modes** Starting from the equilibrium structure, stress due to displacement along x ($\partial x$) is approximated with a Taylor expansion. Since the initial position is an equilibrium the first derivative is nil, the strain/stress relation is approximated by a quasi-harmonic method using small displacements. This enables to build the hessian matrix, from which the phonon band structure can be derived using the *Phonopy* software (and its python API)[134].

## Homemade ReadWrite package

If we detail the workflow of computational chemistry exposed at the beginning of this annex, we notice that the workflow is seldom a linear process from the initial structure to the final plot but most often requires a great deal of error and trial between the first computation and the one that will be used as a basis for the published result. This error and trial process is symbolized as a loop (dashed arrow) from the pre-processing step – where the structure and computational parameters are defined – and the post-processing step – where the results are read and processed. As an example, an unsatisfactory post-processing (e.g. unconverged relaxation or nonphysical result) will lead to change the parameters and another VASP job. Furthermore, when considering the data structure and the software used to process and convert the data between these steps, and the numerous types of data types used for post-processing (Bader, phonopy, p4v,Lobster,...), it is clear that the conversion and interface is the kinetic barrier for running a smooth

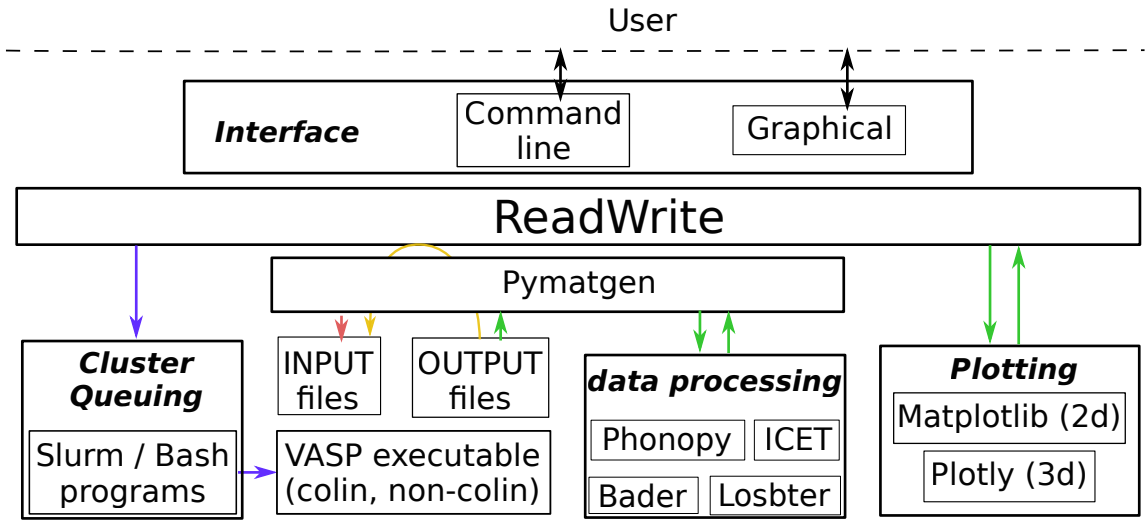


Figure 5: ReadWrite package architecture. The 4 typical workflow are illustrated by colored arrow: Write (red), Launch (blue), Rerun (yellow) and Read (green).

workflow.

To undertake the numerous computations needed for the completion of this study, I first used the Pymatgen library, which allows to interface very efficiently all the external post-processing tools, as indicated in fig. 4. However, I could not find any efficient method to control the workflow, apart form very high end tools such as Fireworks, which is intended for very high throughput calculation. In addition to having a steep learning curve, this tools does not allow for a full control over the computational parameters. I therefore decided to code my own "workflow toolbox" which is based on 4 main commands, which can then be refined interactively: Write, Launch, Rerun and Read. Over time, this toolbox took the form of a python package, called ReadWrite, available publicly on Github at: *https://github.com/JVergnet/read_write*. In order to explain this toolbox, I realized a tutorial (IPython notebooks), available at: *https://github.com/JVergnet/tutorial_readWrite*.

This ReadWrite package is structured as an interface between the user and the computational tools (see fig. 5). The communication with the tools is realized via Pymatgen. Unfortunately, Pymatgen is unable to launch jobs, this is why I also interfaced the package to the cluster via the bash command line and a set of different SLURM jobs which can be queued on the cluster directly via the python code. Finally, in order to analyze the data obtained, the ReadWrite package is also interfaced with 2D and 3D plotting libraries. Hence this package acts as a workflow manager which uses Pymatgen as a interface with the various file format used by other solid state analysis codes.

## Experimental structure of $Na_{2/3}Mg_{1/3}Mn_{2/3}O_2$

– .cif format –

```
#============================
# CRYSTAL DATA
#---------------------------------------------------------------------
data_VESTA_phase_1
_chemical_name_common 'P2-Na2/3[Mg0.3Mn0.7]O2-193'
_cell_length_a 5.01915
_cell_length_b 5.01915
_cell_length_c 11.19101
_cell_angle_alpha 90
_cell_angle_beta 90
_cell_angle_gamma 120
_space_group_name_H-M_alt 'P 63/m c m'
_space_group_IT_number 193
loop_
_space_group_symop_operation_xyz
'x, y, z' '-x, -y, -z' '-y, x-y, z', 'y, -x+y, -z' '-x+y, -x, z' 'x-y, x, -z'
'-x, -y, z+1/2' 'x, y, -z+1/2"y, -x+y, z+1/2' '-y, x-y, -z+1/2' 'x-y, x, z+1/2' '-x+y, -x,
-z+1/2'
'y, x, -z+1/2' '-y, -x, z+1/2' 'x-y, -y, -z+1/2' '-x+y, y, z+1/2' '-x, -x+y, -z+1/2' 'x, x-y,
z+1/2'
'-y, -x, -z' 'y, x, z' '-x+y, y, -z' 'x-y, -y, z' 'x, x-y, -z' '-x, -x+y, z'
loop_
_atom_site_label
_atom_site_occupancy
_atom_site_fract_x _atom_site_fract_y _atom_site_fract_z
_atom_site_adp_type
_atom_site_B_iso_or_equiv
_atom_site_type_symbol
O 1.0 0.354000 0.000000 0.920000 Biso 1.000000 O
Mg 0.7000 0.000000 0.000000 0.000000 Biso 1.000000 Mg
Mn 0.3000 0.000000 0.000000 0.000000 Biso 1.000000 Mn
Mn 1.0 0.333333 0.666667 0.000000 Biso 1.000000 Mn
Na 0.3133 0.301000 0.000000 0.250000 Biso 1.000000 Na
Na 0.3500 0.333333 0.666667 0.250000 Biso 1.000000 Na
```

# List of Figures

# List of Tables